TURN TO DESK

JOURNAL OF THE AERONAUTICAL SCIENCES

THE JOHN CRER APR 1 1 1947 LIBRARY

VOLUME 12 OCTOBER, 1945 NUMBER 4

CONTENTS

Effect of Temperature Lapse Rate on Recovery from Compressibility Dives . . . C. E. PAPPAS AND M. G. HARRISON 379

The Simplification of Flutter Calculations by Use of an Extended Form of the Routh-Hurwitz Discriminant . . . . . S. SHERMAN, J. DIPAOLA, AND H. F. FRISSEL 385

Buckling of Stiffener and Elastic Sheet Combinations Under Pure Bending . . . E. E. WEIBEL 393

Note on Analysis for Bending with Buckled Stringers . . . EDWARD A. MACLEAN 403

Plastic Bending—Approximate Solution . . . . . WM. R. OSGOOD 408

Graphical Analysis of Performance of Hydraulic Shock Absorbers in Aircraft Landing Gears . . . . . ALEXANDER J. YORGIADIS 421

A General Stability Index for Flow Near Plane Boundaries . . . HUNTER ROUSE 429

On the Dynamics of Elastic Buckling . . . . . J. H. MEIER 433

Reverse-Pitch Propellers as Airplane Landing Brakes . . . . . HAROLD B. CROCKETT AND E. ARTHUR BONNEY 441

Influence of Prestressing and Cyclic Stressing on Stress-Strain Characteristics of Magnesium Alloys . . . . . F. A. RAPPLEYEA, R. E. PERRY, AND G. ANSEL 448

The Applicability of Saint-Venant's Principle to Airplane Structures . . N. J. HOFF 455

Shear Lag and Torsion Bending of Four-Element Box Beams . . R. E. NEWTON 461

The Aerodynamic Performance of Small Spheres from Subsonic to High Supersonic Velocities . . . . . A. C. CHARTERS AND R. N. THOMAS 468

A Direct Method of Estimating the Performance of a Helicopter in Powered Flight . . . . . WALTER CASTLES, JR. 477

Instability of Extrusions Under Compressive Loads . . . . . WALTER RAMBERG AND SAMUEL LEVY 485

Letters to the Editor 407, 431, 432, 476

Index to Volume 12 499

Copyright, 1945, by the

INSTITUTE OF THE AERONAUTICAL SCIENCES, INC.

JOURNAL OF THE AERONAUTICAL SCIENCES

VOL. 12 OCTOBER, 1945 NO. 4

PUBLISHED QUARTERLY BY THE INSTITUTE OF THE AERONAUTICAL SCIENCES, INC.

Chairman of the Editorial Board: HUGH L. DRYDEN, *Chief of Mechanics and Sound Division, National Bureau of Standards*

Editor: ROBERT R. DEXTER *Manager:* JOSEPH J. MAITAN

The Institute of the Aeronautical Sciences publishes the JOURNAL OF THE AERONAUTICAL SCIENCES quarterly, in January, April, July, and October, and the AERONAUTICAL ENGINEERING REVIEW monthly.

The JOURNAL OF THE AERONAUTICAL SCIENCES prints papers of scientific and technical interest to Institute members and subscribers. In general, it provides an opportunity for specialists to publish articles disclosing new knowledge and new applications in the field of the aeronautical sciences. The JOURNAL restricts itself to the aeronautical aspects of advances in science and engineering, and papers printed have either been submitted directly to the JOURNAL or have been previously presented at a meeting of the Institute.

The AERONAUTICAL ENGINEERING REVIEW keeps members and subscribers informed regarding the contents of new books and current periodicals in the field of aeronautics. It reviews new developments in the aircraft industry and reports on progress from house organs and catalogues published by aircraft and engine manufacturers and other companies engaged in aeronautical activities. It publishes papers on applied engineering and aircraft production. News of Institute activities is published in the REVIEW.

Statements and opinions expressed in the JOURNAL are to be understood as individual expressions of the authors and not those of the Institute.

SUBSCRIPTION RATES

Journal of the Aeronautical Sciences
Published Quarterly

United States and Possessions		Foreign Countries Including Canada (American Currency Rates)	
1 Year	$7.00	1 Year	$9.00
Single Copies	2.00	Single Copies	2.50

Aeronautical Engineering Review
Published Monthly

United States and Possessions		Foreign Countries Including Canada (American Currency Rates)	
1 Year	$3.00	1 Year	$3.50
Single Copies	0.30	Single Copies	0.35

Notices of change of address should be sent to the Institute at least 30 days prior to actual change of address.

Manuscripts for publication, proofs, and all correspondence should be addressed to the Editorial Office of the JOURNAL.

Correspondence regarding subscriptions may be addressed to Publication Office, 20th and Northampton Sts., Easton, Pa., or to the Editorial Office of the JOURNAL OF THE AERONAUTICAL SCIENCES, 1505 RCA Building West, 30 Rockefeller Plaza, New York 20, New York.

Entered as Second-Class Matter at the Post Office, Easton, Pa., May 1, 1937. Acceptance for mailing at a special rate of Postage provided for in the Act of August 24, 1912. Authorized April 29, 1937.

An Appreciation

TO CORPORATE MEMBERS OF THE INSTITUTE OF THE AERONAUTICAL SCIENCES

Listed below are the leading aeronautical and industrial companies that make possible the publication of the *Journal of the Aeronautical Sciences*.

They enable the Institute to publish scientific and technical papers in the *Journal* and to devote its pages exclusively to editorial material.

Dues from individual members which would normally be used to publish this scientific and engineering quarterly are thus released for additional services to the profession and industry.

Advertising defrays the cost of publishing the *Aeronautical Engineering Review* and the *Aeronautical Engineering Catalog*.

These publications provide a comprehensive technical information service for the benefit of the aircraft and related industries.

ACADEMY OF AERONAUTICS
ADEL PRECISION PRODUCTS CORPORATION
AERO INSURANCE UNDERWRITERS
AEROJET ENGINEERING CORPORATION
AERONAUTICAL PRODUCTS, INC.
AEROQUIP CORPORATION
AGAWAM AIRCRAFT PRODUCTS, INC.
AIRCHOX COMPANY DIVISION, JOYCE AVIATION, INC.
AIRCRAFT RADIO CORPORATION
AIREON MANUFACTURING CORPORATION
AIRESEARCH MANUFACTURING COMPANY
AIRESEARCH MANUFACTURING COMPANY OF ARIZONA, INC.
AIREX MANUFACTURING COMPANY, INC.
ALLIS-CHALMERS MANUFACTURING COMPANY
ALLISON DIVISION, GENERAL MOTORS CORPORATION
ALUMINUM COMPANY OF AMERICA
AMERICAN AIRLINES SYSTEM
AMERICAN BOSCH CORPORATION
AMERICAN CENTRAL MANUFACTURING CORPORATION
AMERICAN PHENOLIC CORPORATION
THE AMERICAN ROLLING MILL COMPANY
AMERICAN TUBE BENDING COMPANY, INC.
ASSOCIATED AVIATION UNDERWRITERS
ASSOCIATED FOUNDRIES & MANUFACTURERS, INC.
BAKER STEEL & TUBE COMPANY
BAUSCH & LOMB OPTICAL COMPANY
BEECH AIRCRAFT CORPORATION
BELL AIRCRAFT CORPORATION
BENDIX AVIATION CORPORATION
BENDIX PRODUCTS DIVISION
BENDIX RADIO CORPORATION
ECLIPSE-PIONEER DIVISION
EXPORT DIVISION
JULIEN P. FRIEZ & SONS DIVISION
PACIFIC DIVISION
SCINTILLA MAGNETO COMPANY
THE BG CORPORATION
BOEING AIRCRAFT COMPANY
BOEING SCHOOL OF AERONAUTICS
BOLTON MANUFACTURING CORPORATION
BOOTS AIRCRAFT NUT CORPORATION
BREEZE CORPORATIONS, INC.
ESSEX TOOL & DIE COMPANY
FEDERAL LABORATORIES, INC.
CARRIER CORPORATION
CESSNA AIRCRAFT COMPANY
CHANDLER-EVANS CORPORATION
CHASE NATIONAL BANK OF THE CITY OF NEW YORK
THE CLEVELAND GRAPHITE BRONZE COMPANY
THE CLEVELAND PNEUMATIC TOOL COMPANY
AUTOMOTIVE-AIRCRAFT DIVISION
CLIFFORD MANUFACTURING COMPANY
CONSOLIDATED VULTEE AIRCRAFT CORPORATION
NASHVILLE DIVISION
STINSON AIRCRAFT DIVISION
CONTINENTAL MOTORS CORPORATION
COX AND STEVENS AIRCRAFT CORPORATION
CULVER AIRCRAFT CORPORATION
CURTISS-WRIGHT CORPORATION
AIRPLANE DIVISION
DEVELOPMENT DIVISION
PROPELLER DIVISION
WRIGHT AERONAUTICAL CORPORATION
DOAK AIRCRAFT COMPANY, INC.
DOUGLAS AIRCRAFT COMPANY, INC.
EL SEGUNDO PLANT
LONG BEACH PLANT
THE DOW CHEMICAL COMPANY
DZUS FASTENER COMPANY, INC.
EASTERN AIR LINES, INC.
EATON MANUFACTURING COMPANY
THOMAS A. EDISON COMPANY, INC., INSTRUMENT DIVISION
EDO AIRCRAFT CORPORATION
ELASTIC STOP NUT CORPORATION OF AMERICA
THE ELECTRIC AUTO-LITE COMPANY
ELECTROL INCORPORATED
ENGINEERING AND RESEARCH CORPORATION
ETHYL CORPORATION
THE FAFNIR BEARING COMPANY
FAIRCHILD CAMERA & INSTRUMENT CORPORATION
FAIRCHILD AERIAL SURVEYS, INC.
FAIRCHILD ENGINE AND AIRPLANE CORPORATION
DURAMOLD DIVISION
FAIRCHILD AIRCRAFT DIVISION
RANGER AIRCRAFT ENGINES DIVISION
FEDERAL TELEPHONE AND RADIO CORPORATION
FIRESTONE AIRCRAFT COMPANY
FLEETWINGS DIVISION, KAISER CARGO, INC.
FLETCHER AVIATION CORPORATION
G & A AIRCRAFT, INC.
GENERAL AIRCRAFT EQUIPMENT, INC.
GENERAL AVIATION EQUIPMENT COMPANY, INC.
GENERAL ELECTRIC COMPANY
GENERAL INSTRUMENT CORPORATION
GENERAL MOTORS CORPORATION
AC SPARK PLUG DIVISION
AEROPRODUCTS DIVISION
BUICK MOTOR DIVISION
CADILLAC MOTOR CAR DIVISION
CHEVROLET MOTOR DIVISION
DELCO PRODUCTS DIVISION
DELCO-REMY DIVISION
EASTERN AIRCRAFT DIVISION
FISHER BODY DIVISION
FRIGIDAIRE DIVISION
HARRISON RADIATOR DIVISION
RESEARCH LABORATORIES DIVISION
ROCHESTER PRODUCTS DIVISION
GENERAL TIRE & RUBBER COMPANY
THE B. F. GOODRICH COMPANY
THE GOODYEAR TIRE & RUBBER COMPANY
GRAND CENTRAL AIRPORT COMPANY
THE GRAY MANUFACTURING COMPANY
GRUMMAN AIRCRAFT ENGINEERING CORPORATION
GUIBERSON DIESEL ENGINE COMPANY
W. & L. E. GURLEY
HANNA ENGINEERING WORKS
HASKELITE MANUFACTURING CORPORATION
HAYES INDUSTRIES, INC.
HIGGINS AIRCRAFT, INC.
THE HILLIARD CORPORATION
THE INTERNATIONAL NICKEL COMPANY
JACK & HEINTZ, INC.
JACOBS AIRCRAFT ENGINE COMPANY
JOHNS-MANVILLE SALES CORPORATION
CASEY JONES SCHOOL OF AERONAUTICS, INC.
KELLETT AIRCRAFT CORPORATION
KENYON INSTRUMENT COMPANY, INC.
WALTER KIDDE & COMPANY, INC.
KOLLSMAN INSTRUMENT DIVISION, SQUARE D COMPANY
LAISTER-KAUFFMANN AIRCRAFT CORPORATION
LANGLEY CORPORATION
LAVELLE AIRCRAFT CORPORATION
LEAR INCORPORATED
LIBERTY AIRCRAFT PRODUCTS CORPORATION
LIGHTS, INCORPORATED
LINK AVIATION DEVICES, INC.
THE LIQUIDOMETER CORPORATION
LOCKHEED AIRCRAFT CORPORATION
LONGINES-WITTNAUER WATCH COMPANY, INC.
MAGNAFLUX CORPORATION
THE MARQUETTE METAL PRODUCTS COMPANY
THE GLENN L. MARTIN COMPANY
THE W. L. MAXSON CORPORATION
WARREN McARTHUR CORPORATION
McDONNELL AIRCRAFT CORPORATION
MENASCO MANUFACTURING COMPANY
MICROMATIC HONE CORPORATION
MINNEAPOLIS-HONEYWELL REGULATOR COMPANY
MOORE DROP FORGING COMPANY
NASH-KELVINATOR CORPORATION
NATIONAL CITY BANK OF NEW YORK
NATIONAL CREDIT OFFICE, INC.
THE NATIONAL SCREW & MANUFACTURING COMPANY
THE NEW YORK AIR BRAKE COMPANY
NOORDUYN AVIATION LIMITED
NORMA-HOFFMANN BEARINGS CORPORATION
NORTH AMERICAN AVIATION, INC.
NORTH AMERICAN AVIATION, INC., OF TEXAS
NORTHROP AIRCRAFT, INC.
NORTHWEST AIRLINES, INC.
OTTO AVIATION CORPORATION
OWENS-CORNING FIBERGLAS CORPORATION
PACKARD MOTOR CAR COMPANY
PAN AMERICAN AIRWAYS SYSTEM
THE PARKER APPLIANCE COMPANY
PENNSYLVANIA-CENTRAL AIRLINES CORPORATION
PESCO PRODUCTS COMPANY DIVISION, BORG-WARNER CORPORATION
PHILLIPS PETROLEUM COMPANY
PIONEER PARACHUTE COMPANY, INC.
THE PURE OIL COMPANY
REPUBLIC AVIATION CORPORATION
J. P. RIDDLE COMPANY
RIDGEFIELD MANUFACTURING CORPORATION, AIRCRAFT DIVISION
JOHN A. ROEBLING'S SONS COMPANY
ROHR AIRCRAFT CORPORATION
ROMEC PUMP COMPANY
ROOSEVELT FIELD, INC.
THE RYAN AERONAUTICAL COMPANY
SCIAKY BROTHERS
SCOTT AVIATION CORPORATION
SHAKESPEARE PRODUCTS COMPANY
SHELL OIL COMPANY, INC.
SIMMONDS AEROCESSORIES, INC.
SKYDYNE, INC.
SOCONY-VACUUM OIL COMPANY
SOLAR AIRCRAFT COMPANY
SPERRY GYROSCOPE COMPANY, INC.
SQUARE D COMPANY
STANDARD OIL COMPANY OF CALIFORNIA
STANDARD OIL COMPANY (INDIANA)
STANDARD OIL COMPANY OF NEW JERSEY
STEEL IMPROVEMENT & FORGE COMPANY
SUMMERILL TUBING COMPANY
SWEDLOW AEROPLASTICS CORPORATION
TELEFLEX LIMITED
THE TEXAS COMPANY
THOMPSON PRODUCTS, INC.
TINNERMAN PRODUCTS, INC.
TITEFLEX, INC.
TRANSCONTINENTAL & WESTERN AIR, INC.
TRIPLETT & BARTON, INC.
UNION CARBIDE AND CARBON CORPORATION
BAKELITE CORPORATION
HAYNES STELLITE COMPANY
LINDE AIR PRODUCTS COMPANY
NATIONAL CARBON COMPANY
UNITED AIRCRAFT CORPORATION
CHANCE VOUGHT AIRCRAFT DIVISION
HAMILTON STANDARD PROPELLERS DIVISION
PRATT & WHITNEY AIRCRAFT DIVISION
PRATT & WHITNEY AIRCRAFT CORPORATION OF MISSOURI
SIKORSKY AIRCRAFT DIVISION
UNITED AIR LINES, INC.
UNITED STATES AVIATION UNDERWRITERS, INC
UNITED STATES RUBBER COMPANY
DOMINION RUBBER COMPANY, LTD.
UNIVERSAL MOULDED PRODUCTS CORPORATION
THE VARIETY AIRCRAFT CORPORATION
VICKERS, INC.
VICTOR ADDING MACHINE COMPANY
VIDAL RESEARCH CORPORATION
THE WACO AIRCRAFT COMPANY
WARNER AIRCRAFT CORPORATION
THE WEATHERHEAD COMPANY
WESTERN AIRLINES, INC.
WESTINGHOUSE ELECTRIC CORPORATION
WESTON ELECTRICAL INSTRUMENT CORPORATION
WYMAN-GORDON COMPANY
YOUNG RADIATOR COMPANY

INSTITUTE of the AERONAUTICAL SCIENCES

President

CHARLES H. COLVIN

Vice-Presidents

W. A. M. BURDEN
LEROY R. GRUMMAN
I. M. LADDON
ARTHUR E. RAYMOND

Executive Vice-President

BENNETT H. HORCHLER

Past-Presidents

J. C. HUNSAKER
CHARLES L. LAWRANCE
D. W. DOUGLAS
GLENN L. MARTIN
CLARK B. MILLIKAN
T. P. WRIGHT
GEORGE W. LEWIS
JAMES H. DOOLITTLE
FRANK W. CALDWELL
HALL L. HIBBARD
HUGH L. DRYDEN
R. H. FLEET

Assistant to the President

GEORGE R. FORMAN

Secretary

ROBERT R. DEXTER

Treasurer

EARL D. OSBORN

Controller

JOSEPH J. MAITAN

COUNCIL

LESTER D. GARDNER, *Chairman*

P. R. BASSETT
REX B. BEISEL
GEORGE W. BRADY
WILLIAM K. EBEL
SHERMAN M. FAIRCHILD
CHARLES FROESCH
R. PAUL HARRINGTON
C. S. JONES
OTTO E. KIRCHNER
JOHN C. LESLIE
ALFRED MARCHEV
ELMER A. SPERRY, JR.

ADVISORY BOARD

WALTER BEECH
LAWRENCE D. BELL
C. L. EGTVEDT
ALLAN D. EMIL
R. H. FLEET
JACK FRYE
R. T. GOODWIN
ROBERT E. GROSS
R. M. HAZEN
J. C. HUNSAKER
TH. VON KÁRMÁN
J. H. KINDELBERGER
P. W. LITCHFIELD
F. W. MAGIN
CHARLES MARCUS
GLENN L. MARTIN
THOMAS A. MORGAN
R. C. MUIR
JOHN K. NORTHROP
W. A. PATTERSON
E. T. PRICE
F. W. REICHELDERFER
FRED H. ROHR
T. CLAUDE RYAN
J. T. TRIPPE
GUY W. VAUGHAN
J. G. VINCENT
EDWARD P. WARNER
E. E. WILSON

HONORARY MEMBERS

GRIFFITH BREWER
LYMAN J. BRIGGS
W. A. M. BURDEN
F. O. CARROLL
ARTEMUS L. GATES
HARRY F. GUGGENHEIM
ROBERT A. LOVETT
CLEMENTS MCMULLEN
GEORGE B. PROCTOR
L. WELCH POGUE
J. LAURENCE PRITCHARD
D. C. RAMSEY
F. W. REICHELDERFER
EUGEN G. REINARTZ
C.-G. A. ROSSBY
T. P. WRIGHT

HONORARY FELLOWS

H. H. ARNOLD
D. W. DOUGLAS
HUGH L. DRYDEN
W. F. DURAND
SIR RICHARD FAIREY
SIR ROY FEDDEN
J. C. HUNSAKER
SIR MELVILL JONES
GEORGE W. LEWIS
GLENN L. MARTIN
GEORGE J. MEAD
SIR FREDERICK HANDLEY PAGE
D. R. PYE
IGOR I. SIKORSKY
G. I. TAYLOR
TH. VON KÁRMÁN
EDWARD P. WARNER
ORVILLE WRIGHT

BENEFACTOR MEMBERS

EDWIN E. ALDRIN
HART O. BERG (Deceased)
E. L. CORD
D. W. DOUGLAS
SHERMAN M. FAIRCHILD
SIR RICHARD FAIREY
R. H. FLEET
FLORENCE GUGGENHEIM (Deceased)
C. D. HANSCOM
JOHN P. V. HEINMULLER
ALEXANDER KLEMIN
PAUL KOLLSMAN
BELLA C. LANDAUER
WILLIAM LANDAUER
GROVER LOENING
EDMUND C. LYNCH (Deceased)
F. W. MAGIN
GLENN L. MARTIN
GEORGE J. MEAD
S. A. REED (Deceased)
L. S. ROCKEFELLER
EDWARD P. WARNER

AMERICAN FELLOWS

JOHN D. AKERMAN
EDWIN E. ALDRIN
KARL ARNSTEIN
J. L. ATWOOD
PAUL S. BAKER
RALPH S. BARNABY
P. R. BASSETT
WELLWOOD E. BEALL
REX B. BEISEL
G. M. BELLANCA
DON R. BERLIN
HENRY A. BERLINER
B. C. BOULTON
GEORGE W. BRADY
LYMAN J. BRIGGS
W. G. BROMBACHER
CHARLES P. BURGESS
FRANK W. CALDWELL
CHARLES H. CHATFIELD
ALLAN CHILTON
V. E. CLARK
CHARLES H. COLVIN
KARL T. COMPTON
JOHN W. CROWLEY, JR.
RALPH S. DAMON
LUIS DE FLOREZ
SMITH J. DE FRANCE
J. P. DEN HARTOG
WALTER S. DIEHL
JAMES H. DOOLITTLE
C. S. DRAPER
IVAN H. DRIGGS
WILLIAM K. EBEL
C. L. EGTVEDT
FREDERIC FLADER
CHARLES FROESCH
JACK FRYE
GARLAND FULTON
LESTER D. GARDNER
RICHARD C. GAZLEY
MICHAEL E. GLUHAREFF
MELVIN N. GOUGH
LEROY R. GRUMMAN
R. M. HAZEN
ALBERT F. HEGENBERGER
EDWARD H. HEINEMANN
S. D. HERON
HALL L. HIBBARD
L. S. HOBBS
PAUL E. HOVGAARD
WILLIAM HOVGAARD
ROBERT INSLEY
EASTMAN N. JACOBS
CLARENCE L. JOHNSON
ALEXANDER KARTVELI
PAUL H. KEMMER
J. H. KINDELBERGER
OTTO E. KIRCHNER
ARTHUR L. KLEIN
ALEXANDER KLEMIN
W. B. KLEMPERER
PAUL KOLLSMAN
OTTO C. KOPPEN
B. V. KORVIN-KROUKOVSKY
S. M. KRAUS
I. M. LADDON
E. S. LAND
CHARLES L. LAWRANCE
JOHN G. LEE
CHARLES A. LINDBERGH
WILLIAM LITTLEWOOD
GROVER LOENING
W. RANDOLPH LOVELACE, II
EUGENE E. LUNDQUIST
R. D. MACCART
ERLE MARTIN
WM. H. MCAVOY
C. J. MCCARTHY
CLARK B. MILLIKAN
ROBERT J. MINSHALL
JOSEPH S. NEWELL
ALFRED S. NILES
JOHN K. NORTHROP
ARTHUR NUTT
SHATSWELL OBER
ROBERT R. OSBORN
W. BAILEY OSWALD
GEORGE A. PAGE, JR.
F. W. PAWLOWSKI
F. W. PENNOYER, JR.
A. A. PRIESTER
ARTHUR E. RAYMOND
F. W. REICHELDERFER
ELLIOTT G. REID
H. J. E. REID
H. C. RICHARDSON
LEONARD E. ROOT
C. E. ROSENDAHL
WILLIAM T. SCHWENDLER
JAMES M. SHOEMAKER
MAC SHORT
IGOR ALEXIS SIKORSKY
SELDEN B. SPANGLER
ELMER A. SPERRY, JR.
JOHN STACK
WILLIAM B. STOUT
HARRY A. SUTTON
C. FAYETTE TAYLOR
EDWARD S. TAYLOR
PHILIP B. TAYLOR
TH. THEODORSEN
T. E. TILLINGHAST
S. TIMOSHENKO
STARR TRUSCOTT
L. B. TUCKERMAN
RALPH H. UPSON
J. G. VINCENT
RICHARD VON MISES
P. V. H. WEEMS
FRED E. WEICK
R. D. WEYERBACHER
JOHN B. WHEATLEY
ANDREW V. WILLGOOS
DONALD H. WOOD
ROBERT J. WOODS
T. P. WRIGHT
JOHN E. YOUNGER
ALBERT F. ZAHM
STEPHEN J. ZAND

JOURNAL OF THE AERONAUTICAL SCIENCES

VOLUME 12 OCTOBER, 1945 NUMBER 4

Effect of Temperature Lapse Rate on Recovery from Compressibility Dives

C. E. PAPPAS* AND M. G. HARRISON†

Republic Aviation Corporation

SUMMARY

It is shown in the main body of the paper that the effect of a temperature inversion may be such as to make recovery from a compressibility dive impossible. Statistical data show that more accidents have resulted from compressibility dives between late November and early May and in northern areas where the ground temperatures might be expected to be low.‡ Because of the airplane's high speed and high wing loading, a Mach Number is reached in the dive where the airflow adjacent to the airfoil breaks down and there develops what is known as a compression shock. It is proved that the Mach Number depends only on the equivalent air speed and pressure. For a constant value of drag and C_L, the Mach Number is a function of the pressure only. Airplane inertia effects are shown to be an important consideration in determining the Mach Number during the dive when temperature inversions occur.

Charts are included to enable the pilot to determine the Mach Number knowing the pressure altitude and equivalent air speed.

SYMBOLS

a = velocity of sound under nonstandard conditions, m.p.h.
a_s = velocity of sound under standard conditions, m.p.h.
A = deceleration, ft. per sec.^{2}
C_D = drag coefficient, dimensionless
C_L = lift coefficient, dimensionless
D = drag force, lbs.
g = acceleration due to gravity, ft. per sec.^{2}
K = C_p/C_v adiabatic exponent of air, dimensionless
m = mass of the airplane, slugs
M = Mach Number under nonstandard conditions, dimensionless
M_s = Mach Number under standard conditions, dimensionless
P = fluid pressure, lbs. per sq.ft.
P_I = fluid impact pressure, lbs. per sq.ft.
P_0 = fluid pressure at rest, lbs. per sq.ft.
P_s = fluid pressure under standard conditions, lbs. per sq.ft.
P_{st} = static fluid pressure, lbs. per sq.ft.
R = standard gas constant for air = 53.33, ft. per °F. abs.
S = wing area, sq.ft.
T = absolute temperature, °F.
T_s = standard absolute temperature, °F.
V = true speed of airplane, m.p.h.
V_e = equivalent air speed of airplane ($V_e = V\sqrt{\sigma}$), m.p.h.
V_s = true air speed of airplane under standard conditions, m.p.h.
V_{es} = equivalent air speed of airplane under standard conditions, m.p.h.
W = gross weight of airplane, lbs.
ρ = mass density of air, lbs. sec.^{2} per ft.^{4}
ρ_0 = mass density of air at the stagnation point, lbs. sec.^{2} per ft.^{4}
ρ_s = mass density of air under standard conditions, lbs. sec.^{2} per ft.^{4}
$\rho_{s\text{-}l}$ = mass density of air at sea level for standard conditions, lbs. sec.^{2} per ft.^{4}

Received December 29, 1944.

* Chief, Aerodynamics Department.

† Mathematics Consultant to the Aerodynamics Department.

‡ The authors are indebted to Mr. L. L. Brabham of Republic Aviation Corporation for raising the question of the effect of weather conditions on recovery from compressibility dives.

INTRODUCTION

WITH THE ADVENT of heavy wing loading and good aerodynamic cleanliness, pursuit airplanes have attained in recent years dive speeds approaching the velocity of sound. It is to be expected that all airplanes will run into difficulty—that is, exhibit unusual flying characteristics—at speeds approaching the velocity of sound. The ratio of the airplane speed to the speed of sound is most important and is known as the Mach Number. With the introduction of turbosuperchargers, the critical altitude of the airplane has increased materially so that the airplane can reach its terminal velocity at extremely high altitudes where the velocity of sound is much lower than at medium altitudes of 15,000 to 20,000 ft. In addition to the foregoing items, the pilot is subjected to high-altitude operation, and as a result he may be affected physiologically.

It is interesting to note that all accidents resulting from compressibility dives have occurred between late November and early May and in northern areas where

the ground temperatures might be expected to be low. One might, at first, suspect that recovery from compressibility dives is dependent upon air temperature. It is shown in this paper that under normal summer or winter atmospheric conditions the airplane should encounter no difficulties. Should abnormal conditions of the atmosphere exist, however, the airplane's Mach Number can change. The items that will cause such a change are:

(1) Variation in barometric pressure from standard pressure.
(2) Temperature inversion.

Later in the paper the effects of variation in barometric pressure due to atmospheric conditions and temperature inversion on Mach Number will be discussed. It will be shown that temperature inversion causes a rapid deceleration of the airplane which results in a material increase in the apparent weight of the airplane. For this case, the airplane inertia causes a higher diving speed than would be normally expected.

Derivation of Formulas

Dependence of Mach Number on Equivalent Air Speed and Pressure Altitude

The Mach Number is defined as the ratio of the velocity of the airplane to the velocity of sound at the particular altitude in question, viz.,

$$M = V/a$$

Denoting by the subscript s standard conditions at the particular altitude in question,

$$M_s/M = (V_s/a_s)/(V/a)$$

or

$$M = M_s(V/a)(a_s/V_s) \tag{1}$$

But $V_s = V_{es}\sqrt{\rho_{s.l./\rho_s}}$ and $V = V_e\sqrt{\rho_{s.l./\rho}}$.
Furthermore, $a_s = 33.5\sqrt{T_s}$ and $a = 33.5\sqrt{T}$.
Eq. (1) then becomes

$$M = M_s(V_e/V_{es})\sqrt{\rho_s/\rho}\sqrt{T_s/T} \tag{2}$$

Furthermore, $\rho_s/\rho = (P_s/P)(T/T_s)$.
Eq. (2) then becomes

$$M = M_s(V_e/V_{es})\sqrt{P_s/P} \tag{3}$$

When $V_e = V_{es}$, then $M = M_s\sqrt{P_s/P}$.
But at a given altitude $P_s \cong P$ and $M = M_s$.
This last relation shows that the Mach Number at a given altitude is equal to the Mach Number under standard conditions when the equivalent air speed is constant, viz., $V_e = V_{es}$.

Taking the logarithm and derivative of both sides of Eq. (3), the result is:

$$dM/M = (dV_e/V_e) - {}^1/_2(dP/P) \tag{4}$$

Eq. (4) shows the per cent change in Mach Number in terms of percentage changes in equivalent air speed and pressure. Since the minus sign occurs in front of the expression ${}^1/_2(dP/P)$ in Eq. (4), the maximum increase in Mach Number will occur when the existing pressure is below the standard value.

Relationship Between Mach Number and Pressure Altitude at a Constant Drag and Lift Coefficient

The basic drag equation is

$$D = {}^1/_2(\rho V^2 C_D S)$$

Since in a terminal velocity dive the drag equals the weight, $D = W$,

$$W = {}^1/_2(\rho V^2 C_D S) \tag{5}$$

Multiplying the right-hand side of Eq. (5) by a^2 and dividing by a^2, the result is

$${}^1/_2(\rho a^2)(M^2 C_D)S = W$$

or

$$M^2 C_D = 2W/S\rho a^2$$

But

$$\rho = \rho_s(P/P_s)(T_s/T)$$

and

$$a^2 = (T/T_s)a_s^2$$

Therefore,

$$M^2 C_D = 2W/S\rho_s(P/P_s)a_s^2$$

If $P = P_s$, then

$$M^2 C_D = 2W/S\rho_s a_s^2 \tag{6}$$

Since C_D is a function of M and $2W/S\rho_s a_s^2$ is a function of the altitude or pressure only, $M^2 C_D$ is a function of

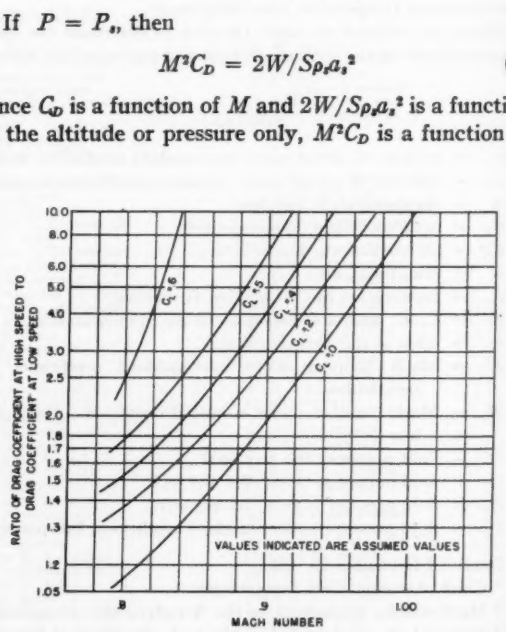

FIG. 1. Ratio of drag coefficient at high speed to drag coefficient at low speed vs. Mach Number.

the pressure only for a given drag and C_L. Therefore, at a given drag and lift coefficient, the Mach Number is a function of the pressure altitude only. This can be seen from Figs. 1–4, inclusive.

Determination of Mach Number from the Equivalent Air Speed and Pressure Altitude

It will now be shown that, starting with the Bernoulli equation for compressible flow, the ratio of impact to static pressure may be expressed as a function of Mach Number (M) and the ratio of specific heats of air (K).

The generalized Bernoulli equation may be expressed as:

$$(V^2/2) + \int dP/\rho = \text{constant}$$

and for a compressible fluid where the adiabatic relation ($P\rho^{-K} = \text{constant}$)

$$P/\rho^K = P_0/\rho_0{}^K$$

or

$$1/\rho^K = P_0/\rho_0{}^K P$$

$$1/\rho = P_0{}^{1/K}/\rho_0 P^{1/K} = P_0{}^{1/K} P^{-1/K}/\rho_0 \qquad (7)$$

Therefore,

$$(V^2/2) + (P_0{}^{1/K}/\rho_0) \int P^{-1/K} dP = \text{constant}$$

or

$$(V^2/2) + (P_0{}^{1/K}/\rho_0)[K/(K-1)](P/P^{1/K}) = \text{constant}$$

$$\frac{V^2}{2} + \left(\frac{K}{K-1}\right)\left(\frac{P}{\rho}\right) = \text{constant} = \frac{V_0{}^2}{2} + \left(\frac{K}{K-1}\right)\left(\frac{P_0}{\rho_0}\right)$$

Assume that P_0 is the pressure at the stagnation point of a fluid where $V_0 = 0$.

Then

$$[K/(K-1)](P_0/\rho_0) = (V^2/2) + [K/(K-1)](P/\rho)$$

$$(\rho/\rho_0)(P_0/P) = 1 + [(K-1)/K](\rho/P)(V^2/2)$$

Since KP/ρ is the expression for the speed of sound squared (a^2)

$$\rho P_0/\rho_0 P = 1 + [(K-1)/2](V^2/a^2)$$

But $M = V/a$ and

$$\rho = \rho_0 P^{1/K}/P_0{}^{1/K}$$

from Eq. (7); therefore,

$$(\rho_0 P^{1/K}/P_0{}^{1/K})(P_0/\rho_0 P) = 1 + [(K-1)/2]M^2$$

The last expression can now be written as

$$(P_0/P)^{(K-1)/K} = 1 + [(K-1)/2]M^2$$

$$P_0/P = \{1 + [(K-1)/2]M^2\}^{K/(K-1)} \qquad (8)$$

where P_0 is the pressure at the stagnation point or impact pressure (P_i) and P is the static pressure (P_s).

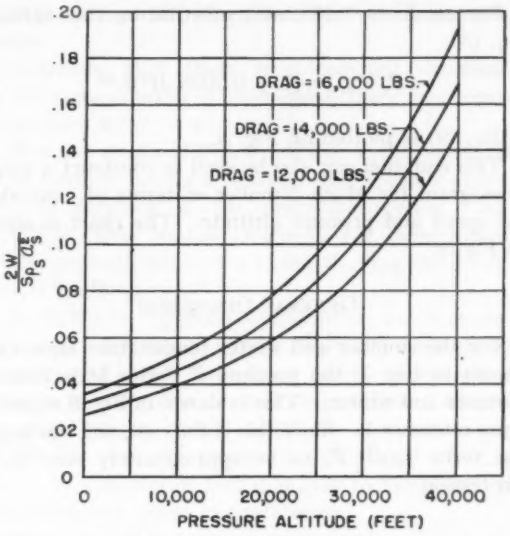

Fig. 2. Variation of $2W/S\rho_s a_s^2$ vs. pressure altitude, $S = 300$ ft.^{2}

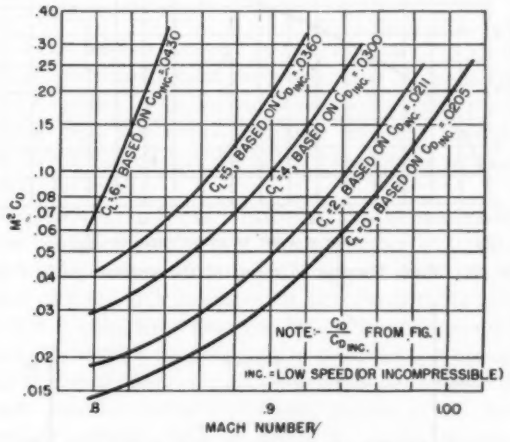

Fig. 3. Variation of $M^2 C_D$ vs. Mach Number.

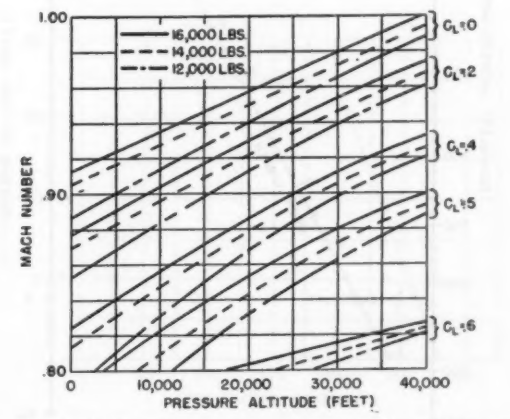

Fig. 4. Mach Number vs. pressure altitude for various drag values and lift coefficients.

For air $K = 1.405$, and substituting this value in Eq. (8)

$$P_t/P_{st} = (1 + 0.2025\ M^2)^{3.469} \qquad (9)$$

Eq. (9) is plotted on Fig. 5.

This equation can also be used to construct a simple nomogram for Mach Number in terms of equivalent air speed and pressure altitude. The chart is shown in Fig. 6.

General Discussion

For the summer and winter temperature lapse rates shown in Fig. 7, the pressure P varies little between summer and winter. This is shown in Fig. 8 replotted from reference 1. Since this is the case, one can expect the term $^1/_2(dP/P)$ to be approximately zero in the expression

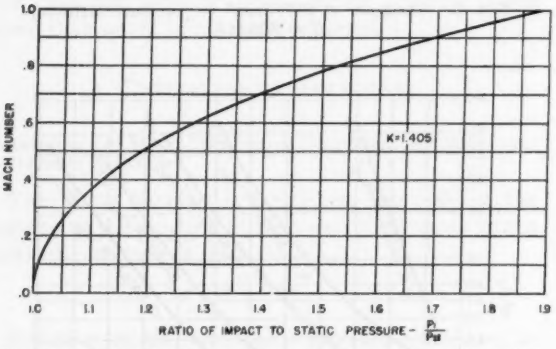

Fig. 5. Mach Number in terms of the pressure ratio P_t/P_{st}.

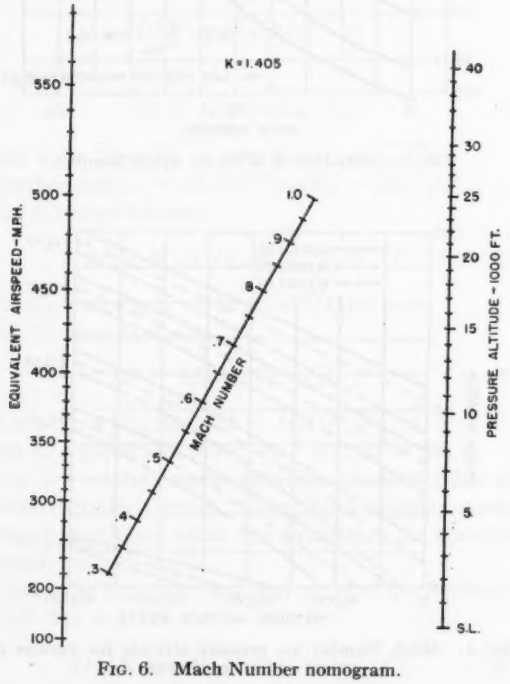

Fig. 6. Mach Number nomogram.

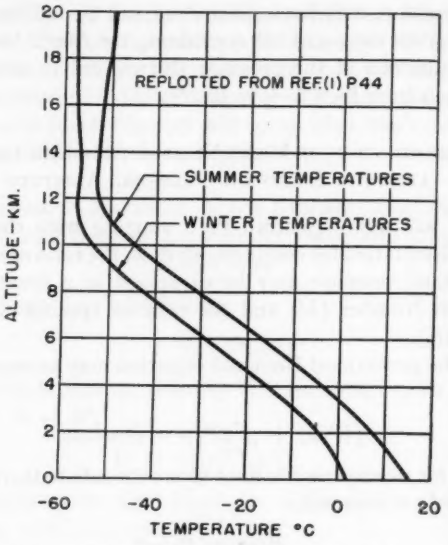

Fig. 7. Winter and summer vertical distribution of temperature over Europe.

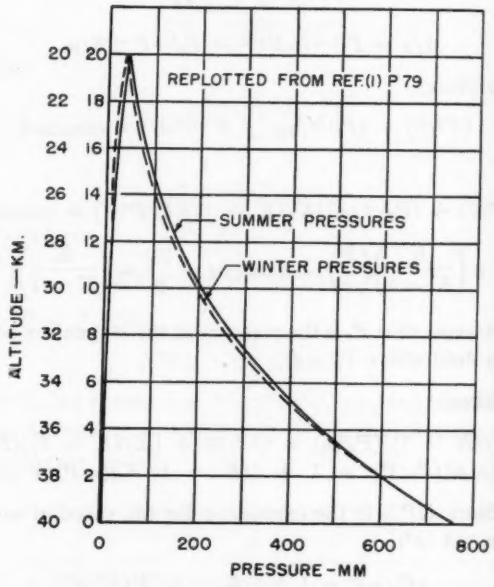

Fig. 8. Summer and winter pressures at various elevations.

$$dM/M = (dV_e/V_e) - {}^1/_2(dP/P)$$

When the barometric pressure P is such that P is greater than P_s, the Mach Number will be reduced. When P is less than P_s, the Mach Number will be increased. It may be better to regard changes in barometric pressure as affecting the altitude at which a pull-out may be accomplished. Thus, on a day when P is greater than P_s, the pressure existing normally at 10,000 ft., for example, may now exist at 11,000 ft.; conversely, when P is less than P_s. From this point of view, the existing normal changes in barometric

pressure will not cause too great a change in the altitude available for pull-out from a dive.

In a vertical terminal velocity dive the drag is constant and equal to the weight of the airplane plus the engine thrust. The Mach Number attained in a vertical terminal velocity dive at a given altitude and lift coefficient will depend only on the pressure at the altitude under consideration, and, since the pressure changes only slightly between extreme summer and winter, the Mach Number will be the same the year round at a given altitude. This statement will be slightly modified because of inertia effects.

Effect of Inertia on Mach Number

Standard Condition—i.e., Constant Lapse Rate

As a first approximation it is assumed that the airplane weight is equal to its drag. Then, if the airplane weighs 12,000 lbs., it is seen from Fig. 4 that for $C_L = 0$ the Mach Number is 0.988 at 40,000 ft. pressure altitude and 0.888 at sea level pressure altitude. Under standard conditions the velocity of sound at 40,000 ft. is 975 ft. per sec. Therefore, the airplane speed is $0.988 \times 975 = 962$ ft. per sec. at 40,000 ft. Similar calculation shows that the speed of the airplane at sea level is 999 ft. per sec. The change in speed is then $999 - 962 = 37$ ft. per sec. or roughly 25 m.p.h. Now the time taken to cover this distance is given closely by dividing the distance by the average speed. Thus, $\Delta t = 2 \times 40{,}000/(999 + 962) = 40.8$ sec. Hence, the acceleration, which is the change in velocity per unit time, is $37/40.8 = 0.91$ ft. per sec.^{2}. This is $0.91/32.2 = 0.0282g$. Because of this acceleration the airplane is apparently lighter by $0.0282 \times 12{,}000 = 340$ lbs.

Fig. 4 shows that such a change in apparent weight would decrease the Mach Number between 0.002 and 0.004 units. The latter figure applies at sea level.

From the small magnitude of the change it is seen that the original assumption that the drag is equal to the weight is true to an extremely high order of approximation.

Nonstandard Conditions—i.e., Temperature Inversion

Now assume that a temperature inversion such as that shown in Fig. 9 exists. According to the analysis of the preceding section a slight acceleration will occur in the dive until a pressure altitude of 10,000 ft. is reached. The airplane then enters a region where the velocity of sound decreases so that the Mach Number tends to rise and bring the drag up. This rise is added to an increasing drag caused by the increasing density so that an appreciable increase in drag occurs with a consequent decrease in velocity. However, the airplane velocity change lags behind the sound velocity change so that the Mach Number increases substantially.

Assuming that there is a constant deceleration A when equilibrium is established, there is a constant drag given by $D = m(A + g)$.

Now, by means of Fig. 4 and Fig. 9, the acceleration of an airplane having a constant drag is easily obtained by the methods of the preceding section. For a 12,000-lb. drag in the inversion, the deceleration is 7.7 ft. per sec.^{2}, while at a 14,000-lb. drag the deceleration is 7.5 ft. per sec.^{2}

A 12,000-lb. airplane would have an incremental weight of 2,850 lbs. at a drag of 12,000 lbs. and 2,800 at a drag of 14,000 lbs. From these considerations it appears that equilibrium will be established when the apparent weight of the 12,000-lb. airplane is about 14,800 lbs. and the deceleration is about 7.5 ft. per sec.^{2} As a matter of fact it is easy to verify that this condition does result in equilibrium.

The transient has a time constant given by $(1/m) \times (dD/dV)$. From Fig. 4 dD/dV is found to be approximately 150 lbs. per ft. per sec. Hence, the time constant of the transient is about 0.4 so that the transient dies out to 37 per cent of its original value in 2.5 sec. Since this motion occupies 10 sec., the transient should be negligible throughout the greater part of the motion. This reasoning is further substantiated when it is considered that the actual entrance into the inversion will be gradual so that the initial value of the transient should be small.

By referring to Fig. 4 it is found that the new equilibrium condition results in a Mach Number of 0.909 at sea level pressure altitude. Compared with the old value of 0.888 this indicates an increase of 0.021 units, or, if it is considered that the Mach Number would be decreased slightly under standard conditions, it appears that the total effect of an inversion will be to cause the Mach Number to be 0.025 units greater at sea level pressure altitude than it would be under standard conditions.

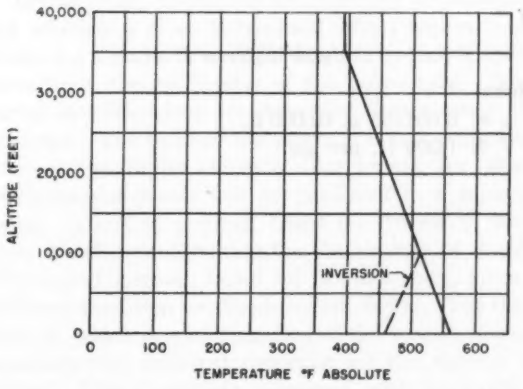

Fig. 9. Assumed temperature variation vs. altitude with inversion at 10,000 ft.

Examples

Example 1

Assume that the pilot sets his altimeter to zero when operating out of an airport at 6,000 ft. altitude. When his altimeter reads 10,000 ft. he is then at an actual altitude of 16,000 ft. His pressure is then in error by 20.58 − 16.21 = 4.37 in. of mercury. Applying Eq. (4), we find that there is $\frac{1}{2}(4.37/20.58) = 10.6$ per cent error in the Mach Number. This means that, if the placard speeds correspond to 0.80 Mach Number, the pilot is actually at $0.8 + 0.106 \times 0.8 = 0.885$ Mach Number when flying at the placard speed.

Example 2

Suppose the pilot decides to exceed the equivalent placard speed 40 m.p.h. in an otherwise normal flight. Suppose this speed were 400 m.p.h. In that case Eq. (4) shows that the per cent change in Mach Number is equal to the per cent change in V_e. In this case $dV_e/V_e = 10$ per cent. Hence, if the placard is designed for 0.8 Mach Number, the pilot has exceeded this by $0.1 \times 0.8 = 0.08$ units and is flying at 0.88 Mach Number.

Example 3

Suppose the pilot is in a compressibility dive. Experience shows that the pilot can usually start a pull-out at around 10,000 ft. According to Fig. 4 his Mach Number is then 0.965 − 0.914 = 0.051 units less than it was at 30,000 ft. In normal conditions the Mach Number decreases still further as he continues the pull-out. In a temperature inversion, however, about 2,800 lbs. must be added to the airplane's weight. According to Fig. 4 his Mach Number then rises somewhat and does not again reach the value at 10,000 ft. until the pilot reaches a pressure altitude of about 3,000 ft.

Example 4

Suppose the stick forces are high but the pilot can still attain a lift force of 1g. The resulting C_L is given by

$$\tfrac{1}{2}(\rho V^2 C_L S) = L$$

where

$\rho = 0.001756$ at 10,000 ft.
$V \cong 1{,}000$ ft. per sec.
$S = 300$
$L = 12{,}000$

Then

$$C_L = \frac{12{,}000 \times 2}{0.001756 \times 10^6 \times 300} = 0.0455$$

According to Fig. 4 this will result in $(0.0455/0.2) \times (0.914 - 0.882) = 0.007$ units change in Mach Number.

Example 5

Suppose the pressure altitude is 800 ft. different from the true altitude. This is most readily interpreted as a change of 800 ft. in the altitude at which to expect a given phenomena. For example, a pull-out that can ordinarily be started at 10,000 ft. on a normal day cannot be started until 9,200 ft. on a day with a low barometric pressure.

Conclusions

(1) It has been shown that for standard summer and winter conditions, the variation in Mach Number is small and that, if the airplane is flying slightly below the upper safe limit of M, the pilot should experience no trouble in pulling out of a dive provided the equivalent air speed does not vary.

(2) A temperature inversion, change in equivalent air speed, or an appreciable change in pressure may put the airplane in an unsafe zone as far as recovery from a compressibility dive is concerned.

(3) If a normal temperature lapse rate exists, the airplane Mach Number in a dive tends to decrease with altitude while the velocity rises slightly. With a temperature inversion the Mach Number will rise suddenly as the inversion is entered. It will then decrease slightly while the velocity decreases more markedly.

(4) If a normal temperature lapse rate exists, the airplane inertia effects are small, and the assumption that the drag is equal to the weight is true to a high order of approximation. In a temperature inversion the inertia effects are important since the apparent weight of the airplane acting as thrust in a dive is appreciably increased because of the rapid deceleration that takes place.

Reference

[1] Humphreys, W. J., *Physics of the Air*, 3rd Ed., pp. 44 and 79; McGraw-Hill Book Company, Inc., New York, 1940.

The Simplification of Flutter Calculations by Use of an Extended Form of the Routh-Hurwitz Discriminant

S. SHERMAN,* J. DiPAOLA,† AND H. F. FRISSEL†

Curtiss-Wright Corporation

SUMMARY

Methods are presented for determining the stability of the solution of the flutter polynomial by a finite (not approximate) calculation. The method is a generalization of Routh's and Hurwitz's discriminant to cover the case with complex coefficients. Use of the extended discriminant presented in this paper should save considerable time in flutter calculations. Further possibilities are opened up for machine methods. Full mathematical proofs and further development of these ideas are reserved for a later paper. Additional reports are planned applying the ideas to airplane and helicopter stability calculations.

INTRODUCTION

CALCULATIONS FOR THE DYNAMIC STABILITY of airplanes and for the flutter of airfoils have many points of similarity. In each case a stability determinant is set equal to zero and the character of the roots of the resulting equation indicates the presence (or absence) of instability. In the case of dynamic instability a polynomial with real coefficients is set equal to zero. Although considerable literature[1] has been devoted to the solution of such equations, the process is fairly laborious. Fortunately, such actual solutions prove to be unnecessary, since, for the conventional calculation, stability is equivalent to the condition that all of the roots have negative real parts. Routh[2] and Hurwitz[3] and Duncan, Frazer, and Collar in their rephrasing of Routh's discriminant[4] have shown that the roots of

$$\sum_{k=0}^{n} p_k z^{n-k} = 0$$

are stable if, for p_k real, $0 \leq k \leq n$, and $p_k = 0$, $k > n$;

$$D_1 = p_1$$

$$D_2 = \begin{vmatrix} p_1 & p_0 \\ p_3 & p_2 \end{vmatrix}$$

$$D_3 = \begin{vmatrix} p_1 & p_0 & 0 \\ p_3 & p_2 & p_1 \\ p_5 & p_4 & p_3 \end{vmatrix}$$

$$D_n = \begin{vmatrix} p_1 & p_0 & 0 & 0 \cdots\cdots 0 \\ p_3 & p_2 & p_1 & p_0 \cdots\cdots 0 \\ p_5 & p_4 & p_3 & p_2 \cdots\cdots 0 \\ \cdots\cdots\cdots\cdots\cdots\cdots\cdots \\ p_{2n-1} & p_{2n-2} & p_{2n-3} & p_{2n-4} \cdots\cdots p_n \end{vmatrix}$$

are each greater than zero. This fact makes possible considerable saving of time in stability calculations.

In stability problems of more recent origin the Routh-Hurwitz discriminant stated above cannot be directly applied because (a) the coefficients, p_k, are complex and (b) the complete criterion for stability is no longer that the real parts of the roots be negative.

In the flutter polynomial the coefficients are complex valued functions of $v/b\omega$ because the wake induces a phase lag between the aerodynamic forces and the displacements. In addition, structural damping causes a phase lag between the elastic forces and the displacements. In flutter the condition that the roots have negative real parts is a sufficient but not necessary condition for stability and, as a sufficient condition, is not generally useful, since few of the flutter polynomials occurring in practice will satisfy it. However, the question of the possibility of using the coefficients in the flutter polynomial directly to indicate the presence or absence of flutter has been proposed.[5, 6]

In this paper, procedures are presented for determining whether a given polynomial with complex coefficients has a stable or unstable solution by simple operations upon the coefficients of the polynomial. Some useful simplifications for detecting flutter speed are included. The basis of the procedures is a generalization of the Routh-Hurwitz discriminant for which mathematical proofs will be published in a separate paper. The first method, based on Hurwitz's work, gives a sufficient condition for the absence of flutter. The second method, based on Routh's work, gives a sufficient condition for the absence of flutter. The third method, which is a continuation of the second, gives a necessary and sufficient condition for the absence of flutter. These methods, tempered with engineering judgment, can expedite, from a knowledge of the flut-

Received November 10, 1944. To have been presented at the I.A.S. Thirteenth Annual Meeting, which was canceled to cooperate with a Government appeal (January, 1945) to refrain from holding conventions and meetings.

* Formerly Head of Flutter and Vibration Section, Airplane Division—Research Laboratory. Now Assistant Professor of Mathematics at the University of Chicago.

† Junior Flutter Engineers. Now Structures Engineers, Airplane Division—Research Laboratory.

ter polynomials, conclusions pertinent to the likelihood of flutter in the airplane. In the following, the flutter problem is emphasized, although similar considerations apply to other types of stability calculations.

Discussion

Generalization of the Hurwitz Discriminant

Let $f_0(z)$ be a polynomial in z with complex coefficients p_k.

$$f_0(z) = z^n + p_1 z^{n-1} + \ldots + p_n \tag{1}$$

An iterative process on the coefficients p_k^m, where the superscript indicates the mth polynomial obtained by the process, is given by the following definitions. If p is any complex number, let

$$p = p_R + jp_I, \qquad p_R, p_I \text{ real} \tag{2}$$

$$R(p) = p_R \tag{3}$$

$$I(p) = p_I \tag{4}$$

$$p_k^m = 0, \text{ for } k > (n - m),\ 0 \leq m \leq (n-1) \tag{5}$$

$$p_k^0 = p_k,\ k \leq n \tag{6}$$

$$\mathfrak{A}(p_k^m) = \begin{cases} jp_{kI}^m, & k \text{ even} \\ p_{kR}^m, & k \text{ odd} \end{cases} \tag{7}$$

$$\left.\begin{aligned} q_0^1 &= p_{1R}^0 p_1^0 - \mathfrak{A}(p_2^0) \\ q_1^1 &= p_{1R}^0 p_2^0 - \mathfrak{A}(p_3^0) \\ &\ldots\ldots\ldots\ldots\ldots\ldots \\ q_k^1 &= p_{1R}^0 p_{k+1}^0 - \mathfrak{A}(p_{k+2}^0),\ 0 \leq k \\ q_k^m &= p_{1R}^{m-1} p_{k+1}^{m-1} - \mathfrak{A}(p_{k+2}^{m-1}),\ 0 \leq k \end{aligned}\right\} \tag{8}$$

$$p_k^1 = \frac{q_k^1}{q_0^1},\ p_k^m = \frac{q_k^m}{q_0^m},\ 1 \leq m \leq (n-1) \tag{9}$$

If all the roots of $f(z)$ have negative real parts, $f(z)$ is called a Hurwitz polynomial. By the methods of Hurwitz[3] the following may be shown.

Theorem 1. A necessary and sufficient condition that $f(z)$ be a Hurwitz polynomial is that

$$p_{1R}^m > 0,\quad 0 \leq m \leq (n-1)$$

A Sufficient Condition for the Absence of Flutter

The range of damping coefficients occurring in aircraft structures is such that

$$(1 + jg_1)(1 + jg_2) \doteq 1 + j(g_1 + g_2) \tag{10}$$

Assume a fixed value of $v/b\omega$ and let the damping in the ith degree of freedom be $g_i + g$, where g_i is a conservative estimate of the structural damping coefficient in the ith degree of freedom and g, the additional damping required, is to be determined. When use is made of the approximate equality given above, the expanded determinant has the form

$$g(z) = z^n + b_1 z^{n-1} + \ldots + b_n = 0 \tag{11}$$

where $z = (\omega_r/\omega)^2(1 + jg)$. If z_{gr} and $1 \leq r \leq n$ are the roots of $g(z) = 0$, then a sufficient condition for the absence of flutter is

$$I(z_{gr}) < 0,\ 1 \leq r \leq n \tag{12}$$

A solution satisfying this condition means that negative damping is required to induce flutter. If the value $g_i = 0,\ 1 \leq i \leq n$ is assumed, then the polynomial $g(z)$ is identical with that used by the Matériel Center.[5] In the illustrative examples of this paper the assumption $g_i = 0,\ 1 \leq i \leq n$ is made.

Application of Theorem 1 to Flutter Analyses

From Theorem 1 and condition (12) a sufficient condition for the absence of flutter may be derived. Let

$$p_k^0 = (-j)^k b_k \tag{13}$$

and let

$$f(z) = \sum_{k=0}^{n} p_k^0 z^{n-k} \tag{14}$$

If $(z_{fr}),\ 1 \leq r \leq n$ are the n roots of $f(z) = 0$, then

$$z_{fr} = -jz_{gr} \tag{15}$$

and

$$R(z_{fr}) = R(-jz_{grR} + z_{grI}) = I(z_{gr})$$

and condition (12) is equivalent to

$$R(z_{fr}) < 0,\quad 1 \leq r \leq n$$

Therefore: *Theorem 2.* The condition $R(p_1^m) > 0$, $0 \leq m \leq (n-1)$ is a sufficient (not necessary) condition for the absence of flutter.

Tabular arrangements of calculations for p_1^m are given in a separate section of this paper.

Generalization of Routh Method

A second method for testing a flutter polynomial may be derived from Routh's discriminant. Take the flutter polynomial

$$g(z) = z^n + b_1 z^{n-1} + \ldots + b_n$$

and let

$$f(z) = g(z) = z^n + p_1^0 z^{n-1} + \ldots + p_n^0 \tag{16}$$

For

$$z = x,\ f(x) = S_0(x) + jS_1(x) \tag{17}$$

where $S_0(x)$ and $S_1(x)$ are real valued polynomial functions of x. Form the Sturm sequence[7]

$$\left.\begin{aligned} S_0(x) &= q_1 S_1(x) - S_2(x) \\ S_1(x) &= q_2 S_2(x) - S_3(x) \\ &\ldots\ldots\ldots\ldots\ldots\ldots \\ S_{N-2}(x) &= q_{N-1} S_{N-1}(x) - S_N \end{aligned}\right\} \tag{18}$$

where $S_m(x)$, $m < N$ is a polynomial in x; S_N is a constant independent of x; and $q_m(x)$ is a polynomial in x

and degree $S_{k+1}(x) <$ degree $S_k(x)$. The assumption is made that $S_N \neq 0$, although the special case $S_N = 0$ would merely simplify the problem.

Another Sufficient Condition

Let the leading coefficients of $S_0, S_1, \ldots, S_N$ be

$$A_0^0, A_0^1, A_0^2, \ldots, A_0^N \tag{19}$$

Let the constant terms in these polynomials be

$$C^0, C^1, C^2, \ldots, C^N \tag{20}$$

Call the number of variations in sign in the sequence (19) V_∞. Change the sign of those terms A_0^m, which are coefficients of x raised to an odd power. The number of variations in sign in this sequence is called $V_{-\infty}$.

Theorem 3. If $V_{-\infty} - V_\infty = n$ where n is the number of roots of $g(z) = 0$, then the flutter polynomial equation has no unstable roots.

Corollaries to Theorem 3

(1) If $p_{11}{}^0$ is negative, the sufficient condition for the absence of flutter given by Theorem 3 is no longer satisfied.

(2) If there are $n + 1$ terms in the sequence $(S_0, S_1, \ldots, S_N)$ and if the leading coefficients, $A_0^0, A_0^1, \ldots, A_0^N$ are all of the same sign, then the sufficient condition of Theorem 3 is automatically satisfied.

(3) If there are less than $n + 1$ terms in the sequence $(S_0, S_1, \ldots, S_N)$ then the sufficient condition of Theorem 3 is not satisfied.

Further Generalization of Routh Method

If a given polynomial does not satisfy the sufficient condition of Theorem 3, a third method may be employed. The third method consists first in applying the second method to get

$$A_0^0, A_0^1, \ldots, A_0^N \tag{21}$$

and the constant terms

$$C^0, C^1, \ldots, C^N \tag{22}$$

Let $z = jy$ and obtain

$$f(z) = {}'S_0(y) + j\,{}'S_1(y) \tag{23}$$

Form a Sturm sequence using $'S_0$ and $'S_1$ as the first two terms.

$$\left.\begin{aligned} {}'S_0(y) &= q_1{}'S_1(y) - {}'S_2(y) \\ {}'S_1(y) &= q_2{}'S_2(y) - {}'S_0(y) \\ &\cdots\cdots\cdots\cdots\cdots\cdots \\ {}'S_{M-2}(y) &= q_{M-1}{}'S_{M-1}(y) - {}'S_M \end{aligned}\right\} \tag{24}$$

where $'S_m$, $m < M$ is a polynomial in y; $'S_M$ is a constant independent of y; and q_m a polynomial in y and for $k \geq 1$ degree $'S_{k+1}(y) <$ degree $'S_k(y)$. Again consider the coefficients of the leading terms, this time in $'S_0, 'S_1, \ldots, 'S_M$, to obtain

$$'A_0^0, 'A_0^1, \ldots, 'A_0^M \tag{25}$$

and the constant terms

$$'C^0, 'C^1, \ldots, 'C^M \tag{26}$$

The number of variations in sign in sequences (21), (22), (25), and (26) are called, respectively, V_∞, V_{0R}, $V_{j\infty}$, V_{j0}.

The Necessary and Sufficient Condition That a Flutter Polynomial Have No Unstable Roots

Theorem 4. For n, the degree of the flutter polynomial, *even* a necessary and sufficient condition for the absence of flutter for fixed $v/b\omega$ is

$$V_{j\infty} - V_{j0} + V_{0R} - V_\infty = n/2 \tag{27}$$

Theorem 5. For n *odd* and $'S_0/'S_1 \underset{y\to\infty}{\longrightarrow} 0^+$, the necessary and sufficient condition for the absence of flutter for fixed $v/b\omega$ is

$$V_{j\infty} - V_{j0} + V_{0R} - V_\infty = (n-1)/2 \tag{28}$$

Theorem 6. For n *odd* and $'S_0/'S_1 \underset{y\to\infty}{\longrightarrow} 0^-$, the necessary and sufficient condition for the absence of flutter for a given value of $v/b\omega$ is

$$V_{j\infty} - V_{j0} + V_{0R} - V_\infty = (n+1)/2$$

Applications to Flutter Analysis Procedure

In applying any of the three methods, one first forms the flutter polynomials for either the range of $v/b\omega = 1/k$ suspected to be critical from previous information or, if there is no previous experience to draw upon, for a range starting with the lowest tabulated value of $1/k > 0$. A good upper bound to use for the values of $1/k$ is $v_0(1.2)/b\omega_e$ where v_0 is the true terminal velocity of the airplane in feet per second, b is the representative semichord of the wing in feet, and ω_e is the estimated flutter frequency of the airfoil in radians per second. For flutter analyses involving a torsional mode a good estimate of ω_e would be

$$\omega_e = 0.8\omega_\alpha$$

where ω_α is the torsional frequency.

After the flutter polynomials have been set up for the required values of $v/b\omega$, it is desirable to apply either the sufficient condition of Method I or that of Method II. In general, either the criterion will be satisfied for all the required values of $1/k$, in which case no further work need be done, or there exists a value $1/k_1$ beyond which the flutter polynomial fails to satisfy the sufficient condition. If the latter alternative results from applying the sufficient condition, one either (a) gets an estimate of the flutter speed for the last value $1/k = 1/k_1$ for which the stability condition held, or (b) applies Method III.

For alternative (a), suppose the sufficient condition to be satisfied for $1/k_1$ and not satisfied for the succeeding value $1/k = 1/k_2$, $1/k_1 < 1/k_2$. Then, by arguing from the stability present for $1/k = 1/k_1$ and the estimated flutter frequency, one arrives at a conservative

estimate of the flutter speed; but, if this estimate indicates a critical flutter speed, one solves the polynomial equation for $1/k_1$ and $1/k_2$ determining in each case the damping coefficients, g, and the corresponding flutter speeds v_F. In most practical cases at least one of the dampings corresponding to $1/k_2$ will be positive, and the damping corresponding to the same branch of the curve of v_f versus g will be negative at $1/k_1$. The straight line joining these two points in a plot of v_F versus g intersects the line $g = 0$ at a value of v_F equal to the flutter speed of the airplane. Should all the g's corresponding to $1/k_2$ be negative, then it is recommended that the stability polynomials be solved for the succeeding values of $1/k$ or that Method III be employed.

For alternative (b) apply Method III for $1/k = 1/k_2$ and continue to apply it until the necessary and sufficient condition fails to be satisfied. In that event solve the polynomial equations for values of $1/k$ just before and just after the instability occurs and thus obtain a conservative estimate of the flutter speed. Even when procedure (b) is necessary, considerable time is saved by avoiding solutions of irrelevant complex polynomial equations.

Types of Flutter Analyses to Which Methods I, II, and III May Be Applied

The theorems of the preceding discussion are of a general nature and may be applied to any polynomial of finite degree with complex coefficients in any problem where it is advantageous to know whether condition (12) is satisfied. Application is made to flutter problems for two or three degrees of freedom because these provide the most immediately useful application of the principles. The methods may be applied equally well to equations of higher degree. It should also be borne in mind that in many flutter problems it is not desirable to obtain flutter velocity as a function of the additional damping required in the structure in order that the conditions for the onset of flutter be satisfied. In cases where it is desirable to obtain flutter velocity as a function of a natural frequency ratio, the graphical method developed by Lt. Comdr. L. Arnold (Bureau of Aeronautics)[8] has been found to be extremely useful.

In first attacking a flutter problem the analyst must decide what method is best suited to his particular problem. Where flutter velocity versus damping represents a suitable solution, the application of the stability tests described in this paper is recommended.

Illustration of the Stability Test Calculations

To apply the generalized Hurwitz condition of Theorem 2 to a flutter polynomial equation

$$g(z) = 0$$

a new equation

$$f_0(z) = 0$$

is derived by multiplying the roots of $g(z) = 0$ by $-j$. The detached coefficients of $f_0(z) = 0$ are then used to calculate the terms $p_k^m[0 \leq m \leq (n-1)]$.

From Eqs. (8) and (9) it is evident that

$$p_k^m = \frac{p_{1R}\, {}^{m-1}p_{k+1}{}^{m-1} - \mathfrak{A}(p_{k+2}{}^{m-1})}{p_{1R}\, {}^{m-1}p_1{}^{m-1} - \mathfrak{A}(p_2{}^{m-1})}$$

where $\mathfrak{A}(p_k^m)$ is governed by definition (7) and the other terms are defined by relations (2), (3), (4), (5), and (6).

A convenient procedure for calculating p_k^m is illustrated in Table 1.

The following notation is adopted. Let

$$f_m = \{q_0^m, q_1^m, \ldots, q_{n-m}{}^m\}$$

and

$$f_m' = f_{m\,(\text{normalized})} = \{1, p_1^m, \ldots, p_{n-m}{}^m\}$$

f_0' is the set of coefficients of $f_0(z)$ defined above.

Inspection of Table 1 reveals that for all values of m, p_1^m lies in the first quadrant and, hence, the sufficient condition of Theorem 2 is satisfied. The work of dividing through the polynomial f_m by its leading coefficient to obtain the coefficient of $f_m'(z)$ may, of course, be done by operating with either the polar or rectangular

TABLE 1

$g(z) = z^3 + (-2.164 + 2.539j)z^2 + (-1.421 - 5.711j)z + 1.190 + 2.075j$. Eq. (a)

Coefficient	p_0	p_1	p_2	p_3
Rule to obtain f_{n+1} from f_n'	$p_{1R}p_1 - jp_{1I}$	$p_{1R}p_2 - p_{2R}$	$p_{1R}p_3 - jp_{3I}$	$p_{1R}p_4 - p_{3R}$
f_0'	1.00 + 0j	2.539 + 2.164j	1.421 + 5.711j	−2.075 + 1.190j
f_1	6.447	5.683	− 5.268	0
	−0.217j	+14.500j	+ 3.021j	
•	41.611	33.492	−34.618	
		+94.715j	+18.333j	
f_1'	1.00	0.805	− 0.832	
	0j	+ 2.276j	+ 0.441j	
f_2	0.648	− 0.670		
	+1.391j	+ 0.355j		
•	2.355	0.0596		
		+ 1.1620j		
f_2'	1.00	0.0253		
	+0j	+ 0.4934j		

form of the complex numbers depending upon the preference of the computer.

An estimate of the relative amount of work involved in making this calculation for polynomials of different degrees may be obtained by considering the number of squares to be filled. For an nth degree flutter polynomial, $(3n^2/2) + (5n/2) - 2$ squares must be filled.

Experience has shown that the angle of $p_1^n - 1$, when plotted against $v/b\omega$, gives a good graphical representation of the change in the stability of the polynomial equations as $v/b\omega$ varies. Such a plot makes possible the choice of a suitable range of $v/b\omega$ for more detailed analysis. This type of graph is compared qualitatively in Figs. 1, 2, and 3, with the final results of flutter velocity versus damping for three flutter problems actually encountered.

Method II. To apply the extended Routh discriminant to the polynomial $g(z)$, S_0 and S_1 are determined according to Eq. (17). A sequence (S_m), satisfying Eq. (18) is to be determined. Instead of obtaining (S_m) directly, it is sufficient to consider the terms of S_m multiplied by a positive quantity. The sequence $(\bar{S}_m)$ is defined by

$$\bar{S}_m(x) = K^2 S_m(x)$$

Hence, the number of variations in sign in the leading or constant terms will be the same whether one considers S_m or $\bar{S}_m$. Reference 4 (page 152) gives a convenient pattern for computing the coefficients of the functions $\bar{S}_m$. To obtain $\bar{S}_2$ from S_0 and S_1, an auxiliary sequence, indicated by a star, is first obtained by cross multiplication. Thus

$$A_0^* = A_0^1 A_1^0 - A_1^1 A_0^0$$

The cross-multiplication process is repeated using the starred row and S_1 to obtain $\bar{S}_2$. S_3 is obtained by repeating the process starting with S_1 and $\bar{S}_2$. If the leading coefficients in each of the terms $\bar{S}_m$ are of the same sign, the sufficient condition of Theorem 3 will be satisfied. If, for example, the flutter polynomial to be tested is

$$g(z) = z^3 + (-4.3306 + 0.5400j)z^2 + (5.6056 - 1.3747j)z - 1.9857 + 0.6531j$$

the test functions are given in Table 2.

From the sequence $(\bar{S}_m)$ the quantities V_∞ and $V_{-\infty}$ necessary for applying Theorem 3 are obtained, or V_∞ and V_{0R} for applying the criterion of Theorem 4, 5, or 6.

TABLE 2

S_0	1	−4.3306	5.6056	−1.9857
S_1	0.5400	−1.3747	0.6531	
*	−0.9638	2.3739	−1.0723	
$\bar{S}_2$	0.0430	−0.0504		
*	−0.0319	0.0281		
$\bar{S}_3$	0.0004			

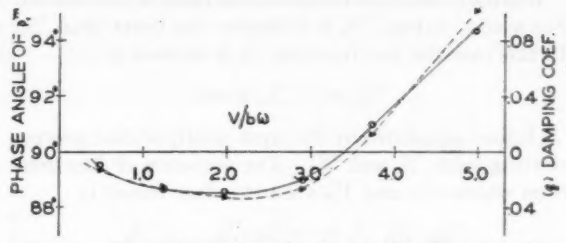

FIG. 1. Comparison of results for a wing flexure-torsion-aileron ternary case. The phase angle of p_1^m is plotted for a range of values of $v/b\omega$. This curve compares qualitatively with the damping coefficient associated with the most critical root found by actually solving the equations. The phase angle of p_1^m is indicated by a circle and the value read from the left-hand scale. The damping coefficient is indicated by a triangle, and its value is read on the right-hand scale.

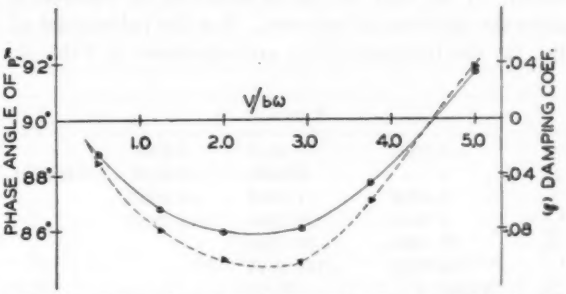

FIG. 2. Comparison of results for a wing flexure-torsion binary case. Circle indicates phase angle of p_1^m. Triangle indicates damping coefficient associated with the most critical root.

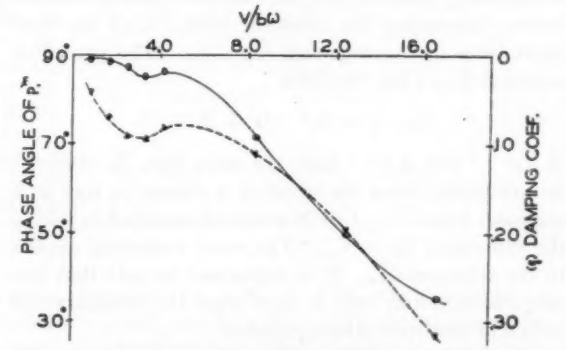

FIG. 3. Comparison of results for a fuselage vertical bending, stabilizer bending, elevator rotation ternary case. Circle indicates phase angle of p_1^m. Triangle indicates damping coefficient associated with the most critical root.

Method III. If the necessary and sufficient condition for the absence of flutter is to be applied to the polynomial equation, the sequence $('S_m)$ must be calculated in order to determine $V_{j\infty}$ and V_{j0}. To obtain $('S_m)$ it is necessary to distinguish between the calculations when n is *even* and when n is *odd*. When n is *even*, since $p_0 = 1$, $'S_0$ will have its leading term positive and the degree of $'S_0$ will be one higher than $'S_1$. For convenience, every term in $g(z)$ may be multiplied by -1 so that the leading term of $'S_0$ will be positive. In this case the calculation of $('S_m)$ is made in a manner exactly analogous to the calculation of (S_m).

When n is *odd* a few modifications must be introduced. For n odd, p_0 real, $'S_0$ is of degree one lower than $'S_1$. In this case the test function $'S_2$ is defined as

$$'\bar{S}_2 = -\ 'S_0,\ n \text{ odd}$$

$'\bar{S}_3$ is then calculated by the cross-multiplication process starting with $'S_1$ and $'\bar{S}_2$. The sequence of functions from which $V_{j\infty}$ and V_{j0} are to be determined is

$$'S_0,\ 'S_1,\ '\bar{S}_2 = -'S_0,\ '\bar{S}_3,\ \ldots,\ '\bar{S}_N$$

After determining $V_{j\infty}$ and V_{j0} it is necessary to decide whether Theorem 5 or Theorem 6 is applicable. This can be quickly done by examining the signs of the leading coefficients in $'\bar{S}_0$ and $'\bar{S}_1$. If $'A_0{}^0$ and $'A_0{}^1$ are of the same sign, Theorem 5 gives the appropriate criterion. If $'A_0{}^0$ and $'A_0{}^1$ are of unlike signs, Theorem 6 gives the appropriate criterion. For the polynomial of Eq. (a) the functions $('\bar{S}_m)$ are calculated in Table 3.

TABLE 3

$'S_0$	−4.3306	−1.3747	1.9857	
$'S_1$	1	0.5400	−5.6056	−0.6531
$'S_2$	4.3306	1.3747	−1.9857	
•	0.9638	−22.2899	−2.8283	
$'\bar{S}_3$	97.8536	10.3344		
•	89.7652	−194.3079		
$'\bar{S}_4$	19,941.4			

In applying the necessary and sufficient condition it is frequently possible to terminate the Sturm procedure before calculating the constant term. Call the constant term in the sequence $(\bar{S}_m)$, S_N. The preceding function $\bar{S}_{N-1}$ has the form

$$\bar{S}_{N-1} = A_0{}^{N-1}x + A_1{}^{N-1}$$

If $A_0{}^{N-1}$ and $A_1{}^{N-1}$ have the same sign, $\bar{S}_N$ need not be calculated, since the effect of a change in sign as n increases from $N-1$ to N would be canceled in taking the difference $V_0 - V_\infty$. The same reasoning applies to the sequence $'\bar{S}_m$. It is important to note that this simplification may only be used when the necessary and sufficient condition is being applied.

Use of the Test Functions to Approximate the Most Critical Root

After the polynomial equations have been tested by either of the discriminants, it may appear desirable to obtain the solution of polynomial equations for one or two values of $v/b\omega$. The flutter speed is determined from the real part of the root according to the relation

$$V_F = (v/b\omega)(\omega/\omega_r)\omega_r b$$

Before actually solving the equation it is advantageous to know approximately the value of the real part of that root which has the smallest imaginary part. When a good approximation for $(\omega_r/\omega)^2$ is known, it is possible to estimate the flutter speed with reasonable accuracy. Moreover, it is possible to obtain the most critical of the n roots first. When this critical root has been obtained, it is usually not necessary to solve for the other $n-1$ roots. It can easily be shown that the modulus of $p_1{}^{n-1}$ is approximately equal to $(\omega_r/\omega)^2$, but for angles close to 90°, $p_{1I}{}^{n-1} \doteq |p_1{}^{n-1}|$; hence, we may take as an approximation of the flutter speed

$$V_F = (v/b\omega)(1/\sqrt{p_{1I}{}^{n-1}})b\omega_r$$

If more exact values are desired, then in Newton's method let the first approximation be $(p_{1I}{}^{n-1} + 0j)$. There will then be rapid convergence because of the good first approximation.

If the polynomials have been tested by the condition of Theorem 3, then a first approximation for the critical root of $g(z) = 0$ may be obtained by solving $S_1(x) = 0$ and choosing that real root, or real part of a complex root, which is most nearly equal to 1. This approximation will usually be sufficient to obtain the most critical root of $g(z) = 0$ first but does not permit so close an estimate of the flutter speed before actually solving the equation as the use of the term $p_1{}^{n-1}$. In general, a solution by Newton's method is desirable to ensure an accurate value of ω_r/ω from which to obtain the flutter speed.

NUMERICAL EXAMPLES

(A) *Flexure, Torsion, Aileron Ternary Case*

The true terminal velocity of airplane A was not known; hence, to obtain an upper bound for the parameter $v/b\omega$, the velocity of sound at sea level, V_s, and the lowest natural frequency were used and the quantity

$$V_s/b\omega_1 = 4.70$$

was taken as an approximate upper bound. The reference frequency and semichord are given as 155.8 rad. per sec. and 3.28 ft., respectively. Flutter polynomial equations were set up for values of $v/b\omega$ in the range

$$0.50 \leq v/b\omega \leq 5.00$$

Application of the stability tests of Method I showed that the condition of Theorem 2 was satisfied for $v/b\omega \leq 2.94$ and not satisfied for $v/b\omega \geq 3.75$. Fig. 1 is a plot of $p_1{}^m$ for this case. Tables 4 and 5 show the stability calculations for $v/b\omega = 2.94$ and $v/b\omega = 3.75$. The value of $p_{1I}{}^2$ for each of the polynomial equations is used to obtain an approximate value for the most critical root. For $v/b\omega = 2.94$ the real part of the most critical root is approximately 1.421, and 1.683 for $v/b\omega = 3.75$. By using these two roots as approximate values of $(\omega_r/\omega)^2$, the flutter speed V_F is found to lie in the range

$$859 \text{ m.p.h.} < V_F < 1{,}007 \text{ m.p.h.}$$

Since it is bizarre to apply the conventional incompressible air forces or any of the empirical corrections hitherto suggested to the case where the Mach Number is close to or greater than 1.0, no further investigation was made.

TABLE 4

$g(z) = z^3 + (0.377 + 9.94j)z^2 + (-75.5 - 54.9j)z + 104.00 + 55.10j$

$v/b\omega = 2.94$

Coefficient, Rule	p_0 $p_{1R}p_1 - jp_{2I}$	p_1 $p_{1R}p_2 - p_{2R}$	p_2 $p_{1R}p_3 - jp_{4I}$	p_3 $p_{1R}p_4 - p_{3R}$
	1.00	9.940	75.50	−55.10
	+0j	−0.377j	+54.90j	+104.00j
f_1	98.80	805.57	−547.69	
	−58.65j	+545.71j	+1,033.76j	
•	13,201.26	47,584.42	−114,741.80	
		+101,162.83j	+ 70,013.47j	
f_1'	1.00	3.60	−8.69	
	+0j	+7.66j	+5.30j	
f_2	12.96	−31.28		
	+22.28j	+19.08j		
•	664.36	+19.71		
		+944.20j		
f_2'	1.00	0.0297		
	+0j	+1.421j		

TABLE 5

$g(z) = z^3 + (7.61 + 12.50j)z^2 + (-145.5 - 52.00j)z + (219.00 + 55.40j)$

$v/b\omega = 3.75$

Coefficient Rule	p_0 $p_{1R}p_1 - jp_{2I}$	p_1 $p_{1R}p_2 - p_{2R}$	p_2 $p_{1R}p_3 - jp_{4I}$	p_3 $p_{1R}p_4 - p_{3R}$
f_0'	1.00	12.50	145.50	− 55.40
	+0j	− 7.61j	+52.00j	+219.00j
f_1	156.25	1,874.15	−692.50	
	−147.13j	+650.00j	+2,737.50j	
•	46,061.30	197,201.44	−510,971.50	
		+377,306.19j	+325,846.85j	
f_1'	1.00	4.28	−11.09	
	+0j	+8.19j	+ 7.07j	
f_2	18.32	−47.47		
	+27.98j	+30.26j		
•	1,118.50	−22.98		
		+1,882.57j		
f_2'	1.00	−0.0205		
	+0j	+1.6831j		

Example A

Example A is covered in Tables 4 and 5.

Example B

Methods II and III will be applied to the same flutter analysis used in Example A. The sufficient condition of Theorem 3 was applied to the flutter polynomials, and it was found that the condition was satisfied for $v/b\omega \leq 2.94$ and not satisfied for $v/b\omega \leq 3.75$. The necessary and sufficient condition was applied to the flutter polynomial for $v/b\omega = 3.75$. The flutter polynomial failed to satisfy the necessary and sufficient condition, and hence it was known that, for this particular value of the parameter $v/b\omega$, $g(z) = 0$ had an unstable root. In order to obtain a first approximation for the critical root, the equation $S_1(x) = 0$ was solved when $v/b\omega = 2.94$ and $v/b\omega = 3.75$. In each case, the values 1.318 and 2.08 were used as a first approximation in Newton's method. The critical root of the polynomial equation for $v/b\omega = 2.94$ was found to be $1.506(1 - .059j)$, and for $v/b\omega = 3.75$ the critical root is $1.690(1 + .017j)$. These results yield two points on a plot of flutter velocity versus damping.

g	V_F m.p.h.
−0.059	835
+0.017	1,005

Linear interpolation gives as value of V_F for $g = 0$ a flutter speed of 967 m.p.h.

Calculations of the Sturm functions for Example B are given in Tables 6, 7, and 8. In performing the calculations, it was often convenient to multiply through one row of the table by a power of 10. This gave numbers of convenient order of magnitude. This procedure, of course, does not affect the results, since it is the sign and not the magnitude of the terms which is being considered.

TABLE 6

$v/b\omega = 2.94$

S_0	1	0.377	−75.500	104.00
S_1	9.94	−54.90	55.10	
*	58.65	−805.57	1,033.76	
S_2	+47.87	−70.44		
*	−19.28	26.38		
S_3	95.27			

TABLE 7

$v/b\omega = 3.75$

S_0	1	7.61	−145.50	219.00
S_1	12.50	−52.00	55.40	
*	147.13	−1,874.15	2,737.50	
S_2	157.76	−260.68		
*	−49.45	87.40		
S_3	−8.976			

TABLE 8

$v/b\omega = 3.75$

$'S_0$	7.61	−52.0	−219.0	
$'S_1$	1	12.50	145.50	−55.40
$'S_2$	−7.61	52.00	219.00	
*	−147.13	−1,326.26	421.59	
$'S_3$	−177.44	−290.13		

From Table 8

$$V_{j\infty} - V_{j0} = -2$$

$$V_{j\infty} - V_{j0} + V_{0R} - V_\infty \neq (n-1)/2$$

For $v/b\omega = 3.75$
Let $S_1(x) = 0$

$$12.50x^2 - 52.00x + 55.40 = 0$$

$$x = 2.08 \pm (1/25)\sqrt{-66}$$

For $v/b\omega = 2.94$
Let $S_1(x) = 0$

$$9.94x^2 - 54.90x + 55.10 = 0$$

$$x_1 = 4.205$$

$$x_2 = 1.318$$

CONCLUSIONS AND RECOMMENDATIONS

(1) The theorems of Routh and Hurwitz have been extended to polynomials with complex coefficients and more varied stability conditions.

(2) The time required to determine the stability of a cubic flutter polynomial has been reduced from $2^1/_2$ hours to 10 min.

(3) Application of the methods described in this paper should reduce the time required for estimating the flutter speed from the stability polynomials to one-fifth the time previously required.

(4) Extension of the ideas and methods of this paper to helicopter dynamic stability and airplane dynamic stability calculations is contemplated, and discussion is reserved for a separate report.

REFERENCES

[1] von Kármán, Th., and Biot, M. A., *Mathematical Methods in Engineering*, Chap. VI, Sec. 7, p. 258; McGraw-Hill Book Company, Inc., New York, 1940.

[2] Routh, E. J., *Dynamics of a System of Rigid Bodies*, 6th Ed., Part II, p. 221 ff.; Macmillan and Company, London, 1905.

[3] von Mises, R., *Riemann-Webers Partiellen Differentialgleichungen der Mathematischen Physik*, p. 162; Mary S. Rosenberg, New York, 1943.

[4] Frazer, R. A., Duncan, W. J., and Collar, A. R., *Elementary Matrices*, p. 155 and p. 162; Cambridge University Press, Cambridge, England, 1938.

[5] Army Air Forces Technical Report No. 4798 (Restricted) p. 130; Matériel Center, July, 1942.

[6] It has recently come to the author's attention that Prof. M. V. Barton, University of Texas, has undertaken a study of this possibility with some success.

[7] Dickson, L. E., *First Course in the Theory of Equations*, p. 75; John Wiley & Sons, Inc., New York, 1922.

[8] Arnold, L., *A Vector Solution of the Flutter Stability Determinant*, Structures Memorandum No. 26 (Restricted), Navy Department, Bureau of Aeronautics, Washington, D. C., May, 1944.

Important Announcement

The Officers and Council of the Institute of the Aeronautical Sciences are pleased to announce that the *Journal of the Aeronautical Sciences* will resume publication as a monthly starting in January, 1946. This change has been made possible because of the relaxation of restrictions controlling the use of paper. There will be no change in subscription rates.

Buckling of Stiffener and Elastic Sheet Combinations Under Pure Bending

E. E. WEIBEL*
University of California

ABSTRACT

Stiffened sheet covering, for example in seaplane hulls, may be subjected to bending moments that produce compressive bending stress in the unsupported stiffener areas. The critical value of bending moment is desired at which stiffeners of open section will buckle torsionally. The present solution introduces the effect of the elastic bending properties of the sheet into the stiffener buckling problem. The stiffener now carries a portion of the total moment plus a compressive force that is equal to the tensile force in the sheet. The expression for the elastic moments transmitted from the sheet is obtained by a linear treatment of the actually nonlinear problem.

Adding to the problems treated by Wagner and Kappus, Goodier, in those problems considered by him, finds the critical loads or moments as the solutions of algebraic equations derived from the differential equations of the problem. In the present problem the sheet-bending deflection is expressed in the Levy type Fourier form, which avoids the differential equation in the variational problem and introduces a transcendental term into an otherwise algebraic equation. Trial-and-error solution is indicated to obtain the critical value of bending moment.

INTRODUCTION

THE TORSIONAL BUCKLING of open section members has been discussed by Timoshenko,[1, 2] Wagner,[3, 4] Kappus[5] and Goodier.[6, 7, 8] Equations have been derived by the last named (Eqs. 31 and 32, reference 7) for the buckling of bars attached to an ideal inextensible and perfectly flexible sheet when the bars are subjected to a combination of pure bending moments and central end load. The idealized sheet served as a kinematic link providing a relation between the rotations and the sheetwise displacements of cross sections of the bar and did not provide any of the terms in the energy expressions which were used in deriving the differential equations referred to above.

The sheet in an actual stiffened sheet panel under pure bending will have deformations and stresses somewhat as described below. Bending produces a cylindrical sheet surface, departures from which are caused by the combined effect of curvature and tensile sheet stress, equivalent to a lateral load on the sheet. These prebuckling deflections tend to reduce the longitudinal sheet stress near the center of the panel width and to induce lateral median stresses, as well as bending stresses, in the sheet. Rotation of stiffener cross sections either before or during the buckling is resisted by the elastic median stresses and by bending stresses in the sheet. An analysis based on large deflection equations for an initially cylindrical elastic plate would be necessary to account for these stresses. The nonlinear problem is difficult, and at best an approximate solution would be time-consuming.

In the absence of a solution of the actual problem, the following idealization is introduced which reduces the problem to a linear one while taking account of the bending stiffness of the sheet in the presence of assumed uniform median stresses. The small deflection, flat plate equations are used for the sheet, neglecting the cylindrical curvature mentioned above but assuming uniform tensile sheet stresses in two directions. The longitudinal tensile stress σ_z represents the stress due to bending and is proportional to the applied bending moment M per panel width b. The assumed lateral tensile stress of value $k\nu\sigma_z$ is an induced or Poisson's ratio stress. The panel considered may be at the center of a group of panels or it may be at one edge. In the former case $k = 1/[1 + (at/B)]$, where at/B is the ratio of sheet area to frame cross-section area. In the latter case k approaches zero. The assumption of uniform sheet stresses permits the solution of the plate equation and the derivation of "spring constant" functions for the elastic bending resistance of the sheet. Expressions for the potential energy of the elastic resisting moments of the sheet are combined with those given by Goodier (pp. 13 and 14, reference 7) for the strain energy of the stiffener and for the potential energy of the stiffener end moments and forces. Minimizing of the total energy expression leads to the prebuckling values of stiffener cross-section displacements and rotations. Additional procedures yield the critical or buckling values of applied moment.

STIFFENER NOTATIONS AND DISPLACEMENTS

The positive directions for end moments M_1 and M_2 and forces P on stiffeners[7] are shown in Fig. 2. Coordinate x and y axes in any cross section have their origin at the shear center S, Fig. 3, whose displacement has components u and v. The stiffener centroid C has coordinates (x_0, y_0). Rotation of any cross section is measured by angle β, positive clockwise. The variables u, v, and β are functions of $\bar{z}$, the coordinate in the longitudinal direction of the stiffener. The notation $\bar{z}$ is used to distinguish this linear quantity from a di-

Received December 21, 1944. To have been presented at the I.A.S. Thirteenth Annual Meeting, which was canceled to cooperate with a Government appeal (January, 1945) to refrain from holding conventions and meetings.

* Associate Professor of Mechanical Engineering.

mensionless variable z used in the sheet analysis. In the present study, in order to relate the expressions for resisting moments of the sheet to the displacements of the stiffeners, it will be convenient to express u, v, and β as Fourier sine series in either of the forms

$$v = \sum_{m=1}^{\infty} v_m \sin \frac{m\pi\bar{z}}{a}, \quad 0 \leqslant \bar{z} \leqslant a \tag{1}$$

or

$$v = \sum_{m=1}^{\infty} v_m \sin m\pi z, \quad 0 \leqslant z \leqslant 1 \tag{2}$$

and similarly for u and β.

Symbols

For Stiffener

- S = shear center of cross section
- x, y = axes with origin at S
- $\bar{z}$ = coordinate in direction of stiffener axis
- a = distance between stiffener supports. Panel length
- x_0, y_0 = coordinates of centroid (C) of cross section
- u, v = components in x and y directions of displacement of S
- β = angle of rotation of cross section, positive clockwise
- S', x', y' = displaced positions of S, x, y
- g, h = x and y coordinates to point of attachment of sheet to stiffener
- I_1, I_2 = moment of inertia of stiffener section about stiffener centroidal axes parallel to the y and x axes, respectively
- I_{12} = corresponding product of inertia
- P = end thrust acting at centroid of stiffener area
- A = stiffener cross-section area
- E = Young's modulus
- G = shear modulus
- GC = the torsional rigidity of stiffener[7]
- C = of the type $bc^3/3$ for thin open sections[10]
- Γ = C_{bd} of Wagner,[3] C_{BT} of Lundquist and Fligg.[11] Defined by Goodier.[8] A geometrical constant of the section = $\int (w_1 - \bar{w}_1)^2 dA$, where $(w_1 - \bar{w}_1)$ is "warping per unit twist." Dimensions of $\Gamma = [L^6]$
- ρ = polar radius of gyration of stiffener area about shear center (reference 6, p. 17) (reference 7, pp. 7 and 8). $A\rho^2 = \int (x^2 + y^2) dA$
- $\mu_1 = \dfrac{-I_1 I_2}{I_1 I_2 - I_{12}^2}\left(\dfrac{M_1}{I_1} - \dfrac{M_2}{I_2}\dfrac{I_{12}}{I_1}\right)$ (reference 7, p. 14)
- $\mu_2 = \dfrac{-I_1 I_2}{I_1 I_2 - I_{12}^2}\left(\dfrac{M_2}{I_2} - \dfrac{M_1}{I_1}\dfrac{I_{12}}{I_2}\right)$
- M_1 = moment about an axis parallel to the y axis, positive when it produces tension stress for $(x - x_0)$ positive. $M_1 = 0$ in the present problem
- M_2 = moment about an axis parallel to the x axis, positive when it produces tension stress for $(y - y_0)$ positive
- κ_1 = $\int x(x^2 + y^2) dA - x_0 A\rho^2$; (reference 7, pp. 8 and 14)
- κ_2 = $\int y(x^2 + y^2) dA - y_0 A\rho^2$
- σ_b = bending stress in stiffener at a point (x, y) (stiffener stresses only are positive in compression)
- σ_p = P/A, uniform compressive stress in stiffener due to force P at stiffener centroid
- σ = $\sigma_b + \sigma_p$, total compressive stress at any point of cross section of stiffener

For Stiffened Sheet Combination

- M = pure bending moment about an axis parallel to the x axis, applied to a stiffener and sheet of width b. It produces tensile stress in the sheet
- M_2' = couple acting on end of sheet of panel width b
- σ_x = mean sheet tensile stress assumed independent of $\bar{x}$ and $\bar{z}$
- t = sheet thickness
- B = cross sectional area of cross frames
- k = or $< 1/[1 + (at/B)]$, geometrical factor used to obtain Poisson's ratio stress
- ν = Poisson's ratio

For Sheet

- $\bar{x}, \bar{z}$ = coordinates of a point in the sheet
- a, b = length and width of panel
- $\bar{w}$ = deflection of middle surface of sheet from its initial plane
- σ_z, σ_x = tensile stresses in $\bar{z}$ and $\bar{x}$ directions, respectively, of sheet. Assumed uniform and proportional to the applied moment M
- α = b/a, width to length ratio of panels
- D = flexural rigidity of sheet = $Et^3/12(1 - \nu^2)$
- x = $\bar{x}/b$ dimensionless coordinate
- z = $\bar{z}/a$ dimensionless coordinate
- w = $\bar{w}/t$ dimensionless deflection
- S_x = $\sigma_x b^2 12(1 - \nu^2)/Et^2$ dimensionless tensile stress
- $X = X_m$ = function of x only
- $\lambda = \lambda_m$ = $m\pi(b/a)$
- ϵ = ϵ_m
- ω = ω_m
- p_1 = p_{1m}
- p_2 = p_{2m}
- F_S = F_{Sm}
- F_A = F_{Am}

Tensile Stress in Sheet and End Loads and Moments on Symmetrical Stiffener Caused by Moment Applied to a Panel

A bending moment M applied to width b of the stiffened sheet combination may be resolved into moments M_2 and M_2' applied to stiffener and sheet, respectively, and forces P acting at the centroids of the respective areas as shown in Fig. 1b. This is expressed by the equation

$$M = M_2 + M_2' + P(h - y_0) \tag{3}$$

The relative importance of the couple M_2' is given by the ratio of sheet moment of inertia $bt^3/12$ to stiffener moment of inertia I_2. This ratio is less than 1 per cent in most applications and consequently in the present analysis the couple M_2' is neglected. Eq. (3) then reduces to

$$M = M_2 + P(h - y_0) \tag{4}$$

The total compressive stress in the stiffener is

$$\sigma = \sigma_p + \sigma_b = \frac{P}{A} - \frac{M_2(y - y_0)}{I_2} \tag{5}$$

where coordinate y is measured from the shear center S

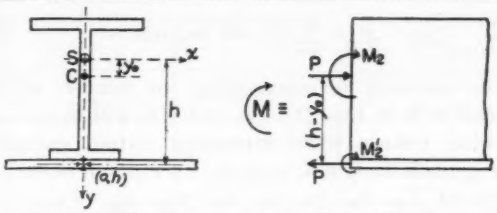

FIG. 1a (*left*). Notation for symmetrical stiffener. FIG. 1b (*right*). End moments and end loads on stiffener and sheet.

as origin (Fig. 1a), and y_0 is the coordinate of the stiffener centroid.

At the "point of attachment" $(0, h)$ of stiffener and sheet, the longitudinal strains will be equal. On the assumption of uniform tensile sheet stresses σ_z and $k\nu\sigma_z$ in the longitudinal and lateral directions, respectively, the longitudinal strain in the sheet is $\sigma_z(1 - k\nu^2)/E$. Equating this to the stiffener strain and noting that compressive stresses are considered positive in the stiffener only and that $P = \sigma_z bt$,

$$\frac{\sigma_z(1 - k\nu^2)}{E} = \frac{M_2(h - y_0)}{EI_2} - \frac{\sigma_z bt}{EA} \tag{6}$$

and

$$\sigma_z = \left\{\frac{(h - y_0)}{I_2[1 - k\nu^2 + (bt/A)]}\right\} M_2 = C_1 M_2 \tag{7}$$

where

$$C_1 = (h - y_0)/I_2[1 - k\nu^2 + (bt/A)] \tag{8}$$

The total force P is given by

$$P = \sigma_z bt = btC_1 M_2 \tag{9}$$

Substitution of Eq. (9) into Eq. (4) leads to an expression for M_2 in terms of M

$$M_2 = \{1/[1 + btC_1(h - y_0)]\}\, M = C_2 M \tag{10}$$

where

$$C_2 = 1/[1 + btC_1(h - y_0)] \tag{11}$$

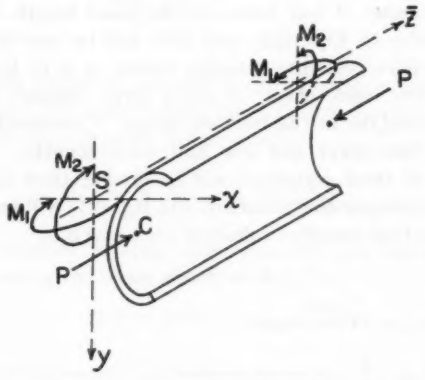

FIG. 2. Notation[7] for stiffener end moments and end loads.

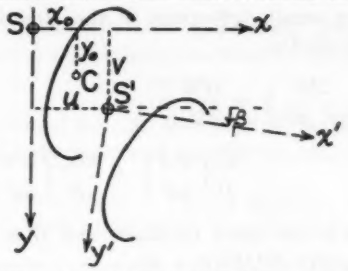

FIG. 3. Notation[7] for stiffener cross section. S = shear center and C = centroid.

Substitution of Eq. (10) into Eqs. (7) and (9), respectively, yields

$$\sigma_z = C_1 C_2 M = C_3 M \tag{12}$$

where $C_3 = C_1 C_2$ is given by Eqs. (8) and (11), and

$$P = btC_1 C_2 M = C_4 M \tag{13}$$

where $C_4 = btC_1 C_2$.

BENDING PROPERTIES OF THE SHEET

The sheet, Fig. 4, assumed to be initially flat, has panel width b and length a. The origin of coordinates $\bar{x}$ and $\bar{z}$ is at the center of the edge of length b. The stiffeners lie along the edges $\bar{x} = \pm b/2$, and frames lie along the edges $\bar{z} = 0$ and $\bar{z} = a$. Uniform applied tensile stress σ_z and induced tensile stress $\sigma_x = k\nu\sigma_z$ are assumed to be caused by, and to be proportional to, the moment M applied to panel width b of the stiffened sheet.

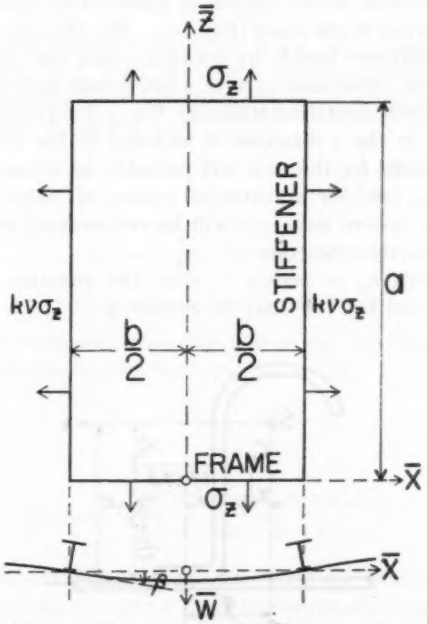

FIG. 4. Sheet notation. Symmetrical stiffeners and symmetrical sheet bending indicated.

Assuming small deflections $\bar{w}$ the equation which must be satisfied is

$$\frac{\partial^4\bar{w}}{\partial\bar{x}^4} + 2\left(\frac{\partial^4\bar{w}}{\partial\bar{x}^2\,\partial\bar{z}^2}\right) + \frac{\partial^4\bar{w}}{\partial\bar{z}^4} = \frac{\sigma_z t}{D}\left(\frac{\partial^2\bar{w}}{\partial\bar{z}^2}\right) + \frac{k\nu\sigma_z t}{D}\left(\frac{\partial^2\bar{w}}{\partial\bar{x}^2}\right) \qquad (14)$$

in which t is the sheet thickness and D is the sheet flexural rigidity $Et^3/12(1-\nu^2)$.

Substitution in terms of dimensionless variables gives the following equation which leads to a form of solution more suitable for computation

$$\frac{\partial^4 w}{\partial x^4} + 2\alpha^2\left(\frac{\partial^4 w}{\partial x^2\,\partial z^2}\right) + \alpha^4\left(\frac{\partial^4 w}{\partial z^4}\right) = S_z\left[\alpha^2\left(\frac{\partial^2 w}{\partial z^2}\right) + k\nu\left(\frac{\partial^2 w}{\partial x^2}\right)\right] \qquad (15)$$

in which $w = \bar{w}/t$, $x = \bar{x}/b$, $z = \bar{z}/a$, $\alpha = b/a$ and $S_z = \sigma_z b^2 12(1-\nu^2)/Et^2$.

On the assumption that sheet deflections are zero at the ends of panels and that no moments are transmitted from panel to panel in the z direction, we take the solution of Eq. (14) as[9]

$$w = \sum_{m=1}^{\infty} X_m \sin m\pi z \qquad (16)$$

in which X_m is a function of x only and all the symbols represent dimensionless quantities. This type of solution in conjunction with the Fourier sine series representation of the stiffener variables u, v, and β, Eq. (1) or (2), would appear to represent satisfactorily the buckling conditions for an extended network of panels having stiffeners whose section is symmetrical about an axis normal to the sheet (Fig. 1a). For this case alternate stiffeners buckle by rotating equal but opposite amounts. The same type of solution will apply to the case of unsymmetrical stiffeners, Fig. 5, if only one panel length in the z direction is included in the analysis. The results for this case will probably be conservative (M_{critical} low) for an extended system of panels as in such a system moments will be transmitted between panels in the z direction.

Letting $\lambda_m = m\pi b/a = m\pi\alpha$, the quantity $m\pi = \lambda_m/\alpha$, and Eq. (16) may be written as

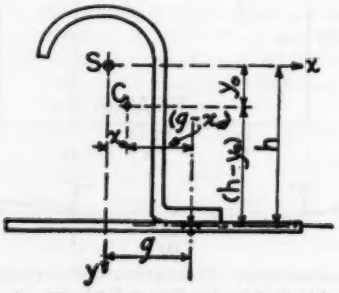

FIG. 5. Notation for unsymmetrical stiffener.

$$w = \sum_{m=1}^{\infty} X_m \sin(\lambda_m/\alpha)z \qquad (17)$$

The subscript m representing the number of the general term in Eqs. (1), (2), and (16) will be omitted in what follows when expressing certain variables. The symbols X, λ, p, ϵ, ω, p_1, p_2, F_S, $F_S{}^*$ will be used to represent X_m, λ_m, p_m, ϵ_m, ω_m, p_{1m}, p_{2m}, F_{Sm}, $F_{Sm}{}^*$ unless for clarity inclusion of the subscript seems advisable.

Substitution of Eq. (17) into Eq. (15) and cancellation of the common factor $\sin(\lambda_m/\alpha)z$ yields the ordinary differential equation for functions X

$$X^{IV} - (2\lambda^2 + k\nu S_z)X'' + (\lambda^4 + \lambda^2 S_z)X = 0 \qquad (18)$$

Assumption of the exponential form of solution

$$X = e^{pz} \qquad (19)$$

and substitution into Eq. (15) gives the quadratic in (p^2)

$$p^4 - (2\lambda^2 + k\nu S_z)p^2 + (\lambda^4 + \lambda^2 S_z) = 0 \qquad (20)$$

The solution of Eq. (20) is

$$\left(\frac{p}{\lambda}\right)^2 = \left[1 + \left(\frac{k\nu}{2}\right)\left(\frac{S_z}{\lambda^2}\right)\right] \pm \sqrt{\left[1 + \left(\frac{k\nu}{2}\right)\left(\frac{S_z}{\lambda^2}\right)\right]^2 - \left(1 + \frac{S_z}{\lambda^2}\right)} \qquad (21)$$

in which the quantity under the radical sign may be negative, zero, or positive. Two types of solution for p and, hence, for the sheet problem are obtained.

The radical is zero when

$$S_z/\lambda^2 = 4(1 - k\nu)/(k\nu)^2 \qquad (22)$$

By the use of Eq. (12) and the definitions of S_z and λ in the list of symbols, the zero value of the radical in Eq. (21) occurs when the applied moment M has the value

$$M = m^2\pi^2 Et^2(1 - k\nu)/3C_3(1 - \nu^2)\alpha^2(k\nu)^2 \qquad (23)$$

C_3 being given by Eqs. (12), (8), and (11) and m being the number of half waves in the panel length a. The left sides of Eqs. (22) and (23) will be less than the right sides, yielding complex values of p in Eq. (21), for very thick sheet or for a large number of half wave lengths in the buckled shape. Conversely, with very thin sheet and few half wave lengths, the left sides of these equations will be greater than the right and corresponding values of p in Eq. (21) will be real.

The four complex values of p are given by

$$p = \pm\epsilon \pm i\omega \qquad (24)$$

where $i = \sqrt{-1}$ and

$$\begin{Bmatrix}\epsilon\\ \omega\end{Bmatrix} = \frac{\lambda}{\sqrt{2}}\sqrt{\sqrt{[1+(S_z/\lambda^2)]} \pm [1+(k\nu/2)(S_z/\lambda^2)]} \qquad (25)$$

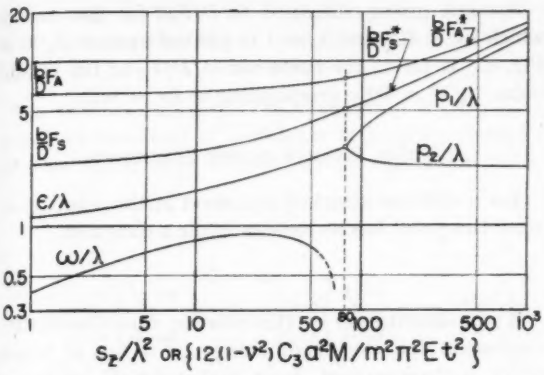

FIG. 6. Log-log plots of ϵ/λ, ω/λ, p_1/λ, p_2/λ for $k\nu = 0.2$ and of rotational spring constant functions $(b/D)F_S$, $(b/D)F_S^*$, $(b/D)F_A$, $(b/D)F_A^*$ for $k\nu = 0.2$ and $\lambda = 1$. For C_3 see Eqs. (8), (11), and (12).

The four real values of p are given by

$$p_1 = \pm \frac{\lambda}{\sqrt{2}}\left[\sqrt{1+\left(\frac{k\nu}{2}\right)\left(\frac{S_z}{\lambda^2}\right)} + \sqrt{1+\frac{S_z}{\lambda_2}} + \sqrt{1+\left(\frac{k\nu}{2}\right)\left(\frac{S_z}{\lambda^2}\right)} - \sqrt{1+\frac{S_z}{\lambda^2}}\right] \quad (26)$$

$$p_2 = \pm \frac{\lambda}{\sqrt{2}}\left[\sqrt{1+\left(\frac{k\nu}{2}\right)\left(\frac{S_z}{\lambda^2}\right)} + \sqrt{1+\frac{S_z}{\lambda^2}} - \sqrt{1+\left(\frac{k\nu}{2}\right)\left(\frac{S_z}{\lambda^2}\right)} - \sqrt{1+\frac{S_z}{\lambda^2}}\right]$$

Curves of ϵ/λ, ω/λ, p_1/λ, p_2/λ are plotted against S_z/λ^2—i.e., against $[12(1-\nu^2)C_3a^2M/m^2\pi^2Et^2]$ in Fig. 6 for the case in which $k\nu = 0.2$. For this case the critical value of S_z/λ^2 given by Eq. (22) is 80, at which $\epsilon/\lambda = p_1/\lambda = p_2/\lambda$ and $\omega/\lambda = 0$.

For other values of $k\nu$ or of λ, curves such as the above may be plotted with little computation.[12]

Resisting Moments for Symmetric Bending of Sheet, First Type of Solution with Complex Values of p

Substitution of Eq. (24) into Eq. (19) leads to a combination of hyperbolic and circular functions[9]

$$X_m = A_m \cosh \epsilon x \cos \omega x + B_m \sinh \epsilon x \cos \omega x + C_m \sinh \epsilon x \sin \omega x + D_m \cosh \epsilon x \sin \omega x \quad (27)$$

For symmetry about the z axis $B_m = D_m = 0$, leaving

$$X_m = A_m \cosh \epsilon x \cos \omega x + C_m \sinh \epsilon x \sin \omega x \quad (28)$$

Replacing $\sin m\pi z$ in Eq. (16) by $\sin (m\pi\bar{z}/a)$

$$w = \sum_{m=1}^{\infty} [A_m \cosh \epsilon x \cos \omega x + C_m \sinh \epsilon x \sin \omega x] \sin (m\pi\bar{z}/a) \quad (29)$$

Assuming that attachment of sheet to stiffener causes the sheet to have a boundary slope equal to the rotation of the stiffener, the boundary conditions along the edges $x = \pm 1/2$ are

$$\left.\begin{aligned} w &= 0 \text{ for all } \bar{z} \\ \partial w/\partial x &= (b/t)(\partial \bar{w}/\partial \bar{x}) = (b/t)\beta \end{aligned}\right\} \quad (30)$$

The first boundary condition in Eq. (30) makes the general terms of Eq. (29) vanish, giving

$$A_m = -C_m \frac{\sinh (\epsilon/2) \sin (\omega/2)}{\cosh (\epsilon/2) \cos (\omega/2)} \quad (31)$$

If we take

$$\beta = \sum_{m=1}^{\infty} \beta_m \sin (m\pi\bar{z}/a) \quad (32)$$

the second boundary condition in Eq. (3) together with Eqs. (31), (32), and (29) lead to an expression for the dimensionless sheet deflection w in terms of the general coefficient β_m in Eq. (32),

$$w = \frac{2b}{t}\sum_{m=1}^{\infty}\left(\frac{-\sinh\frac{\epsilon}{2}\sin\frac{\omega}{2}\cosh \epsilon x\cos\omega x + \cosh\frac{\epsilon}{2}\cos\frac{\omega}{2}\sinh \epsilon x\sin\omega x}{\epsilon\sin\omega + \omega\sinh\epsilon}\right)\beta_m \sin (m\pi\bar{z}/a) \quad (33)$$

M_z, the moment per unit length in the $\bar{z}$ direction with which the sheet resists the rotation β of the stiffener, will be expressed as a sine series

$$M_z = \sum_{m=1}^{\infty} M_{z_m} \sin (m\pi\bar{z}/a) \quad (34)$$

The equation relating edge moment and sheet deflection along the panel side $\bar{x} = -b/2$ is

$$-D(\partial^2\bar{w}/\partial\bar{x}^2)_{\bar{x}=-b/2} = M_z$$

or

$$-D(t/b^2)(\partial^2 w/\partial x^2)_{x=-1/2} = M_z \quad (35)$$

Upon substitution into Eq. (35) of Eqs. (33) and (34), we obtain the relation between M_{x_m} and β_m

$$M_{x_m} = F_S(\epsilon_m, \omega_m)\beta_m \quad (36)$$

where

$$F_S(\epsilon, \omega) = \frac{D}{b}\left[\frac{2\epsilon\omega(\cosh\epsilon + \cos\omega)}{\omega\sinh\epsilon + \epsilon\sin\omega}\right] \quad (37)$$

The function F_S or F_{S_m} (subscript S for symmetrical bending of sheet) is one Fourier coefficient of a rotational "spring constant" having the dimensions of moment per radian per unit width. Examination of Eq. (37) and

of Eq. (25) for ϵ and ω shows that the value of Fs_m depends not only upon the geometry of the sheet and the material properties but also on S_z, which is proportional to the moment M applied to the stiffened sheet combination, and on m, the number of half waves in which the sheet buckles.

A curve giving values of $(b/D)F_S$ for the case in which $k\nu = 0.2$ and $\lambda = 1$ is plotted against S_z/λ^2 in Fig. 6.

Resisting Moments for Symmetric Bending of Sheet, Second Type of Solution with Real Values of p

Substitution into Eq. (19) of $\pm p_1$ and $\pm p_2$, whose values are given in Eq. (26), leads to the expression

$$X_m = A_m \cosh p_1 x + B_m \sinh p_1 x + C_m \cosh p_2 x + D_m \sinh p_2 x \quad (38)$$

For symmetrical bending, $B_m = D_m = 0$, leaving

$$X_m = A_m \cosh p_1 x + C_m \cosh p_2 x \quad (39)$$

and

$$w = \sum_{m=1}^{\infty} [A_m \cosh p_1 x + C_m \cosh p_2 x] \sin (m\pi\bar{z}/a) \quad (40)$$

The boundary conditions of Eq. (30) apply again. Substitution of Eq. (38) into the first of Eq. (30) gives the relation

$$A_m = -C_m[\cosh (p_2/2)/\cosh (p_1/2)] \quad (41)$$

The second boundary condition in Eqs. (30) and Eqs. (40), (41), and (32), lead to the following expression for w

$$w = \frac{b}{t}\sum_{m=1}^{\infty} \frac{\cosh\frac{p_1}{2}\cosh p_2 x - \cosh\frac{p_2}{2}\cosh p_1 x}{p_1 \sinh\frac{p_1}{2}\cosh\frac{p_2}{2} - p_2 \sinh\frac{p_2}{2}\cosh\frac{p_1}{2}} \times \beta_m \sin\frac{m\pi\bar{z}}{a} \quad (42)$$

The relation between resisting moments and angular rotations is obtained upon substitution of Eqs. (34) and (42) into Eq. (35):

$$M_{x_m} = F_S^*(p_{1m}, p_{2m})\beta_m \quad (43)$$

where

$$F_S^*(p_1, p_2) = \frac{D}{b}\frac{p_1^2 - p_2^2}{p_1 \tanh (p_1/2) - p_2 \tanh (p_2/2)} \quad (44)$$

A curve giving values of $(b/D)F_S^*$ for the case in which $k\nu = 0.2$ and $\lambda = 1$ is plotted against S_z/λ^2 in Fig. 6. It meets the curve for $(b/D)F_S$ at the critical value $S_z/\lambda^2 = 80$ corresponding to $k\nu = 0.2$.

Strain Energy of the Stiffener

For a stiffener attached to a sheet at the point (g, h), since this point has no motion in the x direction,

$$u - h\beta = 0^7 \quad (45)$$

Upon substitution of this relation into Goodier's[6,7] expression for the strain energy of a bar of length a, in a "compressed, bent and twisted" state, we obtain

$$W_1 = \frac{P^2 a}{2EA} + \frac{1}{2}\int_0^a \times [(h^2 EI_1 + E\Gamma)\beta''^2 + EI_2 v''^2 + 2hEI_{12}\beta'' v'' + GC\beta'^2] d\bar{z} \quad (46)$$

in which prime represents a differentiation with respect to $\bar{z}$.

For a stiffener having symmetry about an axis normal to the sheet, $I_{12} = 0$ and Eq. (46) reduces to the following expression for strain energy

$$W_1 = \frac{P^2 a}{2EA} + \frac{1}{2}\int_0^a \times [(h^2 EI_1 + E\Gamma)\beta''^2 + EI_2 v''^2 + GC\beta'^2] d\bar{z} \quad (47)$$

Potential Energy of the Stiffener End Moments and Forces

On substitution of Eq. (45) and the end moment value $M_1 = 0$ into Goodier's expression[6,7] for potential energy of the end moments and forces acting on a stiffener, we obtain for a stiffener attached to a sheet

$$-W_2 = -\frac{P^2 a}{EA} - \frac{1}{2}\int_0^a \{Pv'^2 + [P(\rho^2 + h^2) + \mu_1\kappa_1 + \mu_2\kappa_2]\beta'^2 + 2Px_0 v'\beta' + 2h(M_2 - Py_0)\beta'^2 - 2M_2 v''\} d\bar{z} \quad (48^*)$$

For a stiffener having symmetry about an axis normal to the sheet, the following relations hold: $x_0 = 0$, $\mu_1 = 0$, $\mu_2 = -M_2/I_2$, $\kappa_1 = 0$. Substitution of these values into Eq. (48) gives the potential energy expression for a symmetrical stiffener:

$$-W_2 = -\frac{P^2 a}{EA} - \int_0^a \left\{Pv'^2 + \left[P(\rho^2 + h^2) - M_2\frac{\kappa_2}{I_2}\right]\beta'^2 + 2h(M_2 - Py_0)\beta'^2 - 2M_2 v''\right\} d\bar{z} \quad (49)$$

* Dr. Goodier advises that each of the last five terms in his Eq. (30) (p. 14, reference 7) should be multiplied by the factor 2; also that the right sides of his Eqs. (29) should each be preceded by a minus sign. These corrections eliminate apparent disagreement with Eq. (48).

Potential Energy of the Elastic Resisting Moments of the Sheet for Symmetrical Sheet Bending

The potential energy of the moments of M_x, Eq. (34), acting on two sides of a stiffener of length a during a rotation β, Eq. (32), is given by the expression

$$W_3 = 2\,(1/2\int_0^a M_x\beta\,d\bar{z}) \tag{50}$$

or

$$W_3 = \int_0^a \left(\sum_{m=1}^{\infty} M_{x_m}\sin\frac{m\pi\bar{z}}{a}\right)\left(\sum_{m=1}^{\infty}\beta_m\sin\frac{m\pi\bar{z}}{a}\right)d\bar{z} \tag{51}$$

In this expression each of the integrals of the squares of sine terms equals $a/2$, and integrals of other products of sines vanish, leaving

$$W_3 = (a/2)\sum_{m=1}^{\infty} M_{x_m}\beta_m \tag{52}$$

Substitution of Eq. (36) into Eq. (52) gives the potential energy expression for the moments on two sides of one stiffener

$$W_3 = (a/2)\sum_{m=1}^{\infty} F_S(\epsilon,\,\omega)\beta_m^2 \tag{53}$$

where F_S is given in Eq. (37).

Similar substitution of Eq. (43) into Eq. (52) gives the analogous expression

$$W_3 = (a/2)\sum_{m=1}^{\infty} F_S^*(p_1,\,p_2)\beta_m^2 \tag{54}$$

where F_S^* is given in Eq. (44).

Infinite Series Form for the Strain Energy and Potential Energy Expressions

The energy expressions in Eqs. (46), (47), (48), and (49) contain integrals of terms that are of second degree in the $\bar{z}$ derivatives of β and v. In the latter two equations there is an integral of a first degree term in v''. Making use of Eqs. (1) and (32) and the orthogonal properties of the sine and cosine functions, we find that

$$\int_0^a \beta'^2\,d\bar{z} = (a/2)\sum_{m=1}^{\infty}(m^2\pi^2/a^2)\beta_m^2 \tag{55}$$

$$\int_0^a \beta''^2\,d\bar{z} = (a/2)\sum_{m=1}^{\infty}(m^4\pi^4/a^4)\beta_m^2 \tag{56}$$

with similar expressions for other second degree terms and

$$\int^a v''\,d\bar{z} = -2\sum_{m=1,3,5\ldots}^{\infty}(m\pi/a)v_m \tag{57}$$

By the use of Eqs. (55), (56), (57), and similar expressions, Eq. (46) for the strain energy of a stiffener attached to a sheet becomes

$$W_1 = \frac{P^2a}{2EA} + \frac{a}{4}\Bigg[(h^2EI_1 + E\Gamma)\sum_{m=1}^{\infty}\left(\frac{m^4\pi^4}{a^4}\right)\beta_m^2 + EI_2\sum_{m=1}^{\infty}\left(\frac{m^4\pi^4}{a^4}\right)v_m^2 + 2hEI_{12}\sum_{m=1}^{\infty}\left(\frac{m^4\pi^4}{a^4}\right)\beta_m v_m + GC\sum_{m=1}^{\infty}\left(\frac{m^2\pi^2}{a^2}\right)\beta_m^2\Bigg] \tag{58}$$

Similarly Eq. (48) for the potential energy of the end moments and forces on a stiffener becomes

$$-W_2 = -\frac{P^2a}{EA} - \frac{a}{4}\Bigg\{P\sum_{m=1}^{\infty}\left(\frac{m^2\pi^2}{a^2}\right)v_m^2 + [P(\rho^2+h^2) + \mu_1\kappa_1 + \mu_2\kappa_2]\times\sum_{m=1}^{\infty}\left(\frac{m^2\pi^2}{a^2}\right)\beta_m^2 + 2Px_0\sum_{m=1}^{\infty}\left(\frac{m^2\pi^2}{a^2}\right)\beta_m v_m + 2h(M_2 - Py_0)\sum_{m=1,3,5\ldots}^{\infty}\left(\frac{m^2\pi^2}{a^2}\right)\beta_m^2 + \frac{8M_2}{a}\sum_{m=1,3,5\ldots}^{\infty}\left(\frac{m\pi}{a}\right)v_m\Bigg\} \tag{59}$$

The Energy Condition for Equilibrium

The total energy

$$U = W_1 - W_2 + W_3 \tag{60}$$

will be a minimum with respect to β_m and v_m for equilibrium configurations at any value of the applied moment M below the critical value. The equations

$$\partial U/\partial\beta_m = 0 \text{ and } \partial U/\partial v_m = 0 \tag{61}$$

define the equilibrium configuration in terms of moment M.

Equilibrium and Buckling Conditions—Symmetrical Stiffeners—Symmetrical Sheet Bending

By means of Eqs. (10) and (13), P and M_2 in Eqs. (58) and (59) are expressed in terms of the applied moment M and the constants C_2 and C_4 after making the substitutions for a symmetrical stiffener which were used in obtaining Eqs. (47) and (49). Combining with the above Eq. (53) or Eq. (54) in accordance with Eq. (60) and differentiating as in Eq. (61), we obtain the equations defining the equilibrium configuration

$$\frac{\partial U}{\partial\beta_m} = \frac{a}{2}\Bigg\{(h^2EI_1 + E\Gamma)\frac{m^4\pi^4}{a^4} + GC\left(\frac{m^2\pi^2}{a^2}\right) + 2F_S' - M\left(\frac{m^2\pi^2}{a^2}\right)\left[C_4(\rho^2+h^2) - C_2\left(\frac{\kappa_2}{I_2}\right) + 2h(C_2 - C_4y_0)\right]\Bigg\}\beta_m = 0 \tag{62}$$

and

$$\frac{\partial U}{\partial v_m} = \frac{a}{2}\left[EI_2\left(\frac{m^4\pi^4}{a^4}\right) - MC_4\left(\frac{m^2\pi^2}{a^2}\right)\right]v_m - 2C_2\left(\frac{m\pi}{a}\right)M = 0 \text{ (for } m = 1, 3, 5\ldots) \tag{63a}$$

as well as

$$\frac{\partial U}{\partial v_m} = \frac{a}{2}\left[EI_2\left(\frac{m^4\pi^4}{a^4}\right) - MC_4\left(\frac{m^2\pi^2}{a^2}\right)\right]V_m = 0$$

(for $m = 2, 4, 6, \ldots$) (63b)

From Eq. (63a) we obtain

$$v_m = \frac{(4/a)C_2M}{EI_2\left(\frac{m^2\pi^2}{a^2}\right) - C_4M\left(\frac{m\pi}{a}\right)} \quad (m = 1, 3, 5 \ldots) \tag{64}$$

which indicates that v_m is proportional to M until the buckling value of M is approached and that v is a second-degree parabola as expected.

In Eq. (63b) v_m is zero unless the quantity in brackets vanishes, but this is equivalent to vanishing of the denominator of Eq. (64) and provides one critical value of applied moment for symmetrical stiffeners

$$M_{\text{crit.}} = m^2\pi^2EI_2/C_4a^2 \tag{65}$$

In Eq. (62) we note that β_m is zero unless the quantity in square brackets vanishes, which provides the second expression for the critical or buckling moment for symmetrical stiffeners

$$M_{\text{crit.}} = \frac{(h^2EI_1 + E\Gamma)\left(\frac{m^4\pi^4}{a^4}\right) + GC\left(\frac{m^2\pi^2}{a^2}\right) + 2F_S}{\left[C_4(\rho^2 + h^2) - C_2\left(\frac{\kappa_2}{I_2}\right) + 2h(C_2 - C_4y_0)\right]\frac{m^2\pi^2}{a^2}} \tag{66}$$

in which the term $2F_S$ in the numerator gives the effect of the bending stiffness of the sheet. The smaller of the two expressions in Eqs. (65) and (66) will be the buckling moment as given by this approximate analysis. The function F_S in Eq. (66) is a function of $M_{\text{crit.}}$ which is unknown; hence, a trial-and-error solution may be followed, using the curves for F_S and F_S^* of Fig. 6 or similar curves for values of $k\nu$ and λ suitable to the particular problem. A first step would be to solve Eq. (66), either omitting the term in F_S or using the constant value of Fs_0 given in Appendix I for a plate not under tensile stress. This provides a lower limiting value of $M_{\text{crit.}}$. Other higher values for $M_{\text{crit.}}$ and the corresponding values of F_S may be substituted into Eq. (66) until a sufficiently accurate approximation to a solution is obtained.

Unsymmetrical Stiffeners—General

Since unsymmetrical stiffeners are widely used, a solution for this case may be of interest. For this case a combination of symmetric and antisymmetric bending of the sheet, Fig. 7, will be involved. If adjacent stiffeners are numbered 1 and 2, the four variables, β_1, v_1, β_2, and v_2 must now be considered. The usual procedures result in the equating to zero of a fourth order determinant the elements of which are the coefficients of the above variables in four equations corresponding to Eqs. (62) and (63). This equation may be simplified somewhat by omission of the potential energy associated with that part of the sheet deformation shown in Fig. 7c, amounting roughly to less than 10 per cent of the total potential energy of the resisting moments of the sheet.

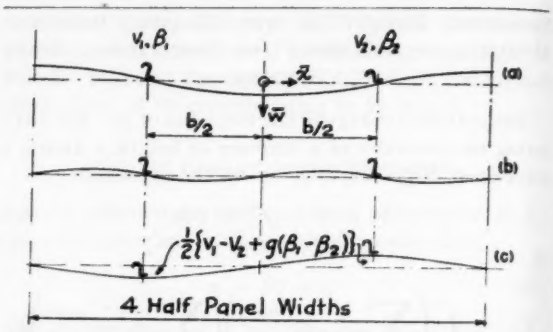

Fig. 7. Types of sheet bending deformation considered. (a) Symmetric. (b) Antisymmetric. (c) Edge Curvature Type.

Rotational Spring Constant Functions for Antisymmetric Sheet Bending

For the antisymmetric type of sheet bending shown in Fig. 7b, the methods of Eqs. (27) to (37) and Eqs. (38) to (44) yield the following functions that might be defined by equations analogous to Eqs. (36) and (43)

$$F_A = \frac{D}{b}\left[\frac{2\epsilon\omega\,(\cosh\epsilon - \cos\omega)}{\omega\sinh\epsilon - \epsilon\sin\omega}\right] \tag{67}$$

and

$$F_A^* = \frac{D}{b}\left[\frac{p_1^2 - p_2^2}{p_1\coth(p_1/2) - p_2\coth(p_2/2)}\right] \tag{68}$$

in which the subscript A refers to the antisymmetric type of bending of the sheet. These functions are similar in form to those for symmetric bending in Eqs. (37) and (44).

Tensile Stress in Sheet and End Loads and Moments on Unsymmetrical Stiffener

At the ends of an unsymmetrical stiffener, we have, instead of Eq. (5) for the total stress,

$$\sigma = \frac{P}{A} - \frac{M_2\{I_1(y - y_0) - I_{12}(x - x_0)\}}{I_1I_2 - I_{12}^2} \tag{69}$$

Following the methods used earlier in this paper, we obtain

$$\sigma_z = \frac{1}{1 - k\nu^2 + (bt/A)} \times \left[\frac{I_1(h - y_0) - I_{12}(g - x_0)}{I_1I_2 - I_{12}^2}\right]M_2 = C_5M_2 \tag{70}$$

$$M_2 = \{1/[1 + btC_5(h - y_0)]\}\ M = C_6M \quad (71)$$

$$\sigma_z = C_5C_6M = C_7M \quad (72)$$

$$P = bt\sigma_z = btC_7M = C_8M \quad (73)$$

The Equation for the Buckling Values of Applied Moment—Unsymmetrical Stiffeners

The total energy expression was set up as in Eq. (60) for a superposition of the three types of deformation shown in Figs. 7a, 7b, and 7c. The deformation of Fig. 7c corresponds to zero rotation of both stiffeners, with relative translation in the $\bar{w}$ or y direction of points along the edges $\bar{x} = \pm b/2$ of the sheet of amount $v_1 - v_2 + g(\beta_1 - \beta_2)$. The terms arising from this type of deformation were omitted in obtaining the result given below.

The complete derivation is too lengthy to be included in this paper. Four linear equations corresponding to Eqs. (61) were obtained. For the buckling condition the nonhomogeneous terms are eliminated by reasoning based on the duality of configuration at the buckling load.[7] The resulting homogeneous set of equations will have nonzero solutions for the β's and v's only if the determinant of their coefficients equals zero.

This equation with terms arising from the deformation of Fig. 7c omitted is

$$H^4 + J^2(K^2 - L^2) = 0 \quad (74)$$

in which

$$\left.\begin{aligned} H &= hEI_{12}\left(\frac{m^4\pi^4}{a^4}\right) - MC_8x_0\left(\frac{m^2\pi^2}{a^2}\right) \\ J &= EI_2\left(\frac{m^4\pi^4}{a^4}\right) - MC_8\left(\frac{m^2\pi^2}{a^2}\right) \\ K &= (h^2EI_1 + E\Gamma)\left(\frac{m^4\pi^4}{a^4}\right) + GC\left(\frac{m^2\pi^2}{a^2}\right) + F_S + \\ F_A &- M\left(\frac{m^2\pi^2}{a^2}\right)\left[C_8(\rho^2 + h^2) + \frac{C_6(I_{12}\kappa_1 - I_{12}\kappa)}{I_1I_2 - I_{12}^2} + \right. \\ &\left. 2h(C_6 - C_8y_0)\right] \\ L &= F_A - F_S \end{aligned}\right\} \quad (75)$$

Angle Stiffeners

Angle stiffeners have been used under the conditions of loading discussed in this paper. Since the shear center of an angle is at the intersection of the legs, the dimension h in Fig. 5 may be taken equal to zero in Eqs. (75). This substitution simplifies somewhat the solution of Eq. (74). A trial-and-error solution is necessary, and a lower limit for the buckling moment may be determined using the constant values of F_{S_0} and F_{A_0} given in Appendix I for a plate not under tensile stress.

Discussion

(1) The limitations of the present analysis should be noted. A linear solution can only approximately describe a nonlinear system. The approximation improves in the present instance with increasing ratio of sheet thickness to panel width.

(2) The curvature of the sheet before buckling, neglected in this analysis, will cause nonuniform median stresses. If experimental or analytical means of approximating the actual distribution of σ_z are applied, they may be utilized in connection with curves of the type of Fig. 6—for example, by replacing b by an equivalent width b_e in Eqs. (6) to (13) inclusive and by using values $\sigma_z = C_5Mb_e/b$ to determine abscissas in Fig. 6 instead of the values of σ_z given by Eq. (12). Similarly, on the basis of experimental or other information about the σ_z stress, the value of $k\nu$ to be used in curves of the type of Fig. 6 may be chosen to agree with available data and values of F_S and F_A obtained from such curves.

(3) This analysis neglects longitudinal ($\bar{z}$ direction) forces between the stiffener and the sheet. For the pure bending case studied, these are not expected to be present until the buckling condition is reached. Their neglect might be compensated by including part of the sheet area as stiffener area (for bending only, and in such manner as not to add twisting strength) and treating the remainder of the sheet area as "sheet" in the derivations of Eqs. (5) to (13) inclusive.

(4) For extremely thin sheet, in obtaining a trial-and-error solution, the value $m = 1$ will be the only significant value; whereas for extremely thick sheet a number of values such as $m = 1$, 2, or 3 may require consideration. In this case sets of curves for corresponding values of $\lambda[= m\pi(b/a)]$ will be required.

(5) The curves of Fig. 6 show the marked effect of tensile stress on the resisting moments of the sheet. For a range of $1.0 < S_z/\lambda^2 < 10^3$ in Fig. 6, we find $2.38 < (b/D)F_S < 15.7$, and $6.25 < (b/D)F_A < 17.04$. These values are higher, as would be expected, than the values: $(b/D)F_{S_0} = 2.34$ and $(b/D)F_{A_0} = 6.2$ given by Fig. 8 of Appendix I for $\lambda = 1$, the value used for the curves of Fig. 6.

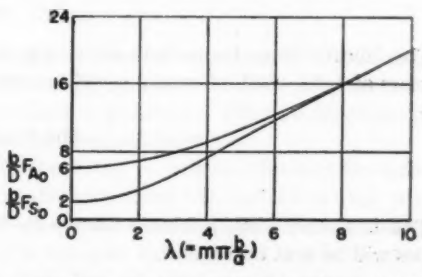

Fig. 8. Rotational spring constant functions $(b/D)F_{S_0}$ and $(b/D)F_{A_0}$ for sheet not under tensile stress

Appendix I

Expressions for the Fourier coefficients for rotational spring constant for the edges of a rectangular sheet under no tensile stresses[9] have been found by the methods used earlier in this paper to obtain Eqs. (37) and (44) and are functions of λ only [$\lambda = m\pi(b/a)$]. They are

$$F_{S_0} = (D/b)[2\lambda(\cosh\lambda + 1)/(\sinh\lambda + \lambda)] \qquad (A1)$$

$$F_{A_0} = (D/b)[2\lambda(\cosh\lambda - 1)/(\sinh\lambda - \lambda)] \qquad (A2)$$

Values of $(b/D)F_{S_0}$ and $(b/D)F_{A_0}$ are plotted in Fig. 8 against values of λ from 0 to 10. Their use in initiating a trial-and-error solution has been suggested.

References

[1] Timoshenko, S., *Einige Stabilitätsprobleme der Elastizitätstheorie*, Zeitschrift für Mathematik und physik, Vol. 58, p. 361, 1910.

[2] Timoshenko, S., *Theory of Elastic Stability*, 1st Ed., p. 340; McGraw-Hill Book Company, Inc., New York, 1936.

[3] Wagner, H., *Torsion and Buckling of Open Sections*, N.A.C.A. T.M. No. 807, 1936.

[4] Wagner, H., and Pretschner, W., *Torsion and Buckling of Open Sections*, N.A.C.A. T.M. No. 784, 1936.

[5] Kappus, R., *Twisting Failure of Centrally Loaded Open-Section Columns in the Elastic Range*, N.A.C.A. T.M. No. 851, 1938.

[6] Goodier, J. N., *The Buckling of Compressed Bars by Torsion and Flexure*, Bulletin 27, Engineering Experiment Station, Cornell University, 1941.

[7] Goodier, J. N., *Flexural-Torsional Buckling of Compressed Bars of Open Section*, Bulletin 28, Engineering Experiment Station, Cornell University, 1942.

[8] Goodier, J. N., *Torsional and Flexural Buckling of Bars of Thin-Walled Open Section Under Compressive and Buckling Loads*, Journal of Applied Mechanics, Vol. 9, No. 3, September, 1942.

[9] Timoshenko, S. *Theory of Plates and Shells*, 1st Ed., p. 199; McGraw-Hill Book Company, Inc., New York, 1940.

[10] Timoshenko, S., *Strength of Materials*, Part I, 1st Ed., p. 77; D. Van Nostrand Company, New York, 1932.

[11] Lundquist, E. E., and Fligg, C. M., *A Theory for Primary Failure of Straight Centrally Loaded Columns*, N.A.C.A. Report No. 582, 1937.

[12] Hayashi, K., *Fünfstellige Tafeln der Kreis- und Hyperbelfunktionen so wie Funktionen e^x und e^{-x};* Walter de Gruyter & Co., Berlin, 1938.

Library Facilities of the Institute of the Aeronautical Sciences

To serve Institute members and others in the aeronautical industry, the Institute of the Aeronautical Sciences offers the facilities of:

The W. A. M. Burden Library
1505 RCA Building West
30 Rockefeller Plaza
New York 20, N. Y.

The facilities of this library are available for reference study at the offices of the Institute.

The Paul Kollsman Library
1505 RCA Building West
30 Rockefeller Plaza
New York 20, N. Y.

This library loans books without charge to members and others in the United States over eighteen years of age. Full information will be sent on request.

The Pacific Aeronautical Library
6715 Hollywood Boulevard
Hollywood, Calif.

This is a service and reference library for West Coast organizations. Full information as to its facilities will be sent on request.

Note on Analysis for Bending with Buckled Stringers

EDWARD A. MACLEAN*
Bell Aircraft Corporation

INTRODUCTION

THE AIRPLANE WING is constructed in many cases with the main beams having heavy chord sections and with comparatively light stringer sections spanning between bulkheads that support the skin. These stringers act as stress-carrying members, and under nominal loads the ordinary flexure formula applies, thus presenting no particular difficulties. A linear distribution of stress is assumed. At loads approaching the ultimate these light stringers may be stressed on the compression side to the point where they buckle as a column or cripple. There is a similar condition in the fuselage with light sections distributed around the periphery. Here again, at loads approaching the ultimate, some of the stringers most distant from the neutral axis may buckle.

The problem is to design a beam, such as a wing, made up of chord and stringer elements under a condition where there is a linear distribution of stress over a part of the section and where the balance of the elements have buckled or crippled. A step-by-step solution for this problem has been in use for several years in which the section properties must be determined each time an element reaches its maximum stress.[1]

If it is assumed that the force in the buckled member can be determined or estimated, the following method of analysis should prove useful to the designer. As far as the writer knows, this "trick" for the analysis of this condition has never been presented to the profession before. It is analogous to a method that was proposed by Odd Albert[2] and others for the analysis of concrete columns. The bulkheads are assumed to retain their shape. Induced diagonal tension effects after buckling occurs are not considered.

Notation

The symbols have the commonly accepted significance.

COMBINED BENDING AND DIRECT STRESS IN GENERAL

If the post shown in Fig. 1 is subjected to an eccentrically located axial load, P, then the stress on any element E at a plane xz may be obtained by the familiar formula.

$$\sigma = (-P/A) \pm (P e_z x/I_z) \pm (P e_x z/I_x) \qquad (1)$$

It is assumed that the plane xz is far enough away from P to avoid the effect of localized stress at the point of application of P. The assumptions that are made in the development of the flexure formula hold here. Also, it is assumed that the member is of such proportions that the principle of superposition holds. Axes through x and z are the principal axes.

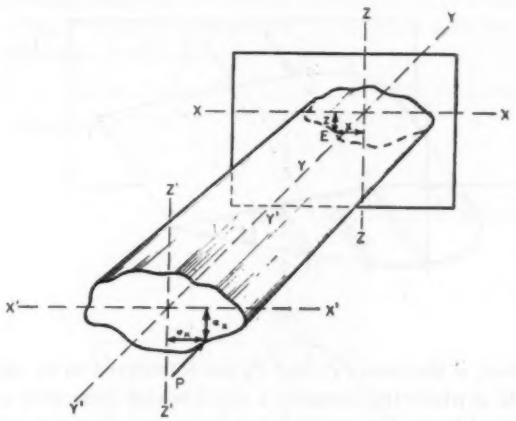

FIG. 1.

If x and z are not the principal axes, then the stress at E may be determined by:[3]

$$\sigma = +(P/A) + ax + bz \qquad (2)$$

where

$$a = (+M_x I_z + M_z I_{xz})/(I_x I_z - I_{xz}^2) \qquad (3)$$

and

$$b = (-M_x I_z - M_z I_{xz})/(I_x I_z - I_{xz}^2) \qquad (4)$$

Positive stress is tension. Positive P causes positive stress across the section. Positive M_x causes negative stress in the first quadrant. Positive M_z causes positive stress in the first quadrant.

It may be noted in passing that a is the unit stress at a unit distance along the x axis from the origin and that b is the unit stress at a unit distance along the z axis. The designer will find that it will be advantageous to keep this physical significance of a and b in mind.

Received January 22, 1945.

* Structural Research Engineer. On leave of absence as Professor of Civil Engineering, Rose Polytechnic Institute.

Application to the Specific Problem

Consider the wing section, Fig. 2, acted upon by the forces H, V and F_1, F_2. The stresses at the plane xz are required. This problem is analogous to the previous example. There are more forces, and the solid section has been changed to a hollow section with the material considered to be concentrated at points 0, 3, 4, 5, 6, and 7. The stress on any element may be obtained from Eq. (2).

$$\sigma = + (P/A) + ax + bz$$

where P would be equal to F_1 plus F_2. A would be the area of elements 0, 3, 4, 5, 6, and 7; I_x, I_z, and I_{xz} would be the moment of inertia and product of inertia of these elements about the x and z axes through the center of gravity of these elements; and M_x and M_z are the moments of *all* the forces, including F_1 and F_2, about x and z.

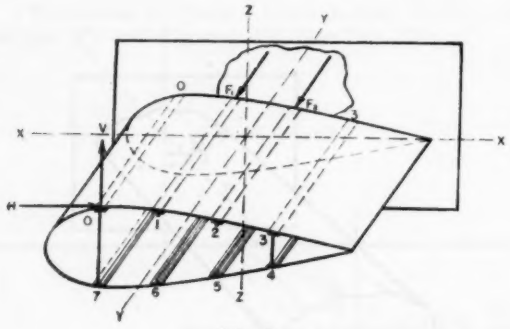

Fig. 2.

Now, if the forces F_1 and F_2 are considered to be the loads at which the elements 1 and 2 buckle instead of as external loads, the problem has in no way changed and can be solved by Eq. 2. It should be emphasized that the area of elements 1 and 2 should not be included in the computation for area, center of gravity, and other properties of the section.

The only additional assumption is that the forces F_1 and F_2 can be determined after buckling occurs. In fact, various values may be assigned to F_1 and F_2 by the designer; thus it is not necessary that F_1 and F_2 buckle either at the same time or at the same stress.

The user of this method will probably compute the section properties including all the elements first in order to determine the elements that will buckle.

Much labor may be saved in determining the section properties, with the buckled elements out, by subtracting the moments and product of inertia of the buckled elements and transferring the result to the new center of gravity.

Examples

Given the box beam shown in Fig. 3, acted upon by a bending couple of 4,800,000 in.lbs.

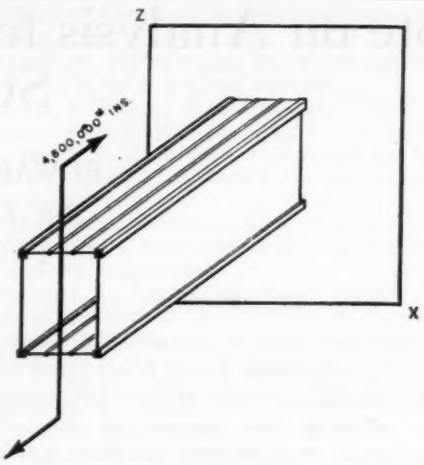

Fig. 3. Box beam.

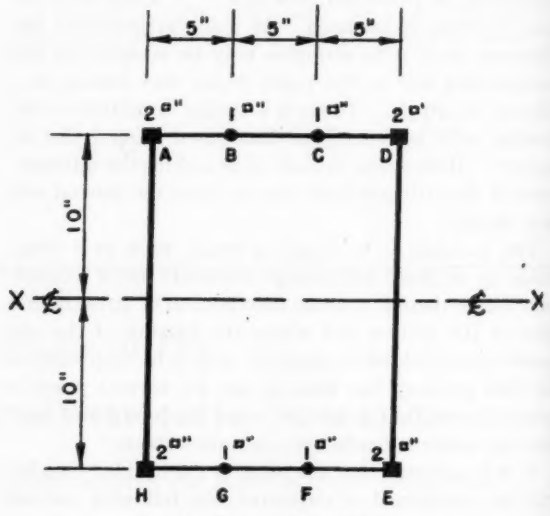

Fig. 4. Cross section of beam.

A cross section of the beam at any plane xz is shown in Fig. 4. The effective skin is assumed to have been incorporated in the beam elements.

The beam is made up of the elements A, B, C, D, E, F, G, and H, with the area of the elements and the dimensions shown.

(A) Determine the stress in the elements due to the bending moment of 4,800,000 in.lbs. using the flexure formula.

$$A = 2 \times (2 + 1 + 1 + 2) = 12 \text{ sq.in.}$$

$$I = 2 \times 6 \times 10^2 = 1{,}200 \text{ in.}^4$$

The stress in all elements is:

$$\sigma = \frac{Mc}{I} = \frac{4{,}800{,}000 \times 10}{1{,}200} = 40{,}000 \text{ lbs. per sq.in.}$$

There is compression in the top elements, A, B, C, and D and tension in the bottom elements, E, F, G, and H.

The compressive force in B and C is:

$$40{,}000 \times 1 = 40{,}000 \text{ lbs. each.}$$

(B) Now assume that B and C buckle at a stress of 40,000 lbs. per sq.in. The force in B and C is 40,000 lbs. Assuming the same moment as before and applying the proposed method, the stress of 40,000 lbs. per sq.in. in each element as determined before should be checked.

Fig. 5 shows a free-body diagram under the assumed conditions and Fig. 6 shows a cross section.

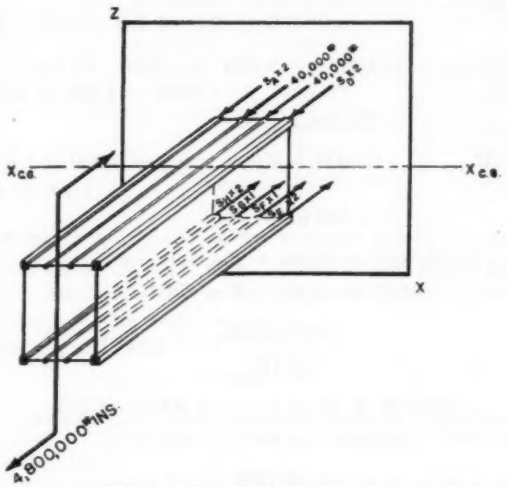

FIG. 5. Free-body diagram of beam elements, "B" and "C" buckled.

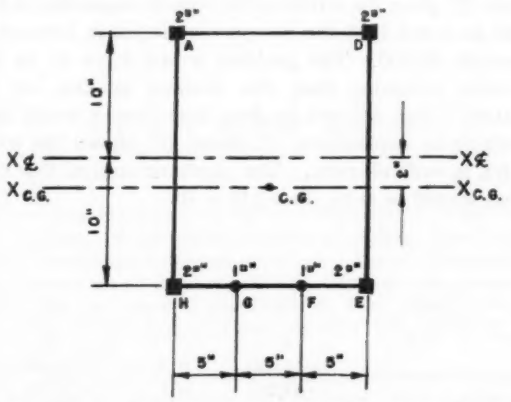

FIG. 6. Cross section of beam elements, "B" and "C" buckled.

The center of gravity (c.g.) has now moved down:

$$(2 \times 10)/10 = 2 \text{ in.}$$

The new section properties are:

$$A = 2 \times 2 + (2 + 1 + 1 + 2) = 10 \text{ sq.in.}$$

$$I_{x_{\text{centerline}}} = 1{,}200 - 2 + \overline{10}^2 = 1{,}000 \text{ in.}^4$$

$$I_{x_{c.g.}} = 1{,}000 - 10 \times \overline{2}^2 = 960 \text{ in.}^4$$

The stress in A is given by:

$$\sigma_A = +(P/A) - (Mc/I)$$

Remember that moments are being taken about $x_{c.g.}$ in Fig. 5.

$$\sigma_A = +\frac{2 \times 40{,}000}{10} - \frac{(4{,}800{,}000 - 2 \times 40{,}000 \times 12)\,12}{960}$$

$\sigma_A = -40{,}000$ lbs. per sq.in. . . . check.

The stress in H is given by:

$$\sigma_H = +(P/A) + (Mc/I)$$

$$\sigma_H = +\frac{2 \times 40{,}000}{10} + \frac{(4{,}800{,}000 - 2 \times 40{,}000 \times 12)\,8}{960}$$

$\sigma_H = +40{,}000$ lbs. per sq.in. . . . check.

(C) An example will now be solved with bending about both the x and z axes. The proposed method seems to have particular advantages in this type of problem which is of frequent occurrence in practice.

Fig. 7 shows a cross section of the beam with the distribution of the material.

$$A = (0.2 + 2 \times 0.1 + 2 \times 0.1 + 0.1)2 = 1.4 \text{ sq.in.}$$

$$I_{x_{\text{centerline}}} = 1 \times 0.2 \times \overline{10}^2 = 20.0$$
$$2 \times 0.1 \times \overline{9}^2 = 16.2$$
$$2 \times 0.1 \times \overline{7}^2 = 9.8$$
$$46.0 \times 2 = 92.0 \text{ in.}^4$$

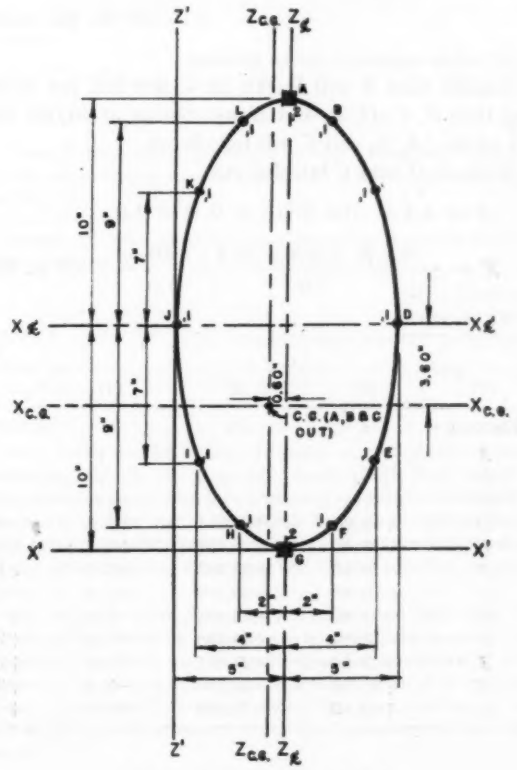

FIG. 7. Cross section of beam.

$$I_{x_{\text{centerline}}} = 2 \times 0.1 \times \overline{2}^2 = 0.8$$
$$2 \times 0.1 \times \overline{4}^2 = 3.2$$
$$1 \times 0.1 \times \overline{5}^2 = 2.5$$
$$6.5 \times 2 = 13.0 \text{ in.}^4$$

The applied couples are:

$$M_x = 450{,}000 \text{ in.lbs.}$$

$$M_z = 60{,}000 \text{ in.lbs.}$$

Solve for the stresses:

$$\sigma_A = -\frac{450{,}000 \times 10}{92} = -48{,}900 \text{ lbs. per sq.in.}$$

$$\sigma_B = -\frac{450{,}000 \times 9}{92} - \frac{60{,}000 \times 2}{13} = -53{,}250 \text{ lbs. per sq.in.}$$

$$\sigma_C = -\frac{450{,}000 \times 7}{92} - \frac{60{,}000 \times 4}{13} = -52{,}700 \text{ lbs. per sq.in.}$$

$$\sigma_D = -\frac{60{,}000 \times 5}{13} = -23{,}100 \text{ lbs. per sq.in.}$$

$$\sigma_L = -\frac{450{,}000 \times 9}{92} + \frac{60{,}000 \times 2}{13} = -34{,}750 \text{ lbs. per sq.in.}$$

$$\sigma_K = -\frac{450{,}000 \times 7}{92} + \frac{60{,}000 \times 4}{13} = -15{,}700 \text{ lbs. per sq.in.}$$

All other elements are in tension.

Assume that A will buckle at 45,000 lbs. per sq.in. and that B, C, D, L, and K will buckle at 40,000 lbs. per sq.in. A, B, and C will buckle out.

With A, B, and C buckled out:

$$A = 1.4 - (0.2 + 0.1 + 0.1) = 1.0$$

$$\bar{X} = -\frac{0.1 \times 2 + 0.1 \times 4}{1.0} = \frac{0.6}{1.0} = -0.6 \text{ in. left}$$

$$\bar{Z} = -\frac{0.2 \times 10 + 0.1 \times 9 + 0.1 \times 7}{1.0} = -3.60 \text{ in. down}$$

$$I_{x_{\text{centerline}}} = 92.0 - 0.2 \times \overline{10}^2 - 0.1 \times \overline{9}^2 - 0.1 \times \overline{7}^2 = 59.0 \text{ in.}^4$$

$$I_{x_{\text{c.g.}}} = 59.0 - 1.0 \times \overline{3.6}^2 = 46.04 \text{ in.}^4$$

$$I_{z_{\text{centerline}}} = 13.0 - 0.1 \times \overline{2}^2 - 0.1 \times \overline{4}^2 = 11.00 \text{ in.}^4$$

$$I_{z_{\text{c.g.}}} = 11.00 - 1.0 \times \overline{0.6}^2 = 10.64 \text{ in.}^4$$

$$I_{x_{\text{c.g.}z_{\text{c.g.}}}} = -0.1 \times 2 \times 9 - 0.1 \times 4 \times 7 - (-0.6)(-3.6) \times 1.0 = -6.76 \text{ in.}^4$$

$$M_{x_{\text{c.g.}}} = 450{,}000 - 9{,}000 \times 13.60 - 4{,}000 \times 12.60 - 4{,}000 \times 10.60 = +234{,}800 \text{ in.lbs.}$$

$$M_{z_{\text{c.g.}}} = -60{,}000 + 9{,}000 \times 0.6 + 4{,}000 \times 2.6 + 4{,}000 \times 4.6 = -25{,}800 \text{ in.lbs.}$$

$$a = \frac{(-25{,}800) \times 46.04 + 234{,}800\,(-6.76)}{46.04 \times 10.64 - (-6.76)^2} = \frac{-2{,}775{,}080}{444.167} = -6{,}248 \text{ lbs. per sq.in.}$$

$$b = \frac{-234{,}800 \times 10.64 - (-25{,}800)\,(-6.76)}{46.04 \times 10.64 - (-6.76)^2} = \frac{-2{,}672{,}680}{444.167} = -6{,}017 \text{ lbs. per sq. in.}$$

Table 1 is a solution of Eq. 2 in tabular form. Column (7) gives the stress in the various elements, and it will be noted that the compressive stress in element L exceeds 40,000. The problem would have to be reworked assuming that this element buckles out at 40,000. This will not be done here since it would add nothing to explanation. Column (9) shows the total force in each element. The algebraic sum of this column should be zero, since $\Sigma H = 0$.

TABLE 1

(1)	(2)	(3)	(4)	(5)	(6)	(7)	(8)	(9)
Element	z	bz	x	ax	P/A	σ	A	σA
A	.....	.....	...	.....	.....	−45,000	0.2	− 9,000.0
B	.....	.....	...	.....	.....	−40,000	0.1	− 4,000.0
C	.....	.....	...	.....	.....	−40,000	0.1	− 4,000.0
D	+ 3.60	−21,661	+5.6	−34,989	+17,000	−39,650	0.1	− 3,965.0
E	− 3.40	+20,458	+4.6	−28,741	+17,000	+ 8,717	0.1	+ 871.7
F	− 5.40	+32,492	+2.6	−16,245	+17,000	+33,247	0.1	+ 3,324.7
G	− 6.40	+38,509	+0.6	− 3,749	+17,000	+51,760	0.2	+10,352.0
H	− 5.40	+32,492	−1.4	+ 8,747	+17,000	+58,239	0.1	+ 5,823.9
I	− 3.40	+20,458	−3.4	+21,243	+17,000	+58,701	0.1	+ 5,870.1
J	+ 3.60	−21,661	−4.4	+27,491	+17,000	+22,830	0.1	+ 2,283.0
K	+10.60	−63,780	−3.4	+21,243	+17,000	−25,537	0.1	− 2,553.7
L	+12.60	−75,814	−1.4	+ 8,747	+17.000	−50,067	0.1	− 5,006.7
								−28,525.4
								+28,525.4
							$\Sigma\sigma A =$	0

TABLE 2

(1) Element	(2) z'	(3) σA	(4) $z'\sigma A$	(5) x'	(6) $x'\sigma A$
A	20	− 9,000.0	−180,000	5	− 45,000
B	19	− 4,000.0	− 76,000	7	− 28,000
C	17	− 4,000.0	− 68,000	9	− 36,000
D	10	− 3,965.0	− 39,650	10	− 39,650
E	3	+ 817.7	+ 2,453	9	+ 7,359
F	1	+ 3,324.7	+ 3,325	7	+ 23,273
G	0	+10,352.0	.....	5	+ 51,760
H	1	+ 5,823.9	+ 5,824	3	+ 17,472
I	3	+ 5,870.1	+ 17,610	1	+ 5,870
J	10	+ 2,283.0	+ 22,830	0	.....
K	17	− 2,553.7	− 43,413	1	− 2,554
L	19	− 5,006.7	− 95,127	3	− 15,020
			−502,190		−166,224
			+ 52,042		105,734
		$\Sigma z'\sigma A$ =	−450,148	$\Sigma x'\sigma A$ =	− 60,490

Table 2 is a check on the moment about two arbitrarily chosen lines x' and z' which should equal 450,000 in.lbs. and 60,000 in.lbs., respectively, the external moments. The check is good.

REFERENCES

[1] Bruhn, E. F., *Analysis and Design of Airplane Structures*, 4th Printing, p. C10.5; John S. Swift Company, Inc., Cincinnati, February, 1944.

[2] Albert, O., *Beam-Method of Design for Eccentrically-Loaded Columns*, Eng. News-Record, Vol. 130, pp. 365–367, March 11, 1943.

[3] Newell, Joseph S., *The Analysis of Leading Edge Wing Beams*, S.A.E. Journal, p. 385, September, 1939.

Letters to the Editor

Dear Sir:

The following remarks can be made about the paper by Prof. Eryk Kosko, "A Simplified Analysis of Hollow Beams with Longitudinal Webs Subjected to Torsional Loads" (JOURNAL OF THE AERONAUTICAL SCIENCES, Vol. 12, No. 1, p. 103, January, 1945), and the Letter to the Editor by Prof. Alfred S. Niles (JOURNAL OF THE AERONAUTICAL SCIENCES, Vol. 12, No. 2, p. 240, April, 1945).

(1) A single-celled tube considered as a membrane is statically determinate, in contradiction with Professor Niles' statement. At each point of the tube, there are three unknown stresses, and three equations of equilibrium, so that there is a statically determined solution, except when there are edge restraints, which do not exist in the case of a tube onto which torques only are applied. Although these facts are well known, the opposite opinion is too often accepted.

(2) Professor Kosko is justified to consider that deformation and least work methods are practically equivalent for many structural problems, and too much time is being lost in discussing the advantages of both methods. However, it is useful to remember that variational methods are generally much more powerful than direct methods—a fact that is proved by the history of analytical dynamics. These methods are much better adapted to approximate solutions (example: Rayleigh-Ritz method) and avoid the use of two sets of unknowns, which is extremely important in intricate problems. The writer has been able to solve many problems of shells by variational methods in a much simpler manner than by considerations of displacements—for instance, in the case of torsion bending.* Especially for membranes, the difficulties that appear in the boundary conditions when displacements are considered disappear when variational methods are applied. In addition, experience shows that it is much easier to train stress analysts to use variational methods, especially in the case of three-dimensional problems, than to determine displacements.

(3) In the solution proposed by the author, preliminary systems of two equations with two unknowns must be solved (his Eqs. (4) and (5)) before the main system of equations is written, which explains the apparent reduction of the number of unknowns. However, when many cells are considered, the author's method leads to equations each containing all the unknowns, while the conventional method leads to equations with three unknowns each, the two end equations containing only two unknowns each, and the system can be easily solved by methods conventional in the case of continuous beams.

Thus, it appears that the author's method is equivalent to the conventional method for two or three cells and is less advantageous for a greater number of cells.

(4) The analysis developed by the author can be replaced by the following developed formulas, which can be established by any method:

Calculate successively:

$$a_1' = a_1 + a_{12};\ a_3' = a_3 + a_{23}$$

$$r_1 = a_{12}/a_1';\ r_2 = a_{23}/a_3';\ p_1 = A_1/a_1';\ p_3 = A_3/a_3'$$

$$B = A_2 + r_1 a_{12} + r_3 a_{23};\ S = a_2 + a_1 r_1 + a_3 r_3$$

$$H = B^2 + S(p_1 A_1 + p_3 A_3);\ c_2 = S/H;\ d = S/B$$

Then:

$$2q_2/T = c_2;\ 2q_1/T = c_1 = c_2(p_1 d + r_1);\ 2q_3/T = c_3(p_3 d + r_3)$$

$$q_{12} = q_1 - q_2;\ q_{23} = q_2 - q_3$$

These formulas give the required results with about 60 per cent of the computations necessitated by the method proposed by the author.

* Beskin, L., *Stress Analysis of Open Membranes*, Journal of the Aeronautical Sciences, Vol. 11, No. 4, p. 343, October, 1944.

LEON BESKIN
Design Specialist
Consolidated Vultee Aircraft Corporation

Dear Sir:

In a Letter to the Editor (JOURNAL OF THE AERONAUTICAL SCIENCES, Vol. 12, No. 2, p. 240, April, 1945), Prof. Alfred S. Niles makes several criticisms regarding statements contained in the writer's paper on "A Simplified Analysis of Hollow Beams with Longitudinal Webs Subjected to Torsional Loads" (JOURNAL OF THE AERONAUTICAL SCIENCES, Vol. 12, No. 1, p. 103, January, 1945).

The writer is ready to agree with Professor Niles that the number of simultaneous equations to be solved, as required by the "standard" method, may be made equal to the number of cells. However, such a reduced system is attained only after one additional unknown—the angle of twist—has been eliminated, and this at the expense of complicating the expressions for the coefficients.

(*Continued on page 428*)

Plastic Bending—Approximate Solution*

WM. R. OSGOOD†

National Bureau of Standards

ABSTRACT

In two previous papers the exact solution of the plastic bending problem was considered. Since the exact solution is cumbersome, an approximation is desirable. This paper gives an approximate solution, which, in particular, makes it possible to determine slopes and deflections. The exact determination of these quantities is usually practically impossible in the plastic range.

INTRODUCTION

As is clear from references 1 and 2, the exact determination of the curves showing the relationships between moment and curvature and between moment and strain-difference in plastic bending, though elementary in principle, is time-consuming in execution, sometimes enormously so. And when it comes to the exact determination of deflections, it may be said that such a determination is practically impossible except in a few simple cases.[1] It has seemed worth while, therefore, to consider approximate solutions of the problem which give promise of reasonable accuracy. The approximation considered here consists of expressing the relations between moment and curvature and between moment and strain-difference by means of relatively simple equations. Two such equations have been found that can be made to express these relations to as high a degree of accuracy as desired.

If the reader wishes to familiarize himself with what has gone before it is suggested that he read reference 2 and refer to reference 1 only as necessary. The equations in the present paper are numbered consecutively with those in references 1 and 2.

NOTATION

The notation used previously and in this paper is here recapitulated for convenience, and new notation is included:

A_1 = cross-sectional area of one flange of beam
A_2 = cross-sectional area of other flange of beam
A_w = cross-sectional area of web of beam
E = modulus of elasticity of material of beam
I = least moment of inertia of cross-sectional area about axis perpendicular to plane of bending
M = absolute value of bending moment at any cross section
W = total load on beam
b_w = thickness of web of beam
$\bar{c}_1$ = distance from centroidal axis of cross section to extreme fiber or fibers on one side
$\bar{c}_2$ = distance from centroidal axis of cross section to extreme fiber or fibers on other side
e_1 = strain in extreme fiber or fibers on one side of neutral axis
e_2 = strain in extreme fiber or fibers on other side of neutral axis
h = depth of cross section of beam
l = length of beam
s = stress in any fiber of beam
v = deflection of beam at x
x = coordinate measured in direction of length of beam
$\epsilon = e_1 - e_2$ (147)
$\kappa = e_1 + e_2$, $\mu = Mh/(EI)$ (38)
$\xi = x/l$
$\sigma = s/E$
σ_1 = value of σ for extreme fiber or fibers on one side of neutral axis
σ_2 = value of σ for extreme fiber or fibers on other side of neutral axis
σ_{y1} = value of σ for extreme fiber or fibers on one side of neutral axis, when stressed to yield point
σ_{y2} = value of σ for extreme fiber or fibers on other side of neutral axis, when stressed to yield point
$\phi = hv/l^2$, called deflection in this paper
$\omega = Whl/(EI)$

THE κ,μ-RELATION

One use that may be made of the relation between κ and μ is in determining slopes and deflections, from the equation[1]

$$d^2\varphi/d\xi^2 = \kappa \tag{70a}$$

It is therefore desirable that κ be expressed as such a function of μ as may be integrated readily, it being borne in mind that μ is a function of ξ. The following expressions satisfy this condition in most cases that arise in practice:

$$\kappa = \mu, \quad \mu \leqq \mu_0 \tag{172}$$

$$\kappa = \kappa_0 + \frac{(\mu_m - \mu_0)(\mu - \mu_0)}{\mu_m - \mu}\,[p_0 + p_1(\mu - \mu_0) + p_2(\mu - \mu_0)^2 + \ldots], \ \mu \geqq \mu_0 \tag{173}$$

where κ_0 and μ_0 are the values of κ and μ at the instant an extreme fiber first becomes stressed to its proportional limit, μ_m is the maximum possible value of μ ($\kappa = \infty$), $p_0 = d\kappa/d\mu$ at $\mu = \mu_0 + 0$, and $p_1, p_2, \ldots$ are coefficients to be determined from known sets of corresponding values of κ and μ. Such sets of corresponding values can always be obtained either by the methods of reference 2 or graphically.

If these sets are designated as (κ_1, μ_1), (κ_2, μ_2), (κ_3, μ_3), ..., then

Received January 29, 1945.

* This paper forms part of a project being carried out at the National Bureau of Standards for the Bureau of Aeronautics, Navy Department. The author is pleased to acknowledge permission of the Bureau of Aeronautics to publish the paper.

† Materials Engineer.

$$p_1 = \frac{\begin{vmatrix} \dfrac{(\kappa_1 - \kappa_0)(\mu_m - \mu_1)}{(\mu_1 - \mu_0)(\mu_m - \mu_0)} - p_0 \;(\mu_1 - \mu_0)^2 \ldots \\ \dfrac{(\kappa_2 - \kappa_0)(\mu_m - \mu_2)}{(\mu_2 - \mu_0)(\mu_m - \mu_0)} - p_0 \;(\mu_2 - \mu_0)^2 \ldots \\ \ldots\ldots\ldots\ldots\ldots\ldots\ldots\ldots \end{vmatrix}}{\begin{vmatrix} \mu_1 - \mu_0 & (\mu_1 - \mu_0)^2 \ldots \\ \mu_2 - \mu_0 & (\mu_2 - \mu_0)^2 \ldots \\ \ldots\ldots\ldots\ldots\ldots\ldots\ldots\ldots \end{vmatrix}} \tag{174}$$

$$p_2 = \frac{\begin{vmatrix} \mu_1 - \mu_0 & \dfrac{(\kappa_1 - \kappa_0)(\mu_m - \mu_1)}{(\mu_1 - \mu_0)(\mu_m - \mu_0)} - p_0 \ldots \\ \mu_2 - \mu_0 & \dfrac{(\kappa_1 - \kappa_0)(\mu_m - \mu_2)}{(\mu_2 - \mu_0)(\mu_m - \mu_0)} - p_0 \ldots \\ \ldots\ldots\ldots\ldots & \ldots\ldots\ldots\ldots\ldots\ldots \end{vmatrix}}{\begin{vmatrix} \mu_1 - \mu_0 & (\mu_1 - \mu_0)^2 \ldots \\ \mu_2 - \mu_0 & (\mu_2 - \mu_0)^2 \ldots \\ \ldots\ldots\ldots\ldots & \ldots\ldots\ldots\ldots\ldots\ldots \end{vmatrix}} \tag{175}$$

p_3 = etc.

The ϵ,μ-Relation

Satisfactory expressions for ϵ are

$$\epsilon = q\mu, \quad \mu \leqq \mu_0 \tag{176}$$

$$\epsilon = \epsilon_0 + \frac{(\mu_m - \mu_0)(\mu - \mu_0)}{\mu_m - \mu}\,[q_0 + q_1(\mu - \mu_0) + q_2(\mu - \mu_0)^2 + \ldots], \quad \mu \geqq \mu_0 \tag{177}$$

where ϵ_0 is the value of ϵ at the instant an extreme fiber first becomes stressed to its proportional limit, $q = (\bar{c}_1 - \bar{c}_2)/h$, $q_0 = d\epsilon/d\mu$ at $\mu = \mu_0 + 0$, and $q_1, q_2, \ldots$ are coefficients to be determined from known sets of corresponding values of ϵ and μ. Such known sets can always be obtained graphically if not otherwise.[2] If these sets are designated as (ϵ_1,μ_1), (ϵ_2,μ_2), (ϵ_3,μ_3), ..., then the expressions for $q_1, q_2, q_3, \ldots$ are the same as those for $p_1, p_2, p_3, \ldots$ (Eqs. (174) and (175)) when p_0 is replaced by q_0 and the κ's are replaced by ϵ's.

Eqs. (172) and (176) are exact. By retaining a sufficient number of the p's and q's in the approximate expressions (173) and (177), the approximation may be made as accurate as desired; but usually it will suffice to retain not more than p_1 and p_2 and q_1 and q_2, in addition, of course, to p_0 and q_0. $p_0 = 1$ and $q_0 = q$ always in the absence of thin flanges.

The coefficients (p's and q's) in Eqs. (173) and (177) are really functions of the shape of the cross section and of the stress-strain diagram. By examining the κ,μ- and the ϵ,μ-relations for a goodly number of cross sections and stress-strain diagrams, it would probably be possible to relate these coefficients empirically to some relatively simple property or properties of the cross sections and the stress-strain diagrams. In this way the somewhat tedious determination of $\kappa_1, \mu_1, \epsilon_1, \kappa_2, \mu_2, \epsilon_2, \kappa_3, \mu_3, \epsilon_3, \ldots$ would be obviated. It must be remembered, however, that there are essentially at least five independent variables present: the shape of the cross section, two parameters defining the tensile stress-strain curve, and two parameters defining the compressive stress-strain curve. This statement optimistically assumes that the cross section can be described by one parameter. If two are required, as is perhaps more likely, the number of independent variables rises to six.

Approximations to the Curves of Reference 2

In order to show the goodness of fit of the approximate curves to the exact curves, the two sets of curves will be compared for the cross sections and the materials studied in reference 2. The exact curves are shown solid in Figs. 3–8, and the adjacent dotted ones are the approximate curves. In some cases the approximate curves cannot be distinguished from the exact curves at the scales used for the drawings. The sets of curves at the right in the figures are the κ,μ-curves; those at the left are the ϵ,μ-curves.

Some of the cross sections are shown in Fig. 1, and the stress-strain diagrams of the materials are shown in Fig. 2. The modulus of elasticity is 10,500,000 lbs. per sq.in. The yield strains, corresponding to the $(2/3)E$-secant yield strengths, 42,000 and 50,000 lbs. per sq.in., are 0.006 and $1/140 = 0.007143$, respectively. The curves marked I and I & III are parabolas. The others are straight lines. Three cases are considered: Case I, in which the stress-strain relations on the two sides of the neutral axis are given by the curves I and I in Fig. 1; Case II, in which they are given by the curves II and II; and Case III, in which they are given by the curves III and III.

The cross sections are identified as follows.

(1) Symmetrical Sections.

(a) Idealized I-section. The idealized I-section consists of a negligibly thin web and of two infinitesimally thin flanges of finite cross-sectional areas. The particular section treated numerically under this heading has equal flanges. Fig. 1d: $A_1 = A_2$, $A_w = 0$.

(b) I-section. The I-section consists of a web and two infinitesimally thin flanges of finite cross-sectional areas, Fig. 1d. The particular section treated numer-

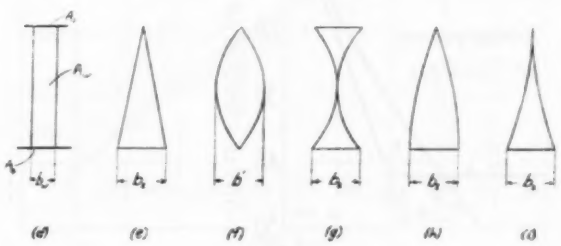

Fig. 1.

ically has the cross-sectional area of each flange equal to that of the web, $A_1 = A_2 = A_w$.

(c) Parabolic section, vertexes in. This section is illustrated in Fig. 1g. It is bounded laterally by the arcs of two parabolas tangent vertically at the center of the section.

(d) Rectangular section. Fig. 1d: $A_1 = A_2 = 0$.

(e) Parabolic section, vertexes out. This section is illustrated in Fig. 1f. It is bounded laterally by the arcs of two parabolas with the vertices out on the centroidal axis of the section.

In the unsymmetrical cross sections the upper stress-strain curves of Fig. 2 apply to the material above the neutral axis and the lower stress-strain curves to the material below the neutral axis.

(2) Unsymmetrical Sections.

(a) Idealized I-section with one flange. This is an idealized I-section in which the cross-sectional area of one flange, the upper one, is infinitesimal. Fig. 1d: $A_1 = 0+$, $A_w = 0$.

(b) T-section with infinitesimal web. In this section the flange, at the bottom, is infinitesimally thin but of finite cross-sectional area, and the web is infinitesimally narrow. Fig. 1d: $A_1 = 0$, $b_w = 0+$, $A_w = 0+$.

(c) T-section. The T-section consists of a web and an infinitesimally thin flange, both of finite cross-sectional areas. These areas are equal in the particular section treated numerically under this heading, and the flange is at the bottom. Fig. 1d: $A_1 = 0$, $A_2 = A_w$.

(d) Triangular section. The base is at the bottom, Fig. 1e.

(e) Semiparabolic section, vertexes in. This section is illustrated in Fig. 1i. It is bounded laterally by the arcs of two parabolas tangent vertically at the top of the section.

(f) Semiparabolic section, vertexes out. This section is illustrated in Fig. 1h. It is bounded laterally by the arcs of two parabolas with the vertexes out, at the bottom of the section.

The computations to establish the approximate curves are indicated in Tables 1–3. The numbers in parentheses in the column headed μ_m are the numbers of the equations from which the values of μ_m were computed. The values taken for ϵ_1, κ_1, and μ_1 are those at which a yield strain is first reached in either extreme fibers, and the values for ϵ_2, κ_2, and μ_2 are those at which the second yield strain is first reached in the opposite extreme fibers. In the columns giving the first yield strain and the second yield strain, the numbers in parentheses are the numbers of the equations in reference 2 from which the corresponding strains in the opposite extreme fibers were computed. Similarly, the numbers in parentheses in the columns of μ_1 and μ_2 are the numbers of the equations in reference 2 used to compute μ_1 and μ_2.

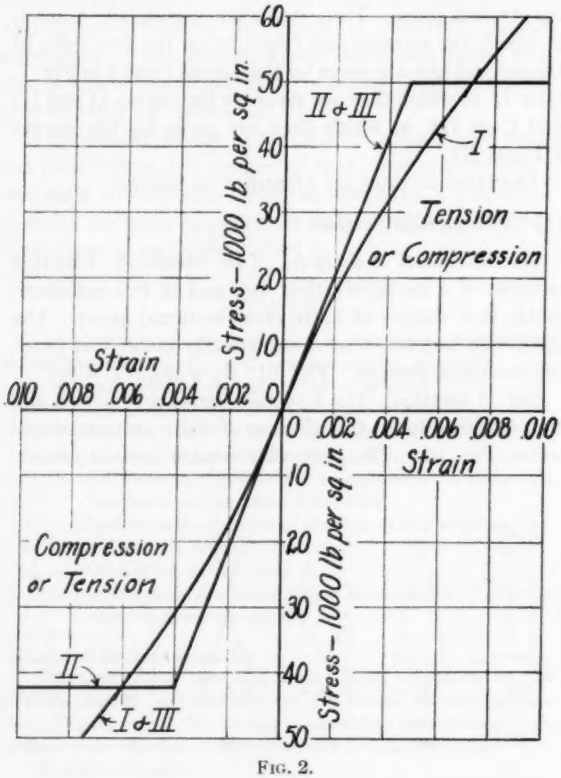

FIG. 2.

Case I

For the stress-strain diagrams of Case I $\mu_m = \infty$, since on both sides of the neutral axis the extreme fiber stresses become infinite with increasing κ. Also $\mu_0 = \kappa_0 = \epsilon_0 = 0$, $p_0 = 1$, and $q_0 = q$ because the proportional limit of the material on at least one side (in the present case both sides) of the neutral axis is zero. It turns out that in the present case, within the range of μ's considered, sufficient accuracy for practical purposes can be obtained by retaining only p_1 and q_1 (in addition to p_0 and q_0) in Eqs. (173) and (177). Equations (173), (174) and its equivalent for q_1, and (177) consequently reduce to

$$\kappa = (1 + p_1\mu)\mu \tag{178}$$

$$\epsilon = (q + q_1\mu)\mu \tag{179}$$

$$p_1 = (1/\mu_1)[(\kappa_1/\mu_1) - 1] \tag{180}$$

$$q_1 = (1/\mu_1)[(\epsilon_1/\mu_1) - q] \tag{181}$$

Moreover, also in the present case, the differences between the exact curves, Figs. 3 and 4, and the approximate curves within the range of μ's considered are so small that no attempt has been made to show the approximate curves.

(1) Symmetrical Sections.

(a) Idealized I-section. For the particular stress-strain diagram chosen for Case I the approximate

TABLE 1. CASE I.

Shape of Section and q	ϵ_0	$\kappa_0 = \mu_0$	p_0	q_0	μ_m	1st Yield Strain and Corresp. Strain in Opp. Ex. Fib.	ϵ_1	κ_1	μ_1	p_1	q_1
I-section, Fig. 1d, $A_1 = A_2 = A_w$, $q = 0$	0	0	1	0	∞	$e_2 = 0.006$, $e_1 = 0.00576$ (152)	−0.00024	0.01176	0.00813 (153)	54.9	−3.63
Parabolic section, vert. in, Fig. 1g, $q = 0$	0	0	1	0	∞	$e_2 = 0.006$, $e_1 = 0.00579$ (156)	−0.00021	0.01179	0.00843 (157)	47.3	−2.95
Rectang. section, Fig. 1d, $A_1 = A_2 = 0$, $q = 0$	0	0	1	0	∞	$e_2 = 0.006$, $e_1 = 0.00589$ (158)	−0.00011	0.01189	0.00871 (159)	41.8	−1.45
Parabolic section, vert. out, Fig. 1f, $q = 0$	0	0	1	0	∞	$e_2 = 0.006$, $e_1 = 0.00593$ (160)	−0.00007	0.01193	0.00908 (161)	34.7	−0.886
T-section, Fig. 1d, $A_1 = 0$, $A_w = 0+$, $q = 1$	0	0	1	1	∞	$e_1 = 0.00714$, $e_2 = 0$ (162)	0.00714	0.00714	0.00513 (163)	76.4	76.4
T-section, Fig. 1d, $A_1 = 0$, $A_2 = A_w$, $q = 1/3$	0	0	1	1/3	∞	$e_1 = 0.00714$, $e_2 = 0.00220$ (164)	0.00494	0.00934	0.00700 (165)	47.9	29.4
Triangular section, Fig. 1e, $q = 1/3$	0	0	1	1/8	∞	$e_1 = 0.00714$, $e_2 = 0.00353$ (168)	0.00361	0.01067	0.00822 (169)	36.4	13.0
Semiparab. section, vert. in, Fig. 1i, $q = 1/2$	0	0	1	1/2	∞	$e_1 = 0.00714$, $e_2 = 0.00233$ (170)	0.00481	0.00947	0.00758 (171)	33.0	17.8
Semiparab. section, vert. out, Fig. 1h, $q = 1/4$	0	0	1	1/4	∞	$e_1 = 0.00714$, $e_2 = 0.00427$ (166)	0.00287	0.01141	0.00866 (167)	36.7	9.47

curves and the exact curves happen to coincide. This will always occur if[2] $n_1 = n_2$: $p_{n_1-1} \neq 0$, $q_{n_1-1} \neq 0$, all other p's and q's equal to zero; $n_1 \neq n_2$: $p_{n_1-1} \neq 0$, $p_{n_2-1} \neq 0$, $q_{n_1-1} \neq 0$, $q_{n_2-1} \neq 0$, all other p's and q's equal to zero. Curves a and a in Fig. 3 show the relations between κ and μ and between ϵ and μ for the section with equal flanges.

(b) I-section. Eqs. (178) and (179) become

$$\kappa = (1 + 54.9\mu)\mu \tag{182}$$

$$\epsilon = -3.63\mu^2 \tag{183}$$

Curves b and b in Fig. 3 show the exact relations and, to the scale of the drawing, the approximate relations.

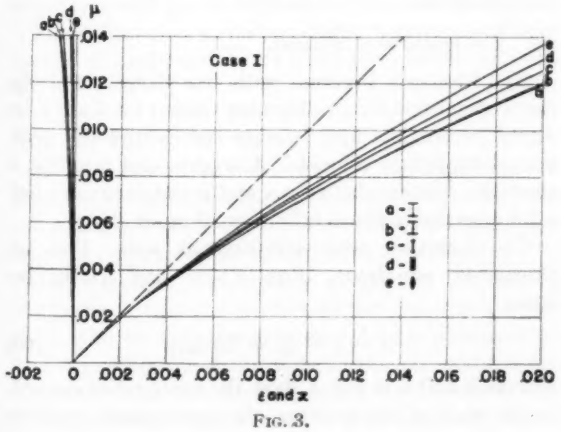

FIG. 3.

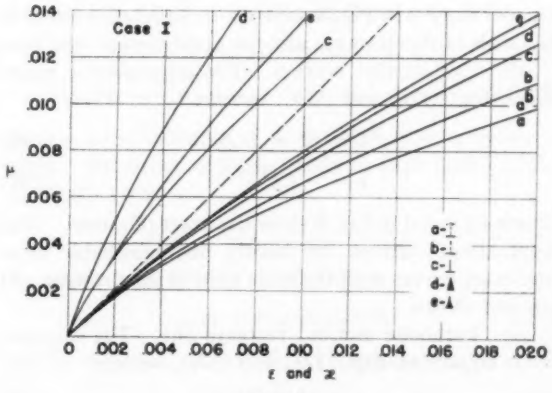

FIG. 4.

TABLE 2. CASE II.

Shape of Section and q	ϵ_0	$\kappa_0 = \mu_0$	p_0	q_0	μ_m	1st Yield Strain and Corresp. Strain in Opp. Ex. Fib.	ϵ_1	κ_1	μ_1	p_1	q_1
I-section, Fig. 1d, $A_1 = A_2 = A_w$ $q = 0$	0	0.008	14/5	−7/5	0.00926 (208)	$\epsilon_2 = 0.006$ $\epsilon_1 = 0.00454$ (152)	−0.00146	0.01054	0.00868 (153)	−1,610	620
Parabolic section, vert. in, Fig. 1g, $q = 0$	0	0.008	1	0	0.01053 (212)	$\epsilon_2 = 0.006$ $\epsilon_1 = 0.00521$ (156)	−0.00079	0.01121	0.00987 (157)	−296	−58.2
Rectang. section, Fig. 1d, $A_1 = A_2 = 0$ $q = 0$	0	0.008	1	0	0.01304 (216)	$\epsilon_2 = 0.006$ $\epsilon_1 = 0.00574$ (158)	−0.00026	0.01174	0.01060 (159)	−117	−18.5
Parabolic section, vert. out, Fig. 1f, $q = 0$	0	0.008	1	0	0.01632 (220)	$\epsilon_2 = 0.006$ $\epsilon_1 = 0.00591$ (160)	−0.00009	0.01191	0.01138 (161)	−92.5	−4.52
T-section, Fig. 1d, $A_1 = 0$ $A_w = 0+$ $q = 1$	0.00476	0.00476	1	1	0.00714 (224)	$\epsilon_1 = 0.00714$ $\epsilon_2 = 0$ (162)	0.00714	0.00714	0.00609 (163)	−152	−152
T-section, Fig. 1d, $A_1 = 0$ $A_2 = A_w$ $q = 1/2$	0.00317	0.00635	1	1/2	0.01127 (227)	$\epsilon_1 = 0.00714$ $\epsilon_2 = 0.00218$ (164)	0.00496	0.00932	0.00835 (165)	−59.7	15.2
Triangular section, Fig. 1e, $q = 1/3$	0.00238	0.00714	1	1/3	0.01557 (231)	$\epsilon_1 = 0.00714$ $\epsilon_2 = 0.00351$ (168)	0.00363	0.01065	0.01026 (169)	−93.5	−25.9
Semiparab. section, vert. in, Fig. 1i, $q = 1/2$	0.00317	0.00635	1	1/2	0.01840 (235)	$\epsilon_1 = 0.00714$ $\epsilon_2 = 0.00237$ (170)	0.00478	0.00951	0.00934 (171)	−69.1	−32.7
Semiparab. section, vert. out, Fig. 1h, $q = 1/4$	0.00190	0.00762	1	1/4	0.01519 (239)	$\epsilon_1 = 0.00714$ $\epsilon_2 = 0.00421$ (166)	0.00293	0.01135	0.01090 (167)	−108	−22.0

(c) Parabolic section, vertexes in. The approximate equations, Eqs. (178) and (179), become

$$\kappa = (1 + 47.3\mu)\mu \tag{184}$$

$$\epsilon = -2.95\mu^2 \tag{185}$$

Curves c and c in Fig. 3 show the exact relations and, to the scale of the drawing, also the approximate relations.

(d) Rectangular section. The approximate equations, Eqs. (178) and (179), become

$$\kappa = (1 + 41.8\mu)\mu \tag{186}$$

$$\epsilon = -1.45\mu^2 \tag{187}$$

Curves d and d in Fig. 3 show the exact relations. The approximate curves are hardly distinguishable from the exact curves with the scale used in the drawing and are not shown.

(e) Parabolic section, vertexes out. The approximate equations, Eqs. (178) and (179), become

$$\kappa = (1 + 34.7\mu)\mu \tag{188}$$

$$\epsilon = -0.886\mu^2 \tag{189}$$

Curves e and e in Fig. 3 show the exact relations. The approximate curves are hardly distinguishable from the exact curves with the scale used in the drawing and are not shown.

(2) *Unsymmetrical Sections.*

(a) Idealized I-section with one flange. For the particular stress-strain diagrams chosen for Case I, as stated before, the approximate curves and the exact curves happen to coincide. Curves a and a in Fig. 4 show the relations between κ and μ and between ϵ and μ for a section with an infinitesimal upper flange.

(b) T-section with infinitesimal web. The approximate equations, Eqs. (178) and (179), become

$$\kappa = \epsilon = (1 + 76.4\mu)\mu \tag{190}$$

Curves b and b in Fig. 4 show the exact relations, and, to the scale of the drawing, the approximate relations

are hardly distinguishable from the exact ones. The approximate curves are not shown.

(c) T-section. The approximate equations, Eqs. (178) and (179), become

$$\kappa = (1 + 47.9\mu)\mu \tag{191}$$

$$\epsilon = (1/2 + 29.4\mu)\mu \tag{192}$$

Curves c and c in Fig. 4 show the exact relations. The approximate relations differ so little that they are not shown.

(d) Triangular section. The approximate equations, Eqs. (178) and (179), become

$$\kappa = (1 + 36.4\mu)\mu \tag{193}$$

$$\epsilon = (1/3 + 13.0\mu)\mu \tag{194}$$

Curves d and d in Fig. 4 show the exact relations. The approximate relations are hardly distinguishable from the exact ones and are not shown.

(e) Semiparabolic section, vertexes in. The approximate equations for this section are

$$\kappa = (1 + 33.0\mu)\mu \tag{195}$$

$$\epsilon = (1/2 + 17.8\mu)\mu \tag{196}$$

Curves e and e in Fig. 4 shows the exact relations. The approximate relations differ so little from the exact ones that they are not shown.

(f) Semiparabolic section, vertexes out. The approximate equations are

$$\kappa = (1 + 36.7\mu)\mu \tag{197}$$

$$\epsilon = (1/4 + 9.47\mu)\mu \tag{198}$$

No curves are shown for this section. As pointed out in reference 2, the κ,μ-curve is close to the curve for the triangular section.

Case II

In order to approximate with sufficient accuracy the exact curves of Case II, it is again necessary to keep only one of the coefficients for each set of curves—namely, p_1 and q_1—in addition of course to p_0 and q_0.

The values of ϵ_0, κ_0, and μ_0, Table 2, corresponding to the end of elastic action, are taken from references 1 and 2.

(*I*) *Symmetrical Sections.*

(a) Idealized I-section. As for Case I the approximate curves and the exact curves coincide. Curves a and a in Fig. 5 show the relations between κ and μ and between ϵ and μ for the section with equal flanges.

(b) I-section. As bending progresses, the passing of a finite portion of any cross section through a stress-strain relation with discontinuous slope is accompanied by a discontinuity of the slope in the κ,μ- and the ϵ,μ-relation. Thus this happens when the I-section with equal thin flanges, each equal in cross-sectional area to

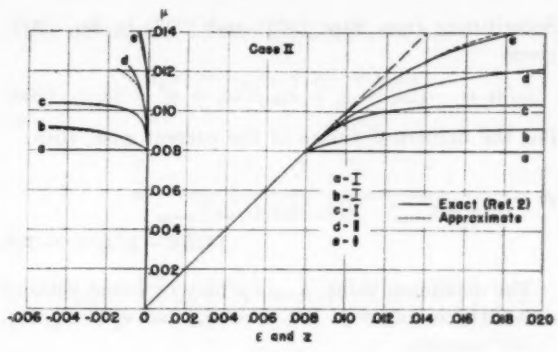

FIG. 5.

that of the web, reaches the condition $\kappa_0 = \mu_0 = 0.008$, as may be seen from curves b and b in Fig. 5. p_0 and q_0 are the reciprocals of the slopes of these curves at $\mu_0 = 0.008 + 0$, and their values must be found if Eqs. (173) and (177) are to be used. For the condition in question, $\sigma_1 = e_1$ and $\sigma_2 = \sigma_{y2}$, and Eq. (153)[2] becomes, with the aid of Eqs. (115),[2]

$$\mu = \frac{12}{7\kappa^2}\left(\kappa e_1^2 + \frac{1}{3}e_1^3 + \kappa e_2\sigma_{y2} + \frac{1}{2}e_2^2\sigma_{y2} - \frac{1}{6}\sigma_{y2}^3\right)$$

Differentiation with respect to κ gives

$$\frac{d\mu}{d\kappa} = -2\left(\frac{\mu}{\kappa}\right) + \left(\frac{12}{7\kappa^2}\right)\left[2\kappa e_1\left(\frac{de_1}{d\kappa}\right) + e_1^2 + e_1^2\left(\frac{de_1}{d\kappa}\right) + \kappa\sigma_{y2}\left(\frac{de_2}{d\kappa}\right) + e_2\sigma_{y2} + e_2\sigma_{y2}\left(\frac{de_2}{d\kappa}\right)\right] \tag{199}$$

Similarly equation (152)[2] becomes

$$(e_1 + e_2)e_1 + 1/2e_1^2 = (e_1 + e_2)\sigma_{y2} + e_2\sigma_{y2} - 1/2\sigma_{y2}^2$$

and by differentiation with respect to κ,

$$(3e_1 + e_2 - \sigma_{y2})\frac{de_1}{d\kappa} = (2\sigma_{y2} - e_1)\frac{de_2}{d\kappa} \tag{200}$$

By differentiating the first of Eqs. (38) with respect to κ, one finds

$$(de_1/d\kappa) + (de_2/d\kappa) = 1 \tag{201}$$

Solving Eqs. (200) and (201) simultaneously gives

$$de_1/d\kappa = (2\sigma_{y2} - e_1)/(2e_1 + e_2 + \sigma_{y2}) \tag{202}$$

$$de_2/d\kappa = (3e_1 + e_2 - \sigma_{y2})/(2e_1 + e_2 + \sigma_{y2}) \tag{203}$$

At $\mu = \mu_0 = 0.008$: $\kappa = \kappa_0 = 0.008$, $e_1 = e_2 = \sigma_{y2} = 0.004$. Substituting these values in Eqs. (199), (202), and (203) gives

$$p_0 = 1/(d\mu/d\kappa)_{\mu=\mu_0} = 14/5$$

To obtain q_0, it may be noted that

$$d\mu/d\epsilon = (d\mu/d\kappa)(d\kappa/d\epsilon) \tag{204}$$

and by differentiation of Eq. (147) that

$$d\kappa/d\epsilon = 1/[(de_1/d\kappa) - (de_2/d\kappa)] \tag{205}$$

Substituting from Eqs. (202) and (203) in Eq. (205) gives

$$d\kappa/d\epsilon = -(2e_1 + e_2 + \sigma_{y2})/(4e_1 + e_2 - 3\sigma_{y2}) \quad (206)$$

For the numerical values of the present case, then,

$$q_0 = \frac{1}{(d\mu/d\epsilon)_{\mu=\mu_0}} = \frac{1}{[(d\mu/d\kappa)(d\kappa/d\epsilon)]_{\mu=\mu_0}} = (14/5)(-1/2) = -7/5$$

The maximum value, μ_m, of μ may be found without difficulty, as follows. For $\sigma_1 = \sigma_{y1}$ and $\sigma_2 = \sigma_{y2}$ Eq. $(152)^2$ becomes

$$\sigma_{y1}(2e_1 + e_2 - {}^1/_2\sigma_{y1}) = \sigma_{y2}(2e_2 + e_1 - {}^1/_2\sigma_{y2})$$

As $\kappa \to \infty$, σ_{y1} and σ_{y2} become negligible compared to e_1 and e_2, so that

$$e_1/e_2 = (2\sigma_{y2} - \sigma_{y1})/(2\sigma_{y1} - \sigma_{y2})$$

or

$$\frac{e_1}{\kappa} = \frac{2\sigma_{y2} - \sigma_{y1}}{\sigma_{y1} + \sigma_{y2}}, \quad \frac{e_2}{\kappa} = \frac{2\sigma_{y1} - \sigma_{y2}}{\sigma_{y1} + \sigma_{y2}} \quad (207)$$

Similarly Eq. $(153)^2$ becomes, when the negligibile terms are omitted,

$$\mu_m = \frac{6}{7}\left[\sigma_{y1}\left(\frac{e_1}{\kappa}\right)\left(2 + \frac{e_1}{\kappa}\right) + \sigma_{y2}\left(\frac{e_2}{\kappa}\right)\left(2 + \frac{e_2}{\kappa}\right)\right] \quad (208)$$

By substituting $\sigma_{y1} = 0.00476$, $\sigma_{y2} = 0.004$ in Eqs. (207) and (208), one finds $\mu_m = 0.00926$.

Finally, for determining p_1 and q_1, it is necessary to pick values of ϵ_1, κ_1, and μ_1. As before, these will be taken as the values of ϵ, κ, and μ when a yield strain is first reached in an extreme fiber, $e_2 = 0.006$ in the present case. From Eq. $(152)^2$ it is then found that $e_1 = 0.00454$ and thus $\epsilon_1 = -0.00146$ and $\kappa_1 = 0.01054$. Eq. $(153)^2$ gives $\mu_1 = 0.00868$. From Eq. (174) and the corresponding equation for q_1, one now finds

$$p_1 = \left[\frac{(0.00254)(0.00058)}{(0.00068)(0.00126)} - \left(\frac{14}{5}\right)\right]/0.00068 = -1{,}610$$

$$q_1 = \left[\frac{(-0.00146)(0.00058)}{(0.00068)(0.00126)} + \left(\frac{7}{5}\right)\right]/0.00068 = 620$$

The approximate Eqs. (173) and (177) may be written

$$\kappa = 0.008 + \frac{2.03(0.00974 - \mu)(\mu - 0.008)}{0.00926 - \mu}, \quad \mu \geqq 0.008 \quad (209)$$

$$\epsilon = -0.781\,\frac{(0.01026 - \mu)(\mu - 0.008)}{0.00926 - \mu}, \quad \mu \geqq 0.008 \quad (210)$$

The solid curves b and b in Fig. 5 show the exact relations. The approximate κ,μ-curve is indistinguishable from the exact curve.

(c) Parabolic section, vertexes in. The maximum value of μ is computed from Eqs. $(156)^2$ and $(157)^2$. When the negligible terms in Eq. $(156)^2$ are omitted, this equation reduces to

$$\sigma_{y1}e_1(e_1^2 + 3e_2^2) = \sigma_{y2}e_2(e_2^2 + 3e_1^2) \quad (211)$$

On introducing $\sigma_{y1} = 0.00476$, $\sigma_{y2} = 0.004$, and solving, it is found that $e_1/\kappa = 0.278$ and $e_2/\kappa = 0.722$. Eq. $(157)^2$ reduces to

$$\mu_m = \frac{10}{3}\left\{\sigma_{y1}\left(\frac{e_1}{\kappa}\right)^2\left[\left(\frac{e_1}{\kappa}\right)^2 + 2\left(\frac{e_1}{\kappa}\right)\left(\frac{e_2}{\kappa}\right) + 3\left(\frac{e_2}{\kappa}\right)^2\right] + \sigma_{y_2}\left(\frac{e_2}{\kappa}\right)^2\left[\left(\frac{e_2}{\kappa}\right)^2 + 2\left(\frac{e_2}{\kappa}\right)\left(\frac{e_1}{\kappa}\right) + 3\left(\frac{e_1}{\kappa}\right)^2\right]\right\} \quad (212)$$

By substituting the numerical values of σ_{y1}, σ_{y2}, e_1/κ and e_2/κ, one finds $\mu_m = 0.01053$. The values of p_1 and q_1 are found as before and are given in Table 2. The approximate equations, Eqs. (173) and (177), become

$$\kappa = 0.008 + \frac{0.750(0.01137 - \mu)(\mu - 0.008)}{0.01053 - \mu}, \quad \mu \geqq 0.008 \quad (213)$$

$$\epsilon = -0.147\,\frac{(\mu - 0.008)^2}{0.01053 - \mu}, \quad \mu \geqq 0.008 \quad (214)$$

The solid curves c and c in Fig. 5 show the exact relations. The approximate κ,μ-curve is indistinguishable from the exact curve.

(d) Rectangular section. The maximum value of μ is computed from Eqs. $(158)^2$ and $(159)^2$ by omitting the terms that become negligible as $\kappa \to \infty$. Eq. $(158)^2$ gives

$$\sigma_{y1}e_1 = \sigma_{y2}e_2$$

from which

$$e_1/\kappa = \sigma_{y2}/(\sigma_{y1} + \sigma_{y2}), \; e_2/\kappa = \sigma_{y1}/(\sigma_{y1} + \sigma_{y2}) \quad (215)$$

Eq. $(159)^2$ gives

$$\mu_m = 6[\sigma_{y1}(e_1/\kappa)^2 + \sigma_{y2}(e_2/\kappa)^2] \quad (216)$$

The values of p_1 and q_1 are given in Table 2, and the approximate equations, Eqs. (173) and (177), become

$$\kappa = 0.008 + 0.591\,\frac{(0.01653 - \mu)(\mu - 0.008)}{0.01304 - \mu}, \quad \mu \geqq 0.008 \quad (217)$$

$$\epsilon = -0.0931\,\frac{(\mu - 0.008)^2}{0.01304 - \mu}, \quad \mu \geqq 0.008 \quad (218)$$

The solid curves d and d in Fig. 5 show the exact relations. The approximate κ,μ-curve is indistinguishable from the exact curve.

(e) Parabolic section, vertexes out. μ_m is computed from Eqs. $(160)^2$ and $(161)^2$. Eq. $(160)^2$ gives

$$\sigma_{y1}e_1^2(e_1 + 3e_2) = \sigma_{y2}e_2^2(e_2 + 3e_1) \quad (219)$$

On introducing $\sigma_{y1} = 0.00476$, $\sigma_{y2} = 0.004$, and solving, one finds $e_1/\kappa = 0.471$ and $e_2/\kappa = 0.529$. Eq. (161)[2] gives

$$\mu_m = 10\left\{\sigma_{y1}\left(\frac{e_1}{\kappa}\right)^3\left[\frac{e_1}{\kappa} + 2\left(\frac{e_2}{\kappa}\right)\right] + \sigma_{y2}\left(\frac{e_2}{\kappa}\right)^3\left[\frac{e_2}{\kappa} + 2\left(\frac{e_1}{\kappa}\right)\right]\right\} \quad (220)$$

When p_1 and q_1 are determined, the approximate equations, Eqs. (173) and (177), become

$$\kappa = 0.008 + 0.769\,\frac{(0.01881 - \mu)(\mu - 0.008)}{0.01632 - \mu}, \qquad \mu \geqq 0.008 \quad (221)$$

$$\epsilon = -0.0376\,\frac{(\mu - 0.008)^2}{0.01632 - \mu}, \qquad \mu \geqq 0.008 \quad (222)$$

The solid curves e and e in Fig. 5 show the exact relations.

(2) *Unsymmetrical Sections.*

(a) Idealized I-section with one flange. The exact curves and the approximate curves, a and a in Fig. 6, coincide.

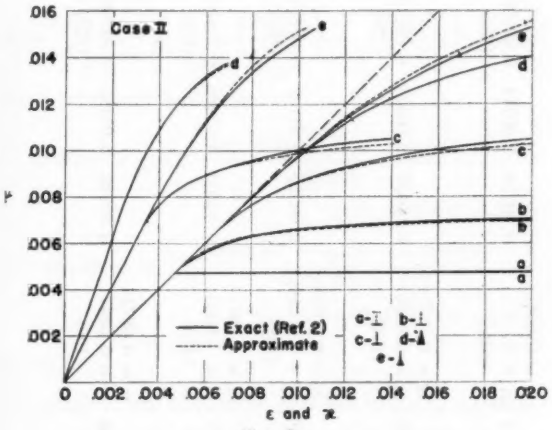

FIG. 6.

(b) T-section with infinitesimal web. Eq. (162)[2] gives, for determining μ_m,

$$e_1/\kappa = 1 \quad (223)$$

and Eq. (163),[2]

$$\mu_m = {}^3/_2\sigma_{y1} \quad (224)$$

The approximate equations are

$$\kappa = \epsilon = 0.00476 + 0.363\,\frac{(0.01133 - \mu)(\mu - 0.00476)}{0.00714 - \mu}, \qquad \mu \geqq 0.00476 \quad (225)$$

The solid curves b and b in Fig. 6 show the exact relations.

(c) T-section. From Eq. (164)[2], for μ_m,

$$\sigma_{y1}e_1 = \sigma_{y2}(e_1 + e_2) + \sigma_{y2}e_2$$

or

$$\frac{e_1}{\kappa} = \frac{2\sigma_{y2}}{\sigma_{y1} + \sigma_{y2}}, \frac{e_2}{\kappa} = \frac{\sigma_{y1} - \sigma_{y2}}{\sigma_{y1} + \sigma_{y2}} \quad (226)$$

and from Eq. (165)[2]

$$\mu_m = \frac{12}{5}\left[\sigma_{y1}\left(\frac{e_1}{\kappa}\right)^2 + \sigma_{y2}\left(\frac{e_2}{\kappa}\right)\left(2 + \frac{e_2}{\kappa}\right)\right] \quad (227)$$

The approximate equations are

$$\kappa = 0.00635 + 0.294\,\frac{(0.02311 - \mu)(\mu - 0.00635)}{0.01127 - \mu}, \qquad \mu \geqq 0.00635 \quad (228)$$

$$\epsilon = 0.00317 + 0.0746\,\frac{(0.02663 + \mu)(\mu - 0.00635)}{0.01127 - \mu}, \qquad \mu \geqq 0.00635 \quad (229)$$

The solid curves c and c in Fig. 6 show the exact relations.

(d) Triangular section. From Eq. (168)[2], for determining μ_m,

$$\sigma_{y1}e_1^2 - {}^1/_2\sigma_{y1}e_1^2 = \sigma_{y2}e_1e_2 + {}^1/_2\sigma_{y2}e_2^2$$

from which

$$\frac{e_1}{\kappa} = \sqrt{\frac{\sigma_{y2}}{\sigma_{y1} + \sigma_{y2}}}, \frac{e_2}{\kappa} = 1 - \sqrt{\frac{\sigma_{y2}}{\sigma_{y1} + \sigma_{y2}}} \quad (230)$$

and from Eq. (169)[2]

$$\mu_m = 6\left\{\sigma_{y1}\left(\frac{e_1}{\kappa}\right)^3 + \sigma_{y2}\left(\frac{e_2}{\kappa}\right)^2\left[3\left(\frac{e_1}{\kappa}\right) + 2\left(\frac{e_2}{\kappa}\right)\right]\right\} \quad (231)$$

The approximate equations are

$$\kappa = 0.00714 + 0.788\,\frac{(0.01784 - \mu)(\mu - 0.00714)}{0.01557 - \mu}, \qquad \mu \geqq 0.00714 \quad (232)$$

$$\epsilon = 0.00238 + 0.218\,\frac{(0.02000 - \mu)(\mu - 0.00714)}{0.01557 - \mu}, \qquad \mu \geqq 0.00714 \quad (233)$$

The solid curves d and d in Fig. 6 show the exact relations. The approximate κ,μ-curve is indistinguishable from the exact curve.

(e) Semiparabolic section, vertexes in. From Eq. (170),[2] for determining μ_m,

$$\sigma_{y1}e_1^3 = \sigma_{y2}e_2(3e_1^2 + 3e_1e_2 + e_2^2) \quad (234)$$

On introducing $\sigma_{y1} = 0.00476$, $\sigma_{y2} = 0.004$, and solving, one finds $e_1/\kappa = 0.770$ and $e_2/\kappa = 0.230$. Eq. (171)[2] reduces to

TABLE 3. CASE III.

Shape of Section and q	ϵ_0	$\epsilon_0 = \mu_0$	p_0	q_0	μ_m	1st Yield Strain and Corresp. Strain in Opp. Ex. Fib.	ϵ_1	κ_1	μ_1	2nd Yield Strain and Corresp. Strain in Opp. Ex. Fib.	ϵ_2	κ_2	μ_2	p_1	p_2	q_1	q_2
I-Section, Fig. 1d, $A_1 = A_2 = A_w$ $q = 0$	0	0	1	0	0.01224 (242)	$\epsilon_2 = 0.006$ $\epsilon_1 = 0.00437$ (152)	−0.00163	0.01037	0.00839 (153)	$\epsilon_1 = 0.00714$ $\epsilon_2 = 0.00780$ (152)	−0.00066	0.01494	0.00986 (153)	−80.3	896	−41.5	4,070
Parabolic section, vert. in, Fig. 1g, $q = 0$	0	0	1	0	0.01587 (245)	$\epsilon_2 = 0.006$ $\epsilon_1 = 0.00461$ (156)	−0.00139	0.01061	0.00874 (157)	$\epsilon_1 = 0.00714$ $\epsilon_2 = 0.00865$ (156)	−0.00151	0.01579	0.01125 (157)	−50.0	−227	−24.6	1,880
Rectang. section, Fig. 1d, $A_1 = A_2 = 0$ $q = 0$	0	0	1	0	0.02857 (248)	$\epsilon_2 = 0.006$ $\epsilon_1 = 0.00518$ (158)	−0.00082	0.01118	0.00937 (159)	$\epsilon_1 = 0.00714$ $\epsilon_2 = 0.00808$ (158)	−0.00093	0.01522	0.01147 (159)	−35.8	1,570	−15.3	964
Parabolic section, vert. out, Fig. 1f, $q = 0$	0	0	1	0	0.04762 (251)	$\epsilon_2 = 0.006$ $\epsilon_1 = 0.00546$ (160)	−0.00054	0.01146	0.00984 (161)	$\epsilon_1 = 0.00714$ $\epsilon_2 = 0.00788$ (160)	−0.00074	0.01502	0.01212 (161)	−14.0	635	−7.56	314
T-section, Fig. 1d, $A_1 = 0$ $A_w = 0+$ $q = 1$	0.00476	0.00476	1	1	0.00714 (224)	$\epsilon_1 = 0.00714$ $\epsilon_2 = 0$ (162)	0.00714	0.00714	0.00669 (163)	.....	.....	.....	.....	−152	...	−152	...
T-section, Fig. 1d, $A_1 = 0$ $A_2 = A_w$ $q = 1/3$	0	0	1	1/3	0.01143 (254)	$\epsilon_1 = 0.00714$ $\epsilon_2 = 0.00257$ (164)	0.00457	0.00971	0.00810 (165)	$\epsilon_2 = 0.006$ $\epsilon_1 = 0.00387$ (164)	0.05787	0.06987	0.01123 (165)	−82.5	266	−53.8	1,530
Triangular section, Fig. 1c, $q = 1/3$	0	0	1	1/3	0.02857 (257)	$\epsilon_1 = 0.00714$ $\epsilon_2 = 0.00389$ (168)	0.00326	0.01103	0.00958 (169)	$\epsilon_2 = 0.006$ $\epsilon_1 = 0.01158$ (168)	0.00558	0.01758	0.01256 (169)	−48.0	2,450	−25.6	1,500
Semiparab. section, vert. in, Fig. 1i, $q = 1/2$	0	0	1	1/2	0.03175 (260)	$\epsilon_1 = 0.00714$ $\epsilon_2 = 0.00254$ (170)	0.00460	0.00968	0.00889 (171)	$\epsilon_2 = 0.006$ $\epsilon_1 = 0.01837$ (170)	0.01237	0.02437	0.01533 (171)	−41.7	1,960	−26.5	1,380
Semiparab. section, vert. out, Fig. 1h, $q = 1/4$	0	0	1	1/4	0.03008 (263)	$\epsilon_1 = 0.00714$ $\epsilon_2 = 0.00471$ (166)	0.00243	0.01185	0.01005 (167)	$\epsilon_2 = 0.006$ $\epsilon_1 = 0.00929$ (166)	0.00329	0.01529	0.01177 (167)	−42.1	2,060	−20.7	1,180

$$\mu_m = \frac{20}{3}\left\{\sigma_{y1}\left(\frac{e_1}{\kappa}\right)^4 + \sigma_{y2}\left(\frac{e_2}{\kappa}\right)^2\left[6\left(\frac{e_1}{\kappa}\right)^2 + 8\left(\frac{e_1}{\kappa}\right)\left(\frac{e_2}{\kappa}\right) + 3\left(\frac{e_2}{\kappa}\right)^2\right]\right\} \quad (235)$$

The approximate equations are

$$\kappa = 0.00635 + 0.833\,\frac{(0.02081 - \mu)(\mu - 0.00635)}{0.01840 - \mu}, \qquad \mu \geqq 0.00635 \quad (236)$$

$$\epsilon = 0.00317 + 0.394\,\frac{(0.02163 - \mu)(\mu - 0.00635)}{0.01840 - \mu}, \qquad \mu \geqq 0.00635 \quad (237)$$

The solid curves e and e in Fig. 6 show the exact relations.

(f) Semiparabolic section, vertexes out. From Eq. (166),[2] for determining μ_m,

$$\sigma_{y1}e_1^2(2e_1 + 3e_2) = \sigma_{y2}e_2(3e_1^2 + 6e_1e_2 + 2e_2^2) \quad (238)$$

For $\sigma_{y1} = 0.00476$, $\sigma y_2 = 0.004$, this equation gives $e_1/\kappa = 0.619$ and $e_2/\kappa = 0.381$. Eq. (167)[2] reduces to

$$\mu_m = \frac{40}{19}\left\{\sigma_{y1}\left(\frac{e_1}{\kappa}\right)^3\left[3\left(\frac{e_1}{\kappa}\right) + 4\left(\frac{e_2}{\kappa}\right)\right] + \sigma_{y2}\left(\frac{e_2}{\kappa}\right)^2\left[6\left(\frac{e_1}{\kappa}\right)^2 + 12\left(\frac{e_1}{\kappa}\right)\left(\frac{e_2}{\kappa}\right) + 5\left(\frac{e_2}{\kappa}\right)^2\right]\right\} \quad (239)$$

The approximate equations are

$$\kappa = 0.00762 + 0.817\,\frac{(0.01690 - \mu)(\mu - 0.00762)}{0.01519 - \mu}, \qquad \mu \geqq 0.00762 \quad (240)$$

$$\epsilon = 0.00190 + 0.167\,\frac{(0.01897 - \mu)(\mu - 0.00762)}{0.01519 - \mu}, \qquad \mu \geqq 0.00762 \quad (241)$$

Case III

Although it will always be possible to get a satisfactory fit by retaining enough of the coefficients $p_1, p_2, \ldots$ and $q_1, q_2, \ldots$, the more of these coefficients that are retained, the more complicated the equations of the approximate curves will be. It is desirable, therefore, not to demand a better fit than is strictly necessary. For all but one of the sections under discussion p_1, p_2, q_1, and q_2 will be retained in the approximate equations for Case III. It does not follow that a better fit to the κ,μ-relation, for example, might not be obtained by retaining two other coefficients, rather than p_1 and p_2; but if others are used, μ enters to a higher power and simplicity is sacrified. Moreover, in general, it will not be easy to decide which two coefficients to pick for a best fit.

For Case III $e_1/\kappa = 1$ and $e_2/\kappa = 0$ as $\kappa \to \infty$.

Table 3, similar to Tables 1 and 2, applies to Case III.

(*1*) *Symmetrical Sections.*

(a) Idealized I-section. The approximate curves and the exact curves coincide up to $\mu_m = 0.00952$. Thereafter $\mu = \mu_m = 0.00952$ for all values of κ and ϵ. Curves a and a in Fig. 7 show the relations between κ and μ and between ϵ and μ.

(b) I-section. From Eq. (153)[2]

$$\mu_m = (18/7)\sigma_{y1} \quad (242)$$

After determining p_1, p_2, q_1, and q_2 from Eqs. (174), (175), and the equivalent equations for q_1 and q_2, the approximate equations, Eqs. (173) and (177), become

$$\kappa = [0.01224\mu/(0.01224 - \mu)](1 - 80.3\mu + 896\mu^2) \quad (243)$$

$$\epsilon = 49.9\mu^2(\mu - 0.01018)/(0.01224 - \mu) \quad (244)$$

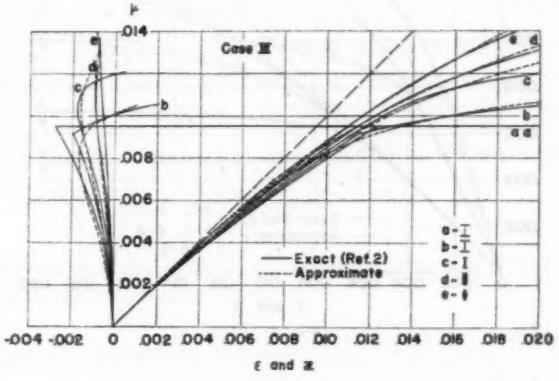

FIG. 7.

The solid curves b and b in Fig. 7 show the exact relations.

(c) Parabolic section, vertexes in. From Eq. (157)[2]

$$\mu_m = (10/3)\sigma_{y1} \quad (245)$$

The approximate equations become

$$\kappa = [0.01587\mu/(0.01587 - \mu)](1 - 50.0\mu - 227\mu^2) \quad (246)$$

$$\epsilon = 29.8\mu^2(\mu - 0.01310)/(0.01587 - \mu) \quad (247)$$

The solid curves c and c in Fig. 7 show the exact relations.

(d) Rectangular section. From Eq. (159)[2]

$$\mu_m = 6\sigma_{y1} \quad (248)$$

The approximate equations are

$$\kappa = [0.02857\mu/(0.02857 - \mu)](1 - 35.8\mu + 1{,}570\mu^2) \quad (249)$$

$$\epsilon = 27.5\mu^2(\mu - 0.01587)/(0.02857 - \mu) \quad (250)$$

The solid curves d and d in Fig. 7 show the exact relations.

(e) Parabolic section, vertexes out. From Eq. (161)[2]

$$\mu_m = 10\sigma_{y1} \tag{251}$$

The approximate equations are

$$\kappa = [0.04762\mu/(0.04762 - \mu)](1 - 14.0\mu + 635\mu^2) \tag{252}$$

$$\epsilon = 15.0\mu^2(\mu - 0.02407)/(0.04762 - \mu) \tag{253}$$

The solid curves e and e in Fig. 7 show the exact relations.

(2) *Unsymmetrical Sections.*

(a) Idealized I-section with one flange. The exact curves and the approximate curves, a and a in Fig. 8, are the same, and the same as for Case II, Fig. 6.

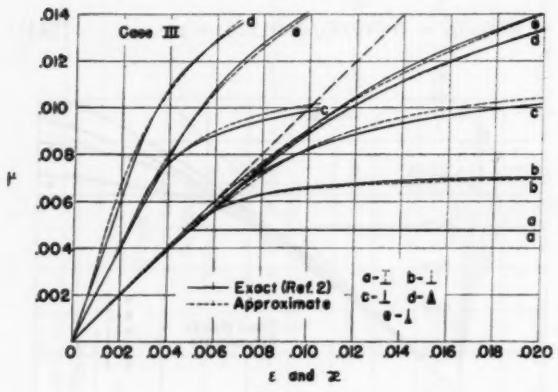

FIG. 8.

(b) T-section with infinitesimal web. The exact curves, b and b in Fig. 8, and the approximate curves are the same as for Case II, and the equations of the approximate curves are Eqs. (225).

(c) T-section. From Eq. (165)[2]

$$\mu_m = (12/5)\sigma_{y1} \tag{254}$$

The approximate equations are

$$\kappa = [0.01143\mu/(0.01143 - \mu)](1 - 82.5\mu + 266\mu^2) \tag{255}$$

$$\epsilon = [0.01143\mu/(0.01143 - \mu)](1/2 - 53.8\mu + 1{,}530\mu^2) \tag{256}$$

The solid curves c and c in Fig. 8 show the exact relations.

(d) Triangular section. From Eq. (169)[2]

$$\mu_m = 6\sigma_{y1} \tag{257}$$

The approximate equations are

$$\kappa = [0.02857\mu/(0.02857 - \mu)](1 - 48.0\mu + 2{,}450\mu^2) \tag{258}$$

$$\epsilon = [0.02857\mu/(0.02857 - \mu)](1/3 - 25.6\mu + 1{,}500\mu^2) \tag{259}$$

The solid curves d and d in Fig. 8 show the exact relations.

(e) Semiparabolic section, vertexes in. From Eq. (171)[2]

$$\mu_m = (20/3)\sigma_{y1} \tag{260}$$

The approximate equations are

$$\kappa = [0.03175\mu/(0.03175 - \mu)](1 - 41.7\mu + 1{,}960\mu^2) \tag{261}$$

$$\epsilon = [0.03175\mu/(0.03175 - \mu)](1/2 - 26.5\mu + 1{,}380\mu^2) \tag{262}$$

The solid curves e and e in Fig. 8 show the exact relations.

(f) Semiparabolic section, vertexes out. From Eq. (167)[2]

$$\mu_m = (120/19)\sigma_{y1} \tag{263}$$

The approximate equations are

$$\kappa = [0.03008\mu/(0.03008 - \mu)](1 - 42.1\mu + 2{,}060\mu^2) \tag{264}$$

$$\epsilon = [0.03008\mu/(0.03008 - \mu)](1/4 - 20.7\mu + 1{,}180\mu^2) \tag{265}$$

DEFLECTIONS

In reference 1 the deflections were considered for a beam the cross section of which was an idealized I-section. Three simple types of loading were assumed, and the three types of material were referred to as Cases I, II, and III. The solutions were exact and were of the few exact solutions practically possible in the plastic range. It is proposed here to obtain a few approximate solutions for a rectangular cross section. Any other of the cross sections that have been considered would involve merely different constants and could be handled in the same way. In each case it is necessary to solve Eq. (70a).

Beam Loaded at the Ends by Couples, Case III

For this simplest type of loading μ = constant and therefore κ = constant. With the origin of coordinates at one end of the beam, integration of Eq. (70a) gives

$$\phi = 1/2\kappa_c\xi(\xi - 1) \tag{266}$$

where κ_c is the constant value of κ and is given for the rectangular section, Case III, by Eq. (249) when the constant value of μ is inserted in that equation. The value of μ straining the extreme fibers on one side to the first yield strain reached, 0.006, is 0.00937, and the corresponding value of κ is 0.01118, Table 3. Therefore for this value of μ

$$\phi = 0.00559\xi(\xi - 1) \tag{267}$$

By the elastic theory, $\mu = \kappa$, and one would have, for $\mu = 0.00937$,

$$\phi = 0.00469\xi(\xi - 1)$$

The ratio of the two deflections is 559/469 = 1.19.

When the opposite extreme fibers are strained to the yield strain of 0.00714, $\mu = 0.01147$ and $\kappa = 0.01522$, Table 3. In this case

$$\phi = 0.00761\xi(\xi - 1) \tag{268}$$

By the elastic theory, for $\mu = 0.01147$,

$$\phi = 0.00573\xi(\xi - 1)$$

The ratio of the two deflections is $761/573 = 1.33$.

Simply Supported Beam; Centrally Loaded, Case II

With the origin of coordinates taken at one end of the beam

$$\mu = {}^1/_2\omega\xi, \quad 0 \leqq \xi \leqq {}^1/_2 \tag{83}$$

When this value of μ is substituted in Eqs. (172) and (173), with $\kappa_0 = \mu_0$ and $p_2 = p_3 = p_4 = \ldots = 0$, those equations may be written

$$\kappa = {}^1/_2\omega\xi, \quad 0 \leqq \xi \leqq \xi_0 \leqq {}^1/_2 \tag{269}$$

$$\kappa = \mu_0 - \frac{\mu_m - \mu_0}{\mu_m - {}^1/_2\omega\xi}\,[\mu_0(p_0 - p_1\mu_0) - {}^1/_2\omega(p_0 - 2p_1\mu_0)\xi - {}^1/_4\omega^2 p_1\xi^2], \quad \xi_0 \leqq \xi \leqq {}^1/_2 \tag{270}$$

where

$$\xi_0 = 2(\mu_0/\omega) \tag{271}$$

Substitution in Eq. (70a) and integration gives

$$\phi = [(1/12)\omega^2\xi^2 + C_0](\xi/\omega), \quad 0 \leqq \xi \leqq \xi_0 \leqq {}^1/_2 \tag{272}$$

$$\phi = {}^1/_2\mu_0\xi^2 + (2/\omega)(\mu_m - \mu_0)\{(p_0 - 2p_1\mu_0 + (3/2)p_1\mu_m)\mu_m\xi - {}^1/_4\omega(p_0 - 2p_1\mu_0 + p_1\mu_m)\xi^2 - (1/24)p_1\omega^2\xi^3 - (2/\omega)[(p_0 - p_1\mu_0)\mu_0 - (p_0 - 2p_1\mu_0)\mu_m - p_1\mu_m^2](\mu_m - {}^1/_2\omega\xi)[\log(\mu_m - {}^1/_2\omega\xi) - 1]\} + C_1(\xi/\omega) + (C_2/\omega^2), \quad \xi_0 \leqq \xi \leqq {}^1/_2 \tag{273}$$

The three constants of integration, C_0, C_1, and C_2, in Eqs. (272) and (273) may be determined from the conditions

$$\xi = \xi_0\text{: } \phi_{\xi=\xi_0-0} = \phi_{\xi=\xi_0+0}, \quad (d\phi/d\xi)_{\xi=\xi_0-0} = (d\phi/d\xi)_{\xi=\xi_0+0}$$
$$\xi = {}^1/_2\text{: } d\phi/d\xi = 0$$

When the values of μ_0, μ_m, p_0, and p_1 for the rectangular cross section (Table 2) are substituted in Eqs. (271) to (273) and when the constants of integration are determined, these equations reduce to

$$\phi = \frac{\xi}{\omega}\,[(1/12)\omega^2\xi^2 - 0.0369\omega^2 - 0.000607\omega + 0.0000746 + 0.0000208\log(0.05216 - \omega)], \quad 0 \leqq \xi \leqq \begin{cases} 0.016/\omega \\ {}^1/_2 \end{cases} \tag{274}$$

$$\phi = \frac{1}{\omega^2}\Big\{0.0491\omega^3\xi^3 - 0.000607\omega^2\xi(1 - \xi) - 0.0369\omega^3\xi + 0.00000242 - 0.00000805\omega\xi + 0.0000208[\omega\xi\log(0.05216 - \omega) + 2(0.01304 - {}^1/_2\omega\xi)\log(0.01304 - {}^1/_2\omega\xi)]\Big\}, \quad 0.016/\omega \leqq \xi \leqq {}^1/_2 \tag{275}$$

The bending moment is a maximum at the middle of the beam, and the value of μ that produces the first yield strain, 0.006, in extreme fibers is 0.01060, Table 2. The corresponding value of the load is determined from Eq. (83)

$$\omega = (2)(2)(0.01060) = 0.0424$$

When this value of ω is substituted in Eqs. (274) and (275), they become

$$\phi = 0.00353\xi(\xi^2 - 0.761), \quad 0 \leqq \xi \leqq 0.377 \tag{276}$$

$$\phi = 0.00208[\xi^3 + 0.291\xi^2 - 1.32\xi + 0.0860 + 0.236(0.615 - \xi)\log(0.615 - \xi)], \quad 0.377 \leqq \xi \leqq {}^1/_2 \tag{277}$$

In an elastic beam the same load produces deflections

$$\phi = 0.000883\xi(4\xi^2 - 3), \quad 0 \leqq \xi \leqq {}^1/_2$$

The ratio of the maximum deflections is $902/883 = 1.02$.

Simply Supported Beam, Uniformly Loaded, Case I

With the origin of coordinates taken at one end of the beam

$$\mu = {}^1/_2\omega\xi(1 - \xi) \tag{88}$$

When this value of μ is substituted in Eq. (178), that equation may be written

$$\kappa = {}^1/_4\omega[2\xi - (2 - p_1\omega)\xi^2 - 2p_1\omega\xi^3 + p_1\omega\xi^4] \quad (278)$$

With this value of κ, integration of Eq. (70a) gives, after determination of the constants of integration,

$$\phi = (\omega/240)\xi(\xi - 1)[2p_1\omega\xi^4 - 4p_1\omega\xi^3 - (10 - p_1\omega)\xi^2 + (10 + p_1\omega)\xi + 10 + p_1\omega] \quad (279)$$

The bending moment is a maximum at the middle of the beam, and the value of μ that produces the first yield strain, 0.006, in extreme fibers is 0.00871, Table 1. The corresponding value of the load is determined from Eq. (88),

$$\omega = (2)(2)(2)(0.00871) = 0.0697$$

When this value of ω and the value of $p_1 = 41.8$ from Table 1 are substituted in Eq. (279), that equation reduces to

$$\phi = 0.00169\xi(\xi - 1)(\xi^4 - 2\xi^3 - 1.22\xi^2 + 2.22\xi + 2.22) \quad (280)$$

In an elastic beam the same load produces deflections

$$\phi = -0.00290\xi(\xi - 1)(\xi^2 - \xi - 1)$$

The ratio of the maximum deflections is 1198/907 = 1.32.

Discussion

A few points are worth noting in considering the approximate solution that has been presented. First of all, Case I is the most nearly typical case that will be met with in practice, in the sense that few materials have stress-strain relations that can be approximated by straight lines, as in Cases II and III. The approximate Eqs. (173) and (177) boil down to simple polynomial expressions, like Eqs. (178) and (179), when, as in Case I, $2 \leqq n \leqq \infty$ in the Eq. (1)[2] for the stress-strain curve. The integrations for determining the deflections are in general simplest for $2 \leqq n < \infty$ because then $\epsilon_0 = \kappa_0 = \mu_0 = 0$ and $\mu_m = \infty$.

It was easy in this paper to tell how many of the coefficients $p_1, p_2, p_3, \ldots, q_1, q_2, q_3, \ldots$ to retain in the approximate equations because the exact κ,μ- and ϵ,μ-relations were known, and it was only necessary to compare the approximate curves with the exact curves. When exact curves are not available, however, as will usually be the case, perhaps the best way to find out whether more than one of the coefficients $p_1, p_2, p_3, \ldots$, for example, is required is to assume first that only one is required, determine that one, draw the resulting approximate κ,μ-curve, then assume two are required, determine them, and draw the corresponding κ,μ-curve. If, within the range of κ's it is desired to cover, the second curve does not depart from the first an unacceptable amount, the first approximation is adequate. In this connection it may be pointed out that in Cases II and III—that is, in cases in which $\mu_m < \infty$—the maximum possible error is limited. The error in μ for any κ and any ϵ cannot possibly be, and need never be, so great as $({}^1/_2) \times (\mu_m - \mu_0)$, for example, if, with only p_1 and q_1 retained, these coefficients are so determined that the exact and the approximate values of κ, ϵ, and μ coincide when $\mu = ({}^1/_2)(\mu_m + \mu_0)$.

The maximum deflections of the three beams of rectangular cross section investigated under the heading "Deflections" varied for the same yield strain first reached, 0.006, all the way from 2 to 32 per cent greater than the maximum elastic deflections. This large variation depends on two factors: the stress-strain characteristics of the material and the type of loading. A stress-strain diagram that is "soft" in the usable range, like the one of Case I, will result in greater deflections than a "stiff" one, like that of Case II. When the loading is such as to strain much of the beam heavily, as, for example, when terminal couples are applied, relatively larger deflections will result than when only a small portion of the beam is severely strained.

The sign of the bending moment did not change in the three beams under discussion. It must be remembered that μ is always positive, and if, as in an overhanging beam, the bending moment changes sign, appropriate changes in sign must be made in integrating Eq. (70a).

Finally, it should be noted that all three papers, references 1 and 2 and the present paper, have been based on materials, a large group,[3] the stress-strain curves of which can be expressed accurately by the equation[2]

$$e = \sigma + K\sigma^n \quad (1)$$

for strains as large as any that would be tolerated in a structural element subjected to flexure. Much in these papers, especially this one, does not depend on the particular stress-strain curve (1).

References

[1] Osgood, Wm. R., *Plastic Bending*, Journal of the Aeronautical Sciences, Vol. 11, No. 3, p. 213, July, 1944.

[2] Osgood Wm. R., *Plastic Bending—Further Considerations*, Journal of the Aeronautical Sciences, Vol. 12, No. 3, p. 253, July, 1945.

[3] Ramberg, W., and Osgood, Wm. R., *Description of Stress-Strain Curves by Three Parameters*, N.A.C.A. T.N. No. 902, Washington, D. C., July, 1943.

Graphical Analysis of Performance of Hydraulic Shock Absorbers in Aircraft Landing Gears

ALEXANDER J. YORGIADIS*
Sonntag Scientific Corporation

SUMMARY

The performance of simple hydraulic shock absorbers has been obtained by the graphical method of analysis. Various elements and features of shock absorbers are presented and analyzed separately, including the variable orifice type of control. Numerical examples are used to illustrate the effects of certain variables.

INTRODUCTION

THE ABSORPTION OF KINETIC ENERGY of moving bodies ranks among the important engineering problems. The deceleration of a machine in motion is often accompanied by shock loads that exceed the normal operating loads of the machine, so that the design of the machine is governed by the magnitude of these shock loads. Shock-absorbing devices are used in conjunction with such machines in order to minimize these shock loads. One important use for such devices is in absorbing the vertical kinetic energy of airplanes at the instant of landing.

For the earlier airplanes, which were lighter and flew at slow speeds, the rubber tires on the landing wheels had sufficient shock-absorbing capacity. With the advent of heavier airplanes, faster speeds, and greater wing loadings, more efficient shock absorbers had to be developed. Most present-day aircraft are equipped with hydraulic shock absorbers of some kind, which are interposed between the landing wheel and the airplane itself. One simple type of such absorber is shown in Fig. 1. It consists of a hollow piston A rigidly attached to the airplane and an oil-filled cylinder B attached to the wheel. The piston head has an orifice connecting cylinder volume B to piston volume A. During landing, the shock force transmitted through the wheel builds up oil pressure in the cylinder; this causes oil to flow past the orifice into volume A, allowing relative motion of piston and cylinder, and absorbing the vertical kinetic energy of the airplane mass.

MATHEMATICAL ANALYSIS OF BASIC SYSTEM WITH CONSTANT ORIFICE AND NO TIRE

The system of Fig. 1 is shown schematically in Fig. 2, with the hydraulic shock absorber as the only yielding member. W is the portion of the airplane weight that is supported by the particular strut at the time of landing. The orifice is assumed to be of the ideal sharp-edge type with turbulent flow past it. Theoretically, the pressure drop across the orifice is therefore proportional to the velocity squared according to the relationship:

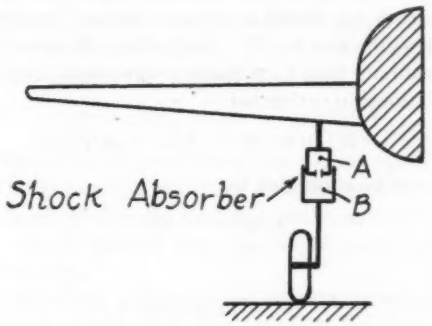

FIG. 1. Shock absorber in aircraft landing gear.

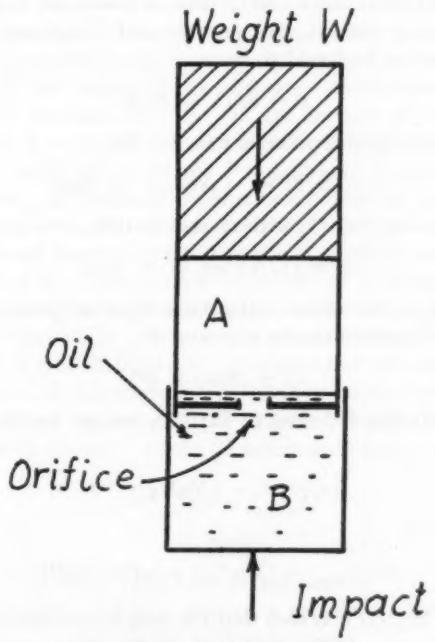

FIG. 2. Shock absorber system.

Received September 12, 1944. Revised and resubmitted May 4, 1945.

* Design Engineer.

$$p_B - p_A = k\rho v^2 F^2/2f^2 \quad (1)$$

where:

- v = velocity of piston relative to cylinder (also velocity of W after impact), in. per sec.
- p_B = pressure in cylinder volume above atmospheric, lbs. per sq.in.
- p_A = pressure in piston volume above atmospheric, lbs. per sq.in.
- F = piston area, sq.in.
- f = orifice area, sq.in.
- ρ = mass density of absorber fluid, lbs.-sec.^{2}-in.$^{-4}$
- k = orifice coefficient (assumed to be equal to one in this analysis)

Actually, the orifice characteristics may differ appreciably from the above idealized relationship, and for practical problems actual experimental curves should be obtained.

Two significant forces in such a system are the inertia force of the decelerating weight W and that due to the oil pressure p_B, which is assumed to act vertically, in opposite direction to W. Neglecting all other effects and assuming that p_A remains atmospheric, the following relationship is derived:

$$-(W/g)(dv/dt) = Fp_B = \rho v^2 F^3/2f^2 \quad (2)$$

which can be simplified to:

$$dv/dt = -Nv^2 \quad (3)$$

where

$$N = \rho F^3 g/2f^2 W \quad (3a)$$

is a constant for a given system. If v_0 is the vertical velocity of contact and if time is measured from the instant of contact, the velocity v of W at any other instant can be found to be:

$$v = v_0/(1 + Nv_0 t) \quad (4)$$

Substituting this value of v in Eq. (3)

$$a = dv/dt = -Nv_0^2/(1 + Nv_0 t)^2 \quad (5)$$

Integrating Eq. (4) with respect to time,

$$y = (1/N)\log_e(1 + Nv_0 t) \quad (6)$$

where y is the stroke of the shock absorber piston. The above equation can be rearranged

$$(1 + Nv_0 t) = e^{yN} \quad (6a)$$

Substituting Eq. (6a) in Eq. (5), we get for the load factor

$$(a/g) = -(Nv_0^2/g)e^{-2Ny} \quad (7)$$

at $t = 0$,

$$(a/g)_{max.} = (Nv_0^2/g) = \rho F^3 v_0^2/2f^2 W \quad (8)$$

From Eq. (7) it is seen that the load factor decreases as y increases. Defining y_t as the value of y at which the acceleration reaches $1/e$ of the maximum value, we get:

$$y_t = 1/2N = f^2 W/\rho F^3 g \quad (9)$$

and

$$(a/g) = -(a/g)_{max.} e^{-y/y_t} \quad (10)$$

which is the expression representing the load factor in terms of stroke y.

As an example, assume a shock absorber supporting a weight W of 10,000 lbs.; orifice area of absorber, f = 0.10 sq.in.; piston area of absorber, F = 10 sq.in.; density of oil, ρ = 0.00008 lb.-sec.^{2}-in.$^{-4}$; and velocity of contact, 136 in. per sec. These values substituted in Eq. (8) and (9) yield

$$y_t = 3.24 \text{ in.}, \quad (a/g)_{max.} = 7.4$$

so that the load factor of Eq. (10) becomes:

$$(a/g) = 7.4e^{-y/3.24} \quad (11)$$

In analyzing the performance of actual shock absorbers, there are many other effects that have to be considered. Usually, volume A is under air pressure and, as oil flows through the orifice in this space, the air pressure increases, slowing the flow of oil somewhat. Frictional forces between cylinder and piston may be important. In the preceding analysis the mass of the airplane was assumed to be rigid, while actually the structure deflects under load. Furthermore, the elasticity and energy-absorbing qualities of the tire itself, as well as the weight of the wheel assembly, should be taken into consideration in an analysis of actual systems. Some shock absorbers have orifices whose effective area varies along the stroke. The outline of a rather lengthy mathematical solution taking some of these factors into consideration has recently been published.[1] It appears to be a valuable contribution to the field in that it makes use of the tools of advanced mathematics toward the solution of the problem. However, it still involves simplifying approximations in order to make the solution practically possible.

Graphical Analysis

Recently, a graphical method has been developed for solving problems involving forces and motions in mechanical, hydraulic, and other elastic systems in a transient state. This graphical method has been successfully used to solve complex problems that could not be conveniently solved by mathematics alone. The shock absorber systems just described are only special cases of the general mechanical-hydraulic system, the graphical analysis of which has been studied by De-Juhasz[2] and Bergeron[3], who present a complete derivation of the theory involved. A concise explanation of the method has recently been published.[4] Only a brief outline of the method is offered in this paper, but for more complete explanations the reader is referred to the above-mentioned publications.

The graphical analysis is based on the fact that the relationships between the various variables, which are complex if taken over a relatively long interval of time, are nearly linear functions over time intervals that are extremely short. The complete phenomenon to be studied is therefore subdivided into successive small intervals, denoted Δt time intervals. This interval is chosen small enough so that linearity can be assumed and yet large enough to cover the complete phenomenon in a convenient number of Δt intervals. The graphical analysis operates with two coordinate systems, the time-location or t-x chart, and the force-velocity or P-v chart. The history diagram of force, velocity, or acceleration of any point in the system can be drawn from data made available by these two charts. Other charts of displacement, kinetic energy, etc., at any instant can be calculated from these same data.

Each of the components of the mechanical system is represented on the P-v chart by a line called "directrix" whose slope is termed its "surge constant." The value of the surge constant depends upon the nature of the component; its physical properties, such as its mass, elasticity, etc.; and the chosen Δt interval. The concept of the Δt interval is that it represents the time necessary for a disturbance to traverse a given part of the system.

The system solved mathematically in Eq. (11) is analyzed graphically in Fig. 3. The t-x diagram is shown in Fig. 3a. The time of contact is taken at $t = 0$, and the disturbance thus started is assumed to travel back and forth at a virtual velocity so that it takes one Δt interval for one traversal from the orifice to the weight W. The value of Δt is arbitrarily chosen at 0.01 sec. This separates the t-x chart into triangular areas marked 1, 2, 3, etc. Fig. 3b is the force-velocity chart. As weight W is subjected to an unbalanced force P for a time element Δt, its velocity is changed by Δv according to the relationship:

$$(W/g)(\Delta v/\Delta t) = \pm \Delta P \qquad (12)$$

where g is the acceleration due to gravity. The rate of change of force relative to velocity representing the surge constant for W can be obtained by dividing Eq. (6) by Δv,

$$\Delta P/\Delta v = \tan \gamma = \pm W/g\Delta t \qquad (13)$$

Substituting the actual values yields $\tan \gamma = 2{,}600$, which represents the load in pounds of unbalanced force which, if applied to W for a period of 0.01 sec., will change its velocity by 1 in. per sec.

Eq. (1), representing the flow past an orifice in terms of the pressure differential, is used to characterize the orifice on the $P-v$ diagram. The resulting curve is a parabola, termed the "efflux parabola,"

$$\Delta P = F(p_B - p_A) = \rho v^2 F^3/2f^2 \qquad (14)$$

Using the actual values of the particular example, $\Delta P = 4v^2$. The pressure in chamber A is assumed to remain atmospheric so that the vertex of the parabola is at the origin. In the general case, the vertex of the parabola is at $P = Fp_A$.

The following procedure is used to construct the $P-v$ chart of Fig. 3b. The mass W is subjected at one end to the conditions of forces and motions characterized by the flow past the orifice—that is, the efflux parabola. The other end of the system is not subjected to accelerating forces if the lift of the wings is equal to the weight of the airplane—and is characterized by the line $P = 0$. At the instant of contact ($t = 0$), $v = v_0$ and $P = 0$, which is the starting point in the construction of the P-v diagram. Points 1, 2, 3, 4, etc., are obtained by alternately drawing positive and negative directrices between the two above-mentioned lines—namely, the efflux parabola and the line $P = 0$. These points represent the state of force and velocity in regions similarly numbered on the t-x chart—that is, in this case, the state of mass W after 1, 2, 3, 4, etc., Δt intervals. The stroke of the absorber piston is its displacement, y, relative to the cylinder as measured from the initial extended position at the instant of contact. It can be calculated from:

$$y = \sum_1^n \Delta y = \sum_1^n v_m \Delta t \qquad (15)$$

where

y = stroke in in. after $n\,\Delta t$ intervals
v_m = mean velocity during a certain Δt interval, taken as the arithmetic mean

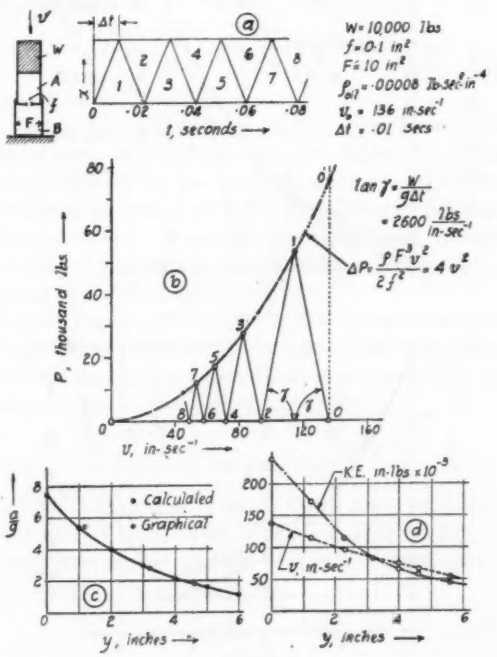

FIG. 3. Graphical analysis of basic shock absorber system with constant orifice and no tire. (a) t-x diagram. (b) P-v diagram. (c) Graphical and calculated data of load factors versus piston stroke. (d) Variation of kinetic energy and velocity of W with stroke.

i.e.,

$$y = \left(\frac{v_0 + v_1}{2} + \frac{v_1 + v_2}{2} + \ldots \frac{v_{n-1} + v_n}{2}\right) \Delta t \quad (16)$$

The vertical kinetic energy of weight W at any instant can be calculated from:

$$\text{K.E.} = Wv^2/2g \quad (17)$$

The data of Fig. 3b and relationships (16) and (17) are used to prepare Table 1.

TABLE 1

Time t, Sec.	Velocity v, In. per Sec.	Mean Velocity, v_m In. per Sec.	Δy	Stroke y, In.	Kinetic Energy, In.Lbs.
0	136		0	0	240,000
0.01	115	125.5	1.255	1.255	171,000
0.02	94	104.5	1.045	2.300	114,000
0.03	83	88.5	0.885	3.185	89,500
0.04	72	77.5	0.775	3.960	67,000
0.05	65	68.5	0.685	4.645	54,700
0.06	58	61.5	0.615	5.260	43,500
0.07	53	55.5	0.555	5.815	36,400
0.08	49	51	0.51	6.325	33,600

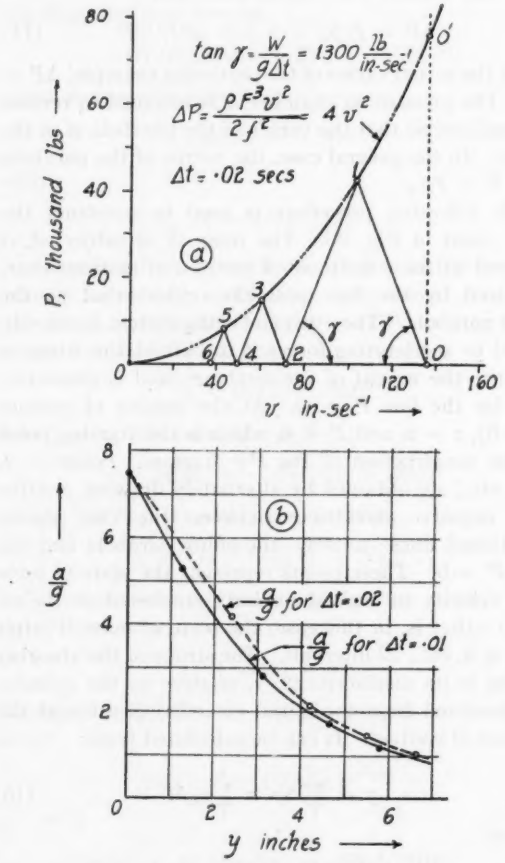

FIG. 4. Effect of Δt interval on the results of the graphical analysis. (a) P-v diagram with Δt = 0.02 sec. (b) Load factor versus stroke curves for Δt = 0.01 and 0.02 sec.

Fig. 3c represents both graphical and calculated values of the load factor a/g or P/W, as a function of the stroke y. The graphical values are those of Fig. 3b and Table 1, while the calculated values were obtained from Eq. (11). There is close agreement between the two independently obtained results. Fig. 3d shows the variation of velocity and kinetic energy of mass W.

EFFECT OF INCREASING Δt INTERVAL

The analysis of Fig. 3 was made with the Δt interval arbitrarily assumed to be 0.01 sec. In Fig. 4 the same system is analyzed by choosing 0.02 sec. as the Δt interval. The larger interval is expected to yield a result less accurate than the former while saving some labor. Fig. 4a is the new P-v diagram, which differs from Fig. 3a in that the slope of the directix is now half of its original value since Δt occurs in the denominator of the expression for tan γ. The load factor is plotted on Fig. 4b and the result is compared with that obtained in Fig. 3. The error does not exceed 10 per cent anywhere and is more pronounced in the early period, reaching asymptotically the correct value as the stroke advances.

Since the result with Δt of 0.01 sec. was near the exact calculated value, there is no necessity to analyze the system with an interval smaller than 0.01 sec., because the added labor would not be justified.

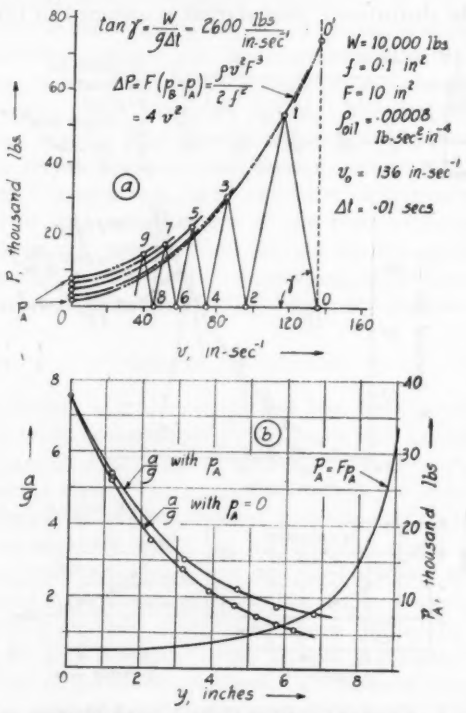

FIG. 5. Graphical analysis of shock absorber system considering the increase of air pressure in chamber A. (a) P-v diagram. (b) Air pressure in chamber A, and load factors plotted versus piston stroke.

Effect of Air Pressure in Discharge Chamber A

In Fig. 5, a graphical study is made of the system of Fig. 3, considering this time the effect of the increase in pressure in discharge chamber A. The effect of this increase on the P-v diagram is to raise the efflux parabola so that its vertex is no longer at $P = 0$ but is at $P = P_A = Fp_A$.

The system when fully extended ($y = 0$) has an air volume of 100 cu.in. in chamber A, at a pressure of 200 lbs. per sq.in. The pressure in A, corresponding to other values of y, can be calculated from the known area of the piston and the approximate relationship for air:

$$p_A V_A^{1.2} = \text{constant} \tag{18}$$

This result is plotted in one of the curves of Fig. 5b in terms of the total force, P_A, versus stroke.

The P-v diagram cannot be obtained directly as was done in Figs. 3 and 4, since the location of the vertex of the parabola is not known in advance. The method of successive approximations is therefore resorted to. In the first approximation the value of P_A determining the position of the efflux parabola is assumed to be that existing at the beginning of the particular interval under study. Consider that the analysis has reached the end of the rth interval, so that v_r and y_r are known. The value of the velocity at the end of the $(r + 1)$th interval is obtained at the intersection of the directrix with the assumed parabola. The piston stroke after the particular Δt interval is obtained from:

$$y_{r+1} = y_r + \Delta y = y_r + \left(\frac{v_r + v_{r+1}}{2}\right)\Delta t \tag{19}$$

This value of y_{r+1} gives a corrected value for P_A, the vertex of the new parabola. A new value of v_{r+1} can then be obtained and the process repeated. However, the accuracy at this stage is usually sufficient for engineering purposes. A second approximation for the case of Fig. 5 produced no noticeable improvement in the result of the first approximation.

The load factor plotted on Fig. 5b is compared with the result of Fig. 3, where p_A was zero. The air pressure reduces the rapid drop in load factor as the stroke advances and, hence, has a desirable effect.

Effect of Friction

The effect of friction between shock absorber piston and cylinder is considered in the example of Fig. 6. The system is similar to that of Fig. 3, except that a friction force exists expressed by:

$$P_f = -v \tan \gamma - R_2 \tag{20}$$

where $v \tan \gamma$ is the viscous component proportional to the relative velocity between piston and cylinder and where R_2 is the Coulomb friction component which is independent of velocity.

The effect of this friction is similar to a hypothetical negative force acting on the free end of W, which end is characterized by $-P_f$ as shown in Fig. 6b.

The efflux parabola and the directrix of W remain the same as in Fig. 3. Fig. 6b is the P-v diagram, and in Fig. 6c is plotted the load factor versus stroke for the cases with and without friction.

Variable Orifice Type of Shock Absorber

For practical reasons it is desirable to absorb the kinetic energy of W with as small a peak value of shock force as possible for a given total stroke of piston. An ideal shock absorber should, therefore, decelerate W at a constant rate throughout the stroke. The absorbers of Figs. 3 and 5 do not satisfy this condition as seen by their load factor curves.

One of the ways of improving the characteristics of these absorbers is by using a so-called variable orifice—that is, an orifice system whose effective area changes as the stroke advances. Assuming the absorber system of Fig. 5, it is proposed to design a variable orifice system that will absorb the kinetic energy with a uniform load factor throughout the stroke.

Given the contact velocity $v_0 = 136$ in. per sec. and the total stroke $y_T = 9$ in., the load factor under these conditions is given by:

$$a/g = v_0^2/2gy_T = 2.66 \tag{21}$$

The P-v diagram for this case is shown in Fig. 7a. Different efflux parabolas are needed for each Δt inter-

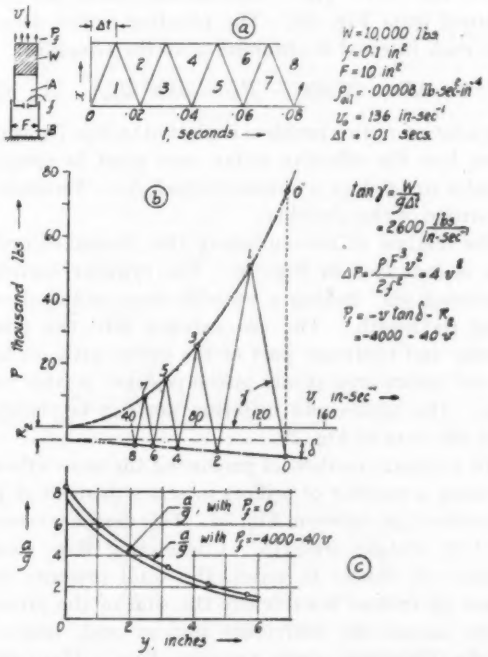

Fig. 6. Effect of friction analyzed graphically. (a) t-x diagram. (b) P-v diagram. (c) Load factor versus stroke.

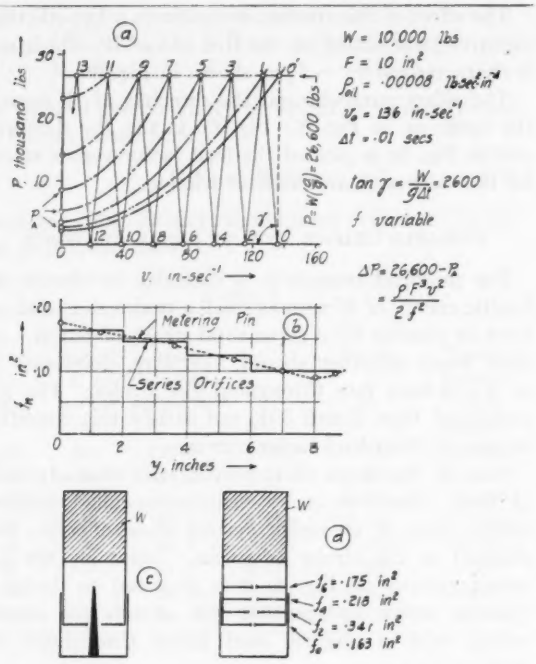

FIG. 7. Design of variable orifice type of shock absorber for constant deceleration of weight W. (a) P-v diagram. (b) Orifice area versus stroke. (c) Metering pin type of absorber. (d) Series orifice type of absorber.

val, since both the area f_n of the orifice and the vertex P_A change. The value of y at each instant is calculated from the known initial velocity and the deceleration of Eq. (21). The corresponding values of P_A are obtained from Fig. 5b. The effective orifice area f_n after each interval is obtained from the equation:

$$\Delta P = 26{,}600 - P_A = \rho F^3 v^2 / 2 f_n^2 \qquad (22)$$

The solution of this problem is plotted in Fig. 7b, which shows how the effective orifice area must be changed in order to produce a constant shock force throughout the stroke of the absorber.

One method of accomplishing this change of orifice area is indicated in Fig. 7c. The cylinder carries a "metering pin" having a variable cross-sectional area along its length. The pin extends into the piston volume and obstructs part of the orifice area, so that the net orifice area at any piston position is also variable. The orifice and metering pin can be designed from the data of Fig. 7b.

An alternate method of producing the same effect is by using a number of orifices in series (instead of just one orifice), as shown in Fig. 7d. This device is covered by U.S. Patent 2048418. Considering flow past a number of orifices in series, the total pressure drop across all orifices is evidently the sum of the pressure drops across the individual orifices and, hence, is greater than any single pressure drop. The orifices in series therefore behave similar to a single orifice that has a certain "effective" area smaller than any of the individual orifices. The following mathematical expression is derived from Eq. (1):

$$\frac{1}{f_n^2} = \frac{1}{f_1^2} + \frac{1}{f_2^2} + \frac{1}{f_3^2} \qquad (23)$$

where f_n = effective area of given number of orifices in series (f_1, f_2, f_3 are individual orifice areas).

Consider now the absorber similar to that of Fig. 7d. The piston volume is separated into many compartments which are joined by orifices. At the beginning of the stroke the liquid has to flow past the first orifice only, so that its area represents the effective orifice area of the system. After the volume between the first and second orifices has been filled with oil, the orifice area of the system becomes that of the resultant of the two orifices in series and, hence, smaller than it was previously. As each successive space is filled, the liquid has to flow past more and more orifices, rendering the effective orifice area of the system smaller and smaller.

The function "effective orifice area" versus stroke of such a system is discontinuous at the values of stroke where orifices are located. The curve of Fig. 7b is approximated by a stepped function, having discontinuities 2 in. apart, where orifices are located. Eq. (23) is used to calculate the required orifice areas f_0, f_2, f_4, f_6 representing orifices 0, 2, 4, 6 in., respectively, along the stroke.

Basic Shock Absorber with Elastic Spring (Tire)

In the preceding analyses it was assumed that the shock absorber was the only yielding member in the system. Absorbing systems of aircraft landing gears also include the rubber tire on the landing wheel. The tire possesses both elasticity and energy-absorbing qualities that are significant. In the cases to follow, the elasticity of the rubber tire is its only property taken in consideration. Under such limitations, the tire acts as a mechanical spring and is characterized by its "spring constant" C, the number of units of force required to cause unit deflection. The surge constant of this element on the P-v diagram is expressed by:

$$\tan \pm \alpha = \Delta P / v = \pm C \Delta t \qquad (24)$$

The analysis of a shock-absorber system including a tire is presented in Fig. 8. The weight W carried by the absorber is taken at 10,000 lbs.; the orifice area (fixed), 0.06 sq.in.; piston area, 10 sq.in.; oil density, 0.00008 lb.-sec.^{2}-in.$^{-4}$; spring rate of the tire, C = 5,000 lbs. per in.; initial contact velocity, v_0 = 136 in. per sec.; Δt interval chosen at 0.02 sec.

The pressure at A is assumed to remain atmospheric and friction is neglected. Fig. 8a is the t-x diagram, which has three reference points—namely, the fixed end of the spring (tire) in contact with the ground, the free end of the spring, and the weight W. Dis-

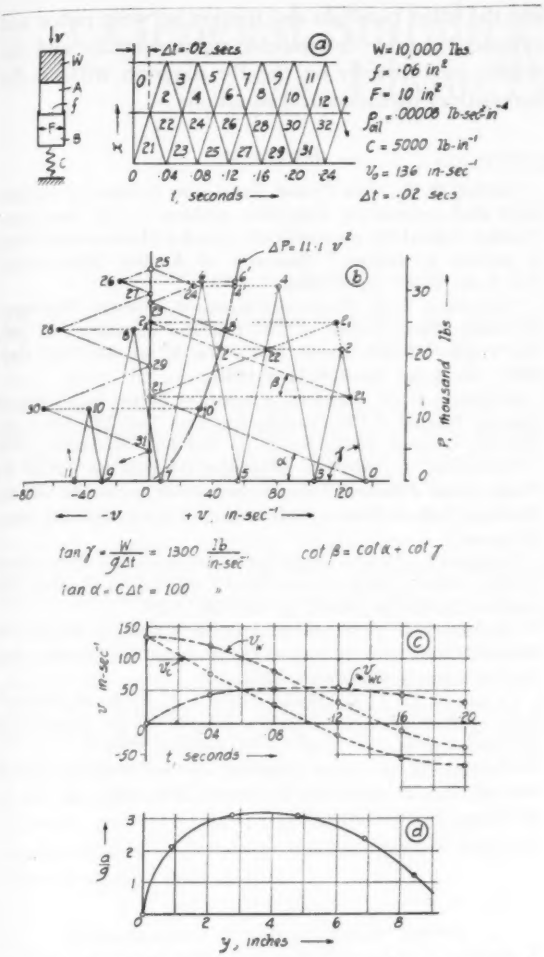
Δt = .02 secs
W = 10,000 lbs
f = .06 in²
F = 10 in²
C = 5000 lb-in⁻¹
Δt = .02 secs
t, seconds
P, thousand lbs
ΔP = 11·1 v²
tan γ = W/gΔt = 1300 lb/in-sec
tan α = CΔt = 100
cot β = cot α + cot γ
v in-sec⁻¹
y, inches

FIG. 8. Graphical analysis of shock absorber system with elastic spring (tire) and constant orifice. (a) t-x diagram. (b) P-v diagram. (c) History diagrams of velocities v_W, velocity of W, v_C, velocity of absorber cylinder, and v_{WC}, velocity of piston relative to cylinder. (d) Load factor versus stroke.

turbances are assumed to travel back and forth between these limits, taking one Δt interval for one traversal of an element, thus separating the plane in triangular areas. Numbers 3, 5, 7, etc., identify the free end of the weight and are on the $P = 0$ line. Numbers 21, 23, 25, 27, etc., refer to the end of the tire in contact with the ground, for which the velocity is zero. Points 2, 4, 6, etc., represent the end of weight W which is subjected to the hydraulic pressure, and points 22, 24, 26, etc., identify the states of tire axle (or shock absorber cylinder). Fig. 8b is the P-v diagram. Values of tan α and tan γ, as well as the equation for the efflux parabola, were obtained from the known values of the components and are indicated on the diagrams.

The construction of the P-v diagram is based on the relationship

$$v_W = v_C + v_{WC} \tag{25}$$

where:

v_W = velocity of W at any instant, in. per sec.
v_C = velocity of tire axle at any instant, in. per sec.
v_{WC} = velocity of absorber piston relative to cylinder, in. per sec.

The initial state of the system is at point 0 ($P = 0$, $v = v_0$). As the tire hits the ground, its state changes along the $-\alpha$ directrix, and, since it comes to rest at the point of contact with the ground, the next state of the tire is found to be point 21. This disturbance is reflected to the free end of the tire along the $+\alpha$ directrix. Had there been no absorber between tire and weight W, the state at the next Δt interval would be the point 2_1, which is the intersection of the $+\alpha$ directrix from 21 and the $-\gamma$ directrix from point 0. However, v_W is larger than v_C because of the flow past the orifice. The geometrical construction used to locate point 2 is shown on Fig. 8b. Constant P lines are drawn from 2_1 to 2_2 and 21 to 21_1. Points 2_2 and 21_1 are joined to meet the parabola at 2′. A constant P line is drawn from this point to meet the $+\alpha$ directrix at 22 and the $-\gamma$ directrix at 2. Point 2 is the state of mass W at $t = 2\Delta t$. Point 22 is the state of the tire axle (or of the absorber cylinder) at this same instant. The geometric construction is such that Eq. (25) is satisfied. It should be noted that line 2_2 to 21_1 makes an angle β with the v-axis so that

$$\cot \beta = \cot \alpha + \cot \gamma \tag{26}$$

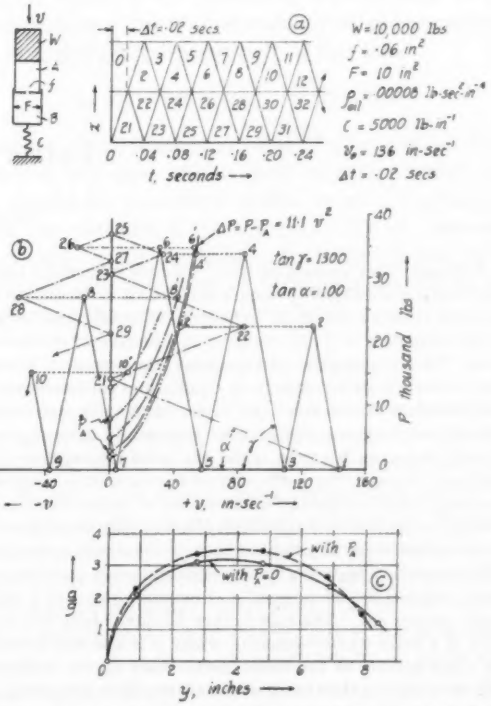

FIG. 9. Graphical analysis of system of Fig. 8, including effect of increase of air pressure in chamber A. (a) t-x diagram. (b) P-v diagram. (c) Load factor versus stroke.

Continuing the construction, $\alpha + \gamma$ directrix is drawn from 2 to meet the $P = 0$ line at 3. From 22 the $-\alpha$ directrix is drawn to meet the $v = 0$ line at 23. From this point on the same process is repeated to get points 4 and 24, as was used to get points 2 and 22. The remainder of the construction is shown in Fig. 8b. Fig. 8c is a history diagram of the various velocities, while the load factor is plotted in Fig. 8d.

Effect of Air Pressure in Discharge Chamber on the Performance of Absorber with Tire

Fig. 9 is an analysis of the effect of air pressure in chamber A on the performance of the shock-absorber system of Fig. 8. P_A increases with the stroke y according to the data of Fig. 5b. Fig. 9a, the t-x diagram, is similar to Fig. 8a. Fig. 9b is the P-v diagram, which differs from Fig. 8b in that P_A, the vertex of the efflux parabola, is raised to satisfy the data of Fig. 5b. The method of successive approximations is used to construct the P-v diagram, and the points are obtained as in Fig. 8b. Fig. 9c is a plot of the load factor versus stroke for cases with and without pressure at A.

The number of cases treated in this report are relatively few and have been presented primarily with the view of illustrating the method. The basic analysis can be expanded to take account of other factors, the accuracy of the result being increased at the expense of added labor. Some of the component characteristics, like the efflux parabola and friction between piston and cylinder, can be determined experimentally and the results used directly on the P-v diagram without the necessity of mathematical equations.

References

[1] Keller, E. G., *Some Present Non-Linear Problems of the Electrical and Aeronautical Industries*, problem 7, "A Non-Linear Problem of two Oleo-pneumatically Coupled Masses one of which is Subject to Impact," Quarterly of Applied Mathematics, Vol. 2, pp. 82–86, April, 1944.

[2] DeJuhasz, K. J., *Graphical Analysis of Transient Phenomena in Linear Flow*, Journal of The Franklin Institute, Vol. 223, No. 4, pp. 463–493, April, 1937; No. 5, pp. 643–654, May, 1937; No. 6, pp. 751–778, June, 1937.

DeJuhasz, K. J., *Graphical Analysis of Surges in Mechanical Springs*, Journal of The Franklin Institute, Vol. 226, No. 4, pp. 505–526, October, 1938; No. 5, pp. 631–644, November, 1938.

[3] Bergeron, L., *Méthode Graphique Générale de Calcul des Propagations d'Ondes Planes*, Memoires de la Société des Ingenieurs Civils de France, Bulletin July-August, 1937 (93 pages, 43 figures).

Bergeron, L., *Méthode Graphique de Resolutions des Propagations d'Ondes Planes*, Fifth International Congress for Applied Mechanics, Cambridge, Mass., pp. 694–699, 1938.

[4] DeJuhasz, K. J., *Graphical Analysis of Delay of Response in Airspeed Indicators*, Journal of the Aeronautical Sciences, Vol. 10, No. 3, pp. 91–97, March, 1943.

DeJuhasz, K. J., *Graphical Analysis of Response Characteristics of Rate-of-Climb Indicators*, Journal of the Aeronautical Sciences, Vol. 11, No. 1, pp. 48–54, January, 1944.

[5] Semion, W. A., *Shock Absorbing Systems*, Aviation, Part I, Vol. 39, No. 12, pp. 80–81, December, 1940; Part II, Vol. 40, No. 3, pp. 54–55, March, 1941.

Letter to the Editor

(*Continued from page 407*)

Professor Niles' contention that "a simple tube under torsional load is not statically determinate and cannot be treated as one if accurate results are desired" appears to contradict the derivation of the formula $q = T/2A$, as given in a textbook* of which Professor Niles is coauthor. In the book, the argument leading to this formula is based entirely on equilibrium considerations, and the structure thus treated (or, more exactly, its stress system) should therefore be considered as a statically determinate one. To this writer, such a tube, under the usual assumptions (elastic isotropic material, thin walls with no discontinuities in curvature, no longitudinal restraints, conservation of initial cross-sectional shape), presents a typical example of a statically determinate shell in the sense of the membrane theory. Its stress system is fully defined without resorting to any principle other than that of the static equilibrium of internal and external forces at a conveniently chosen cut. The case is then fundamentally the same as that of a beam on two supports, where it is also well known that an exact picture of the stress distribution cannot be found by statics alone; in the theory of structures, such a beam is, nevertheless, considered as statically determinate.

Finally, the writer is accused of treating the Maxwell-Mohr method as a less respectable substitute for the method of "least work." It would seem that a more careful reading of the paper under discussion should help to dissipate this misunderstanding. In the second paragraph of the first column on page 104, it is stated that the stresses in redundant members can be determined by either method and that the author considers both methods as being practically equivalent. In column 2 of the same page, a suggestion is made as to how the problem may be solved by considering the continuity at the cuts; this means that the Maxwell-Mohr method has actually been put forward. Fearing, however, that the reader may be unfamiliar with the expressions for the coefficients (or "quantities of displacement") to be introduced into the equations of continuity, the writer thought it more expedient to have these expressions derived by means of "least work," showing at the same time that both methods yield identical results. He thinks it rather strange to be blamed for putting to work a method so strongly advocated by Professor Niles.

* Niles, A. S., and Newell, J. S., *Airplane Structures*, 3rd Ed., Vol. II, p. 185; John Wiley & Sons, New York, 1943.

Eryk Kosko
Assistant Professor of Aircraft Structures
École Polytechnique, Montreal

A General Stability Index for Flow Near Plane Boundaries

HUNTER ROUSE*
University of Iowa

Introduction

Since the time of Osborne Reynolds, the stability problem in fluid mechanics has consistently withstood every effort toward a general solution. The mathematical method of superposing a periodic disturbance upon a parallel flow has, to be sure, yielded qualitative results in specific cases, and experimental studies have supplied quantitative information in terms of characteristic Reynolds Numbers wherever required. However, a general criterion for stability is not yet at hand (as evidenced by the wide numerical range of critical Reynolds Numbers even for related types of flow), nor have existing analyses provided a physical picture of the controlling factors which is within the grasp of the average engineer. The stability index proposed in this paper does not have the justification of rigorous mathematical derivation, nor has it evolved from extensive laboratory study. Yet it does stem from logical and almost self-evident dimensional and physical concepts, and its general significance is indicated by experimental data already at hand for several basically different types of fluid motion.

Formulation of the Stability Index

A popular belief among engineers is that turbulence will develop at any point in laminar flow at which the velocity gradient becomes sufficiently high—this despite the fact that the gradient is invariably highest at the boundary itself and becomes still higher in the stable laminar sublayer between the boundary and the turbulent zone.

Quite inconsistently, however, disturbances in high-velocity zones far from the boundary are often blamed for the onset of turbulence, even though the velocity gradient is lowest in that region. Although the velocity gradient is assuredly a factor that tends toward instability fully as much as the viscosity of the fluid tends toward stability, the far greater effect of the boundary proximity is seldom given credit. As a matter of fact, unless the normal distance y from the boundary is considered as essential a variable as the velocity gradient dv/dy and the kinematic viscosity ν, the formulation of a general criterion of stability will be out of the question. If, however, these three variables are assumed to be the essential ones involved in the basic stability problem they may be related in the general functional form

$$\varphi(y, dv/dy, \nu) = 0$$

for which only one dimensionless combination is obtainable:

$$\varphi'[y^2(dv/dy)/\nu] = 0$$

Since dv/dy is invariably a maximum along a plane boundary when y is zero and since, with increasing values of y, the gradient decreases more and more rapidly, in any case of laminar motion the product $y^2(dv/dy)$—and hence its ratio to ν—should attain a maximum value at some point within the flow. From the structure of the dimensionless ratio of the three variables, it is evident that this optimum point represents the zone of minimum stability for the flow in question. Since, however, only one dimensionless parameter is involved in the functional relationship, it must necessarily be a constant for the conditions assumed. In other words, if the parameter is designated as the stability index χ, the limit of stability should correspond to a constant critical magnitude of this index:

$$\chi_{cr} = [y^2(dv/dy)/\nu]_{cr} = \text{constant}$$

Evidently, if the maximum value of χ for a given state of flow is less than this critical magnitude, then the flow should be inherently stable to all disturbances. If, on the contrary, the maximum value of χ exceeds this critical magnitude, then at the corresponding point within the flow the onset of turbulence should be expected once the necessary disturbance occurs.

Flow Along a Flat Plate

Consider, for instance, flow in a laminar boundary layer along a flat plate, the well-known velocity distribution of which is plotted dimensionlessly in Fig. 1a.[1] In Fig. 1b is shown the corresponding plot of χ in its ratio to the square root of a Reynolds Number based upon the velocity v_0 at a point far removed from the plate and the distance x from the leading edge. The stability index evidently varies from zero at the boundary to a maximum value of $1.44\sqrt{v_0 x/\nu}$ at the boundary distance $y = 3.1\sqrt{x\nu/v_0}$, beyond which it again approaches zero. Then this point of maximum χ is the location at which the onset of turbulence is to be expected, provided that the absolute magnitude of the

Received January 18, 1945.

* Director, Iowa Institute of Hydraulic Research.

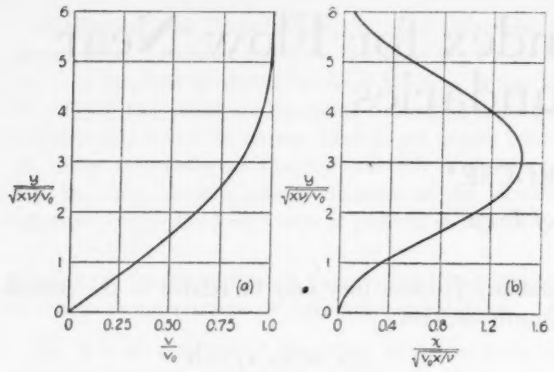

FIG. 1.

index exceeds its critical value and the necessary disturbance occurs. If one takes the Reynolds Number $v_0x/\nu = 1.5 \times 10^5$ as the lowest probable limit for boundary-layer turbulence,[2] the critical value of the index will be found to be approximately $\chi_{cr} = 560$.

Flow Through Pipes

A related, although considerably different, type of flow is that through a long pipe of uniform diameter, which is generally considered to be stable to all disturbances if a Reynolds Number based upon the average velocity V and the pipe radius r_0 is lower than 1,000. Since, according to the Poiseuille relationship,[3] the velocity gradient may be expressed in terms of the intensity of boundary shear τ_0, the dynamic viscosity μ, and the relative distance from the boundary,

$$dv/dy = (2\tau_0/\mu r_0)(r_0 - y)$$

and since, therefore,

$$\tau_0 = 2\mu V/r_0$$

it will be found that

$$\chi = \frac{y^2(dv/dy)}{\nu} = \frac{4Vr_0}{\nu}\left(\frac{r_0y^2 - y^3}{r_0{}^3}\right)$$

Placing the derivative of χ with respect to y equal to zero,

$$\frac{d\chi}{dy} = \frac{4Vr_0}{\nu}\,\frac{2r_0y - 3y^2}{r_0{}^3} = 0$$

from which it follows that $\chi = \chi_{max.}$ when $y = 2r_0/3$. This, then, should be the zone of initial instability in a long pipe, provided that the index exceeds its critical value and that a disturbance occurs. If, furthermore, the χ criterion is as general as assumed, its critical value for the pipe should be numerically equal to that for the boundary layer along a plate. From the foregoing development it will be found that

$$\chi_{max.} = (16/27)(Vr_0/\nu)$$

whence, for the value $Vr_0/\nu = 1{,}000$, $\chi_{cr} = 590$.

Flow Between Parallel Boundaries

Although little experimental information is at hand for the critical limit of laminar flow between stationary parallel boundaries or of laminar free-surface flow down a sloping boundary, such flow should obviously be subject to the same general stability criterion. Since the velocity distribution for laminar flow in either instance follows a parabolic curve similar to that of the pipe, the point of maximum χ should again be located two-thirds of the distance y_0 from the boundary to the mid-section between the boundaries or to the equivalent free surface. If, as is customary, the critical limit of either type of flow is estimated from tests on pipes in terms of the so-called hydraulic radius (i.e., the ratio of the cross-sectional area of flow to the "wetted" boundary perimeter), the Reynolds Number based on the mean velocity V and the distance y_0 is found to have a magnitude of 500. However, experimental evidence for open-channel flow,[4] as well as the location of the intersection of the dimensionless resistance curves for the corresponding laminar and turbulent regimes, indicates that this value should be at least as high as 800 to be fully comparable. Under such circumstances

$$\chi_{max.} = (4/9)(Vy_0/\nu) \text{ and } \chi_{cr} = 380$$

As a final test, flow that is produced by the motion of one plane boundary past another should be considered. Experimental data are available only for the case of rotating cylinders, but it appears from extrapolation[5] that cylinders of infinite radius would yield, for stability, the condition

$$\Delta v\ \Delta r/\nu \approx 2{,}000$$

While the velocity gradient is constant between the inner and outer boundaries, variation in y would make χ a maximum midway between them, at which point

$$\chi_{max.} = \left(\frac{\Delta r}{2}\right)^2\left(\frac{\Delta v}{\Delta r\nu}\right) = \left(\frac{1}{4}\right)\left(\frac{\Delta v\ \Delta r}{\nu}\right)$$

Under such circumstances the value of $\chi_{max.}$ at which instability should exist is found to be $\chi_{cr} = 500$.

General Significance of the Stability Index

Although four somewhat different values (560, 590, 380, and 500) have been obtained herein for an index that was asserted to be a constant, it should be noted that three of these values have been computed from commonly accepted critical limits without any attempt at readjustment and that the lowest is based upon a limit that itself is not yet fully established. In every case $\chi_{max.}$ is directly proportional to the Reynolds Number or is, in fact, a special form of the Reynolds Number, just as the Richardson Number is a special form of the Froude Number. Nevertheless, only by arbitrary manipulation of the length term in the Reynolds Number would it be possible to obtain comparable critical

values in the several cases, while the χ criterion at once yields values that depart so little from the average $\chi_{cr} \approx 500$ that it would appear to have both physical and numerical significance.

Essentially different from the foregoing case of transformation from laminar to turbulent flow is the question of the limit of stability of the laminar sublayer—the zone of demarcation between laminar and turbulent motion occurring simultaneously in neighboring regions. The latter problem nevertheless involves the same three variables comprised in the χ parameter, which may readily be evaluated from existing measurements on smooth pipes.[6] According to these measurements, the nominal thickness δ of the laminar sublayer may be expressed as

$$\delta = 11.6\nu/\sqrt{\tau_0/\rho}$$

in which τ_0 is the intensity of boundary shear and ρ the fluid density. Since, in obtaining this value, it is necessarily assumed that

$$(dv/dy)_{y=\delta} = v_\delta/\delta = \tau_0/\mu$$

it follows that

$$\chi_{cr} = \frac{\delta^2\tau_0}{\nu\mu} = (11.6)^2 = 134$$

Because of the essential difference between these two phases of the stability problem, it is hardly to be expected that the respective values of χ_{cr} should be numerically equal. That they are nonetheless of the same order of magnitude is therefore probably of greater interest than significance. As a matter of fact, the constancy of χ_{cr} indicated by the initial dimensionless relationship is wholly dependent upon the similarity of flow conditions tacitly assumed in the analysis. Whether or not the slight variation in χ_{cr} for the four cases previously discussed is also due to inherent differences in the flow conditions must remain subject to further investigation. On the other hand, if such additional variables as boundary curvature or density gradient were involved in the problem, the same stability index would then obviously assume the role of a dependent variable, its magnitude for critical conditions becoming a function of the boundary geometry or of either the Froude Number or the Richardson Number.

References

[1] Blasius, H., *Grenzschichten in Flüssigkeiten mit kleiner Reibung*, Z. Math. und Physik, Vol. 56, 1908.

[2] Kármán, Th. von, *Skin Friction and Turbulence*, Journal of the Aeronautical Sciences, Vol. 1, No. 1, 1934.

[3] Lamb, H., *Hydrodynamics*, p. 585, Cambridge University Press, London, 1932.

[4] Robertson, J. M., and Rouse, H., *On the Four Regimes of Open-Channel Flow*, Civil Engineering, Vol. 11, March, 1941.

[5] Taylor, G. I., *Fluid Friction Between Rotating Cylinders*, Proc. Roy. Soc., Vol. A157, Nos. 892–893, 1936.

[6] Nikuradse, J., *Gesetzmässigkeiten der turbulenten Strömung in glatten Rohren*, Forschungsheft, Vol. 3, No. 356, September-October, 1932.

Letters to the Editor

Dear Sir:

In the paper "Bending Beyond the Proportional Limit" by M. Yachter (JOURNAL OF THE AERONAUTICAL SCIENCES, Vol. 12, p. 21, January, 1945) and in the Letter to the Editor by Karol and Goran (JOURNAL OF THE AERONAUTICAL SCIENCES, Vol. 12, p. 251, April, 1945) there are errors that lead the authors to incorrect results. Fundamentally, the error in both cases amounts to the assumption that, as the stress (S) is increased *or reduced* in the region above the proportional limit, the strain may be represented by the abscissa of a point moving back and forth along the original stress-strain curve.

Thus, in Eq. (6) of the original paper, when $\alpha\eta(z)$ is added to $S(z)$, and α is allowed to vary from unity to zero, it is assumed that the stress-strain relationship may be represented by the original stress-strain curve. Physically, this is not true. As α reduces from unity, the point departs from the original stress-strain curve and moves along a line having the slope E_0. Thus, it is seen that the derivative $\epsilon_m'(s) = d\epsilon_m(s)/dS$ is not only discontinuous but is discontinuous at every point of the stress-strain curve above the proportional limit. Therefore the second derivative $\epsilon_m''(s)$ becomes infinite at all such points. Similarly, in the Letter to the Editor, the derivative dA_e/dS is discontinuous above the proportional limit. Both of these derivations are therefore in error. Both assume an imaginary material that may be loaded above the proportional limit and then unloaded to zero strain. This is equivalent to assuming a nonlinear *elastic* law. Real materials do not behave in this manner. Energy that is used in producing plastic flow is not recoverable. It escapes from the system in the form of heat. The system is therefore nonconservative, and setting the variation of the total work (δW) equal to zero becomes an absurdity.

Now, considering two identical, short, axial elements of a beam with nonlinear strain distribution and with constant moment as in the accompanying figure, it may be seen that the two elements are not compatible—i.e., they will not fit together.

This simple approach leads to the conclusion that the only possible manner in which compatibility of adjacent elements may be achieved is for the strain distribution to be linear across the depth of the beam.

It must be concluded that the results of both references are erroneous and that extension of the least work principle into the plastic range will lead to incorrect results.

The assumption of linear strain distribution appears to be the only practical solution to the problem of plastic bending of prismatic bars.

WILLIS J. BENCKERT
Stress Group Engineer
The Glenn L. Martin Company

Dear Sir:

In the article entitled "A Note on Bending Beyond the Proportional Limit" by M. Yachter (JOURNAL OF THE AERONAUTICAL SCIENCES, Vol. 12, No. 1, p. 21, January, 1945), a fundamental mistake was made in using the Principle of Least Work in a case for which this principle does not apply.

It has been pointed out by F. Engesser in his article "Ueber statisch unbestimmte Träger bei beliebigen Formänderungs-Gesetze und über den Satz von den kleinsten Ergänzungsarbeit" (*Zeitschrift des architekten- und Ingenieur-Vereins zu Hannover*, Vol. 35, 1889, column 733–744, especially 738–744) that the Principle of Least Work applies only in the case of a stress-strain relation of the form

$$s = c\epsilon^n \tag{1}$$

where s denotes the stress, ϵ the strain, and c and n are constants characteristic of the material. Hooke's law, $s = c\epsilon$, is, of course, a special case of Eq. (1), with $n = 1$. For stress-strain relations of any form other than Eq. (1), the Principle of Least Work is not valid but must be replaced by Engesser's Principle of Least Complementary Energy (see, for instance, the section on the Theory of Structures by Grüning in the *Encyklopädie der mathematischen Wissenschafter*, Vol. 4, subvolume 4, Leipzig, pp. 453–454, 1907–1914).

As work is an integral of force times increment of distance or of stress times increment of deformation, so is complementary energy an integral of distance times increment of force or of deformation times increment of stress. Referring to Fig. 1, the complementary energy per unit volume is represented by the shaded area and is defined as

$$w_c = \int \epsilon \, ds \tag{2}$$

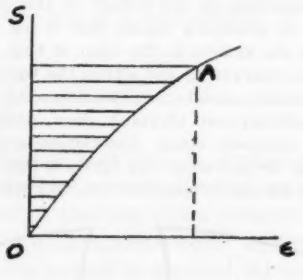

The Principle of Least Complementary Energy states that among all the statically possible states of stress in a rigidly supported structure, the correct one is that which renders the complementary energy of the internal stresses a minimum.

If one were to define $\epsilon m(s)$ as

$$\epsilon m(s) = \epsilon(s)(A_{ss}/A_T)$$

where A_{ss} is the area $\overline{OAS}$ between the axis of S and the original curve (Fig. 1, Yachter's paper), then by the Principle of Least Complementary Energy, the same theoretical results would be obtained as in Yachter's paper. The numerical results obtained in Yachter's paper, however, are not correct.

CHI-TEH WANG
Brown University

Dear Sir:

Several errors can be noted in the paper "Stresses in a Ring Loaded Normal to Its Plane" by E. R. Walters (JOURNAL OF THE AERONAUTICAL SCIENCES, Vol. 12, No. 2, p. 235, April, 1945).

(1) The sign of the second members of Eqs. (6) should be minus.

(2) The sixth equation (7) is generally incorrectly written, because the torques must be calculated about the twist center, which does not generally coincide with the centroid. This fact, well known for open sections, has been completely elucidated by Prof. J. N. Goodier[1] in the case of closed sections. It results that the quantities, x, y, α in Eq. (7) must be replaced by the corresponding quantities that define the line of the twist centers.

(3) When tubes are considered, the flexural rigidity is a function of the radius of curvature of the tube and cannot be represented by EI; this expression must be divided by a factor D, this reduction being caused by the flattening of the tube. Numerical values of D have been calculated by the writer in the case of round tubes.[2] For this reason, the curves for torque and moment plotted on Fig. 3 are valid only for round bars and not for round tubes, as stated by the author.

REFERENCES

[1] Goodier, J. N., *A Theorem on the Shearing Stress in Beams with Applications to Multicellular Sections*, Journal of the Aeronautical Sciences, Vol. 11, No. 3, p. 272, July, 1944.

[2] Beskin, L., *Bending of Curved Thin Tubes*, Journal of Applied Mechanics, Vol. 12, No. 1, p. A-1, March, 1945.

LEON BESKIN
Design Specialist
Consolidated Vultee Aircraft Corporation

Dear Sir:

In the derivation of Eq. (73) in an article by Hsue-shen Tsien and Lester Lees entitled, "The Glauert-Prandtl Approximation for Subsonic Flows of a Compressible Fluid," which appeared in the April, 1945, issue of the JOURNAL OF THE AERONAUTICAL SCIENCES, the writer wishes to point out that this equation is identical with the following one

$$\left(\frac{dC_L}{d\alpha}\right)_c = \frac{(dC_l/d\alpha)_c}{1 + [(dC_l/d\alpha)_c/\pi R]}$$

where $(dC_l/d\alpha)_c = (dC_l/d\alpha)_i/\sqrt{1 - M^2}$. It is immediately recognized that the equation for the wing lift-coefficient curve slope for the compressible fluid is similar to that for the incompressible fluid according to Prandtl's lifting-line theory with the section-lift-coefficient curve slope increased by the Glauert's factor, $1/\sqrt{1 - M^2}$. With the equation in this form, it is more readily apparent that Husk's assumption that $(dC_L/d\alpha)_c$ is increased by the ratio $1:\sqrt{1 - M^2}$ is in error as pointed out by the authors.

HOSHEN LU
Aerodynamicist
Republic Aviation Corporation

On the Dynamics of Elastic Buckling

J. H. MEIER*
Bucyrus-Erie Company

Introduction

The classic theory of elastic buckling is based on the equilibrium of external and internal bending moments. It does not consider, however, the time elements and the inertia forces involved. The lateral vibration of compressed bars has been investigated,[1] but the use of formulas so obtained for the experimental determination of elastic buckling loads apparently has not been widespread. Yet, this method has many promising aspects. Little information seems to be available on buckling under impact, although this problem must confront many engineers.

In this article, time-deflection relations are investigated when an axial force is rapidly applied to a nearly straight bar. Distinction is made between two cases: In the first, the force applied is smaller than Euler's load for elastic buckling; in the second, it is greater.

The investigation is limited to cases where the center deflection of compressed bars stays relatively small with respect to the length of the bars. The curvature of the elastic line is therefore assumed to be proportional to the bending moment, independent of the slope. A rigorous analysis, using the strict equation for the curvature and considering inertia forces, would become unduly complicated. However, calculations[2] show that a center deflection of 11 per cent of the original hinge distance increases the elastic buckling force by only 1.5 per cent, while the hinge distance is decreased by 3 per cent. The method of analysis set forth here should therefore cover the large majority of practical cases.

Damping is not considered in this analysis. However, where it is of importance and the damping constants can be established, a correction factor for damping can readily be applied to the respective equations.

Nomenclature

- P = force applied to hinged bar, line of action passing through hinges
- P_E = Euler's load for elastic buckling of hinged bar
- x = distance from hinge
- y = instantaneous deflection at distance x from hinge
- f = instantaneous deflection at center of bar
- f_0 = initial deflection at center of bar, assumed relatively small
- f_1 = deflection at center of bar when force P is released
- $f_{max.}$ = maximum deflection at center of bar
- v_c = lateral velocity at center of bar when force P is released
- l = length of bar, approximately equal to initial distance between hinges
- A = area of cross section of bar, assumed constant
- I = axial moment of inertia of cross section, assumed constant
- r = radius of gyration of cross section
- R = initial radius of curvature at center of bar. $1/R$ is generally referred to as "maximum curvature"
- S = section modulus of cross section of bar
- E = modulus of elasticity of bar
- ρ = density of bar
- σ = stress
- Q = vibration energy of bar
- M_e = external bending moment acting on bar
- M_i = internal bending moment of bar, opposing deflection
- M_a = bending moment due to inertia forces, opposing the rate of change of deflection
- a = distance defined by Eq. (9)
- p = factor defined by Eq. (11)
- q = factor defined by Eq. (18)
- t = time
- Δt = time element
- F = frequency of vibration
- C_1, C_2 = constants of integration

Condition of Dynamic Equilibrium

Given: a hinged bar of length l and center deflection f_0 (Fig. 1). For convenience, the shape of the axis is assumed to be a sine curve at all times, i.e.,

$$y = f \sin (\pi x/l) \tag{1}$$

This corresponds to the first mode of vibration and the shape of the elastic line when the bar undergoes buckling.

If a force P is applied, bending tends to increase deflection and the elements of the bar undergo transverse accelerations.

Immediately after the force is applied, three bending moments are present. Their distribution along the bar is sinusoidal (analogous to Eq. (1)), and they can therefore be identified by the respective values at the center.

- M_e = the external bending moment due to the force P and the instantaneous center deflection f
- M_i = the internal bending moment due to the stiffness of the bar and the instantaneous bending deflection $(f - f_0)$
- M_a = the bending moment due to inertia forces opposing the instantaneous acceleration d^2f/dt^2

The moment M_e tends to increase deflection, while the moment M_i opposes deflection and the moment M_a retards it, thus acting in the same sense as M_i. The

Received December 18, 1944.
* Research Engineer.

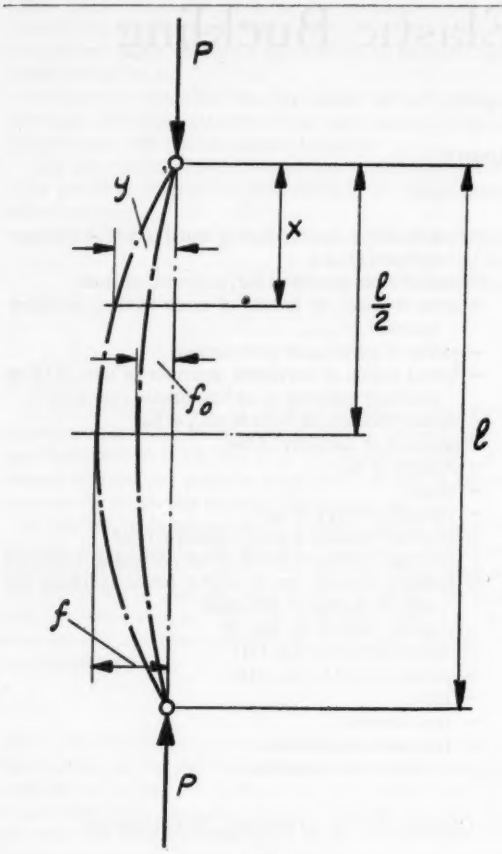

FIG. 1.

three bending moments form a system of equilibrium, i.e.,

$$M_e = M_i + M_a \tag{2}$$

MAGNITUDE OF THE BENDING MOMENTS

The External Bending Moment

$$M_e = Pf \tag{3}$$

The Internal Bending Moment: M_i

At center of bar:

Internal bending moment = M_i.

At any point:

Internal bending moment = $M_i \sin(\pi x/l)$.

Change in slope due to bending

$$-(M_i/IE) \sin(\pi x/l)\, dx$$

Slope due to bending

$$(M_i/IE)\,(l/\pi) \cos(\pi x/l)$$

Deflection due to bending

$$(M_i/IE)\,(l^2/\pi^2) \sin(\pi x/l)$$

At center of bar:

Deflection due to bending

$$f - f_0 = (M_i/IE)\,(l^2/\pi^2)$$

hence,

$$M_i = (\pi^2 IE/l^2)\,(f - f_0) = P_E(f - f_0) \tag{4}$$

where P_E is Euler's load for elastic buckling.

The Bending Moment Due to Inertia Forces: M_a

At center of bar:

Transverse acceleration = d^2f/dt^2.

Inertia force

$$-A\rho\,(d^2f/dt^2)\,dx$$

At any point:

Inertia force

$$-A\rho \sin(\pi x/l)\,(d^2f/dt^2)\,dx$$

Shear due to inertia forces

$$A\rho(l/\pi) \cos(\pi x/l)\,(d^2f/dt^2)$$

Bending moment due to inertia forces

$$A\rho\,(l^2/\pi^2) \sin(\pi x/l)\,(d^2f/dt^2)$$

At center of bar:

Bending moment due to inertia forces

$$M_a = A\rho(l^2/\pi^2)\,(d^2f/dt^2) \tag{5}$$

DIFFERENTIAL EQUATION FOR TRANSVERSE MOTION OF POINT AT CENTER OF BAR

The differential equation of the transverse motion of the point at the center of the bar is found from Eq. (2) by substituting the respective values for the bending moments as established by Eqs. (3), (4), and (5).

$$Pf = P_E(f - f_0) + (l^2A\rho/\pi^2)(d^2f/dt^2) \tag{6}$$

or

$$\left(\frac{d^2f}{dt^2}\right)\left(\frac{l^2A\rho}{\pi^2}\right) + (P_E - P)f - P_Ef_0 = 0$$

and

$$\frac{d^2f}{dt^2} + \left(\frac{\pi^2}{l^2A\rho}\right)(P_E - P)f - \left(\frac{\pi^2}{l^2A\rho}\right)P_Ef_0 = 0 \tag{7}$$

Introducing a new variable,

$$f_1 = f - a \tag{8}$$

where

$$a = \frac{(\pi^2/l^2A\rho)P_E f_0}{(\pi^2/l^2A\rho)(P_E - P)} = \left(\frac{P_E}{P_E - P}\right)f_0 \tag{9}$$

the differential equation becomes:

$$(d^2f_1/dt^2) + (\pi^2/l^2A\rho)(P_E - P)f_1 = 0 \tag{10}$$

The physical meaning of the quantities involved is better understood if numerator and denominator of the second term are multiplied by Euler's load for elastic buckling,

$$P_E = \pi^2 IE/l^2$$

which leads to

$$\frac{d^2f_1}{dt^2} + \left(\frac{\pi^4}{l^4}\right)\left(\frac{IE}{A\rho}\right)\left(\frac{P_E - P}{P_E}\right)f_1 = 0 \qquad (10a)$$

Case I. $P < P_E$, Stable Condition

Solution of Differential Equation

In Eq. (10a), introduce

$$p^2 = (\pi^4/l^4)(IE/A\rho)[(P_E - P)/P_E] \qquad (11)$$

which brings the differential equation to the reduced form

$$(d^2f_1/dt^2) + p^2f_1 = 0 \qquad (12)$$

The solution of this differential equation can be written as

$$f_1 = C_1 \cos pt + C_2 \sin pt \qquad (13)$$

where C_1 and C_2 are constants of integration and have to be determined from the known conditions at any particular time.

Recalling Eq. (8), the solution for the deflection f becomes

$$f = a + C_1 \cos pt + C_2 \sin pt \qquad (14)$$

Assuming the bar is at rest and the force P is applied suddenly at the time $t = 0$, the constants of integration are determined as follows:

$$t = 0; \quad f = f_0 = a + C_1$$

from which $C_1 = f_0 - a$.

$$t = 0; \quad df/dt = 0 = pC_2$$

from which $C_2 = 0$.

Hence,

$$f = a + (f_0 - a) \cos pt \qquad (14a)$$

Replacing a in Eq. (14a) by the value given in Eq. (9) leads to

$$f = f_0\left(\frac{P_E}{P_E - P}\right) + f_0\left(1 - \frac{P_E}{P_E - P}\right)\cos pt$$

or

$$f = f_0[(P_E - P \cos pt)/(P_E - P)] \qquad (14b)$$

The transverse speed at the center of the bar is

$$df/dt = f_0[Pp \sin pt/(P_E - P)] \qquad (14c)$$

and the transverse acceleration at the center of the bar is

$$\frac{d^2f}{dt^2} = f_0[Pp^2 \cos pt/(P_E - P)] \qquad (14d)$$

Interpretation and Application of Solution

The quantity a introduced by Eq. (9) has a physical meaning in the stable case. It is the center deflection about which the bar vibrates, and, when vibration ceases, the bar has assumed this deflection at the center. This deflection is obviously the same as the one obtained by applying the force P gradually. Accordingly, Eq. (9) is readily recognized as the equation of the center deflection given by the theory of buckling of hinged bars.*

$P_E/(P_E - P) = a/f_0$ can be considered as a magnification factor representing the influence of the compressive force upon the static transverse deflection.

The frequency of vibration of the bar is

$$F = p/2\pi \qquad (15)$$

and, introducing the value for p from Eq. (11), one obtains the natural frequency of a compressed bar as

$$F = (\pi/2l^2)\sqrt{IE/A\rho}\sqrt{(P_E - P)/P_E} \qquad (15a)$$

For $P = 0$—i.e., for a hinge supported bar with no compressive force—the natural frequency becomes

$$F' = (\pi/2l^2)\sqrt{IE/A\rho} \qquad (15b\dagger)$$

Eq. (15a) can also be expressed as

$$F = p/2\pi = (\pi/2l)(r/l)\sqrt{E/\rho}\sqrt{(P_E - P)/P_E} \qquad (15c)$$

since introducing the radius of gyration, $r = \sqrt{I/A}$, in Eq. (11) leads to

$$p = (\pi^2/l)(r/l)\sqrt{E/\rho}\sqrt{(P_E - P)/P_E} \qquad (16)$$

The physical meaning of the individual factors in Eqs. (15c) and (16) is readily recognized:

- $\pi/2l$ and π^2/l, respectively, are length factors.
- r/l is the reciprocal of the slenderness ratio.
- $\sqrt{E/\rho}$ is a factor representing the properties of the material; it is the speed of sound propagation in the bar.
- $\sqrt{(P_E - P)/P_E}$ is a correction factor for the compressive force acting on the bar. It is of interest to note that the natural frequency of a compressed bar varies inversely with the square root of the magnification factor for static deflections.

Eq. (15a) should be useful for the experimental determination of Euler's load for elastic buckling. It establishes a nondestructive method of finding Euler's

* See reference 2, p. 33 and p. 177.

† See reference 1, p. 339, Eq. (144). For $n = 1$ (first mode of vibration), the equations are identical.

load for actual structures or small scale models. By means of electrical strain gages, the natural frequency of bars with and without compressive forces can be accurately determined. Then, by plotting natural frequency versus applied force and extrapolating by means of Eq. (15a), Euler's load is obtained at the point of zero frequency. Good accuracy can be expected, even when bars of variable stiffness and latticed structures are investigated.

For instance, if the natural frequency is F_1 without a compressive force and F_2 with a compressive force P, one obtains

$$F_2/F_1 = \sqrt{(P_E - P)/P_E} \tag{17}$$

and

$$P_E = P[F_1^2/(F_1^2 - F_2^2)] \tag{17a}$$

All the above equations are based on substantially constant forces P. In the experimental determination of Euler's load by means of frequency relations, care should be taken to fulfill this condition as nearly as possible. Spring loading may lead to more accurate results than loading by weights, because the force exerted by weights varies due to the accelerations in the direction of the bar axis.

All equations for Case I hold also for tension forces P, providing the sign of P is reversed.

Case II. $P > P_E$, Unstable Condition

Solution of Differential Equation

In Eq. (10a), introduce

$$q^2 = (\pi^4/l^4)(IE/A\rho)[(P - P_E)/P_E] \tag{18}$$

which brings the differential equation to the reduced form

$$(d^2f_1/dt^2) - q^2f_1 = 0 \tag{19}$$

The solution of this differential equation can be written as

$$f_1 = C_1 \cosh qt + C_2 \sinh qt \tag{20}$$

where C_1 and C_2 are constants of integration and have to be determined from the known conditions at any particular time.

Recalling Eq. (8), the solution for the deflection f becomes:

$$f = a + C_1 \cosh qt + C_2 \sinh qt \tag{21}$$

Assuming that the bar is at rest and the force P is applied suddenly at the time $t = 0$, the constants of integration are determined as follows:

$$t = 0; \quad f = f_0 = a + C_1$$

from which $C_1 = f_0 - a$.

$$t = 0; \quad df/dt = 0 = qC_2$$

from which $C_2 = 0$.

Hence,

$$f = a + (f_0 - a) \cosh qt \tag{21a}$$

Discussion of Solution

Quantity a expressed by Eq. (9) is negative for the unstable case, and its physical meaning is not so readily explained as in the stable case. Elimination of a by combining Eqs. (9) and (21a) leads to

$$f = f_0\left(\frac{P_E}{P_E - P}\right) + f_0\left(1 - \frac{P_E}{P_E - P}\right)\cosh qt$$

or

$$f = f_0[(P \cosh qt - P_E)/(P - P_E)] \tag{21b}$$

The transverse speed at the center of the bar is obtained as

$$df/dt = f_0[Pq \sinh qt/(P - P_E)] \tag{21c}$$

and the transverse acceleration as

$$d^2f/dt^2 = f_0[Pq^2 \cosh qt/(P - P_E)] \tag{21d}$$

It is thus seen that the bar buckles out with progressive speed. However small the initial eccentricity f_0 may be and however little the applied force P exceeds Euler's load P_E, the bar will soon assume large deflections, because the terms cosh qt and sinh qt increase rapidly with time.

Analogous to Eq. (16), the factor q governing the speed of buckling can be split up into several factors, the physical meaning of which is easily understood:

$$q = (\pi^2/l)(r/l)\sqrt{E/\rho}\sqrt{(P - P_E)/P_E} \tag{22}$$

It is of interest to note that, if two bars with equal slenderness ratio and geometrically similar initial axes are compressed by forces that are equal multiples of the respective Euler's loads for elastic buckling, the center deflection of the shorter bar increases faster.

For structural elements the product of the first three factors of Eq. (22) is generally so large that they will buckle rapidly when the applied force exceeds Euler's load for elastic buckling. For derricks and booms this product may become considerably smaller, but, as a rule, forces on such structures are applied through ropes and are therefore slow in being applied and released. Therefore, the lateral inertia of bars, struts, and structures is usually of small influence in providing extra capacity for short duration forces.

However, the lateral inertia has considerable influence on the behavior of slender bars used for impact texting and studies on wave propagation. Here, the factor q frequently is relatively small and the time element is usually extremely short. Such bars can thus be subjected to a multiple of Euler's load for elastic buckling without assuming excessive deflections.

If the force P is applied for a short time only and if the original deflection f_0 is small, the deflection f_r when

the force is released is also relatively small. Because of the kinetic energy of the transverse motion, the bar will continue to deflect for some time when the force P is released.

Considerations Holding for Case I and Case II

Transverse Motion of Bar After Force Is Released

When the force P is released, the bar has, in general, a center deflection f_r and a transverse velocity v_r at the center. The values of f_r and v_r can be calculated by means of the equations established above. After the force P is released, the elastic behavior of the bar is characterized by the equations derived for Case I. The bar vibrates around its position of static equilibrium. Since no force is acting, this is obviously the initial center deflection f_0. The factor p is obtained from Eq. (11), and, because there is no compressive force, it is only a function of the properties of the bar.

A new time origin is introduced for this analysis, so that $t = 0$ at the moment the force P is released. Using Eq. (14) and recalling that $a = f_0$ when there is no compressive force, one finds for $t = 0$:

$$f_r = f_0 + (f_r - f_0) = f_0 + C_1 \cos pt + C_2 \sin pt$$

which leads to

$$f_r = f_0 + C_1; \quad \text{hence, } C_1 = f_r - f_0 \tag{23}$$

and

$$v_r = pC_2; \quad \text{hence, } C_2 = (1/p)v_r \tag{24}$$

The maximum deflection is found from the theory of harmonic vibration as

$$f_{max.} = f_0 + \sqrt{C_1^2 + C_2^2} \tag{25}$$

or, by using Eqs. (23) and (24),

$$f_{max.} = f_0 + \sqrt{(f_r - f_0)^2 + (1/p^2)v_r^2} \tag{26}$$

Similarly, the speed at which the center of the bar passes the position of equilibrium is obtained as

$$\text{max. } df/dt = p\sqrt{C_1^2 + C_2^2} \tag{27}$$

or, by using Eqs. (23) and (24),

$$\text{max. } df/dt = \sqrt{p^2(f_r - f_0)^2 + v_r^2} \tag{28}$$

The vibration energy of the bar is found as

$$Q = {}^1/_2 A\rho(df/dt)_{max.}^2 \int_{x=0}^{x=l} \sin^2(\pi x/l)dx \tag{29}$$

or, by using Eqs. (23) and (24),

$$Q = {}^1/_4 Al\rho[p^2(f_r - f_0)^2 + v_r^2] \tag{30}$$

Buckling Under Impact Produced by Striking Objects

When impact is produced by a bar striking an object, or vice versa, the time during which the forces act as assumed in the previous discussion (Fig. 1) is relatively short with respect to the time it takes to produce this loading condition.

The time element and the forces involved can be calculated by the theory of wave propagation in solids. In particular, if a free bar moving in the direction of its axis strikes a large, rigid anvil, the contact force acts as long as it takes the stress wave to travel to the far end of the bar and back. (Stress waves and sound waves are identical in nature; their speed of propagation is $\sqrt{E/\rho}$, which for steel is 16,870 ft. per sec.) The compressive stress in the element at the far end acts only for an infinitely short time. For intermediate points, the time element during which the stress acts is given by the linear relation

$$\Delta t = 2(l - x)\sqrt{\rho/E} \tag{31}$$

the point of contact being at $x = 0$. Averaging the time element of Eq. (31) for all elements of the bar yields one-half the contact time.

The accurate investigation of elastic buckling for such impact conditions becomes much involved. Since the duration of stress depends on the location of the element, a bar axis of originally sinusoidal shape changes to a more complex curve during impact. However, by assuming the hypothetical case of the forces acting as shown in Fig. 1 during the entire impact time (thus assuming that all elements are stressed during the entire contact time) and applying the equations derived above, greater lateral deflections are calculated than actually occur. Such a calculation of an "upper limit" is sufficient in most practical cases to estimate the effect of buckling. It shows, for instance, why a slender bar moving in the direction of its axis may not buckle appreciably when it strikes an anvil with a speed that produces an impact force equal to a multiple of Euler's load for elastic buckling. It also explains why a storm can drive a straw into a tree, or why a knitting needle shot from a gun will penetrate into a piece of wood without buckling to the point of failure.

The Early Stages of Elastic Buckling

Assuming a force P suddenly applied to a bar at rest, Eqs. (14a) to (14d) have been derived for the stable case, and Eqs. (21a) to (21d) for the unstable case. The respective equations are analogous and their further study leads to interesting results as to the early stages of buckling under rapidly applied forces. They are also useful in the investigation of the various modes of buckling and vibration.

The transverse acceleration at the center of the bar is in the stable case

$$d^2f/dt^2 = f_0[Pp^2 \cos pt/(P_E - P)] \tag{14d}$$

and in the unstable case

$$d^2f/dt^2 = f_0[Pq^2 \cosh qt/(P - P_E)] \tag{21d}$$

The physical meaning of these equations is better understood if p^2 and q^2 are replaced by the respective values, Eqs. (11) and (18), and if the maximum initial curvature of the bar axis is introduced:

$$1/R = f_0(\pi^2/l^2) \tag{32}$$

This leads in the stable case to

$$d^2f/dt^2 = (1/R)(P/A\rho)\cos pt \tag{33}$$

and in the unstable case to

$$d^2f/dt^2 = (1/R)(P/A\rho)\cosh qt \tag{34}$$

Since cos pt and cosh qt are unity for $t = 0$, the initial acceleration is found in both cases as

$$d^2f/dt^2 = (1/R)(P/A\rho) \tag{35}$$

The initial transverse acceleration at the center of the bar is directly proportional to the applied force and thus is independent of its relation to Euler's load for elastic buckling. This is readily appreciated because, at the beginning of buckling, there is no internal bending moment to counteract the external bending moment produced by the force P and the initial deflection f_0. Hence, the entire external bending moment is available for transverse acceleration of the bar.

Eq. (35) can also be verified by considering the equilibrium of forces on the element at the center of the bar during the initial stage of buckling (Fig. 2).

The resultant of the two forces P is a force acting transverse to the bar. Its magnitude is $P(dx/R)$, while the mass of the element is $A\rho\,dx$.

For small arguments pt and qt, the values of cos pt and cosh qt remain substantially at unity—i.e., the transverse acceleration remains nearly constant. Hence in the early stages of buckling, the transverse speed at the center of the bar can be expressed as

$$df/dt = (P/A\rho)(1/R)t \tag{35a}$$

and the transverse deflection at the center as

$$f = f_0 + (P/A)(1/R)(t^2/2) \tag{35b}$$

If the applied force P equals Euler's load for elastic buckling, P_E, one finds $p = q = 0$, and Eqs. (35) to (35b) hold for arbitrary values of t up to the point where the stiffness of the bar is appreciably affected by the deflection.

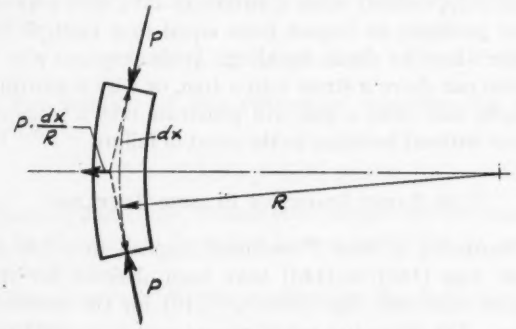

FIG. 2.

VARIOUS MODES OF BUCKLING

Higher modes of vibration and buckling can be investigated by applying the formulas derived to individual half waves. If equal maximum initial curvatures are assumed for the half waves of the various modes of buckling, it is thus seen from Eq. (35a) that in the early stages of buckling the deflections increase at the same rate for all modes. As buckling progresses, however, the greater stiffness of the bar in the higher modes causes the deflections of the higher modes to lag behind those of the lower modes. While a bar may be unstable in its lower modes of buckling for a certain force, there is always a critical mode from which on up it is stable.

The modes of buckling deflection and vibration depend on the shape of the initial deflection line, and various assumptions may have to be made, both as to modes of vibration and corresponding curvatures, in order to find the most critical case. In particular, an extremely long and slender bar subject to impact will have a tendency to buckle in a higher mode, because the section of the bar near the point of contact is stressed longer than the rest. Under such conditions, a section-wise investigation considering the effective time of compression may become necessary.

Investigations of this kind are greatly facilitated by developing the trigonometric terms into series. If p^2 and q^2 are eliminated in the respective terms and if the factor $(P - P_E)$ is introduced, series are obtained that hold for all cases. For the stable case, $P < P_E$, some terms of the series become negative and the series converge. In the critical case, $P = P_E$, the series reduce to the terms shown in Eqs. (35) to (35b). For the unstable case, $P > P_E$, all terms of the series are positive and the series are divergent.

$$f = f_0 + \left(\frac{P}{A\rho}\right)\left(\frac{1}{R}\right)\left\{\frac{t^2}{2!} + (P - P_E)\left(\frac{\pi^2}{l^2A\rho}\right)\left(\frac{t^4}{4!}\right) + (P - P_E)^2\left(\frac{\pi^2}{l^2A\rho}\right)^2\left(\frac{t^6}{6!}\right) + \cdots\cdots\right\} \tag{36}$$

$$\frac{df}{dt} = \left(\frac{P}{A\rho}\right)\left(\frac{1}{R}\right)\left\{t + (P - P_E)\left(\frac{\pi^2}{l^2A\rho}\right)\left(\frac{t^3}{3!}\right) + (P - P_E)^2\left(\frac{\pi^2}{l^2A\rho}\right)^2\left(\frac{t^5}{5!}\right) + \cdots\cdots\right\} \tag{37}$$

$$\frac{d^2f}{dt^2} = \left(\frac{P}{A\rho}\right)\left(\frac{1}{R}\right)\left\{1 + (P - P_E)\left(\frac{\pi^2}{l^2A\rho}\right)\left(\frac{t^2}{2!}\right) + (P - P_E)^2\left(\frac{\pi^2}{l^2A\rho}\right)^2\left(\frac{t^4}{4!}\right) + \cdots\cdots\right\} \tag{38}$$

Numerical Example

A bar of the following dimensions and properties is considered:

Dimensions: Length: $l = 125$ in.
Section: Round, 1 in. diameter
Area: $A = 0.785$ sq.in.
Moment of inertia: $I = 0.0491$ in.^{4}
Section modulus: $S = 0.0982$ in.^{3}
Radius of gyration: $r = 0.25$ in.
Slenderness ratio: $l/r = 125/0.25 = 500$
Initial center deflection: $f_0 = 0.50$ in.
Maximum initial curvature: $1/R = f_0(\pi^2/l^2) = {}^1/_{3,166}$ in.

Material: Steel
Modulus of elasticity: $E = 30{,}000{,}000$ lbs. per sq.in.
Density: $\rho = 0.283/386 = 0.000733$ lbs. sec.^{2} per in.^{4}
Speed of stress propagation: $\sqrt{E/\rho} = 202{,}300$ in. per sec.
Weight of bar: $W = 27.81$ lbs.

Euler's Load for Elastic Buckling:

$$\pi^2(IE/l^2) = (3.1416)^2(0.0491)[30{,}000{,}000/(125)^2] = 930 \text{ lbs.}$$

It is further assumed that a force of $P = 10{,}040$ lbs. is suddenly applied. (Note that $P = 10.8P_E$; hence, the equations for Case II apply in this example.)

Eq. (22) now yields

$$q = \left(\frac{9.87}{125}\right)\left(\frac{1}{500}\right)(202{,}300)\sqrt{\frac{10{,}040 - 930}{930}}$$
$$= (0.07896)(0.002)(202{,}300)(3.130) = 100.0$$

The deflection at the center is calculated from Eq. (21b) as

$$f = 0.50[(10{,}040 \cosh (100t) - 930)/(10{,}040 - 930)]$$

or

$$f = 0.5510 \cosh (100t) - 0.0510$$

From Eq. (21c) the transverse speed at the center is obtained as

$$df/dt = 0.50[(10{,}040)(100) \sinh (100t)/(10{,}040 - 930)]$$

or

$$df/dt = 55.10 \sinh (100t)$$

and from Eq. (21d) the transverse acceleration at the center is found as

$$\frac{d^2f}{dt^2} = 0.50\left[\frac{(10{,}040)(100)(100) \cosh (100t)}{10{,}040 - 930}\right]$$

or

$$d^2f/dt^2 = 5{,}510 \cosh (100t)$$

Table 1

Calculation of Deflection, Transverse Speed, and Acceleration

				At Center of Bar		
Time, t, Sec.	Cosh $100t$	Sinh $100t$	$0.5510 \times$ Cosh $100t$	Deflection f, in.	Transverse speed, df/dt, in. per sec.	Transverse acceleration, d^2f/dt^2, in. per sec.^{2}
0.000	1.0000	0.0000	0.5510	0.5000	0	5,510
0.002	1.0201	0.2013	0.5621	0.5111	11.094	5,621
0.004	1.0811	0.4108	0.5957	0.5447	22.635	5,957
0.006	1.1855	0.6366	0.6532	0.6022	35.077	6,532
0.008	1.3374	0.8881	0.7369	0.6859	48.934	7,369
0.010	1.5431	1.1752	0.8502	0.7992	64.754	8,502
0.012	1.8107	1.5095	0.9977	0.9467	83.173	9,977
0.014	2.1509	1.9043	1.1851	1.1341	104.927	11,851
0.016	2.5775	2.3756	1.4202	1.3692	130.896	14,202
0.018	3.1075	2.9422	1.7122	1.6612	162.116	17,122
0.020	3.7622	3.6269	2.0730	2.0220	199.842	20,730

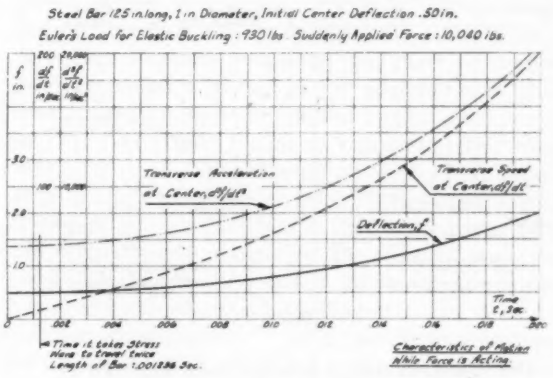
Steel Bar 125 in. long, 1 in Diameter, Initial Center Deflection .50 in.
Euler's Load for Elastic Buckling: 930 lbs. Suddenly Applied Force: 10,040 lbs.
Transverse Acceleration at Center, d²f/dt²
Transverse Speed at Center, df/dt
Deflection, f
Time t, Sec.
Time it takes Stress Wave to travel twice Length of Bar: 1.001236 Sec.
Characteristics of Motion while Force is Acting

Fig. 3.

Table 1 gives the values for f, df/dt, and d^2f/dt^2 for times up to 0.020 sec. Fig. 3 shows the respective curves.

Assuming that the force P is released at the time $t = t_r$, the deflection f_r and the transverse speed v_r at the moment of release are available as the corresponding values of f and df/dt in Table 1. The maximum deflection is thus obtained from Eq. (26) as

$$f_{max.} = 0.50 + \sqrt{(f_r - 0.50)^2 + [1/(31.95)^2]v_r^2}$$

since, in the case of $P = 0$, $p = (\pi^2/l)(r/l)\sqrt{E/\rho} = (0.07896)(0.002)(202{,}300) = 31.95$ (from Eq. 11).

The maximum bending moment is calculated by means of Eq. (4):

$$\text{max. } M_t = 930(f_{max.} - 0.50)$$

This leads to the maximum bending stress

$$\sigma_{max.} = \frac{\text{max. } M_t}{S} = \left(\frac{930}{0.0982}\right)(f_{max.} - 0.50) = 9{,}470(f_{max.} - 0.50)$$

TABLE 2

Calculation of Vibration Energy, Maximum Deflection, and Bending Stress After Release of Force

Time of Release of Force t_r, Sec.	At Moment of Release: Deflection f_r, in.	Transverse speed, v_r, in. per sec.	$\frac{v_r}{\dot{p}}$	$f_r - f_0$	$\left(\frac{v_r}{\dot{p}}\right)^2$	$(f_r - f_0)^2$	$\Sigma(\ )^2$	Vibration Energy, Q, In.Lbs.	$f_{max.} - f_0$, In.	Maximum Deflection, In.	Maximum Bending Stress, σ Lbs. per Sq.In.
0.000	0.5000	0	0	0	0	0	0	0	0	0.500	0
0.002	0.5111	11.094	0.3473	0.0111	0.1206	0.0001	0.1207	2.21	0.3474	0.8474	3,290
0.004	0.5447	22.635	0.7085	0.0447	0.5020	0.0020	0.5041	9.25	0.7094	1.2094	6,718
0.006	0.6022	35.077	1.0980	0.1022	1.2056	0.0104	1.2160	22.32	1.103	1.603	10,445
0.008	0.6859	48.934	1.5317	0.1859	2.3461	0.0346	2.3807	43.69	1.543	2.043	14,612
0.010	0.7992	64.754	2.0269	0.2992	4.1083	0.0895	4.1978	77.04	2.049	2.549	19,404
0.012	0.9467	83.173	2.6035	0.4467	6.7782	0.1995	6.9777	128.05	2.642	3.142	25,020
0.014	1.1341	104.927	3.2844	0.6341	10.7873	0.4021	11.1894	205.3	3.345	3.845	31,680
0.016	1.3692	130.896	4.0973	0.8692	16.7879	0.7555	17.5434	322.0	4.188	4.688	39,660
0.018	1.6612	162.116	5.0745	1.1612	25.7506	1.3484	27.0990	497.3	5.206	5.706	49,300
0.020	2.0220	199.842	6.2554	1.5220	39.1300	2.3165	41.4465	760.6	6.438	6.938	60,970

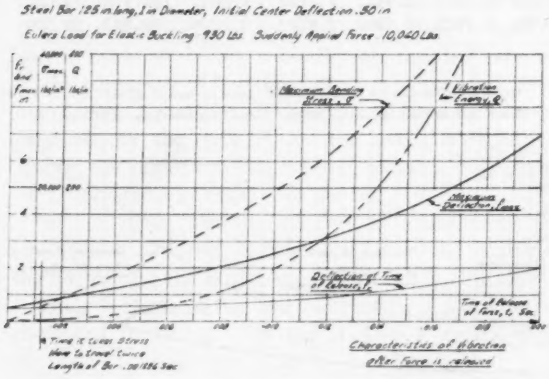
Steel Bar 125 in long, 1 in Diameter, Initial Center Deflection .50 in
Euler's Load for Elastic Buckling 930 Lbs. Suddenly Applied Force 10,040 Lbs
Maximum Bending Stress, σ
Vibration Energy, Q
Maximum Deflection, f
Deflection of Top of Column, f
Time of Release of Force, t, Sec.
Time, t, Sec. Stress, σ
Characteristics of Vibration after Force is removed

FIG. 4.

The vibration energy is found from Eq. (30) as

$$Q = (1/4)(0.785)(125)(0.000733)[(31.95)^2(f_r - f_0)^2 + v_r^2]$$

or

$$Q = 18.351[(f_r - 0.50)^2 + (v_r/(31.95)^2]$$

The values of $f_{max.}$, $\sigma_{max.}$, and Q are given in Table 2. which covers times of action of the force P up to 0.020 sec. The corresponding curves are shown in Fig. 4.

Suppose that the force P is produced by longitudinal impact of two bars of the dimensions and properties described above and that one of the bars is at rest before impact.[3] The time of contact is

$$\Delta t = 2l\sqrt{\rho/E} = (2)(125)(1/202{,}300) = 0.001{,}236 \text{ sec.}$$

An impact force of $P = 10{,}040$ lbs. causes a direct stress

$$\sigma = 10{,}040/0.785 = 12{,}790 \text{ lbs. per sq.in.}$$

This corresponds to a speed of the contact area of

$$\sigma/\sqrt{E\rho} = 12{,}790/\sqrt{30{,}000{,}000(0.000733)} = 12{,}790/148.3 = 87.42 \text{ in. per sec.}$$

Since the area of contact moves at one-half the speed of the striking bar, the velocity of the striking bar is

$$2(87.42) = 174.84 \text{ in. per sec.}$$

and the kinetic energy of the striking bar is

$$[(174.84)^2/2](W/g) = 15{,}285\,(27.81/386) = 1{,}101 \text{ in.lbs.}$$

If the bars are to be checked for buckling by the fictitious but conservative assumption that the full length of the bars is under stress during the entire contact time, Figs. 3 and 4 show that the effect of buckling is indeed small. Calculation for $t_r = 0.001{,}236$ sec. yields:

Center deflection at instant of separation of the bars

$$f_r = 0.5042 \text{ in.}$$

Transverse speed of centers at instant of separation

$$v_r = 6.827 \text{ in. per sec.}$$

Maximum deflection at center of bars

$$f_{max.} = 0.7141 \text{ in.}$$

Maximum bending stress

$$\sigma_{max.} = 2{,}027 \text{ lbs. per sq.in.}$$

Vibration energy

$$Q = 0.84 \text{ in.lbs.}$$

Thus, the maximum bending stress is less than 16 per cent of the direct stress due to impact. Of particular significance, however, is the fact that the vibration energy of less than 1 in.lb. is almost negligibly small in comparison with the energy of 1,100 in.lbs. transmitted from one bar to the other during impact.

REFERENCES

[1] Timoshenko, S., *Vibration Problems in Engineering*, 2nd Ed., p. 364; D. Van Nostrand Company, Inc., New York, 1937.

[2] Timoshenko, S., *Theory of Elastic Stability*, 1st Ed., p. 72; McGraw-Hill Book Company, Inc., New York, 1936.

[3] Timoshenko, S., *Theory of Elasticity*, 1st Ed., p. 387; McGraw-Hill Book Company, Inc., New York, 1934.

Reverse-Pitch Propellers as Airplane Landing Brakes

HAROLD B. CROCKETT* AND E. ARTHUR BONNEY*

Lockheed Aircraft Corporation

ABSTRACT

Reverse-pitch propellers, operating with full engine power, may be as effective in decelerating an airplane during the landing ground run as are conventional wheel brakes. The factors governing the effectiveness of reverse-pitch braking are power loading (W/P), wing loading (W/S), and such propeller characteristics as number of blades, diameter, and activity factor in comparison with conventional wheel braking. The result of varying the first two of the above factors is studied for the case of an airplane with a tricycle landing gear, and the method of calculation is developed.

The great safety advantage of reverse-pitch braking for large airplanes landing on ice-covered, snow-covered, or wet runways is emphasized; the possibility of reducing the landing airport length required by the C.A.A. is discussed; and the reduction in tire and brake maintenance and replacement costs due to everyday use of reverse-pitch braking is considered.

Also considered is the feasibility of reducing the glide plus transition distance by applying reverse-pitch braking during the final stage of the transition to eliminate floating.

INTRODUCTION

INDICATIONS ARE that for acceptable safety in landing on snow- or sleet-covered runways of reasonable length, or in the event of wheel brake failure, the large airliners, cargo planes, and bombers being designed today for immediate and postwar use must be equipped with some type of auxiliary landing brakes such as reverse-pitch propellers.

Besides the great safety advantage of reverse-pitch propellers, there is the advantage of reducing the normal landing or accelerate-stop ground run and that of reducing tire and brake maintenance and replacement. The latter item may represent a considerable saving for airplanes equipped with six or more large wheels.

This paper presents a simple method of estimating the landing ground run of an airplane with tricycle landing gear using reverse-pitch propellers as brakes and also indicates that reverse-pitch braking may be used to reduce the transition distance. The curves given show the calculated increments of landing distance, assuming different reverse-pitch power loadings, wing loadings, and wheel-brake friction coefficients (i.e., ground-resistance coefficients). Although calculations actually were made for a large transport airplane, the results are shown on a percentage basis for the sake of generality. To present the results in this manner is advantageous because the lift-drag relationships of various tricycle-geared airplanes in the landing run position are nearly enough equal to make the braking distance curves similar percentagewise.

As will become apparent, some of the numerical results and discussion are considered from the question, outside of safety, of most concern to the airplane manufacturer—that is, how much will the use of reverse thrust reduce the landing or take-off airport length required by the Civil Air Regulations? This point of view, which means comparing the effect of reverse-pitch propellers with that of *full application* of wheel brakes, does not show the effect of reverse-pitch propellers in so favorable a light as comparing their effect with that of the *normal* application of wheel brakes. Even if the advisability of using reverse-pitch propellers appeared questionable in this unfavorable light, the writers would recommend their use on large airplanes for the sake of gains in safety, brake maintenance, and ease of ground handling.

Other investigators[3, 4, 6] have indicated procedures for calculating the braking due to reverse-pitch propellers. By comparison, it may be seen that the method used in this paper differs from that of the references chiefly in the determination of the thrust of the reverse-pitch propellers. Herein, derivation of the ground run equation is shown in detail; however, the curves calculated from the equation are of most general interest. These are presented first.

RESULTS

The accompanying figures present the effect on total landing distance, and in particular on ground run, of using reverse-pitch propellers alone or in conjunction with wheel brakes. Note that *all the curves and subsequent derivations are for an airplane having four-bladed propellers, a tricycle landing gear, and landing flaps down unless otherwise noted.*

Calculations actually were made for a large transport airplane powered with four engines, but the results are presented on a percentage basis so that they may be more general. A separate investigation of the landing run of a medium-sized twin-engined airplane indicates that the curves of this paper give correct trends of the effect of using reverse-pitch propellers for braking two- as well as four-engined airplanes.

Received November 13, 1944. To have been presented at the I.A.S. Thirteenth Annual Meeting, which was canceled to cooperate with a Government appeal (January, 1945) to refrain from holding conventions and meetings.

* Aerodynamicists.

No flight tests of airplanes equipped with reverse-pitch propellers have been made at Lockheed. However, the results of this study are in agreement with the statement of McCoy[2] that reverse-pitch propellers may be as effective in decelerating an airplane during the landing ground run as are conventional wheel brakes. The results are also in agreement with the tests reported by Sheets and MacKinney.[6]

In the interest of clarity the following statements are made concerning, among other items, the approximations used, even though some of these may also be mentioned later. For more detailed calculations than required by preliminary design work, the approximations may be eliminated.

(a) W/S = airplane gross weight (lbs.) for condition considered divided by wing area (sq.ft.).
W/P = airplane gross weight (lbs.) for condition considered divided by total power (b.hp.) for condition considered.

(b) The airplane is assumed to land at stalling air speed, even though the average airplane landing ordinarily is made at 1.05 to 1.1 times the stalling speed.

(c) A 3-sec. free rolling period at stalling speed is assumed—i.e., the deceleration is neglected during this time.

(d) For simplicity, the braking force is assumed to be based on a normal force equal to the total airplane weight minus the lift. It is believed that most tricycle gears employ braking on the main gear only; hence, the above assumption is unconservative for a refined calculation. In the latter instance, the total braking force would be *free-roll ground resistance coefficient* times *weight minus lift on nose gear* plus *braking coefficient* times *weight minus lift on main gear.*

(e) In the calculation of the braked or unbraked ground run without use of the reverse-pitch propellers, the drag of the windmilling propellers is neglected. For the unbraked roll the effect might be appreciable, although the free-roll μ of 0.05 assumed and defined below should be high enough to account for it.

(f) No reduction in lift after application of reverse thrust is assumed. This assumption is conservative.

A short discussion of the braking coefficients μ and μ_e and of the landing speeds assumed precedes the discussion of the figures.

Braking Coefficients

The wheel-braking coefficient μ is a measure of the effectiveness of the wheel brakes and is defined as the ratio of the rolling friction (horizontal resistance) to the normal force (weight minus lift). For comparative purpose, it is convenient to define an *effective braking coefficient* μ_e as that obtained using reverse-pitch propellers alone or in combination with wheel brakes. By definition, the coefficients μ and μ_e are numerically equal for equal airplane stopping distances.

The wheel-braking coefficient μ with brakes fully applied varies from 0.4 to 0.6 for airplanes having tricycle gear operating on a macadam or concrete runway. Table 1 shows representative values of μ for various landing surfaces determined by Der Muhll,[3] the N.A.C.A.,[7] Lockheed, etc.:

TABLE 1

Type of Surface	Brakes Off	Brakes Fully Applied
	Average ground-resistance coefficient	Average wheel-braking coefficient
Concrete or macadam	0.03 to 0.05	0.4 to 0.6
Hard turf	0.05	0.4
Firm and dry	....	0.33
Soft turf	0.07	....
Wet concrete	0.05	0.30
Wet grass	0.10	0.20
Snow- or ice-covered field	0.02	0.07 to 0.10

Landing Speeds

In the curves, various factors are plotted with wing loading as a parameter—that is, the airplane is assumed to land at different weights. Further, the assumption is made that the airplane touches the ground at the stalling speed. With the same $C_{L\text{stall}}$ used for landing at any weight, the landing speeds for the wing loadings considered become as follows:

W/S	Landing Speed, Mph.
45	82
40	77
35	72
30	67

Distance to Land over a 50-Ft. Obstacle with and Without Propellers Reversed

The C.A.A. specifies in CAR 04.7533-T and CAR 61.7124 that the landing runway used by a transport airplane must be the minimum distance required for landing over a 50-ft. obstacle, divided by 0.6. Where flight tests have not been made, this minimum distance is calculated in the following increments:

(a) Horizontal distance needed to lose 50 ft. of altitude at a gliding speed of 1.3 times the landing-flaps-down stalling speed = $1.3V_{\text{stal}}$

(b) Horizontal distance required for transition at the ground = from $1.3V_{\text{stall}}$ to V_{stall}.

(c) Rolling distance before braking is applied. Unless otherwise noted, the free rolling distance herein is considered to be that for a 3-sec. run at stalling speed.

This assumption takes care of pilot reaction time, airplane inertia effects, etc. The 3-sec. run is conservative, for Lockheed Constellation flight tests indicate only 2 sec. taken.

(d) Braking distance with maximum braking force available.

Fig. 1a shows the relative values of the above increments for a large transport airplane having a wing loading of 44, and either power off, a reverse-pitch power loading of 32 (two engines operating), or of 16 (four engines operating) and with or without wheel brakes applied. Note that the minimum landing distance with power off and wheel brakes fully applied ($\mu = 0.5$) is taken as 100 per cent in Fig. 1a. This 100 per cent divided by 0.6 gives 167 per cent, the runway length required by the C.A.A. and indicated on the figure.

Neglecting, for a moment, consideration of the solid triangles and circles on Fig. 1a, the following observations hold:

(a) If the brakes failed or the field were icy and no reverse-pitch power were available—that is, $\mu = 0.05$—the airplane would run off the runway specified by the C.A.A. regulations. The high wing loading upon landing and the great rolling distance occasioned by brake failure when a tricycle landing gear is used are the factors that tend to make the emergency landing distance greater than the runway length required by the C.A.A. From Fig. 3, to be discussed later, may be established the fact that for $\mu = 0.05$, an in-bounds brakes-off landing may be made at a wing loading of about 30 instead of 44; and as a matter of interest, a separate calculation shows that, were the airplane with a wing loading of 44 equipped with a conventional gear, the total landing distance would be 174 per cent with brakes off, as compared with the 214 per cent for the airplane with tricycle gear and the 167 per cent required. The writers do not suggest an increase of the runway length required by the C.A.A. but, rather, propose that safe landings may be made on presently authorized fields under icy conditions or in the event of brake failure if the airplane in question is equipped with reverse-pitch propellers.

(b) In Fig. 1a, with two engines operating at a total reverse-pitch power loading of 32 and without brakes applied, the airplane will stop in 138 per cent of the best wheel-braking-only distance (i.e., normal minimum landing distance), as compared with the 167 per cent required.

(c) In the example of Fig. 1a, the braking distance X_b is less with wheel brakes operating alone than with four reverse-pitch propellers operating alone. As will be shown later, these distances may be equal if the reverse-pitch power loading is less (i.e., power more); on smaller airplanes, a wheel-braking μ of 0.4 may be the maximum obtainable, and, hence, the basis of comparison rather than μ of 0.5, in which case the propellers will be more effective comparatively.

(d) With wheel-braking $\mu = 0.5$, the braking distance is only 20 per cent of the total landing distance; therefore, the reduction in total landing distance due to *supplementing full wheel-braking* is relatively small. This fact tends to emphasize again that reverse-pitch braking may best be utilized (1) to increase safety and (2) to reduce wheel-brake and tire maintenance and replacement by using only moderate wheel-braking in conjunction with moderate reverse-pitch braking.

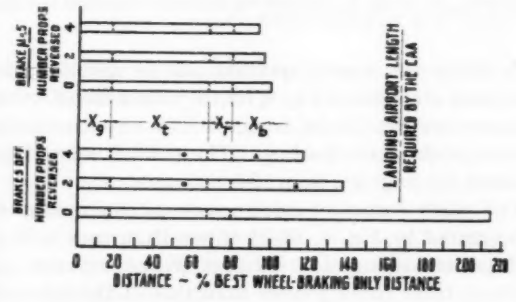

FIG. 1a. Distance to land over a 50-ft. obstacle with and without propellers reversed. $W/S = 44$; $W/P = 16$ with four propellers reversed, and $W/P = 32$ with two propellers reversed.
Key: X_g = glide distance; X_t = transition distance; X_r = rolling distance before brakes and/or reversed propellers are applied; X_b = braking distance.

Reduction in Transition Distance

From Fig. 1a, it appears that the easiest way to reduce the total landing distance a sizable amount is to cut down the transition distance. The solid triangles on Fig. 1a indicate the total landing distance if reverse-pitch power is applied when the airplane is in the final stages of transition (3 to 4 ft. off the ground). The solid circles indicate the point at which the airplane touches the ground if the assumptions are made that the pilot calls for reverse pitch as the plane passes 75 per cent of the calculated transition distance and that the copilot or engineer supplies the reverse-pitch power within 2 sec. of the request. Note that in this case the free roll on the ground is eliminated and this distance is saved, in addition to the 20–22 per cent of calculated transition distance saved.

No doubt certain aerodynamic,* mechanical, and psychological problems will have to be solved,[6] but the practicability of reducing the transition distance is substantiated by Fig. 1b, wherein a comparison of calculated and flight-test glide-plus-transition distance ($X_g + X_t$) is given. Lockheed Constellation (Model 49) test glide and transition distances are compared with values calculated by the methods of this paper from the aerodynamic report for that airplane. Fig. 1b shows that in one case floating (4 ft. up) occurred, which caused the airplane to land at 120 per cent

* The aerodynamic effects such as increased stalling speed and lessening of control due to interference with the slipstream are recognized and must be allowed for when considering the reverse-pitch propellers for reducing this distance.

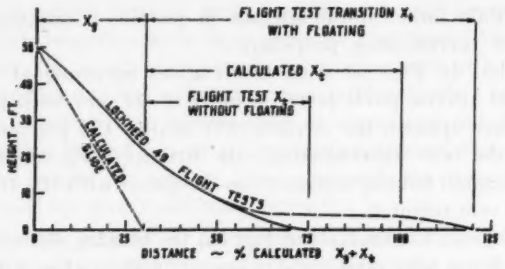

FIG. 1b. Comparison of calculated and flight-test glide plus transition distance.

calculated $X_g + X_t$; however, in the other instance the airplane landed at 75 per cent $X_g + X_t$. In each of these flights the pilot held a gliding speed of 1.3 V_{stall}. If negative thrust had been applied in the first case when the airplane was about 4 ft. off the ground, the floating would have been eliminated. Sheets and MacKinney[6] indicate, on the basis of tests, that applying negative thrust when the plane is 10 ft. off the ground is much too drastic; however, the writers of the present paper feel that, as the use of reverse-pitch propellers becomes more common, techniques will be developed for eliminating floating during the final stage of transition.

For ease of discussion, reference is made to "reverse-pitch propellers operating alone" and "reverse-pitch power loading." However, all ground run distances calculated with power on include the effect of rolling friction with brakes off—that is, $\mu = 0.05$.

Effective Braking Coefficient μ_e with and Without Propellers Reversed

Fig. 2 shows the effective braking coefficients μ_e corresponding to the braking distances X_b shown in Fig. 1a. The distance C required to stop with wheel brakes having a μ of 0.5 and with power off is taken as 100 per cent.

For the power conditions of the example of Fig. 2, the four reverse-pitch propellers ($W/P = 16$) develop an effective braking coefficient of only 0.26. However, as may be seen from the figures following, which are of a general nature, decreasing the reverse-pitch power loading sufficiently will increase the effective braking coefficient μ_e to any desired value up to a maximum of about 0.5.

General Curves

The wheel-braking distance is shown for various wing loadings in Fig. 3. Because the landing speed is greater for greater wing loading at any constant μ, the landing distance is greater. Of particular interest is the fact that the braking distance rapidly increases for μ less than 0.3.

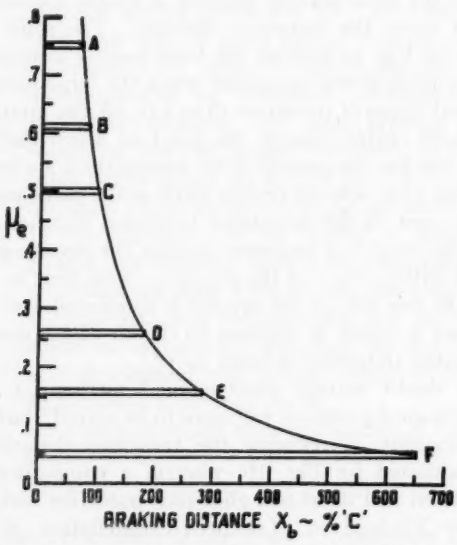

FIG. 2. Effective braking coefficient μ_e with and without propellers reversed. $W/S = 44$.

Key: A = wheel-braking μ of 0.5; four propellers reversed; $W/P = 16$.
B = wheel-braking μ of 0.5; two propellers reversed; $W/P = 32$.
C = wheel-braking μ of 0.5; no power.
D = no wheel braking ($\mu = 0.05$); four propellers reversed; $W/P = 16$.
E = no wheel braking ($\mu = 0.05$); two propellers reversed; $W/P = 32$.
F = no wheel braking, no power; $\mu_e = L = 0.05$.

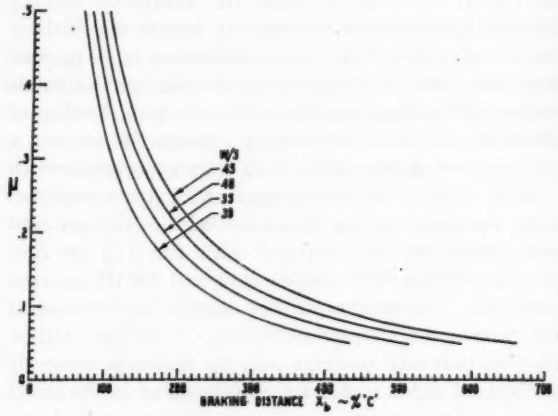

FIG. 3. Wheel-braking distance vs. wheel-braking coefficient. No power. As in Fig. 2, C is braking distance with wheel-braking μ of 0.5, W/S of 44, and no power.

Probably the most important curves developed in this paper are those of Fig. 4, for they show the effective braking coefficient to be expected from any reasonable reverse-pitch power loading. The distinct advantage of power loadings less than 12 is indicated.

The safety feature of using reverse-pitch propellers is accentuated by Fig. 4, which shows that, even with a high power loading of 36—that is, with low power—μ_e is about three times greater than that of the value of 0.05 which holds for the condition of no braking. Referring to Fig. 2, one may see that the above fact means a reduction in ground run to less than half that necessary with no wheel brakes or power.

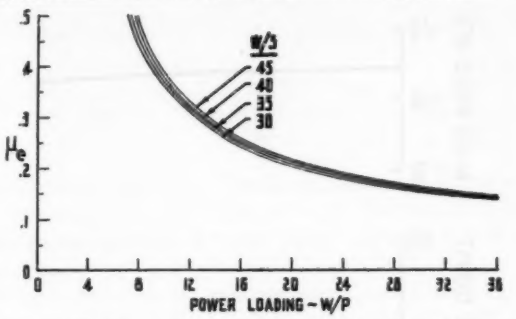

FIG. 4. Effective braking coefficient obtainable with various reverse-pitch power loadings.

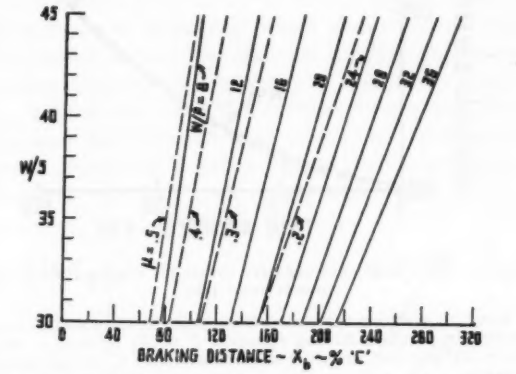

FIG. 5. Variation of braking distance with wing loading. Landing speeds vary from 67 to 82 m.p.h. for wing loadings from 30 to 45, respectively.

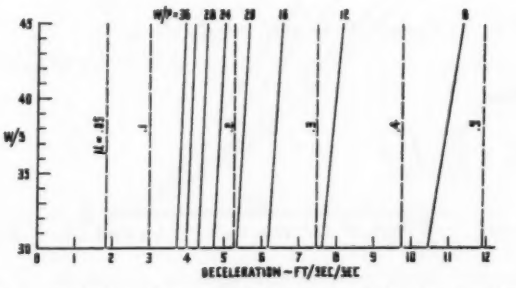

FIG. 6. Variation of average deceleration with wing loading.

Fig. 5 shows a straight-line increase of braking distance X_b with wing loading for both lines of constant wheel-braking coefficient μ and lines of constant reverse-pitch power loading. This variation is to be expected for the constant μ lines from the equation for braking distance X_b given later if one considers that $V_s^2 \div (1/C_{L_s})$ is proportional to W/S. It is not obvious from the equation for X_b that the constant power loading lines should be straight.

Fig. 6 shows the variation of average deceleration with wing loading for both lines of constant coefficient μ and lines of reverse-pitch power loading. That the deceleration is constant with wing loading for any wheel-braking coefficient μ is to be anticipated from the definition of μ, since a constant value of μ implies a constant ratio between the decelerating force and the normal force.

For all the constant power loading curves herein, the approximation is made that thrust/power remains constant for any given speed. Therefore, since negative thrust increases with speed, the deceleration for constant power loading increases with wing loading.

Fig. 6 gives a deceleration of 11.9 ft. per sec. per sec. for $\mu = 0.5$ (wheel brakes applied alone). Wheel braking in combination with reverse-pitch braking gives even higher decelerations. For comparative purposes, it may be stated that reference 5 indicates the maximum deceleration of the Douglas DC-3 during the landing run to be about 7 ft. per sec. per sec. For ordinary landings, decelerations of 6 to 7 ft. per sec. per sec. are desirable.

DERIVATION OF FORMULAS

The nomenclature used in the derivation of the formulas for landing distance is as follows:

Basic Symbols

- X = ground distance, ft.
- D = drag, lbs.
- L = lift, lbs.
- W = landing weight, lbs.
- m = mass of airplane = W/g = lb.-sec.^{2} per ft.
- T = total negative thrust of one propeller
- F = total retarding force at any point during braking distance
- C_L = lift coefficient
- C_D = drag coefficient
- μ = coefficient of friction ($\mu = 0.05$ with no wheel braking or reverse-pitch braking)
- V = speed in m.p.h.
- v = speed in ft. per sec.
- S = wing area
- σ = density ratio at altitude
- a = acceleration (negative if deceleration) in ft. per sec.^{2}
- n = number of engines operating with propellers in reverse pitch
- g = acceleration due to gravity, ft. per sec.^{2}

Subscripts

- g = gliding
- t = transition
- r = rolling (no retarding force)
- b = braking (wheel and/or negative thrust of propellers)
- s = stalling conditions (power-off)
- run = conditions at ground-run attitude

The landing distance is the sum of the glide distance from a height of 50 ft., the transition distance, the distance covered in the 3 sec. required to apply the brakes and/or decrease propeller pitch, and the ground run required for stopping after the brakes are applied. The method of computation in this analysis is derived as follows:

Glide from 50 Ft.

Gliding angle

$$\theta = \tan^{-1}(D/L)_g = \tan^{-1}(50/X_g)$$

$$X_g = 50\,(L_g/D_g) = 50\,(C_{L_g}/C_{D_k})$$

Transition from V_g to V_s, Where $V_g = 1.3\,V_s$

From the relation

$$X_t = 2.15 \int_{V_g}^{V_s} (V\,dV)/a$$

wherein the acceleration can be expressed as

$$a = -F/m = -F_g/W = -[(D_g + D_s)/2](g/W)$$

the expression for the transition distance in terms of the known quantities can be derived and is shown here:

$$X_t = W/S[18.00/(1.69\,C_{D_g} + C_{D_{s_{\text{ground}}}})\sigma]$$

In the event that no wind-tunnel data are available from which to determine the drag coefficient at stalling speed at the ground $C_{D_{s_{\text{ground}}}}$ it may be assumed conservatively that the reduction in drag coefficient due to the ground effect is equal to the drag coefficient increment of the landing gear.

Rolling Distance for 3 Sec.

$$X_r = (3)(V_s)(1.467) = 4.4\,V_s$$

Distance To Stop with Wheel Brakes Applied and Propellers in Reverse Pitch with Power On

Braking distance,

$$X_b = \int_{v_s}^{0} (v\,dv)/a = \int_{v_s}^{0} dv^2/2a$$

where $a = -Fg/W$.

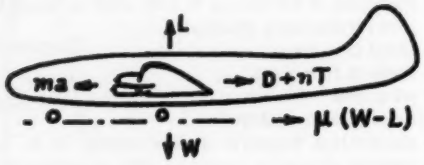

The total retarding force F is the sum of the airplane drag, the negative thrust of the reverse-pitch propellers, and the wheel-braking resistance, as follows:

$$F = D + nT + \mu(W - L)$$

Here, conservatively, the reduction in lift due to reverse slipstream effects is neglected.

The negative thrust of one propeller T is found by the method outlined in reference 4* and in general will closely approximate a parabolic curve when plotted against speed, as shown in Fig. 7. Hence, the thrust can be represented by an equation as follows:

$$T = K_1 + K_2 v^2$$

* Later data than those given in reference 4 are available but have a security rating of "Restricted."

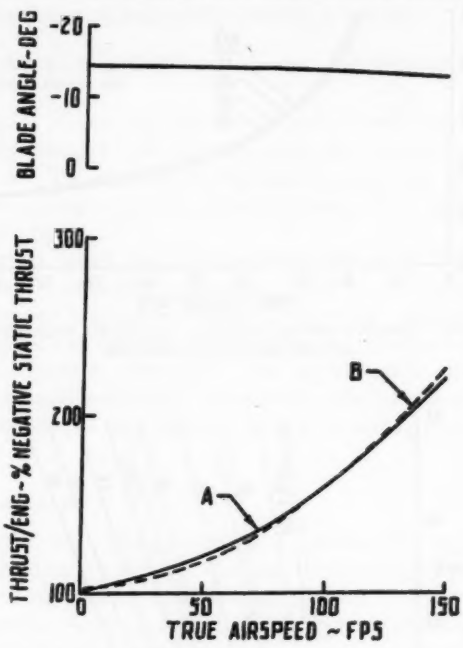

FIG. 7. Blade angle and negative thrust per engine at M.E.T.O. power and r.p.m.

Key: A = thrust calculated from propeller data and B = approximate parabola having equation $T = K_1 + K_2 v^2_{ps}$, where $K_1 \approx 100$ per cent negative static thrust and K_2 = appropriate constant.

Therefore,

$$F = {}^1/_2\,C_D \sigma \rho_0 v^2\,S + n(K_1 + K_2\,v^2) + \mu(W - {}^1/_2 \sigma \rho_0 C_L\,v^2 S)$$

Now,

$$X_b = \frac{W}{2g} \int_{v_s}^{0} \times \frac{dv^2}{-\mu W - K_1 n + v^2\,(\mu\,{}^1/_2 \sigma \rho_0\,C_L S - {}^1/_2\,\sigma \rho_0 C_D S - K_2 n)}$$

$$= \frac{W/2g}{\mu\,{}^1/_2 \sigma \rho_0\,C_L S - {}^1/_2\,\sigma \rho_0\,C_D S - K_2 n} \times \log_e \frac{\mu W + K_1 n}{\mu W + K_1 n - v^2\,(\mu\,{}^1/_2\,\sigma \rho_0\,C_L S - {}^1/_2\,\sigma \rho_0\,C_D S - K_2 n)}$$

However,

$${}^1/_2\,\sigma \rho_0\,v_s^2\,S/W = 1/C_{L_s}$$

Therefore,

$$X_b = \frac{v_s^2/2g}{[(\mu C_L - C_D)/C_{L_s}] - (K_2 n v_s^2/W)} \times \log_e \frac{\mu + (K_1 n/W)}{\mu + (K_1 n/W) + (K_2 n\,v_s^2/W) - [(\mu C_L - C_D)/C_{L_s}]}$$

or,

$$X_b = \frac{0.0334\ V_{sm.p.h.}^2}{[(\mu C_L - C_D)/C_{L_s}] - (2.15\ n\ K_2\ V_{sm.p.h.}^2/W)} \times$$

$$\log_e \frac{\mu + (K_1 n/W)}{\frac{\mu + K_1 n}{W} + \frac{2.15\ K_2 n V_{sm.p.h.}^2}{W} - \frac{\mu C_L - C_D}{\dot{C}_{L_s}}}$$

Notice that if the terms containing items due to propeller thrust are removed (i.e., $n = 0$), the conventional formula for braking distance using only wheel brakes remains.

Figs. 8 and 9 show, without units, data from which the negative thrust at constant propeller speed is calculated. The thrust is calculated as shown in any textbook on aerodynamics. Constant negative blade angle operation gives about the same negative thrust as constant speed operation, which means that choice between the two may be made by the propeller manufacturer, airplane manufacturer, or operator. In support of the statement of McCoy[2] that the negative blade angle need be no greater than −30°, Fig. 9 indicates a definite maximum negative thrust coefficient C_T obtainable as the blade angle is increased negatively.

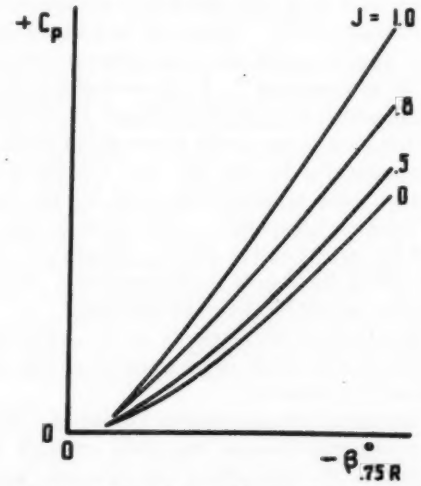

FIG. 8. Typical C_p vs. $\beta_{.75R}$ with propeller blades reversed. C_p = power coefficient; β = blade angle; J = advance ratio.

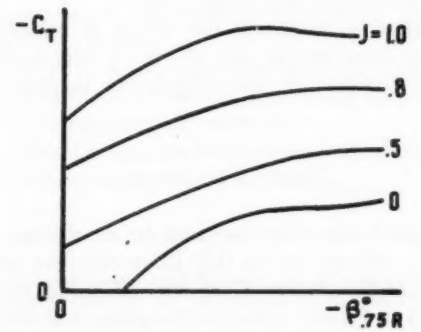

FIG. 9. Typical C_T vs. $\beta_{.75R}$ with propeller blades reversed. C_T = thrust coefficient; β = blade angle; J = advance ratio.

CONCLUSIONS

(1) Reverse-pitch propellers, operating with full engine power, may be as effective in decelerating an airplane during the landing ground run as are conventional wheel brakes.

(2) The greatest advantage of, and a sufficient one for using, reverse-pitch braking on airplanes having tricycle gear and a high wing loading is that of safety in landing on snow- or ice-covered runways or in bringing the airplane to a stop after wheel brake failure.

(3) By using reverse-pitch braking to reduce the transition distance and to eliminate the free rolling distance, the minimum landing distance may be reduced substantially. Therefore, when the Civil Aeronautics Administration allows the use of reverse-pitch propellers in air-line landing procedure, the required airport length for planes so equipped may be reduced.

(4) In calculating the braking distance X_b for the condition where reverse-pitch propellers are used, the speed versus negative thrust curve may be approximated by a parabola. This simplifies integration of the general equation for X_b.

(5) The problem of failure of an engine during reverse-pitch operation may be serious, particularly if the reverse-pitch power is applied while the airplane is still in the air in order to reduce the landing transition distance.

(6) McCoy[2] states that there is no danger of the engine's overheating during the ground run with full reverse-pitch power because only 20 sec. are required to make the stop.

(7) McCoy[2] also indicates that a maximum rate-of-pitch change of about 45° per sec. is desirable for reversing pitch at full throttle conditions, although flight tests by Sheets and MacKinney[6] show satisfactory operation at appreciably lower rates of pitch change. In any event, the rate of change must be fast enough to prevent the engine from overspeeding as the blade goes through 0°. Naturally, the quicker the reverse thrust is applied, the more effective it will be for braking. McCoy infers that 45° per sec. pitch change is, or soon will be, available and that the power required for changing the pitch of a four-bladed propeller at that rate will vary from ½ to 1 per cent of the normal rated power.

REFERENCES

[1] Der Muhl, A. V., *The Realization of the Aircraft Propeller Landing Brake*, Flugwehr u. Technik, Vol. 5, No. 2, pp. 51–54, February, 1943. Reprinted in the *Journal of The Royal Aeronautical Society*, Vol. 47, No. 395, p. 617, November, 1943.

[2] McCoy, H. M., *Propeller Design Requirements*, Journal of the Aeronautical Sciences, Vol. 11, No. 3, p. 261, July, 1944.

[3] Der Muhll, A. V., *The Effectiveness of the Propeller as a Landing Brake*, Flugwehr u. Technik, Vol. 5, No. 5, pp. 211–217, August, 1943. Reprinted in the *Journal of The Royal Aeronautical Society*, Vol. 47, No. 395, November, 1943. Also reprinted in more detail in *The Engineer's Digest*.

(*Continued on page 484*)

Influence of Prestressing and Cyclic Stressing on Stress-Strain Characteristics of Magnesium Alloys

F. A. RAPPLEYEA,* R. E. PERRY,† AND G. ANSEL†

The Dow Chemical Company

ABSTRACT

The factors that produce Bauschinger effects in most metals operate in magnesium. In addition, the stress-strain curves of magnesium upon prestressing or cyclic loading are influenced by the mechanisms of deformation (slip and twinning) occurring in this metal.

Data on the influence of prestressing and cyclic loading of wrought and cast commercial Dowmetal alloys are presented. The effects of recovery on the stress-strain curve are covered. The results are analyzed, and recommendations as to how to cope with the few problems caused by prestressing or cyclic loading are made.

This work demonstrates the following points:

(1) In service, cyclic stressing at stresses up to the yield point will result in no harmful effects on the magnesium structure.

(2) Accidental precompression loading of a magnesium-alloy structure beyond the yield strength is not detrimental to the strength of the structure upon reversal of stress. In the case of accidental pretension, immediate subsequent column action results in strengths slightly lower than the design values.

(3) Any deleterious effects caused by forming or fabrication can be eliminated by appropriate treatments.

INTRODUCTION

ONE OF THE IMPORTANT ITEMS of information which the designer must have in order to use a metal is the stress-strain curve. It is well known that the shape of this curve may be affected by cold-work or plastic deformation. In consequence, it is of interest to determine the effects on service characteristics of forming operations during fabrication of or accidental plastic deformation in service. The purpose of this paper is to present such information for magnesium alloys.

The problem of cyclic stressing of materials is not new. Investigators have already determined the effect of cyclic stressing on iron, steel, brass, etc.[1–7] It has been only recently that other investigators[8, 9, 11] have studied the effects of cyclic static stressing on magnesium alloys. It was found by these investigators that the stressing of wrought magnesium alloys in compression beyond the yield strength, followed by subsequent stressing in tension, produced a lowered tangent modulus curve. This does not, however, mean that the initial modulus of elasticity is lowered, since it is constant, being determined by the distance between atoms in the crystal structure. Extensive statistical studies as given in reference 10 have shown that a value of 6,500,000 lbs. per sq.in. is acceptable for the modulus of elasticity of commercial magnesium alloys.

The lowering of the tangent modulus curve as found upon tension stressing of compressed wrought magnesium alloys has led some designers to conjecture as to its possible effect upon the use of magnesium alloys as a structural material. However, it is to be pointed out that steel, copper, and brass show similar lowering of the proportional limit and therefore a reduction in the tangent modulus curve. Aluminum has shown similar effects, at least for cases where the tension stressing is followed by compression.[12] In the case of magnesium, however, in addition to the Bauschinger effects present in the other metals, the cyclic stress-strain studies are further complicated by the fact that the stress-strain characteristics are strongly influenced by the mechanisms of deformation operating, and the preferred orientation of the grains in the metal. These facts do not seriously affect the use of magnesium as a structural material, for, as will be shown in this work:

(1) In service, cyclic stressing at stresses up to the yield strength will result in no harmful effects on the magnesium-alloy structure.

(2) Accidental precompression loading of a magnesium-alloy structure beyond the yield strength is not detrimental to the strength of the structure upon reversal of stress. In the case of accidental pretension, immediate subsequent column action results in strengths slightly lower than the design values.

(3) If it is necessary, the effects of cold-forming can be avoided by the use of one of two methods—e.g., hot-forming or low-temperature thermal treatments.

TESTING TECHNIQUE

The specimens were prepared by machining round bars to a reduced section 0.75 in. in diameter and $1^1/_2$ in. long at the center of the bar. The bar was then threaded at the ends with the exception of $^1/_4$ in. at the extreme ends, which was machined to a diameter slightly less than the root diameter of the threads (see Fig. 1).

Received December 15, 1944. To have been presented at the I.A.S. Thirteenth Annual Meeting, which was canceled to cooperate with a Government appeal (January, 1945) to refrain from holding conventions and meetings.

* Development Engineering, Magnesium Division.

† Metallurgical Department.

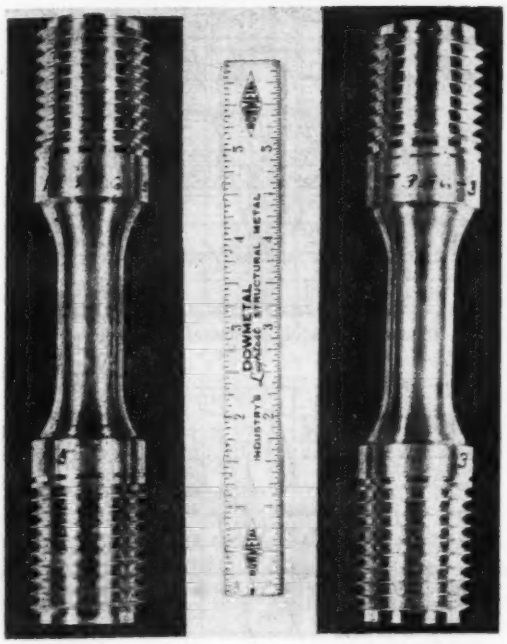

FIG. 1. Test specimen.

Tests were made in a 60,000-lb. Riehle universal testing machine. Tuckerman gages of 1-in. length were used to measure the strain in most cases. On the other tests autographic Templin recorders were used. In order to obtain axial alignment in compression, a ball-in-socket head was used. One of the difficulties of these tests was the fact that it was desired to run the test continuously without removal of the specimen from the machine. Obviously, this was impossible. In order to solve this problem, a change from the compression setup to the tension setup was made as rapidly as possible with care. Thus, creep and recovery were reduced to a minimum.

The materials investigated in this report are:

(1) Magnesium-alloy sand castings with random orientation and equal compression and tension yield strengths.

(2) Magnesium-alloy extrusions with preferred orientation and a compression yield strength 0.7 of the tension yield strength.

(3) High-strength magnesium-alloy extrusions with preferred orientation and a compression yield strength equal to the tension yield strength.

The typical properties of the classes of material used for this report are presented in Table 1.

TABLE 1
Typical Properties of Material Used

Dowmetal Alloy	Form	Tensile Strength, Lbs. per Sq.In.	Tensile Yield Strength, Lbs. per Sq.In.	Compressive Yield Strength, Lbs. per Sq.In.	Elongation in 2 In., Per Cent
C-HT	Casting	40,000	16,000	16,000	10
H-HT	Casting	40,000	14,000	14,000	12
FS-1	Extruded bar	40,000	30,000	17,000	15
O-1HTA	Extruded bar	52,500	38,500	36,000	8

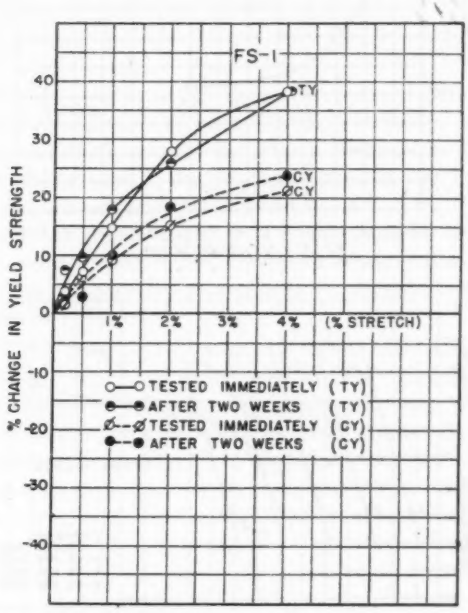

FIG. 2. Effect of prestretch on yield strengths of Dowmetal FS-1 extruded bar.

EXPERIMENTAL RESULTS

Effect of Prestressing and Recovery on Tension and Compression Properties of Dowmetal FS-1 and Dowmetal O-1HTA Extrusions

The material for this part of the work was obtained from 1-in. extruded rounds. The test bars were stretched or compressed to permanent deformations of 0.2, 0.5, 1.0, 2.0, and 4 per cent.

After prestressing, some bars were tested immediately. Stress-strain curves were obtained by autographic methods. The time between reversals of stress averaged about 2 min. A portion of the bars was held at room temperature for 2 weeks after prestressing and before final testing. Other bars were given a low-temperature thermal treatment of 1 hour at 350°F.

In Fig. 2 the effect of prestressing in tension upon the tension and compression yield strengths of Dowmetal FS-1 extrusions is presented. It is to be noted that this material, which has a compression to tension yield ratio of about 0.7, shows no lowering of the compression yield due to the initial tension stressing. On the contrary, the compression yield is raised by the stretching.

In the case of Dowmetal O-1HTA extrusions, which have a compression yield to tension yield ratio of 0.9–1.0, there is a definite decrease in compression yield due

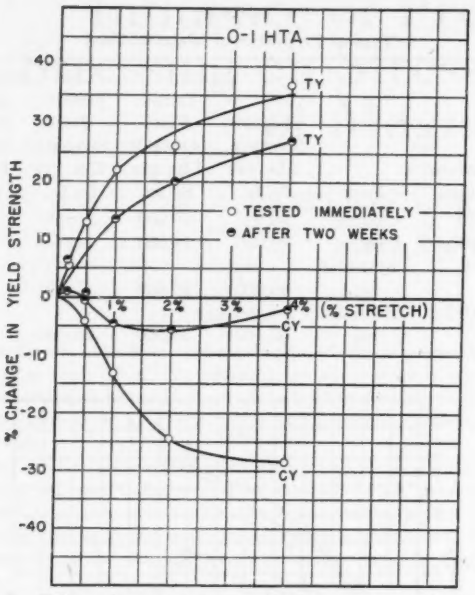

FIG. 3. Effect of prestretch on yield strengths of Dowmetal O-1HTA extruded bars.

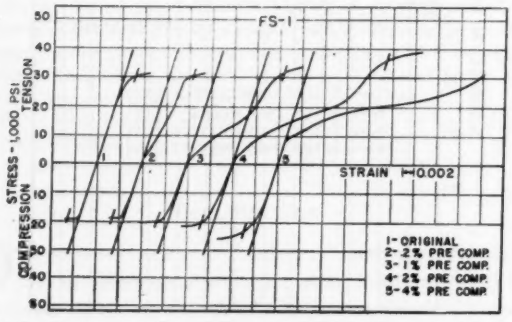

FIG. 4. Precompression of Dowmetal FS-1 alloy tested immediately. No. 5 tested in 20 min.

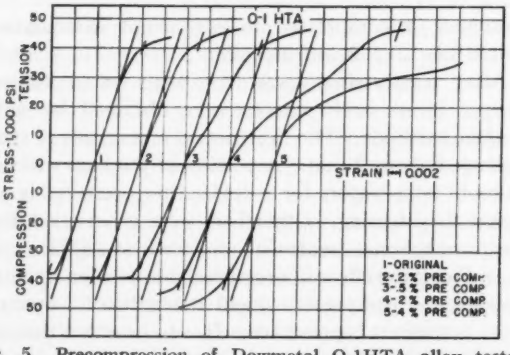

FIG. 5. Precompression of Dowmetal O-1HTA alloy tested immediately. No. 5 tested in 20 min.

to prestretching. As can be seen in Fig. 3, the effect is of considerable magnitude when the prestretch amounts to 2 per cent or more. Room temperature storing (2 weeks) allows substantial recovery of the compression-

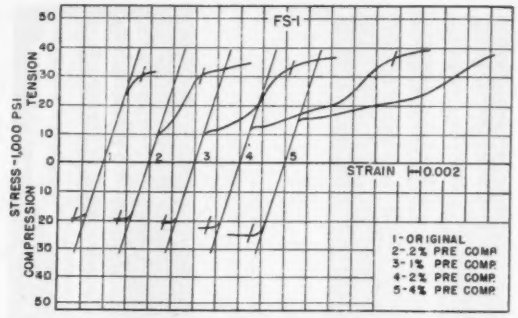

FIG. 6. Precompression of Dowmetal FS-1 alloy tested after 2 weeks.

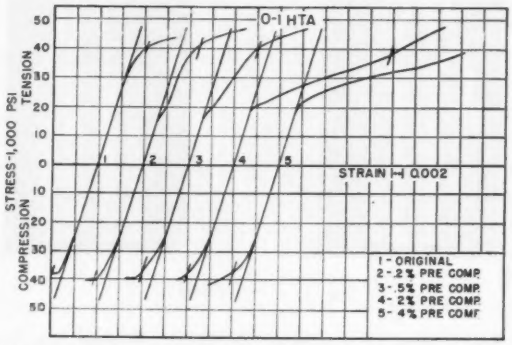

FIG. 7. Precompression of Dowmetal O-1HTA alloy tested after 2 weeks.

yield properties. Additional experiments have indicated that the original compression stress-strain curve is completely restored by a 1 hour anneal at 350°F. following the prestretch.

When a magnesium-alloy extrusion is subjected to precompression and then tested immediately in tension, the resulting stress-strain curve will show a deviation from the 6,500,000 lbs. per sq.in. modulus line at extremely low stresses—i.e., the proportional limit of this material is extremely low. Figs. 4 and 5 illustrate these effects on Dowmetal extrusions FS-1 and O-1HTA. These curves, as well as those in Figs. 6, 7, and 8, have been adjusted to a constant modulus of 6,500,000 lbs. per sq.in. for uniformity by laying off the strain at various loads from the 6,500,000 lbs. per sq.in. modulus line equivalent to the strain from the actual test modulus. In actual test the autographic moduli varied from about 6,000,000 to 7,000,000 lbs. per sq.in.

The majority of the curves in Figs. 4 and 5 were made by immediate testing after precompression. However, the stress-strain curves of the material precompressed 4 per cent (Curve 5 in Figs. 4 and 5) show the effect of a 20-min. recovery period on the proportional limit in tension. The 20-min. wait on the 4 per cent precompressed specimen was caused by inability to reload axially without machining. The influence of room temperature recovery is further illustrated in Figs. 6 and 7, which represent the stress-strain curves of precompres-

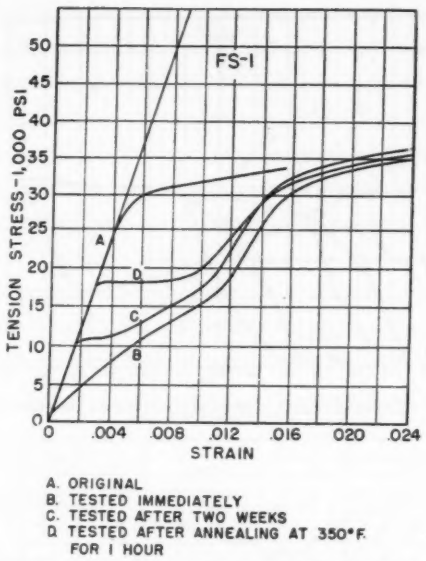

FIG. 8. Effect of 1.0 per cent precompression and recovery upon tension stress strain characteristics of Dowmetal FS-1.

sed extrusions after holding at room temperature for 2 weeks. It will be noted that, though room temperature recovery partially restores the original elastic characteristics, the stress and 0.2 per cent deviation from the modulus in tension is still lower than the original tension yield.

In Fig. 8 the effect of 1.0 per cent precompression on various stress-strain curves in tension is illustrated for Dowmetal FS-1. The influence of room temperature recovery and of a low temperature thermal treatment upon the elastic properties is quite pronounced. In fact, the curve for the 350°F. treatment indicates that the residual stresses have been reduced to a negligible amount. The yield strength in tension now equals the original compression yield.

The effect of precompression on the tension characteristics involves the largest departure from the normal stress-strain curve of any of the data presented. However, it is to be noted on the curves presented in Figs. 4, 5, 6, and 7 that the stress (indicated by the slanted line) at the strain corresponding to the original tension yield strain, plus the compression strain to which the bar was subjected, is equal to the original yield stress.

Ordinarily, precompression strains greater than the original compression yield strain will only be encountered in forming operations. Even in these cases, the high amounts of compression will most likely have taken place in a bending operation, where only a portion of the cross section is subject to plastic compression. In addition, a majority of formed parts will be stressed at right angles to the direction of forming, for which manner of loading there is no lowering of properties. For example, a hat section roll formed from Dowmetal FS-1a sheet exhibited the same stress-strain characteristics as the original sheet.

TABLE 2

Influence of Forming Temperature on Tension and Compression Properties of Extruded Dowmetal J-1

	Properties in Compression Prestrained Areas		Properties in Tension Prestrained Areas	
Condition	Tensile Yield Strength, Lbs. per Sq.In.	Compressive Yield Strength, Lbs. per Sq.In.	Tensile Yield Strength, Lbs. per Sq.In.	Compressive Yield Strength, Lbs. per Sq.In.
As extruded	34,000	19,000	34,000	19,000
Formed at room temperature	17,600	36,000	42,500	23,900
Formed at 600°F.	33,100	20,300	36,000	21,200

Service experience has shown no cases of failure or excessive deflection of formed parts. However, if it is suspected that excessive deflections might occur, it has been shown that, if the forming is done at 600°F., the decrease in tension yield is avoided. A $1^1/_2$ by $1^1/_2$-in. square bar of Dowmetal J-1, compression to tension yield ratio of about 0.7, was bent to a $9/^1/_2$-in. radius both at room temperature and at 600°F. Results are presented in Table 2.

In the case of Dowmetal O-1HTA extrusions the above procedure cannot be used without an additional step consisting of a reheat-treatment and age. If the above treatment is impractical, an alternative method would be one in which the material is formed before aging and then aged for 24 hours at 350°F. Both of these methods will restore the properties of the formed part almost to those of unformed Dowmetal O-1HTA.

Influence of Prestressing in Tension Upon Column Properties of a Dowmetal O-1HTA Extrusion

As has been shown in Fig. 3, the compression yield strength of Dowmetal O-1HTA is decreased when the metal has been prestretched immediately beforehand. The effects of this lowered compression yield strength on the column properties of Dowmetal O-1HTA are of interest. For that reason some Dowmetal O-1HTA was stretched to approximately 1 per cent permanent set and then immediately tested (within 8–50 min.) as a pin-ended column. The resultant curve is shown in Fig. 9. On this curve is also shown a column curve for Dowmetal O-1HTA from the same stock in the original unstretched condition. A comparison of these curves shows about a 10 per cent decrease in column strength for the stretched material at values of slenderness ratio (l/i) less than 100.

It is to be strongly emphasized that the above results are not peculiar to magnesium alloys but will occur under similar circumstances in any metal exhibiting the Bauschinger phenomenon.

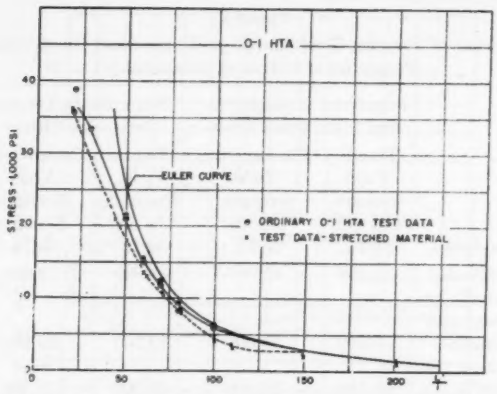

FIG. 9. Plot of column data for Dowmetal O-1HTA prestretched 1.0 per cent in tension and also as fabricated. Nominal size 1/2-in. round extrusions—pin-ended tests.

Cyclic Testing—Wrought and Cast Magnesium Alloys

To complete the study on cyclic stressing of magnesium alloys, different types of cycles on both cast and wrought alloys were run. These cycles were as follows:

(1) Tension to 1 per cent, tension to 2 per cent, tension to 3 per cent.

(2) Compression to 1 per cent, compression to 2 per cent, compression to 3 per cent.

(3) Tension to 1 per cent, compression to 1 per cent, tension to 1 per cent.

(4) Compression to 1 per cent, tension to 1 per cent, compression to 1 per cent.

(5) Multicycle stressing, loading first in compression and keeping the limits of strain to 1 per cent compression and 1 per cent tension.

(6) Compression to 0.7 per cent and tension to 0.7 per cent.

Dowmetal alloys C-HT, H-HT, and O-1HTA (with a ratio of compression yield strength to tension yield strength of one) were tested. These alloys were chosen to give a general picture of the behavior of alloys with random orientation of crystals versus alloys with preferred orientation. All strains were measured by means of Tuckerman extensometers, and the resulting stress-strain diagrams are given in Figs. 10–20.

A detailed study of Figs. 10–20 is presented below:

In the case of Figs. 10 and 11, representing successive cycles of tension, it is to be noted that the yield strength is raised by the prestressing. In the case of Dowmetal O-1HTA, Fig. 11, the proportional limit is decreased by the prestressing. Similar results have been found in iron and steel.[13] In the case of the cast material there appears to be an increase in the proportional limit.

Figs. 12 and 13 indicate that the behavior of magnesium alloys when subjected to successive compression cycles is similar to that occurring in cyclic tension stressing.

Figs. 14 and 15 indicate that the proportional limit in compression decreases because of prestressing in tension, thus exhibiting the characteristic Bauschinger

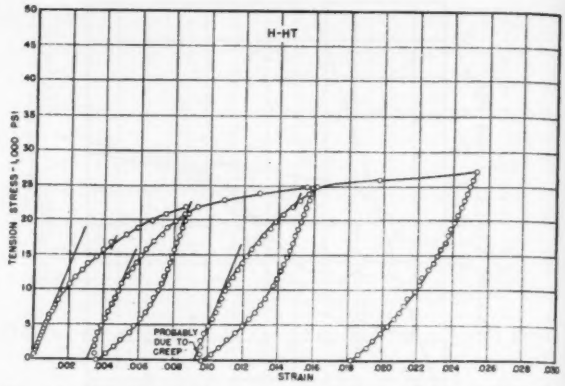

FIG. 10. Effect of repeated tension stressing on Dowmetal H-HT.

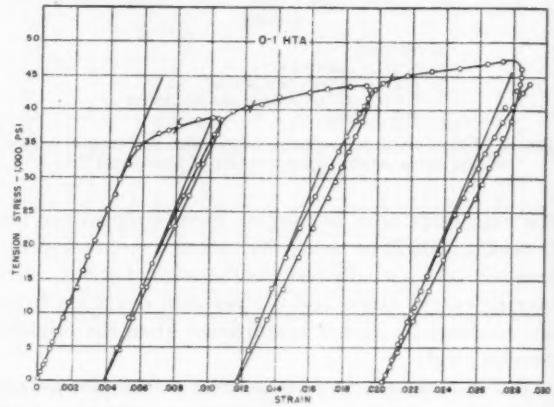

FIG. 11. Effect of repeated tension stressing on Dowmetal O-1HTA.

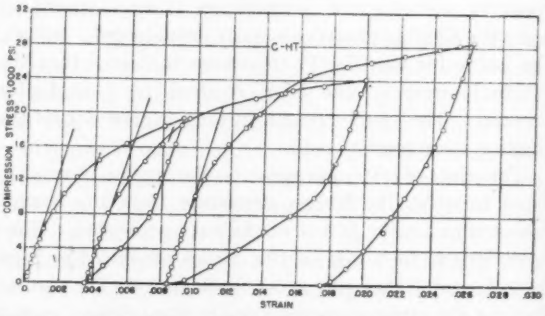

FIG. 12. Effect of repeated compression stressing on Dowmetal C-HT.

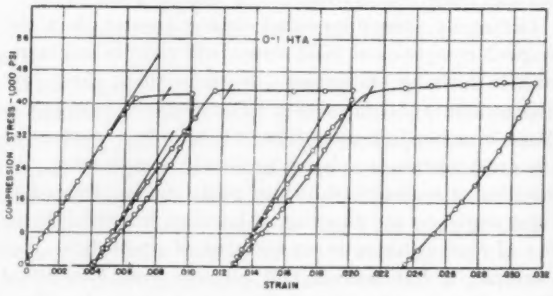

FIG. 13. Effect of repeated compression stressing on Dowmetal O-1HTA.

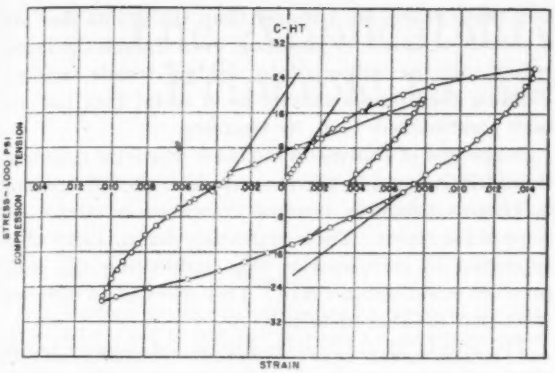

FIG. 14. Effects of cyclic stressing on Dowmetal C-HT tension-compression-tension.

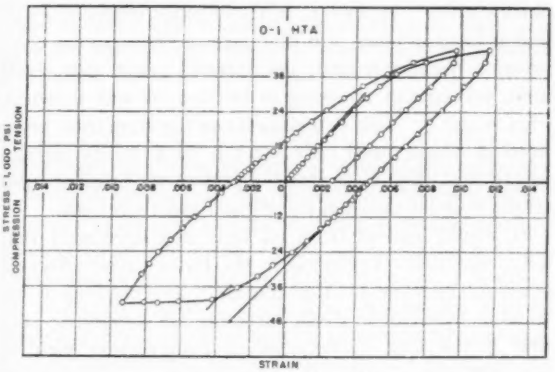

FIG. 15. Effects of cyclic stressing on Dowmetal O-1HTA tension-compression-tension.

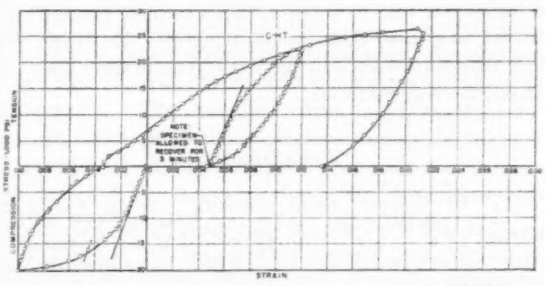

FIG. 16. Effects of cyclic stressing on Dowmetal C-HT compression-tension-compression.

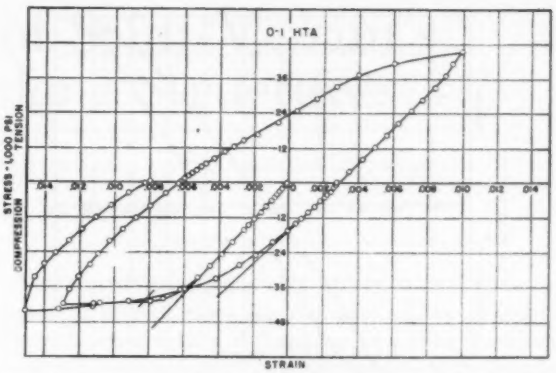

FIG. 17. Effects of cyclic stressing on Dowmetal O-1HTA compression-tension-compression.

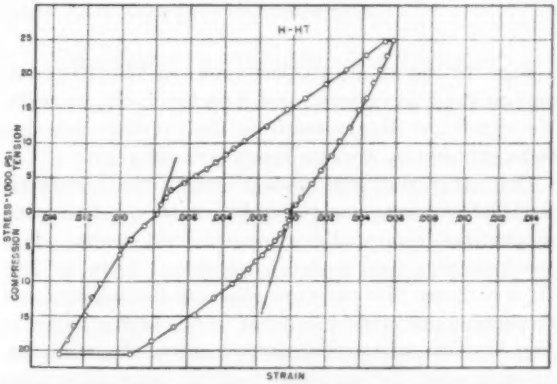

FIG. 18. Effect of compression-tension cyclic stressing for 15 cycles on Dowmetal H-HT. Last cycle is recorded here.

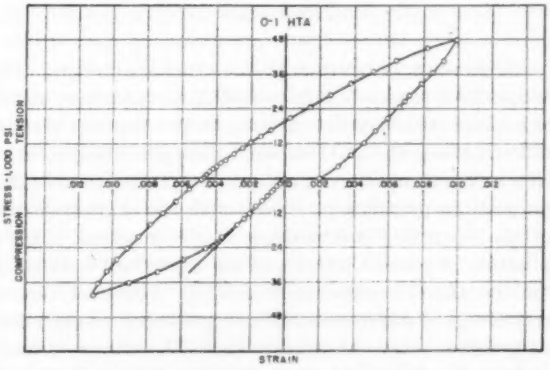

FIG. 19. Effect of compression-tension cyclic stressing for 8 cycles on Dowmetal O-1HTA. Last cycle is recorded here.

effect. However, in agreement with Fig. 3 for small amounts of permanent stretch, there is little lowering of the compression yield strength in Dowmetal O-1HTA. Upon reapplication of tension stressing there is an early deviation from the 6,500,000 lbs. per sq.in. modulus. In the case of the cast material, a small portion of the original elastic properties are recovered. Further examination of the curve of the second tension cycle shows that the stress at a strain from the zero point equal to the original tension yield strain is approximately equal to the original tension yield stress.

In Figs. 16 and 17, the Dowmetal alloys were first subjected to compression and then loaded in tension. Upon application of the tension loads there again is an early deviation from the modulus line, and, once more, the stress at a strain from the zero point equal to the original tension yield strain is approximately equal to the original tension yield stress. In Fig. 16, a second tension loading was applied and in this case elastic properties and yield strength were fully recovered. In the case of Fig. 17, the reapplication of compression after tension produced an effect similar to that shown in Fig. 15.

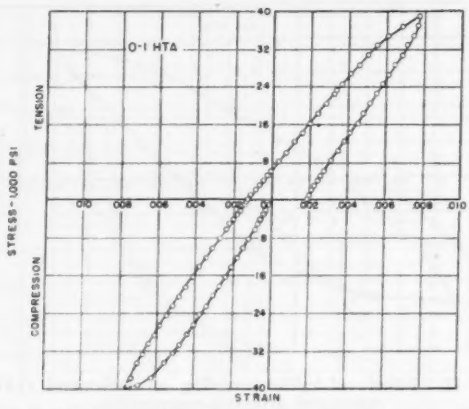

FIG. 20. Effect of cyclic stressing below the yield strength on Dowmetal O-1HTA.

Figs. 18 and 19 are the last cycles of 15-cyclic loadings on the cast material and 8 cycles on the wrought. No significant departures from the previous data are to be seen in this work on repetitive cycles.

One other test was made in which the Dowmetal O-1HTA specimen was stressed to a strain between the proportional limit and compression yield strains. This specimen was then loaded in tension. Here, in Fig. 20, it is shown that the same effects of Bauschinger and retwinning are present, but not to the degree shown in Fig. 17. The effects of slight permanent strain in compression would be practically negligible upon subsequent tension stressing.

DISCUSSION

Magnesium, in contrast to the other engineering materials that possess a cubic crystalline structure, has a hexagonal structure that undergoes two types of plastic deformation—slip and twinning. The preferred orientation or lining up of crystallographic planes in wrought magnesium products combined with the characteristics of the operating mechanisms of deformation act to produce, in general, a material more resistant to tension yielding than to compression yielding. However, recent metallurgical improvements have produced an extruded magnesium alloy, Dowmetal O-1HTA, whose tension and compression yield strengths are substantially equal and of a high order. The differences in the reaction of extruded Dowmetal FS-1 and O-1HTA to the effects of prestressing as presented in the experimental results can be rationalized on the basis of the compression to tension yield ratio. In the case of Dowmetal FS-1, which does not exhibit the normal Bauschinger behavior, the results can be explained in the following manner. The grains least favorably oriented for twinning in compression and, consequently, more favorably oriented for slip in tension are plastically deformed in the pretension cycle and are under residual compression stresses upon unloading. In subsequent compression these grains are stronger than the grains that are favorably oriented for twinning, even though the latter grains may be subjected to residual tensile stresses. Yielding then occurs exactly as in metal that has not been prestretched—e.g., by twinning.

In the case of Dowmetal O-1HTA where the compression yield is equal to the tension yield, the prestressing in tension produces residual compression stresses in some of the grains. These grains now deform early when subjected to compression, thus influencing the compression stress-strain curve. This effect is no different from that in other metals.

The effects of precompression on subsequent tensile stress-strain curves in the wrought magnesium alloys are complex because of the varied influence of orientation, deformation mechanisms, and the Bauschinger phenomenon. However, in those cases where a structure is fixed in place and then stressed beyond the compression yield strength, no harmful effect will result upon subsequent stressing in tension, as was shown in Figs. 4 and 5. This is true because the structure, being fixed in place, need only stretch back to its original length and then to a strain equal to its original yield strain in order to reach its original yield strength.

It would appear from all that has been said that magnesium alloys respond to the Bauschinger effect, in general, the same as other metals. Two obvious deviations in behavior in cyclic stressing are apparent. The first is the lack of decrease of compression yield in wrought alloys, with a 0.7 compression to tension yield ratio, subjected to pretension. Second, the lowering of the tangent modulus curve in tension, following precompression due to retwinning as well as Bauschinger effects, is greater than for most metals. However, this has little significance in the use of magnesium alloys as an engineering material.

CONCLUSIONS

(1) In service, cylic stressing up to the yield strength will not influence the ability of the structure to carry the original design loads within the allowable limit deformations.

(2) Accidental precompression loading of a magnesium-alloy structure beyond the yield strength is not detrimental to the strength of the structure upon reversal of stress; nor will the original design limit deformations be exceeded. In the case of accidental pretension beyond the yield strength of Dowmetal O-1HTA, immediate subsequent column action results in strengths slightly lower than the design values.

(3) If necessary, the effects of cold-forming can be avoided in the case of Dowmetals FS-1 and J-1 by forming at temperatures over 600°F., where the tendency to twin is greatly reduced. In the case of the high-strength extrusion, forming is recommended prior to the final aging treatment.

(*Continued on page 460*)

The Applicability of Saint-Venant's Principle to Airplane Structures

N. J. HOFF*

Polytechnic Institute of Brooklyn

SUMMARY

It is common practice in engineering to disregard the local effects of loads and to calculate the stresses in elements of structures and machinery from formulas valid only at some distance from the region in which the loads are applied. Whenever this is done, use is made of Saint-Venant's principle either consciously or unwittingly. It is shown in the present paper that in thin-walled structures, like monocoque cylinders, the region in which the stresses are materially influenced by the manner in which the loads are applied may be extended enough to render conventional formulas entirely unreliable.

INTRODUCTION

ALMOST ALL THE FORMULAS developed under the titles Strength of Materials and Theory of Structures are valid only at some distance from the point of application of the loads. They do not take into account local effects dependent upon the manner in which the loads are applied. Experience has shown that in the heavy, solid-section elements of structural engineering and machinery the predictions of the formulas are in good agreement with reality. It is understandable, therefore, that in many cases the aeronautical engineer made use of them without first scrutinizing their applicability to airplane structures. In recent years, however, several discrepancies have been observed between conventional theory and the strains measured in experiments. The so-called shear lag effect encountered in many problems of airplane stress analysis may be mentioned as an example. There are many more problems in which long-accepted stress formulas are unreliable when applied to airplane structures.

The validity of the classic formulas of Strength of Materials is founded upon Saint-Venant's principle. Since in a bent beam of solid rectangular section deviations from the straight line law for the normal stress distribution and the parabolic law for the shear stress distribution are noticeable only within a distance from the point of application of concentrated loads equal to the width (or depth) of the beam, in the major portion of the beam the stresses can be predicted by simple beam theory with an accuracy entirely satisfactory for engineering purposes. It will be shown in this paper that the region in a monocoque cylinder in which local effects are of importance may extend over a distance equal to several times the diameter of the cylinder. Since the cross section of a fuselage or a wing is seldom constant over such a distance, the validity of the simple formulas is doubtful. In the future, therefore, airplane stress analysts will have to investigate local effects much more than they did in the past.

Received November 6, 1945. To have been presented at the I.A.S. Thirteenth Annual Meeting, which was canceled to cooperate with a Government appeal (January, 1945) to refrain from holding conventions and meetings.

* Associate Professor of Aeronautical Engineering.

STATEMENT OF SAINT-VENANT'S PRINCIPLE

The principle is stated by Love[1] in the following manner:

"According to this principle the strains that are produced in a body by the application, to a small part of its surface, of a system of forces statically equivalent to zero force and zero couple, are of negligible magnitude at distances which are large compared with the linear dimensions of the part."

The principle can be used in the following manner to calculate the stresses in a beam simply supported at its ends and loaded in the middle with a concentrated load. A transverse section can be imagined through the beam on each side of the concentrated load and at an infinitesimal distance from it. Similarly, a transverse section may be assumed an infinitesimal distance from each end of the beam. The actual stress distribution in these sections is unknown, but it is certain that the normal stresses add up to a bending moment, and the shear stresses add up to a shear force of magnitudes that can be calculated from the requirements of static equilibrium. The Bernoulli-Navier theory of bending gives linearly distributed normal stresses and parabolically distributed shear stresses. Let the actually prevailing system of stresses be denoted by S_0, and let a system S_1 of stresses, equal and opposite to that corresponding to the Bernoulli-Navier theory, be applied to each of the sections. The system S_1 will be in equilibrium with the system S_0 of stresses actually prevailing. But according to Saint-Venant's principle the effect of the system $S_0 + S_1$ of self-equilibrating forces is negligible at some finite distance from the sections where it is applied. Consequently, the beam will be in a state of stress only in a region the length of which is of the order of magnitude of the width (or depth) of the beam when the system $S_0 + S_1$ is acting.

In order to nullify the effect of the system S_1 introduced arbitrarily and without any justification, let one more system S_2 of stresses, equal and opposite to S_1, be introduced in the same sections. The simultaneous

application of S_1 and S_2 obviously cannot change the stress distribution caused by the actual loading of the beam. On the other hand, since the system $S_0 + S_1$ is in equilibrium and was taken into account, the remaining loading of the beam is equivalent to the action of the system S_2 alone in each section. But in S_2 the stresses are distributed in accordance with the Bernoulli-Navier theory. Consequently, the stresses along the beam must be equal to those predicted by this theory except that, in the immediate vicinity of the load and the reactions, the local effects of the system $S_0 + S_1$ are superimposed.

Therefore, it is considered unimportant whether, for example, the reaction at the end of the beam is applied through the pressure of a knife-edge or through some skilfully realized parabolic distribution of the shear stresses in the end section. Beyond a distance equal to the depth of the beam, the stresses will not be influenced noticeably by these details of the load application.[2]

The principle was enunciated by Saint-Venant as a fact of experience. Southwell[3] and Goodier[4] showed that it is a consequence of the principle of conservation of energy and the principle of superposition. Goodier's reasoning will be followed now in order to estimate the size of the region in which local effects may be of importance in a thin-walled airplane structure.

First, let it be assumed that a monocoque cylinder consisting of a thin cylindrical sheet, reinforced longitudinally with stringers and transversely with rings, is loaded at one end section with stresses distributed over its cross section. The stresses are assumed to constitute a system of equilibrium. The diameter of the cylinder is denoted by D, and the thickness of an "effective" sheet by t. The effective thickness is defined as the total cross-sectional area of stringer and sheet covering divided by the length of the circumference of the cylinder. The order of magnitude of the applied stress is s. Let one element of the loaded area be regarded as fixed both in position and orientation. If E is the modulus of elasticity (or, in the more general case, the slope of the stress-strain curve of the material), then the strain is of order s/E, and, consequently, the displacements of points in the section are not greater than of order Ds/E. The work done by the applied load is the sum of the work done by the stresses on all the infinitesimal elements of the area. Evidently part of the section may be displaced in the direction and part opposite to the direction of the stress prevailing there, so that part of the external work may be positive and part negative. If all of it were positive, the order of magnitude of the work would not be greater than

$$s(\pi Dt)(Ds/E) = \pi D^2 t s^2/E$$

Consequently, it is safe to state that the order of magnitude of the work of the applied load must be smaller than, or equal to, $\pi D^2 t s^2/E$.

The size of the portion of the cylinder can now be estimated in which the stress is of the same order of magnitude s as is the applied stress. Obviously, if the stress is of order s, the strain energy stored is of order s^2/E per unit volume. It follows, therefore, from the requirement that the work done be equal to the strain energy stored, that the region in which the stress is of order s must be of order $\pi D^2 t$. Since the cross-sectional area of the cylinder is πDt, the length of the cylinder affected by local stress is of the order of magnitude of the diameter of the cylinder.

Examples in Which Conventional Theory Breaks Down

The typical difference between the behavior of a solid section and that of a thin-walled section is shown now in a numerical example. The structural element considered is a straight bar 20 in. long, one end of which is rigidly fixed to a rigid wall while the other end is free (Fig. 1). At the free end, a torque of 10 in.lbs. is applied by means of shear stresses distributed according to the requirements of the theory of pure torsion. Because of the restrictions to warping at the fixed end, normal stresses are introduced in the bar in addition to the shearing stresses of Saint-Venant torsion.

The magnitude of the normal stresses in the rectangular bar is calculated from Timoshenko's[5] approximate theory. The maximum value at the fixed end is equal to 157 lbs. per sq.in. Curve 1 in Fig. 2 presents the

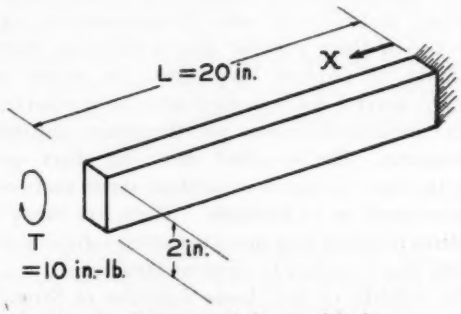

Fig. 1. Torque applied to straight bar.

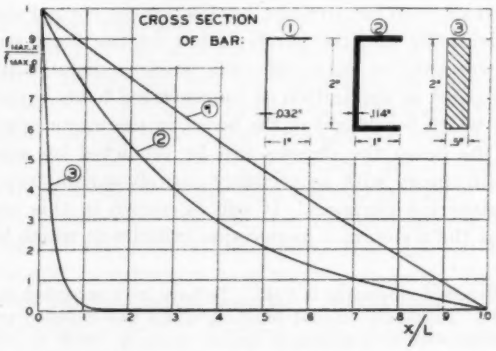

Fig. 2. Normal stress caused by restraint at fixed end of straight bar.

ratio maximum normal stress $f_{max.\,x}$ in any section x divided by the maximum normal stress $f_{max.\,0}$ in the fixed end section, plotted against the ratio distance x of the section from the fixed end of the bar divided by the total length L of the bar.

The other two sections considered are channel sections. The normal stress in them was calculated from the theory of torsion of thin-walled sections with nonuniform warping.[6] The thicker section has a wall thickness of 0.114 in.; the thinner one, of 0.032 in. The maximum normal stress in the fixed end section of the former was found to be 1,230 lbs. per sq.in.; the latter, 10,900 lbs. per sq.in. Curves 2 and 3 in Fig. 2 are plots of the stress ratio, defined earlier, against the distance ratio for the case of the two channel sections. Inspection of the curves reveals that, while in the case of the solid rectangular section the normal stress caused by the restriction to warping at the fixed end is highly localized, it has appreciable values over the entire length of the channel section bars. Consequently, reliance on Saint-Venant's principle in the calculation of the stresses caused by torsion is entirely justified with the bar of rectangular section. In contrast, stresses in the thin-walled section bars depend largely upon the end conditions.

As a second example, the stresses are calculated in a cantilever reinforced monocoque (Fig. 3) that is loaded at its free end with a concentrated transverse force $2P$. According to simple beam theory, the intensity of the shear flow q in the sheet covering, defined as shear stress multiplied by sheet thickness, is a sine function of the angle φ in good approximation. The maximum intensity is reached at the end points of the horizontal diameter of the cylinder. It has the value $q_{max.} = 2P/\pi r$. The sine curve is shown in Fig. 4 and is marked "conventional curve."

The figure also contains shear flow curves as calculated by strain energy methods.[7] In these calculations the cylinder was assumed to have a great number of longitudinal reinforcing elements (stringers) and a finite number of ring frames. The shear flow was considered constant between adjacent rings for any given value of the angle φ. Stringers were assumed to have no flexural or torsional rigidity and rings no flexural rigidity in bending perpendicular to their plane and no torsional rigidity. It is believed that these assumptions represent closely enough the actual conditions in many monocoque cylinders.

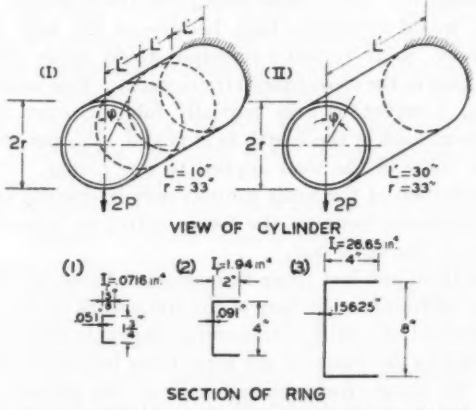

FIG. 3. Monocoque cylinder with concentrated load.

Under these conditions the stress distribution in the cylinder depends on the number of rings and the two nondimensional parameters

$$A = 1.91(I_{tot.}/I_{ring})(r/L')^2$$
$$B = 15.6(A_{tot.}/A_{skin})(r/L')^2$$

where $A_{tot.}$ and $L_{tot.}$ are the cross-sectional area and the moment of inertia of the cross section of the monocoque cylinder, respectively; A_{skin} is the cross-sectional area of the sheet metal covering of the cylinder; I_{ring} is the moment of inertia of the ring section; r is the radius of the cylinder; and L' is the frame spacing.

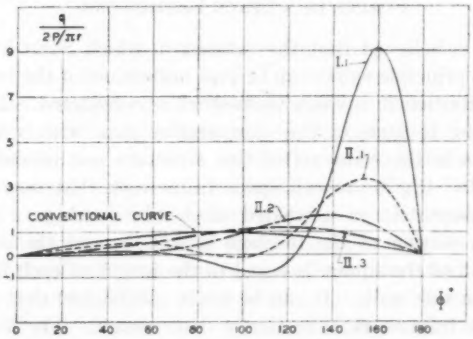

FIG. 4. Shear flow in sheet next to loaded ring of monocoque cylinder.

The shear flow curves of Fig. 4 are marked with a Roman and an Arabic numeral. The former refers to the type of the cylinder; the latter, to the ring section as shown in Fig. 3. In all the four specimens investigated the radius was 33 in. and the thickness of the sheet covering was 0.032 in. With these values $A_{skin} = 6.63$ sq.in. The total cross-sectional area $A_{tot.}$ was assumed to be 19.5 sq.in., and, hence, $I_{tot.} = 10{,}600$ in.^{4} The values of the moment of inertia of the ring sections are noted in Fig. 3. Consequently, the nondimensional parameters have the following values:

Designation of Cylinder	I.1	II.1	II.2	II.3
Parameter A	10^7	370,000	13,700	1,000
Parameter B	500	55.5	55.5	55.5

All of the four curves of Fig. 4 deviate markedly from the sine function of the Bernoulli-Navier theory. The deviations increase with increasing shearing rigidity of the covering and with decreasing flexural rigidity of the ring. The same is true of the curves of normal stress distribution at the fixed end of the cylinder. Fig. 5 presents these curves. Among them Curve II.3 corresponds to the weak sheet and the heaviest ring and

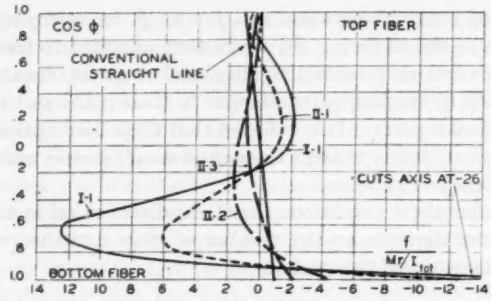

FIG. 5. Normal stress distribution in fixed end section of monocoque cylinder.

therefore approaches most closely the Bernoulli-Navier theory, but even it differs sufficiently from the straight-line law of simple beam theory to make an application of Saint-Venant's principle impossible for the fixed end section.

FORCES IN A SPACE FRAMEWORK

It is believed that the manner in which Saint-Venant's principle works can be best understood if the force distribution in a space framework is considered. This is true because of the comparative ease with which forces in the elements of this structure can be calculated. Fig. 6 shows a space framework that may be representative of a welded steel tube fuselage. The cross section of the fuselage is square, and the edge length of the square is equal to the length of each field of the side walls. It can be easily established that the space framework is statically determinate. The loading of the structure is a "warping group" consisting of four parallel forces applied to one end section. The forces add up to zero force and zero couple. The figures written on the elements of the framework represent the forces acting in the bar measured in the same units as the applied loads. Negative sign indicates compression.

It can be seen that, in spite of Saint-Venant's principle, the effect of the forces at one end of the structure is still noticeable at the other end. The maximum force in the fourth bay amounts to 25 per cent of the concentrated load applied to one corner. Of course, it is known from framework theory that there is only one state of equilibrium possible in a statically determinate framework, so that in such a structure Saint-Venant's principle can hardly be expected to apply. The question arises, therefore, whether the effect of the concentrated loads will become more localized when the structure is transformed into a redundant one through the addition of further bars. Fig. 7 shows the framework after a second diagonal has been added to each rectangular field of the surface of the structure. The framework now has 18 redundant bars, and, consequently, there is an 18 times infinite number of possible states of equilibrium under the action of the applied loads.

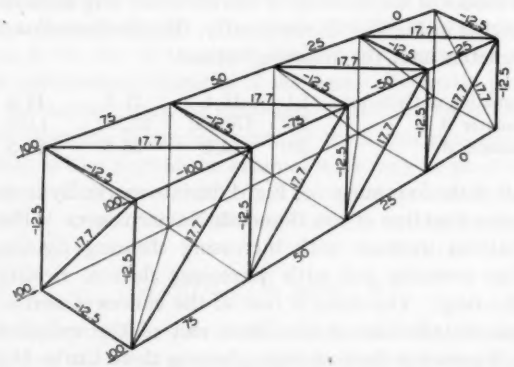

FIG. 6. Forces in statically determinate space framework.

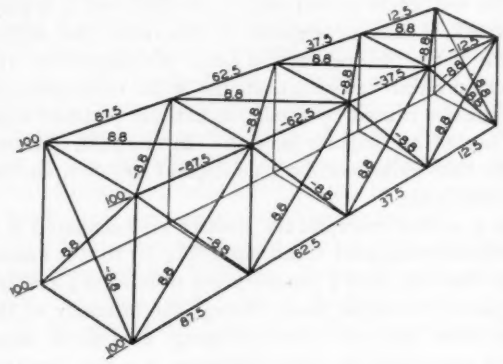

FIG. 7. Forces in space framework having 18 redundant bars.

While in the case of the statically determinate framework the forces in the bars are not affected by the cross-sectional area and the material of the bars, they must be known before the forces in the bars can be calculated in a redundant structure. In the calculations every bar except the diagonals was assumed to have the same cross-sectional area, and each diagonal was assumed to have one-half the area of the other bars. The material was assumed to be the same throughout the structure.

One would anticipate that, because of the high redundancy, Saint-Venant's principle would apply fully in the case of the cross-braced framework. This anticipation, however, is only partially fulfilled, since the maximum load in the fourth field is still $12^1/_2$ per cent of the value of the load applied to one corner. The redistribution of the loads consists only in evening out the differences between the forces acting in adjacent flanges of the same bay.

The third and last space framework is shown in Fig. 8. In addition to the bars of the framework of Fig. 7, it contains three pairs of transverse diagonals which are provided in the planes of the three inner bulkheads and have the same cross-sectional area as the surface diagonals. It may be seen that the addition of the six

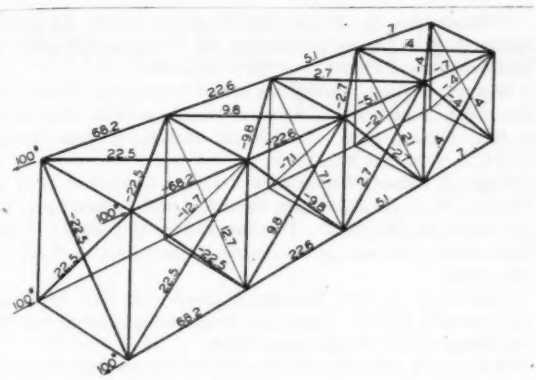

FIG. 8. Forces in space framework having 24 redundant bars.

new redundant bars, which make the structure 24 times redundant, is extremely effective in localizing the internal forces in the structure. In the fourth bay the maximum force is now 0.7 per cent and in the third bay it is 5.1 per cent of the load applied to one corner of the structure. In this case, therefore, appreciable forces appear only within a distance from the points of application of the loads equal to twice the length of a side of the square cross section.

In the calculation of the forces the redundant framework was divided into four units, cells, or cubes, each consisting of four longitudinals, eight uprights, four pairs of crossed surface diagonals, and two pairs of crossed transverse diagonals. Consequently, each bar of the intermediate transverse frames was considered as belonging to two adjacent cells. The actual force in each bar of these frames was the algebraic sum of the forces obtained for the particular bar in the two adjacent cells. Because of the symmetry it was possible to determine, from the conditions of equilibrium alone, the forces caused by a warping group in any single cell. The warping groups acting between adjacent cells were considered as the "unknown quantities" of the redundant force system in the complete space framework. In the case of the structure shown in Fig. 7 the unknowns were calculated from the condition that the actual force in the diagonals of the intermediate transverse frames must be zero, since in this structure there is no intermediate transverse bracing. In the case of the structure of Fig. 8 the unknowns were determined so as to make the total strain energy stored in the framework a minimum.

It is interesting to note that experiments carried out by Pippard[8] on space frameworks led to conclusions similar to those that may be drawn from the foregoing theoretical considerations. In his experiments Pippard loaded a practically pin-jointed cantilever space structure that consisted of four regular hexagonal transverse frames connected by six longitudinals. In part of the experiments the square fields of the sidewalls were braced with single, in others with double (crossed), diagonals. Similarly, the frame at the free end of the cantilever structure and the one adjacent to it were unbraced in some tests, and braced with three diagonals each in others. Different vertical and horizontal forces were applied to the joints of the frame at the free end in such a manner that in each case they added up to the same transverse resultant force. The effect upon the forces in the bars of the structure of changes in the bracing and in the load application was investigated through the actual measurement of the forces in the members of the space framework. The following conclusions were drawn from the experiments:

(1) The principle of Saint-Venant can be applied to the case of a redundant framework.

(2) If the plane of loading is braced, the tendency toward the equalization of strains is pronounced, and the distance required for the variation of strains to become negligible is dependent to a great extent upon the efficiency of the bracing in this and parallel planes.

CONCLUSIONS

The example of the space framework shows clearly that Saint-Venant's principle works only if there is a possibility for it to work, or in other words if there exist paths for the internal forces to follow in order to balance one another within a short distance of the region at which a group of external forces is applied which is statically equivalent to zero force and zero moment. In the structure of Fig. 6 there is just one possible state of equilibrium because the framework is statically determinate. Although the structure shown in Fig. 7 has 18 redundant bars, the redundancy is only on the surface of the structure, and Saint-Venant's principle cannot well be applied. On the other hand, the addition of the six transverse bracing elements in Fig. 8 opens up new paths for the internal forces to follow, and, consequently in the bars that are farther away from the load application the forces are greatly reduced.

The behavior of the reinforced monocoque fuselages of present-day airplanes is not unlike that of the space framework just discussed. Because of the thin gage of the material and the hollow shell-type structure of the monocoque, there are few possible paths for the stresses to follow. Increasing the thickness of the sheet covering has an effect upon the stress distribution similar to that obtained by adding surface diagonals to the original framework. The incorporation of transverse frames having appreciable bending rigidity in their plane amounts to much the same thing as the addition of the space diagonals shown in Fig. 8. It must be noted, however, that the stiffening effect of a simple ring frame is much smaller than that of a pair of crossed diagonals. An effect similar in magnitude to that obtained through the introduction of the internal bracings can be achieved in a monocoque fuselage only by the utilization of a full bulkhead or a rigidly braced frame.

It is concluded, therefore, that in reinforced monocoque structures, and especially in monocoque fuselages, calculation of the stresses by conventional formulas should be replaced to a great extent by more accurate analyses that take into account the local effects of the load application.

REFERENCES

[1] Love, A. E. H., *A Treatise on the Mathematical Theory of Elasticity*, 4th Ed., p. 132; Dover Publications, New York, 1944.

[2] Hildebrand, F. B., and Reissner, Eric, *Distribution of Stress in Built-In Beams of Narrow Rectangular Cross Section*, Journal of Applied Mechanics, Vol. 9, No. 3, p. A-108, September, 1942.

[3] Southwell, R. V., *On Castigliano's Theorem of Least Work and the Principle of Saint-Venant*, Philosophical Magazine, Series 6, Vol. 45, p. 193, January, 1923. *An Introduction to the Theory of Elasticity*, 2nd Ed., p. 98; Oxford University Press, London, 1941.

[4] Goodier, J. N., *A General Proof of Saint-Venant's Principle*, Philosophical Magazine, Series 7, Vol. 23, p. 607, April, 1937. *Supplementary Note on "A General Proof of Saint-Venant's Principle,"* Philosophical Magazine, Series 7, Vol. 24, p. 325, August, 1937. *An Extension of Saint-Venant's Principle, with Applications*, Journal of Applied Physics, Vol. 13, No. 3, p. 167, March, 1942.

[5] Timoshenko, S., *On the Torsion of a Prism, One of the Cross Sections of Which Remains Plane*, Proceedings of the London Mathematical Society, Series 2, Vol. 20, p. 389, 1921. *Theory of Elasticity*, 1st Ed., p. 273; McGraw-Hill Book Company, Inc., New York, 1934.

[6] Timoshenko, S., *Einige Stabilitatsprobleme der Elastizitats-theorie, Part III, Kipperscheinungen des I-Tragers*, Zeitschrift fur Mathematik und Physik, Vol. 58, p. 337, 1910.

Wagner, Herbert, *Verdrehung and Knickung von Offenen Profilen*, 25th Anniversary Volume of the Technische Hochschule, p. 329; Danzig, 1929. *Torsion and Buckling of Open Sections*, N.A.C.A. T.M. No. 807, 1936.

Kappus, Robert, *Drillknicken Zentrisch Gedruckter Stabe mit Offenem Profil im Elastischen Bereich*, Luftfahrtforschung, Vol. 14, No. 9, p. 444, 1937. *Twisting Failure of Centrally Loaded Open-Section Columns in the Elastic Range*, N.A.C.A. T.M. No. 851, 1938.

Goodier, J. N., *The Buckling of Compressed Bars by Torsion and Flexure*, Cornell University Engineering Experiment Station, Bulletin No. 27, December, 1941.

Hoff, N. J., *Stresses in Space-Curved Rings Reinforcing the Edges of Cut-outs in Monocoque Fuselages*, Appendix, The Journal of The Royal Aeronautical Society, Vol. 47, No. 386, p. 64, February, 1943.

Von Kármán, Th., and Christensen, N. B., *Methods of Analysis for Torsion with Variable Twist*, Journal of the Aeronautical Sciences, Vol. 11, No. 2, p. 110, April, 1944.

[7] Hoff, N. J., *Stresses in a Reinforced Monocoque Cylinder Under Concentrated Symmetric Transverse Loads*, Journal of Applied Mechanics, Vol. 11, No. 4, p. A-235, December, 1944.

[8] Pippard, A. J. S., and Clifford, G. H. W., *On an Experimental Investigation of the Applicability of Saint-Venant's Principle to the Case of Frameworks Having Redundant Bracing Members*, Philosophical Magazine, Sriees 7, Vol. 1, p. 243, January, 1926.

Pippard, A. J. S., *Strain Energy Methods of Stress Analysis*, p. 14; Longmans, Green & Co., London, 1928.

Stress-Strain Characteristics of Magnesium Alloys

(*Continued from page 454*)

(4) Operations such as stretching have a beneficial effect on alloys of the Dowmetal FS-1 and J-1 type both in tension and compression yield. In the case of Dowmetal O-1HTA, stretching decreases the compression yield. Properties may be completely restored by a low-temperature thermal treatment.

REFERENCES

[1] Barret, C. S., *Structure of Metals;* McGraw-Hill Book Company, Inc., New York, 1943.

[2] Seitz, F., *Physics of Metals;* McGraw-Hill Book Company, Inc., New York, 1943.

[3] Doan, G. E., *Principles of Physical Metallurgy;* McGraw-Hill Book Company, Inc., New York, 1935.

[4] VanWert, L. T., *Introduction to Physical Metallurgy;* McGraw-Hill Book Company, Inc., New York, 1936.

[5] Dalby, W. E., *Strength and Structure of Steel and Other Materials;* Longmans, Green & Co., New York, 1923.

[6] Keulegan, G. H., *Statical Hysteresis in the Flexure of Bars*, Bureau of Standards, Tech. Paper 332, Vol. 21, 1926.

[7] Keulegan, G. H., *Statical Hysteresis in the Flexure of Bars*, Bureau of Standards, Tech. Paper 365, Vol. 22, 1928.

[8] Templin, R. L., and Sturm, R. G., *Some Stress Strain Studies of Metals*, Journal of the Aeronautical Sciences, Vol. 7, No. 5, p. 189, March, 1940.

[9] Dorn, J. E., and Thomsen, E., *Notes on the Modulus of Elasticity*, Light Metal Age, Vol. 1, p. 10, July, 1943.

[10] Eastman, E. J., McDonald, J. C., and A. A. Moore, *The Relation of Stress to Strain in Magnesium Base Alloys*, Journal of the Aeronautical Sciences, Vol. 12, No. 3, p. 273, July, 1945.

[11] Unpublished Data—The Dow Chemical Company.

[12] Welter, G., *Micro-Deformation Under Tension and Compression Loads of Thin Aluminum Alloy Sheets For Aircraft Construction*, A.S.T.M. 1944, Preprint 31.

[13] Smith and Wood, *Internal Stress Created by Plastic Flow in Mild Steel and Stress Strain Curves for the Atomic Lattice of Higher Carbon Steels*, Proceedings of The Royal Society, Vol. 182, pp. 404–414, June 16, 1944.

Shear Lag and Torsion Bending of Four-Element Box Beams

R. E. NEWTON*

Curtiss-Wright Corporation

ABSTRACT

A method of solution, consistent with the conventional assumptions of shear lag analysis, is developed for the axial and shear stress distribution in four-element box beams of the type frequently used in aircraft structures. Account is taken of the effects of shear lag, beam taper, skin cutouts, and the stresses due to restraint against torsional warping. There are no restrictions on the type of external loading.

The procedure is based upon the determination of a self-equilibrating set of "correction" stresses to be superposed upon the stresses calculated by conventional bending theory. The equations for the "correction" stresses are formulated as recurring pairs of finite-difference equations, which permits the handling of arbitrary variations of flange areas, web thicknesses, and external loads. Solution of the equations is performed by simple tabular calculations that may be done by a computer who does not understand the theory.

Numerical examples are presented for the stress distributions in a cantilever beam, with and without a midspan cutout, under various external loadings. A simple means is provided for determining approximately the errors resulting from the use of finite increments of spanwise length, and it is shown that relatively large increments will normally give satisfactory accuracy.

SYMBOLS

A_m = cross-sectional area of flange m, sq.in.
a, b, c, d = specific flange and web subscripts
B_j = flange flexibility constant at station j $[= (G/E)\underset{m}{\Sigma} C_m^2/(A_m)_j]$, in.$^{-2}$
C_m = axial load constant for flange m $(= Q_a/Q_m)$
E = elastic modulus of flanges, lbs. per sq.in.
G = shear modulus of webs, lbs. per sq.in.
H_j = web energy constant for bending theory shears at station $j[= \underset{m}{\Sigma} K_m[p_m(w_m/t_m)]_j]$, lbs. per in.
J_j = web energy constant for unit value of q_j at station $j[= \underset{m}{\Sigma} K_m^2/K_a)(w_m/t_m)_j]$
j = subscript for spanwise station
K_m = shear flow constant for web $m(= q_m \Delta y/\Delta Q_a)$
m = general subscript for flanges and webs
N_j = constant for cross-sectional distortion at station $j[= G\underset{m}{\Sigma} C_m(v_m)_j]$, lbs. per in.
n = specific value of j denoting tip station
P_m = bending theory axial load in stringer m, lbs.
p_m = bending theory shear flow in web m, lbs. per in.
Q_j = "correction" axial load in flange a at station $j[= (Q_a)_j]$, lbs.
Q_m = "correction" axial load in flange m, lbs.
q_j = "correction" shear flow in web a at station $j[= (q_a)_j]$, lbs. per in.
q_m = "correction" shear flow in web m, lbs. per in.
R_m = net axial load in flange m, lbs.
r_m = net shear flow in web m, lbs. per in.
t_m = thickness of web m, in.
U_e = external work done by virtual loads C_m, in.
U_i = internal energy stored by action of virtual loads C_m on element of length Δy, in.
v_m = displacement (in positive y direction) of point on flange m, in.
w_m = developed width of web m, in.
x, y, z = Cartesian coordinates (see Fig. 2), in.
Δ = change of quantity in progressing from station j to station $j + 2$ $[(\Delta Q_a) = (Q_a)_{j+2} - (Q_a)_j]$
$\underset{m}{\Sigma}$ = summation of quantities with subscript m, letting $m = a, b, c,$ and d. $(\underset{m}{\Sigma} C_m v_m = C_a v_a + C_b v_b + C_c v_c + C_d v_d)$

Received December 11, 1944. To have been presented at the I.A.S. Thirteenth Annual Meeting, which was canceled to cooperate with a Government appeal (January, 1945) to refrain from holding conventions and meetings.

* Head, Structural Methods Unit, Airplane Division. Now with McDonnell Aircraft Corporation.

INTRODUCTION

BOX BEAMS HAVING FOUR FLANGE ELEMENTS connected by thin sheet webs are frequently used in airplane wing and fuselage structures. A general solution for the stresses in such beams is derived here under the following assumptions:

(1) Webs carry only shear.
(2) Flanges carry only axial load.
(3) Ribs or bulkheads are rigid in own plane, but have no resistance to deformation normal to plane.
(4) All elements of flange length are straight.
(5) Cross sections are geometrically similar with respect to locations of flange centroids and web centerlines.
(6) Taper of beam is "moderate."
(7) Hooke's law is assumed, but effective values of material moduli may be used.
(8) External loads are applied at ribs or bulkheads

RESOLUTION OF LOADS

The resultant axial and shear flow loads (R_m, r_m) are resolved into a set of loads (P_m, p_m) as given by classic bending theory† and a set of "correction" loads (Q_m, q_m). By definition, then,

$$\left.\begin{aligned} P_m + Q_m &= R_m \\ p_m + q_m &= r_m \end{aligned}\right\} \qquad (1)$$

† The term "bending theory" as used herein includes the Bernoulli-Navier theory of bending and the Saint Venant theory of torsion as they are customarily employed in airplane stress analysis.

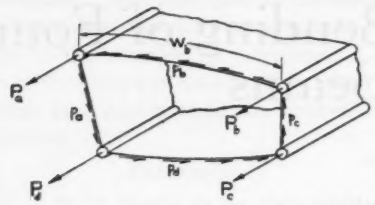

FIG. 1. Positive senses for axial loads and shear flows.

(The subscript system and positive senses for axial loads and shear flows are shown in Fig. 1.)

The method of finding the bending theory loads (P_m, p_m) is well known[1] and needs no discussion here. Since these loads and the resultant loads (R_m, r_m) are in equilibrium with the external forces, it follows that the "correction" loads (Q_m, q_m) are self-equilibrating. For this reason, if the value of Q_a be specified, the values of Q_b, Q_c, and Q_d may be determined from statics. It is convenient to define a set of constants C_a, C_b, C_c, and C_d by the relations

$$Q_m = C_m Q_a \tag{2}$$

By definition, $C_a = 1$ and C_b, C_c, and C_d are determined solely by the locations of the spar cap centroids.

If the value of Q_a be specified at every station, the values of q_a, q_b, q_c, and q_d may be determined from statics. A set of constants K_m is defined by the equations

$$q_m = K_m(\Delta Q_a/\Delta y) \tag{3}$$

(It should be noted that the constants C_m and K_m are independent of y by virtue of Assumption (5).)

Derivation of Compatibility Equations

As the structure has been shown to be once-redundant, a single set of compatibility equations will suffice. For the purpose of formulating these equations in finite difference form it will be useful to divide the span into n equal parts of length $\Delta y/2$. The system of station numbering is shown in Fig. 2.

The method of virtual work is applied in deriving the equations. Self-equilibrating virtual axial loads C_m (magnitudes given in Eq. (2)) are applied at the mid-

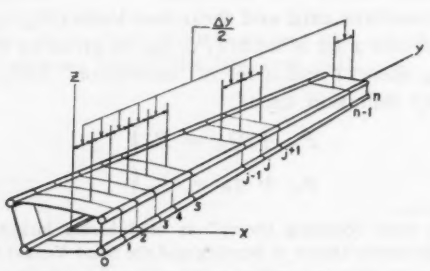

FIG. 2. Coordinate axes and station numbering system.

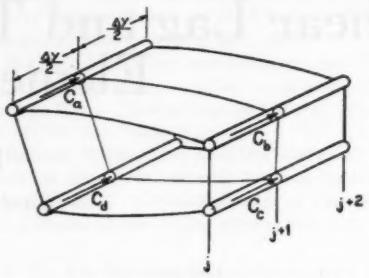

FIG. 3. Virtual loads on beam element.

station of a spanwise element of length Δy (see Fig. 3). If the displacements (due to the loads R_m) of the points of load application in the positive y direction be v_m and the external work done by the virtual loads (during the application of the resultant loads R_m) be U_e, then

$$U_e = \sum_m C_m(v_m)_{j+1}$$

The shear flows accompanying the virtual loading are, from Eq. (3), $K_m/\Delta y$. The work done by these shear flows during the application of the resultant loads is denoted by U_i:

$$U_i = (1/G)\sum_m K_m[r_m(w_m/t_m)]_{j+1}$$

(The internal work done by the virtual cap stresses is omitted since it approaches zero as $\Delta y \to 0$.) Equating the internal work to the external work: $U_e = U_i$; or

$$G\sum_m C_m(v_m)_{j+1} = \sum_m K_m[r_m(w_m/t_m)]_{j+1} \tag{4}$$

It is convenient to define a special symbol for the left-hand side of Eq. (4):

$$N_{j+1} = G\sum_m C_m(v_m)_{j+1} \tag{5}$$

Substituting in Eq. (4):

$$N_{j+1} = \sum_m K_m[r_m(w_m/t_m)]_{j+1} \tag{6}$$

Since Eq. (6) holds for all values of j, it follows that

$$N_{j+1} - N_{j-1} = \sum_m K_m\left[r_m\left(\frac{w_m}{t_m}\right)\right]_{j+1} - \sum_m K_m\left[r_m\left(\frac{w_m}{t_m}\right)\right]_{j-1} \tag{7}$$

Expanding the left-hand side of Eq. (7) gives

$$N_{j+1} - N_{j-1} = G\sum_m C_m(v_m)_{j+1} - G\sum_m C_m(v_m)_{j-1} = G\sum_m C_m[(v_m)_{j+1} - (v_m)_{j-1}]$$

The expression $[(v_m)_{j+1} - (v_m)_{j-1}]$ represents the stretch of cap m between stations $j-1$ and $j+1$ due to the axial load R_m. It follows that

$$(v_m)_{j+1} - (v_m)_{j-1} = (R_m/EA_m)_j \Delta y$$

Therefore, substituting for R_m from Eq. (1):

$$N_{j+1} - N_{j-1} = \frac{G\Delta y}{E}\sum_m C_m\left(\frac{Q_m}{A_m}\right)_j + \frac{G\Delta y}{E}\sum_m C_m\left(\frac{P_m}{A_m}\right)_j \tag{8}$$

The second term on the right-hand side of Eq. (8) vanishes because it is proportional to the work done by virtual loads C_m during a bending theory deformation of the flanges. Since the loads C_m are self-equilibrating and since bending theory axial deformations involve no distortion of cross-sectional planes, this term must be zero. Substituting in the first term for Q_m from Eq. (2) and utilizing the convention that $Q_j = (Q_a)_j$, Eq. (8) becomes

$$N_{j+1} - N_{j-1} = Q_j\Delta y\,\frac{G}{E}\sum_m \frac{C_m^2}{(A_m)_j}$$

or

$$N_{j+1} = N_{j-1} + B_j\Delta y Q_j \tag{9}$$

where

$$B_j = (G/E)\sum_m C_m^2/(A_m)_j \tag{10}$$

Substituting for r_m from Eq. (1), the second term on the right side of Eq. (7) becomes

$$\sum_m K_m\left[r_m\left(\frac{w_m}{t_m}\right)\right]_{j-1} = \sum_m K_m\left[q_m\left(\frac{w_m}{t_m}\right)\right]_{j-1} + \sum_m K_m\left[p_m\left(\frac{w_m}{t_m}\right)\right]_{j-1}$$

From Eq. (3):

$$q_m = K_m(\Delta Q_a/\Delta y);\ q_a = K_a(\Delta Q_a/\Delta y)$$

Whence,

$$q_m = (K_m/K_a)q_a \tag{3'}$$

Defining two new constants,

$$H_{j-1} = \sum_m K_m[p_m(w_m/t_m)]_{j-1} \tag{11}$$

$$J_{j-1} = \sum_m (K^2_m/K_a)(w_m/t_m)_{j-1} \tag{12}$$

and using the convention $q_{j-1} = (q_a)_{j-1}$:

$$\sum_m K_m[r_m(w_m/t_m)]_{j-1} = J_{j-1}q_{j-1} + H_{j-1} \tag{13}$$

Substituting the results of Eqs. (9) and (13), Eq. (7) becomes

$$B_j\Delta y Q_j = J_{j+1}q_{j+1} + H_{j+1} - J_{j-1}q_{j-1} - H_{j-1}$$

or

$$J_{j+1}q_{j+1} = J_{j-1}q_{j-1} + H_{j-1} - H_{j+1} + B_j\Delta y Q_j \tag{14}$$

A second relation between Q and q is obtained by substituting $Q_{j+2} - Q_j = *\Delta Q_a$ in Eq. (3):

$$Q_{j+2} = Q_j + (\Delta y/K_a)q_{j+1} \tag{15}$$

Procedure for Analysis

Detailed consideration will be given to the problem of finding the axial loads and shear flows for a structure having a plane of symmetry at $y = 0$. For the purposes of this discussion it is further assumed that all external loads are applied to the ribs, or bulkheads, in their planes. Any external loading condition may be resolved into a symmetric and an antisymmetric set of loads, and only one-half of the structure need be considered in each case.

The first step is to find the bending theory axial loads and shear flows (P, p). It is usually most practical to find P at rib stations and p at the intermediate stations. It will be assumed that the even values of j represent rib stations and that the odd values represent the intermediate stations.

The next step is to calculate the values of K_a, B_j, and J_j at the appropriate stations. The necessary values of H are also found, using the p's found above.

The calculation of the "correction" axial loads and shear flows (Q, q) is now begun. Eqs. (14) and (15) are a set of recursion formulas which permit the calculation of Q and q at alternate stations if a value of Q and the value of q at an adjacent station are known. The boundary conditions are used to determine these initial values.

For an antisymmetric loading condition the boundary conditions are $Q_0 = Q_n = 0$. The procedure is to assume a value of q_1 and, using Eqs. (14) and (15), to calculate successive values of Q and q until the value of Q_n is obtained. Unless a correct value of q_1 was assumed, this value of Q_n will not be zero. Since, however, Eqs. (14) and (15) are linear and none of the constants depends on the assumed value of q_1, the value of Q_n obtained will be a linear function of q_1. After a second trial assumption for q_1 it is therefore possible to determine the value of q_1 which will give $Q_n = 0$. A further cycle of calculation will establish final values of Q and q.

For a symmetric loading, Q_n will again equal zero. The other boundary condition is provided by the fact that all of the v_m's must be zero at $j = 0$. Using Eq. (5), then, $N_0 = 0$. Substituting the results of Eq. (13) in Eq. (6):

$$N_j = J_jq_j + H_j \tag{16}$$

By inserting the condition $N_0 = 0$ in Eq. (16) the value of q_0 may be determined, and it is then possible to proceed as in the antisymmetric case, though here it is the value of Q_1 which must be assumed. This procedure is quite direct, but it has the disadvantage that the necessary values of p_j are normally obtainable at odd values of j. Further, values of p_j at ribs (even values of j) are of questionable physical significance. This difficulty is avoided by assuming a value of Q_0 and finding the value of q_1 in the following manner.

Eq. (14) may be modified to read

$$J_1 q_1 = J_0 q_0 + H_0 - H_1 + B_{1/2}(\Delta y/2) Q_{1/2}$$

Using Eq. (15), $Q_{1/2}$ may be approximated as

$$Q_{1/2} = Q_0 + (\Delta y/4K_a) q_0$$

Substituting $N_0 = 0$ in Eq. (16) gives

$$J_0 q_0 + H_0 = 0 \quad \text{or} \quad q_0 = -H_0/J_0$$

Using these results, the expression for $J_1 q_1$ becomes

$$J_1 q_1 = B_{1/2}\left(\frac{\Delta y}{2}\right) Q_0 - \left\{H_1 + B_{1/2}\left[\frac{(\Delta y)^2}{8K_a}\right]\left(\frac{H_0}{J_0}\right)\right\} \tag{17}$$

Once a value of Q_0 has been assumed and the corresponding value of q_1 is found from Eq. (17), the symmetric case may be handled in the same manner as the antisymmetric case.

The final step is to compute the values of $(Q_m)_j$ and $(q_m)_j$ from the values of Q_j and q_j, using Eqs. (2) and (3′). These results are then combined with the P_m's and p_m's, using Eqs. (1), to obtain the resultant axial loads and shear flows, R_m and r_m.

Treatment of Cutouts

If one of the webs is incomplete over a part of the span, bending theory no longer gives a unique solution for the loads P and p. The method of this paper may, however, be used to handle this problem. The technique may be most readily explained with reference to a specific hypothetical problem. It will therefore be assumed that the web b is missing from $j = 8$ to $j = 12$, although the method employed will be applicable to all types of cutout problems.

The solution is begun as before. Bending theory axial loads and shear flows (P, p) are found on the assumption that there is no cutout.

The boundary conditions for Q and q at the root are handled as before, and Eqs. (14) and (15) are used alternately until Q_8 has been calculated in the first trial. Now, as t_b approaches zero, Eq. (4) and Eqs. (6), (7), and (14), which are derived from Eq. (4), merely impose the common-sense requirement that the resultant shear flow (r_b) in web b must approach zero. This requirement may be rewritten, using Eqs. (1) and (3′), to give

$$q_j = -(K_a/K_b)(p_b)_j \tag{18}$$

Substituting this result in Eq. (15) gives

$$Q_{j+2} = Q_j - (\Delta y/K_b)(p_b)_{j+1} \tag{19}$$

Eqs. (18) and (19) suffice to define the state of stress in the cutout region. Thus, q_9 and q_{11} may be found from Eq. (18), and Q_{10} and Q_{12} may be found from Eq. (19). When the cutout has been crossed, however, it is necessary to find q_{13}. In order to do this, Eq. (16) is used to find N_7 and then values of N_9, N_{11} and N_{13} are found successively by using Eq. (9). When N_{13} is found, q_{13} may be found from Eq. (16). It is now possible to proceed to the tip using Eqs. (14) and (15). The rest of the procedure is identical with that described previously for structures without cutouts.

Discussion

As in any finite difference process, errors are introduced by the finite length of the increments Δy. It can be seen from Fig. 4 (see Appendix, Example 1), however, that a good approximation is possible in the absence of structural and loading discontinuities, even though Δy is a considerable fraction of the span (the so-called "exact" results of Fig. 4 are obtained by integration of the differential equations that correspond to the finite difference equations used here). A proper choice of Δy to give a desired precision depends upon experience with the method, but it is possible to determine the precision obtained by solving the problem separately for two different values of Δy (see Appendix, Part II). Having followed such a procedure for a number of problems, the user of the method gained confidence in his own ability to make a proper choice for Δy.

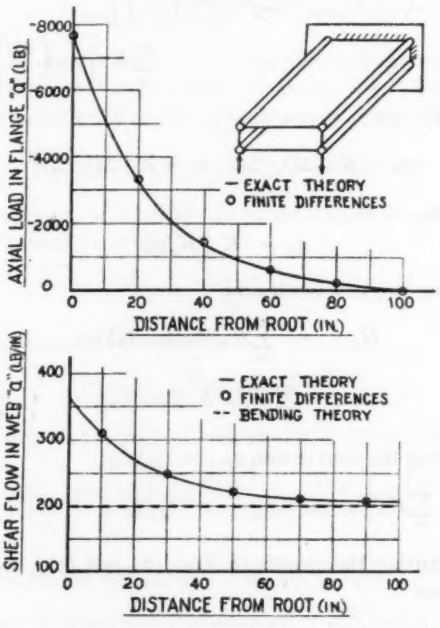

Fig. 4. Example 1, axial loads and shear flows.

Even where small values of Δy are needed and large numbers of equations result, the recurrent form of the equations makes their solution practical. The convergence of the trial-and-error system of solution is independent of the initial guesses, and the amount of labor required is directly proportional to the number of

simultaneous equations. It is noted that a similar method of solution for equations of this kind has been used by Kuhn.[2]

In structures having high shear stiffness it will be found that a small change of Q_0 or q_1 will result in a large change of Q_n (a million-pound change of Q_n for a one-pound change of Q_0 is not unusual). This is a manifestation of Saint Venant's principle (i.e., self-equilibrating forces applied at the tip should have scarcely perceptible effects at the root), and because of this phenomenon it is necessary to perform the solutions on a calculating machine, retaining six or seven significant figures. (It is not necessary to calculate the constants K_a, B_j, H_j, and J_j to a large number of figures, but the values used in each trial must be identical.)

Although the detail development of the theory has been made here for external loads applied in the planes of the ribs or bulkheads, the theory may be used where the flanges are also subjected to external concentrated or distributed axial loads. Treatment of such problems only requires modification of the equilibrium equations; the deformation relations are not affected. Such a problem is treated in the Appendix, Example 3.

Conclusions

The technique of analysis described here is readily applied. As is evident from the examples in the Appendix, the calculations are not lengthy and the approximations resulting from the use of a large value of Δy are quite good. The separation of the shear lag loads from the bending theory loads will be found to be useful in getting a "feeling" for shear lag behavior, and it permits a useful division of labor in the stress analysis.

Appendix

Part I—Examples

The basic structure used in the following examples is a rectangular box beam with built-in root section having the following dimensions:

$w_a = w_c = 5$ in. $\qquad w_b = w_d = 20$ in.
$t_a = t_c = 0.05$ in. $\qquad t_b = t_d = 0.02$ in.
$A_a = A_b = A_c = A_d = 1.0$ in.^{2} $\qquad G/E = 0.25$
$y_n = 100$ in.

The constants K_m, C_m, B_j, and J_j, which are independent of the loading, are determined first.

Let $\Delta Q_a/\Delta y = 1$ in Eq. (3) and consider the resultant of the q's.

Summation of x forces:

$$20(K_d - K_b) = 0 \quad \text{or} \quad K_d = K_b$$

Summation of z forces:

$$5(K_c - K_a) = 0 \quad \text{or} \quad K_c = K_a$$

Summation of moments about axis of cap c:

$$100K_a + 100K_b = 0 \quad \text{or} \quad K_a = -K_b$$

Summation of y forces on cap a over length Δy:

$$\Delta y(K_a - K_b) = \Delta Q_a \quad \text{or} \quad K_a - K_b = 1$$

Therefore

$$K_a = K_c = \underline{0.50}; \qquad K_b = K_d = -\underline{0.50}$$

By inspection: $C_a = C_c = \underline{1.00}$; $C_b = C_d = -\underline{1.00}$.

$$B_j = \frac{G}{E}\sum_m \frac{C_m^2}{(A_m)_j} = \underline{1.00} \text{ (all values of } j)$$

$$J_j = \sum_m \frac{K_m^2}{K_a}\left(\frac{w_m}{t_m}\right)_j = \frac{(0.50)^2}{0.50} \times \left[\frac{5}{0.05} + \frac{20}{0.02} + \frac{5}{0.05} + \frac{20}{0.02}\right] = \underline{1{,}100} \text{ (all values of } j)$$

Example 1

The external loading is a concentrated torque applied at the tip,

$M_y = 40{,}000$ in.lbs.

$$p_a = p_b = p_c = p_d = \frac{M_y}{2w_a w_b} = \frac{40{,}000}{2(5)(20)} = \underline{200 \text{ lbs. per in.}}$$

$$H_j = \sum_m K_m\left(p_m \frac{w_m}{t_m}\right)_j = \underline{-180{,}000 \text{ lbs. per in.}} \text{ (all values of } j)$$

Letting $n = 10$, $\Delta y = 2y_n/n = 20$ in. Then

$$-H_1 - B_{1/2}\frac{(\Delta y)^2}{8K_a}\left(\frac{H_0}{J_0}\right) = 180{,}000 + 1.00\,\frac{(20)^2}{8}\left[\frac{180{,}000}{(0.50)(1{,}100)}\right] = 196{,}363$$

$$B_{1/2}\frac{\Delta y}{2} = (1)(10) = 10 \qquad B_j \Delta y = (1)(20) = 20$$

$$\frac{\Delta y}{K_a J_j} = \frac{20}{(0.50)(1{,}100)} = 0.03636$$

The method of arranging the calculations is shown in Table 1. Calculations for Q_j and q_j are shown in Tables 2 and 3. Since H_j is constant, the lines for $H_{j-1} - H_{j+1}$ are omitted in the latter tables. Results are shown graphically in Fig. 4.

Example 2

Loading is as in Example 1. The structure is altered by removing web b from $y = 40$ in. to $y = 60$ in. Since H_j is constant, it will be satisfactory to keep account of $N_j - H_j$ in crossing the cutout.

$$Q_6 = Q_4 - \left(\frac{\Delta y}{K_b}\right)(p_b)_5$$

TABLE 1

Form for Calculation

j	J_jq_j	Multiplier	Q_j
0	$B_{1/2}\left(\frac{\Delta y}{2}\right)Q_0$	$B_{1/2}\left(\frac{\Delta y}{2}\right)$	Q_0(assumed)
..	$-\left[H_1 + B_{1/2}\frac{(\Delta y)^2}{8K_a}\left(\frac{H_0}{J_0}\right)\right]$	.....	.....
1	J_1q_1[Eq. (17)]	$\frac{\Delta y}{K_aJ_1}$	$\left(\frac{\Delta y}{K_a}\right)q_1$
2	$B_2\Delta yQ_2$	$B_2\Delta y$	Q_2[Eq. (15)]
..	$H_1 - H_3$	.....	.....
3	J_3q_3[Eq. (14)]	$\frac{\Delta y}{K_aJ_3}$	$\left(\frac{\Delta y}{K_a}\right)q_3$
4	$B_4\Delta yQ_4$	$B_4\Delta y$	Q_4[Eq. (15)]
..	$H_3 - H_5$	.....	.....
5	J_5q_5[Eq. (14)]	$\frac{\Delta y}{K_aJ_5}$	$\left(\frac{\Delta y}{K_a}\right)q_5$
.	.	.	.
.	.	.	.
.	.	.	.
.	.	.	.
.	.	.	.

or

$$Q_6 = Q_4 - \frac{20}{(-0.50)}(200) = Q_4 + 8{,}000$$

The last cycle of tabular calculation is given in Table 4, and results for both $\Delta y = 10$ in. and $\Delta y = 20$ in. are shown in Fig. 5.

Example 3

The structure is the same as in Example 1. The loading is a 10,000-lb. axial load, in the positive y direction, applied to flange a at $y = 100$ in.

Bending theory axial loads and shear flows are:

$$P_a = +7{,}500 \text{ lbs.}; \quad P_b = P_d = +2{,}500 \text{ lbs.};$$
$$P_c = -2{,}500 \text{ lbs.}; \quad p_a = p_b = p_c = p_d = 0$$

It follows that $H_j = 0$ (all values of j).

Letting $n = 10$, $\Delta y = 20$ in. Then

TABLE 3

Third Trial, Example 1

j	J_jq_j	Mult.	Q_j	q_j
0	−76,979	10	−7,697.9	
..	196,364	.....	.....	
1	119,385	0.03636	4,340.8	108.5
2	−67,142	20	−3,357.1	
3	52,243	0.03636	1,899.6	47.5
4	−29,150	20	−1,457.5	
5	23,093	0.03636	839.7	21.0
6	−12,356	20	−617.8	
7	10,737	0.03636	390.4	9.8
8	−4,548	20	−227.4	
9	6,189	0.03636	225.0	5.6
10	.....	.....	−2.4	

TABLE 4

Third Trial, Example 2 ($\Delta y = 20$ in.)

j	J_jq_j	Mult.	Q_j	q_j
0	−90,830	10	−9,083.0	.....
..	196,364	.....	.....	.....
1	105,534	0.03636	3,837.2	95.9
2	−104,916	20	−5,245.8	.....
3	618	0.03636	22.5	0.6
4	−104,466	20	−5,223.3	.....
5	−103,848*	.....	8,000.0	200
6	55,534	20	2,776.7	.....
7	−48,314	0.03636	−1,756.7	−43.9
8	20,400	20	1,020.0	.....
9	−27,914	0.03636	−1,015.0	−25.4
10	.....	.....	5.0	.....

* $N_5 - H_5$.

$$-H_1 - B_{1/2}[(\Delta y)^2/8K_a](H_0/J_0) = 0$$

$$B_{1/2}\left(\frac{\Delta y}{2}\right) = 10, \quad \frac{\Delta y}{K_aJ_j} = 0.03636, \quad B_j\Delta y = 20$$

Since $(R_a)_{j=n} = 10{,}000$ lbs. $= (P_a)_{j=n} + Q_n$, $Q_n = 2{,}500$ lbs.

Results for this example are given in Fig. 6.

TABLE 2

First and Second Trials, Example 1

j	J_jq_j	Mult.	Q_j	J_jq_j	Mult.	Q_j
0	−76,000	10	−7,600.0	−77,000	10	−7,700.0
..	196,364	.....	.....	196,364	.....	.....
1	120,364	0.03636	4,376.4	119,364	0.03636	4,340.1
2	−64,472	20	−3,223.6	−67,198	20	−3,359.9
3	55,892	0.03636	2,032.2	52,166	0.03636	1,896.8
4	−23,828	20	−1,191.4	−29,262	20	−1,463.1
5	32,064	0.03636	1,165.8	22,904	0.03636	832.8
6	−512	20	−25.6	−12,606	20	−630.3
7	31,552	0.03636	1,147.2	10,298	0.03636	374.4
8	22,432	20	1,121.6	−5,118	20	−255.9
9	53,984	0.03636	1,962.9	5,180	0.03636	188.3
10	.....	.....	3,084.5	.....	.....	−67.6

Interpolating for Q_6: $Q_6 = -7{,}700.0 + 67.6[(7{,}700.0 - 7{,}600)/(67.6 + 3{,}084.5)] = -7{,}697.856$.

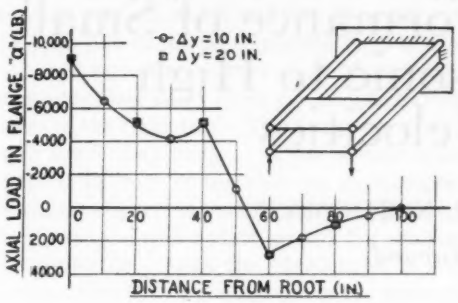

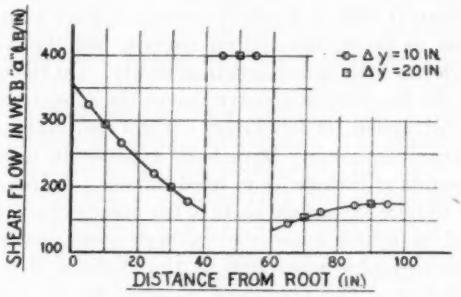

FIG. 5. Example 2, axial loads and shear flows.

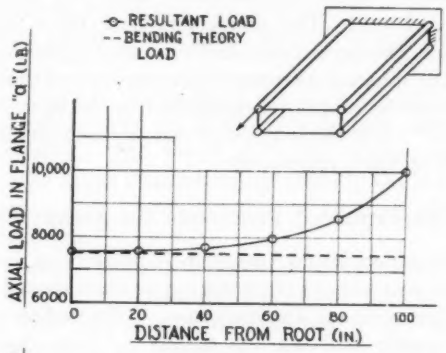

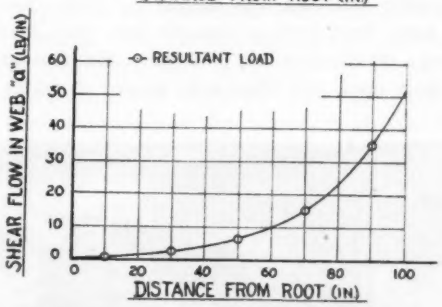

FIG. 6. Example 3, axial loads and shear flows.

PART II—CHOICE OF Δy

The choice of the length increment, Δy, requires a compromise between the labor involved and the precision desired. Until sufficient experience with the method has been acquired, it is helpful to have a means of ascertaining the approximate magnitudes of the errors that result from the use of a chosen length increment, Δy. Basically, these errors are the result of the approximations of the method of numerical integration which is impliedly used in the formulation of the finite-difference equations. In this paper the value of the integrand at the midpoint of the increment is used to approximate the average value over the increment (mid-ordinate rule). The resulting error may be expressed[3] in terms of a power series in Δy. This series converges rapidly and a fair approximation may be obtained by taking only the first term, which involves $(\Delta y)^2$. Applying this result to the present problem it may be inferred that the error due to finite length increment is proportional to $(\Delta y)^2$.

TABLE 5

Errors Due to Δy, Example 2

y	Q_o		Error	Per Cent Error
	$\Delta y = 20$	$\Delta y = 10$	$\Delta y = 10$	$\Delta y = 10$
0	−9,083	−9,008	−25	−0.3
20	−5,246	−5,131	−38	−0.7
40	−5,223	−5,154	−23	−0.4
60	+2,777	+2,846	−23	−0.8
80	+1,020	+1,031	−4	−0.4

Table 5 gives an analysis of the errors in Example 2 using this method. For $\Delta y = 20$ in. the errors are evidently four times as large as for $\Delta y = 10$ in. It follows that the errors for $\Delta y = 10$ in. are one-third the difference between the results for the two increments. With a maximum error of 0.8 per cent it is clear that a 10-in. length increment gives more than sufficient precision. One should not be misled by the spurious accuracy obtainable with small-length increments, since the initial assumptions concerning the idealization of the structure are evidently only approximately fulfilled in practice. For Example 2 it seems likely that a 20-in. length increment would be the best compromise between the conflicting objectives of expediency and accuracy.

REFERENCES

[1] Shanley, F. R., and Cozzone, F. P., *Unit Method of Beam Analysis*, Journal of the Aeronautical Sciences, Vol. 8, No. 6, pp. 246–255, April, 1941.

[2] Kuhn, Paul, *Some Notes on the Numerical Solution of Shear-Lag and Mathematically Related Problems*, N.A.C.A. T.N. No. 704, 1939.

[3] Whittaker, E. T., and Robinson, G., *The Calculus of Observations*, 3rd Ed., p. 140; Blackie & Son, London, 1940.

The Aerodynamic Performance of Small Spheres from Subsonic to High Supersonic Velocities

A. C. CHARTERS* AND R. N. THOMAS*

Aberdeen Proving Ground

ABSTRACT

Smooth spheres, $^9/_{16}$ in. in diameter, were fired through a group of photographic stations spaced at intervals along the trajectory. Each station recorded an image of the sphere and of the pattern of the surrounding shock waves. The successive times of operation of each station were recorded on a precision chronograph and were combined with the distances to determine the retardation and, hence, the drag. The firings were carried out at Mach Numbers from 0.29 to 3.96 and at the corresponding Reynolds Numbers from 9.3×10^4 to 1.3×10^6.

The results show that the drag coefficient is essentially constant at subsonic velocities, rises rapidly through a relatively broad transonic region, and decreases slowly with further increase in velocity in the supersonic region. At subsonic velocities, the drags agree well with the measurements made elsewhere below the critical Reynolds Number. However, a close examination of drags and separation points showed no evidence of a critical Reynolds Number for this size sphere. It is believed that separation phenomena on small spheres at supersonic velocities are controlled by compressibility effects rather than boundary-layer conditions.

Additional firings were carried out with rough $^9/_{16}$-in. spheres, with smooth $^9/_{32}$-in. spheres, and with smooth $1^1/_2$-in. spheres to study the effects of roughness and size. At supersonic velocities these effects change the drag but little. At low transsonic velocities the drag coefficients of the $1^1/_2$-in. spheres fall well below the $^9/_{16}$-in. sphere curve, and this difference, combined with changes in the wake flow pattern, demonstrates the occurrence of a critical Reynolds Number for the $1^1/_2$-in. sphere.

SYMBOLS

t	= time
$a_{(\ )}$	= coefficient in time-distance function
x	= distance along trajectory
x_0	= distance to center of trajectory
K_D	= drag coefficient
K_{D_1}	= drag coefficient for Type I projectile (Gavre)
m	= mass of projectile
ρ	= density of air
d	= diameter of projectile
V	= velocity of projectile
M	= Mach Number
R	= Reynolds Number
ν	= coefficient of kinematic viscosity
S	= angle from trajectory to separation point
α	= angle of shock wave at separation point
β	= wake angle

Received January 2, 1945. To have been presented at the I.A.S. Thirteenth Annual Meeting, which was canceled to cooperate with a Government appeal (January, 1945) to refrain from holding conventions and meetings.

* Ballistic Research Laboratory, Ordnance Research and Development Center.

INTRODUCTION

SPHERICAL SHOT and spherical surfaces have a limited use as projectiles and on aircraft, but the sphere as such has little direct practical utility. On the other hand, its beautiful symmetry makes the sphere a valuable instrument for laboratory control and calibration. For example, spheres have been extensively used for calibration of turbulence in wind tunnels. An occasion arose to take advantage again of the unique characteristics of the sphere in order to calibrate some new ballistic photographic apparatus at the Ballistic Research Laboratory. The apparatus required for its calibration a projectile having an unusually high retardation and whose flight characteristics were free from the effects of yaw. The sphere met both these requirements. The experiments had an added significance in that the sphere is a representative member of that class of projectiles roughly characterized by the term "blunt bodies." It is the purpose of this paper to give a brief report on these experiments.

EXPERIMENTAL PROCEDURE AND APPARATUS

The experimental procedure consisted of firing a sphere past a series of photographic units spaced along the beginning of the trajectory. The spheres were high-quality ball bearings having a $^9/_{16}$-in. diameter. They were fired from a smooth bore gun made by reaming a standard caliber 0.50 tube. Six photographic units were used, and they were spaced at intervals of

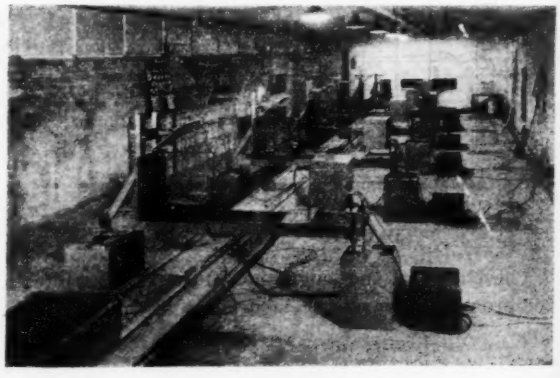

FIG. 1.

10 ft. from 19.25 to 68.25 ft. from the muzzle, except for the first interval which was 9 ft. (Fig. 1).

The operation of the photographic units is based on the old, well-known method of spark photography. A photographic plate and a spark gap are placed on opposite sides of the trajectory. The firings are carried out in an inclosed, dark range. At the instant when the projectile is in front of the plate an appropriate electronic circuit triggers the spark and the light from the spark exposes the entire plate, except the shadow cast by the projectile. Thus the photograph is really a silhouette rather than a photograph in the conventional sense.

The spark gap is powered from a capacitor charged to high voltage. Its discharge surge has an extremely short duration, lasting only a few microseconds, and effectively "freezes" the shell's motion. A signal is coupled from the capacitor discharge and is recorded on a cathode-ray drum chronograph. The chronograph is constructed so that the deflection of the "spot" on a cathode-ray tube is recorded on a strip of film wrapped around the periphery of a rapidly rotating drum. The "spot" is deflected by the spark signals from each unit in turn and every 0.001 sec. by a signal from a multivibrator regulated by a high-precision frequency standard. The signal shapes are narrow spikes, and the chronograph record has the appearance of a row of regularly spaced fence posts with an occasional odd one.

In addition to the image of the projectile, the spark photograph records the shock-wave pattern surrounding the shell. The waves are quite transparent, of course, but act as weak lenses and refract the light from its normal path, causing regions of alternate shadow and highlight.

A photographic unit consists of a framework that holds two 11- by 14-in. photographic plates in horizontal and vertical planes, respectively, and of the spark gap and its associated electronic power and trigger circuits. The vertical plate is exposed directly, and the horizontal plate is exposed by means of an inclined mirror placed above it. Two nicked reference edges mounted rigidly on the framework are silhouetted on the plates. The framework is adjustable, the reference edges are carefully aligned in position, and their angular and linear deviations from common horizontal and vertical planes are accurately surveyed. The distance from the nick on one unit to the next is taped.

Measurement and Reduction

The experimental records for each sphere fired consist of pairs of photographic plates from each of the six units and a film from the drum chronograph. The coordinates of the sphere on each plate are measured from the nicked reference edge. These are combined with the survey and are corrected for conical projection to give the location of the sphere in spatial coordinates common to all units. The time at which each unit in turn operates is recorded on the chronograph film superimposed on a 0.001-sec. scale generated by the controlled multivibrator. The time is measured on the scale by counting whole intervals and measuring fractional intervals.

The final measurements coming from the spark photography range are times and distances at intervals along the trajectory, and the first step in the reduction is to obtain the functional relationship between the two. It is assumed that the time can be given by a power series in the distance measured from the center of the range as follows:

$$t = a_0 + a_1(x - x_0) + a_2(x - x_0)^2 + \ldots$$

that is:

$$t = \sum_{i=0}^{n} a_i(x - x_0)^i$$

The coefficients in the power series are determined from the experimental measurements by a least square method in the conventional manner.

At the center of the range, the derivatives of time with respect to distance are given by

$$\dot{t} = a_1 \qquad \text{at } x = x_0 \text{ where } (\dot{}) = d(\ )/dx$$
$$\ddot{t} = 2a_2$$
$$\dddot{t} = 3!a_3 \qquad \text{and so on}$$

The drag coefficient is defined by the equation

$$K_D = -(m/\rho d^2)(\dot{V}/V)$$

where

m = mass of the projectile
ρ = density of the air
d = diameter of the projectile
V = velocity of the projectile
$\dot{V} = dV/dx$

The number of terms used in the power series will depend on the variation of drag with velocity and change in velocity over the length of the range. In the reduction, the drag coefficient is determined from the coefficients of the power series. On the other hand, it can be seen that these coefficients depend on the value of the drag coefficient and its functional variation with Mach Number. The accuracy with which the coefficients express the drag coefficient function depends on the number of terms used in the time-distance function. If terms through the cubic are used, a more accurate representation of the drag coefficient is realized and it is possible to compute the slope of the drag coefficient function. However, the data from each round were not considered accurate enough to determine this slope, and, since a quadratic equation gave a sufficiently close approximation to the value of the coefficient, it was used to reduce the data throughout. The error in the drag coefficient resulting from the use

of a quadratic rather than a cubic was less than $^1/_{10}$ per cent in the worst case (except possibly at the join points from subsonic to transsonic and from transsonic to supersonic).

One of the purposes of the original experiment was to determine the accuracy of measurement given by the new photographic apparatus. A rough preliminary estimate of the accuracy based on the nature of the apparatus and photographic records indicated that distances should be accurate to a few millifeet (10^{-3} ft.) and times to a few microseconds (10^{-6} sec.). Accordingly, one should expect the distances to be more accurately measured at high velocity than the times, since 1-millifoot travel takes $^1/_3$ microsec. time at 3,000 ft. per sec., and the times more accurately than the distances at low velocity, since 1 microsec. time corresponds to $^1/_2$ millifoot at 500 ft. per sec. Several rounds at high and low velocities were analyzed considering all the error in the times at high velocity and all the error in the distances at low velocity. The results show average standard deviation of 2 microsec. and 6 millifeet. The error in time introduced into the least squares determination of the coefficients in the time-distance function will result in a probable error in K_D of 0.5 per cent in the supersonic range. The error in distance will result in 0.8 per cent in the subsonic range.

Another method of estimating the error in K_D comes from the scatter of the experimental values about the drag coefficient function computed by a least squares method. The residuals from a constant value of K_D in the subsonic range give a probable error in K_D of 1.5 per cent; from a cubic in the transsonic range, of 1.9 per cent; and from an inverse quadratic in the supersonic range, of 0.7 per cent.

Results

Drag Function

The aerodynamic drag acting against the inertia of the sphere to cause its retardation is given by the equation

$$\text{Drag Force} = K_D \rho d^2 V^2$$

K_D represents an empirically determined parameter in this equation whose value depends primarily on Mach Number for a given size sphere. Its variation with Mach Number is given in tabular form in Table 1 and in graphic form in Fig. 2.

The drag coefficient function shows that there are three ranges of velocity in which the drag force changes smoothly and regularly with velocity. These can be called roughly "subsonic" up to $M = 0.5$, "transonic" from 0.5 to 1.4, and "supersonic" beyond $M = 1.4$. Within each range the function is roughly linear and, for qualitative comparison, can be described by the following:

TABLE 1

Sphere Firings: Table of Results

Round	M	K_D	Round	M	K_D
128	3.961	0.373	115	1.588	0.394
131	3.912	0.365	113	1.581	0.399
124	3.712	0.367	71	1.305	0.380
130	3.699	0.368	72	1.225	0.386
129	3.642	0.363	83	1.160	0.358
132	3.489	0.371	82	1.159	0.366
122	3.456	0.372	86	1.119	0.346
123	3.420	0.367	76	0.967	0.315
121	3.283	0.373	74	0.962	0.319
120	3.123	0.371	144	0.951	0.318
119	2.946	0.377	73	0.947	0.305
118	2.913	0.382	75	0.861	0.272
101	2.767	0.376	145	0.642	0.202
66	2.761	0.387	77	0.609	0.212
65	2.725	0.390	78	0.569	0.204
104	2.713	0.377	84	0.465	0.198
68	2.300	0.390	85	0.431	0.192
67	2.257	0.389	88	0.317	0.190
69	1.827	0.394	116	0.286	0.195
70	1.797	0.395	117	0.285	0.187

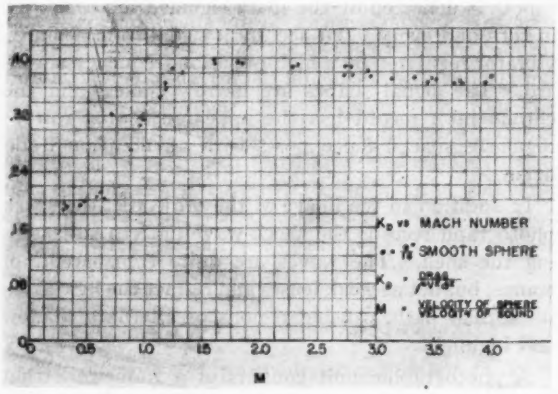

FIG. 2.

"Subsonic" $K_D = 0.192$ (± 0.0029) $0 < M < 0.5$

"Transonic" $K_D = 0.3173 \pm (0.0018) + 0.2711 \pm (0.0090) (M - 1.00)$ $0.5 < M < 1.4$

"Supersonic" $K_D = 0.3812 \pm (0.0006) - 0.0140 \pm (0.0008) (M - 2.75)$ $1.4 < M < 4.0$

The linear functions will be in error near the join points as one range changes to another. In fact, the choice of function will depend largely on its use. For example, the data for $0.4 < M < 1.6$ are fitted more closely by a cubic, as follows:

$$K_D = 0.3198 \pm (0.0036) + 0.2987 \pm (0.0217) (M - 1.0) - 0.0809 \pm (0.0120) (M - 1.0)^2 - 0.3606 \pm (0.0637) (M - 1.0)^3$$

And the data for $1.4 < M < 4.0$ by an inverse quadratic as follows:

$$K_D = \underset{(\pm 0.0055)}{0.3812} + \underset{(\pm 0.0239)}{0.1199}\left(\frac{1}{M} - \frac{1}{2.75}\right) - \underset{(\pm 0.0497)}{0.2375}\left(\frac{1}{M} - \frac{1}{2.75}\right)^2$$

Certain characteristics of the drag coefficient function have an unusual significance. First, the transition from subsonic to supersonic takes place over a relatively wide range of velocities. There is no sudden change as the projectile reaches the velocity of sound. The drag varies smoothly and regularly with velocity, and measurements are quite reproducible in this region. Second, there is no sudden decrease in drag coefficient indicating a critical Reynolds Number. This point will be discussed in detail later, but it should be noted that within each region the function is essentially monotonic.

Effect of Roughness

It was known that under certain circumstances surface roughness can greatly change the drag of a sphere.[1] The ball bearings fired had a smooth, highly polished surface, and it was felt desirable to investigate briefly the effect of roughness at supersonic velocity. The ball bearings were roughened by annealing the hard steel and filing a criss-cross pattern of deep grooves (approximately $^1/_{16}$ in. deep spaced about $^1/_8$ in. apart) over the surface. Three shots were fired near $M = 2.5$ and the drags are given in Fig. 3 by the points marked by triangles. The roughness produced only a slight increase (2.9 per cent) (± 0.2 per cent) in the drag of the $^9/_{16}$-in. sphere at this supersonic velocity.

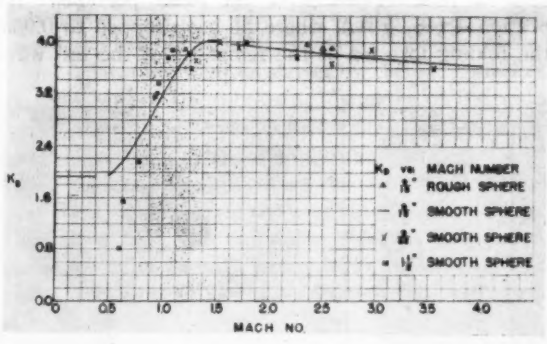

FIG. 3.

Effect of Size

An opportunity arose at a later date to measure the retardation of $^9/_{32}$-in. spheres (just *half* the diameter of the original spheres). The measurements were made with a different type of apparatus, and the accuracy is less and the experimental scatter greater. The drags are given by the X points in Fig. 3.

Recently, some $1^1/_2$-in. spheres were fired at transsonic velocities through modern, high-precision apparatus. The firings were limited to high subsonic and transsonic velocities because of the lack of time for a more extensive program. The drags are given by the ⊡ points in Fig. 3.

At supersonic velocities the $^9/_{32}$-in. results show that reducing the diameter by one-half did not produce a significant change in the drag. This result was not entirely unexpected, since a critical Reynolds Number was not observed and since surface roughness had little effect, at least at supersonic velocities. Scale effects, as changes due to variations in size are called, are usually associated with frictional effects present in the boundary layer. The Mach Number and surface roughness observations indicated that the boundary layer played little part in controlling the drag of a sphere at supersonic velocities, and the absence of any scale effect would further confirm this conclusion. At transsonic velocities there appears to be a change in drag coefficient with size: above the velocity of sound, the $^9/_{32}$-in. values lie below the $^9/_{16}$-in. curve and the $1^1/_2$-in. values lie above.

In the region just leaving the subsonic and entering the transsonic, the $1^1/_2$-in. spheres show the presence of a critical Reynolds Number. The drag coefficients of the $1^1/_2$-in. spheres are less than one-half the drag coefficients of the $^9/_{16}$-in. spheres at the one subsonic velocity fired. As the transsonic region is entered, the drag coefficient of the $1^1/_2$-in. sphere rises rapidly, reaching the value for the $^9/_{16}$-in. sphere slightly below the velocity of sound and exceeding it somewhat thereafter.

Wave Phenomena

The wave patterns at all supersonic velocities ($1.4 < M < 4.0$) have certain general characteristics in common (Fig. 4). The sphere is preceded by a strong head wave, which is inclined to the direction of motion at

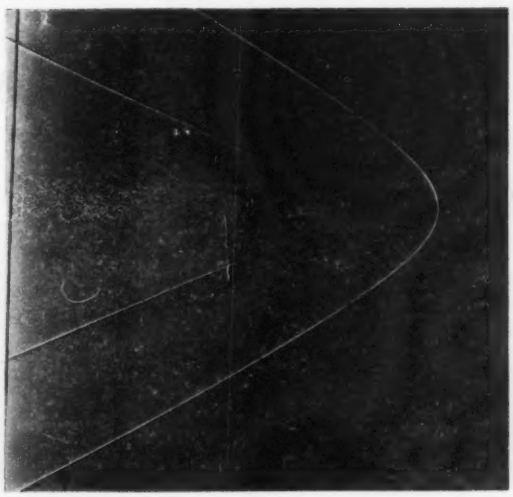

FIG. 4. Round 67, station 4, Mach Number 2.23, velocity 2,496 ft. per sec.

an angle that is somewhat greater than the Mach angle due to the wave's finite amplitude. It curves gradually with distance from the sphere and presumably reaches the true Mach angle far away. Behind the head wave, many weak wavelets emanate from part of the front section of the sphere back to the separation point. These show that the velocity of flow over this part is supersonic. A wave of moderate intensity starts at the separation point. It is strong enough to change the flow direction a little so that the wake does not leave the surface in a tangent direction but leaves inclined slightly outward from the tangent. The wave then converges or diverges, as the case may be, for a diameter or so behind the sphere where it loses its well-defined shape and breaks up into a series of large, irregular vortexes. The irregular vortexes are themselves moving at supersonic velocities and generate a whole field of wavelets, which coalesce into a single strong wave starting near the region of disintegration. This wave is known as the tail wave, and it should be noted that it is associated with the wake. In the vicinity of the sphere the angle of the tail wave is less than that of the head wave. The tail wave angle is less than the Mach angle given by the velocity of the sphere and the velocity of sound in free air. This decrease is probably a result of the expansion of the flow around the sphere. The wave from the separation point is inclined still more and coalesces with the tail wave a short distance from the sphere. The region between the two is filled with small wavelets probably coming from vortices in the wake boundary.

At high supersonic velocities the sphere appears to be flattened in front. This is entirely an optical effect and is caused by refraction of the light over the front of the sphere by the head wave. At high velocities the front of the head wave is located close to the front of the sphere, but, at a Mach Number of around 2, a noticeable separation appears between the two. This separation increases gradually as the velocity is decreased until a velocity near that of sound, where the increase is rapid.

In the immediate neighborhood of the velocity of sound, the wave pattern depends in part on the history of the projectile from the muzzle on. Round 74 is a good illustration of the changes that take place on passing through $M = 1$ (Fig. 5). The sphere left the gun at $M = 1.052$. At the front station, 19.25 ft. away, the sphere has retarded to a Mach Number of 1.012. The wave pattern is still characteristically supersonic, although it should be noted that the head wave is now almost three diameters ahead. The photograph shows a double head wave, but the reasons for the second wave are not clearly understood. By Station 2 (28.25 ft.) M has dropped to 0.992. The pattern is still similar, although the head waves have coalesced and moved seven diameters ahead. By Station 3 (38.25 ft.) M has dropped to 0.972. The head wave has moved out of the range of the plate, and the tail wave is beginning to take on a characteristic transsonic shape. The wave extends some 5 in. out from the wake and dies rapidly to sonic amplitude further out. A reflected wave forms from the outer portion of the tail wave and has the appearance of a bright string across a dark bow. It is possible, of course, that the reflected wave is not a wave but is an optical effect produced by refraction around the rim of the main tail wave. Also, the outer portions of the wave are beginning to fold forward over the inner portions. By Station 4 (48.25 ft.), where M has dropped to 0.953, the folding forward of the remnants of the tail wave

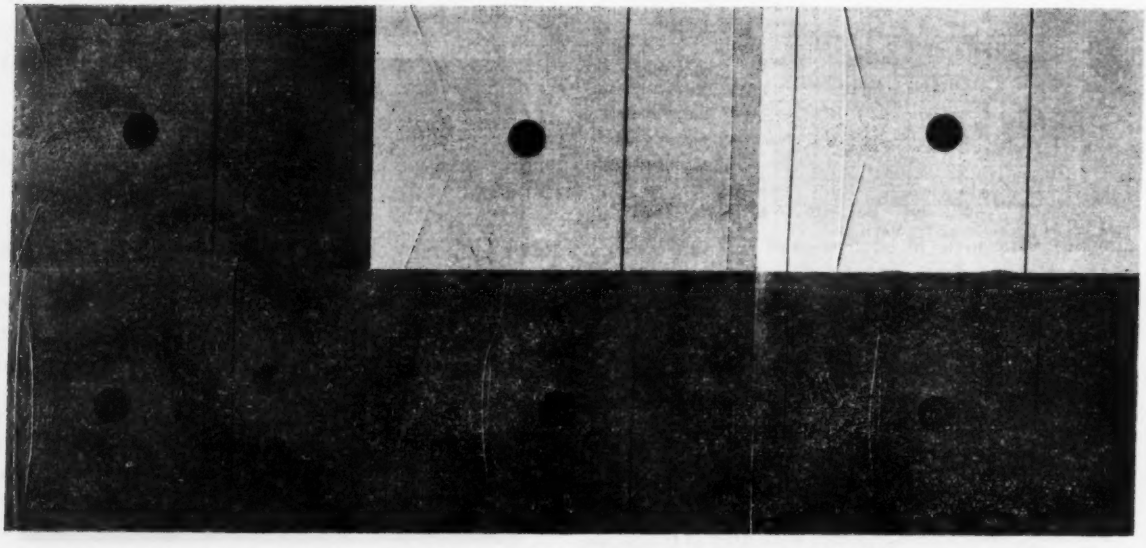

FIG. 5. Round 74. *Top row, left to right:* station 1, velocity 1,140 ft. per sec.; station 2, velocity 1,116 ft. per sec.; station 3, velocity 1,093 ft. per sec. *Bottom row, left to right:* station 4, velocity 1,072 ft. per sec.; station 5, velocity 1,051 ft. per sec.; station 6, velocity 1,031 ft. per sec.

has progressed still further. At this station, two other characteristics of the transonic wave pattern appear. The wave at the separation point has faded away to a short "cat's whisker" and the wake has become a source of flat fronted waves that extend all the way across the plate. Close inspection reveals many of these waves in the vicinity of the sphere. Their characteristics are still more pronounced at Station 5 (58.25 ft., $M = 0.934$). The whole field is filled with waves whose strength is barely more than sonic and yet enough for the wave to be visible. Spark photography records the presence of weak shock waves with unusual sensitivity. The spark pictures shown in Fig. 5 lack the wealth of detail that can be seen in the negatives. Also the spark photographs form a motion picture of the development and action in the wave pattern, since they are successive records along the sphere's trajectory. A close inspection of successive spark photographs shows that the waves in the vicinity of the sphere appear to originate in the wake and sweep forward past the projectile as they travel at sonic speed. At Station 6 (68.25 ft., $M = 0.916$) the same pattern continues. As the velocity decreases still further the waves generated by the wake decrease in number and intensity. Finally, at subsonic velocities the waves disappear altogether and only the wake is visible. A picture of the wake remains, however, even at the lowest Mach Numbers photographed, $M = 0.29$.

It is curious that the wake should generate the last shock waves on passing from transsonic to subsonic velocities. Perhaps the phenomena can be best explained by considering the sphere stationary and the air flowing past it. The main flow has a velocity less than the velocity of sound. The air is accelerated in passage over the sphere until a local velocity of sound is reached at the separation point as shown by the cat's whisker. Past the sphere the increasing diameter of the wake causes still further acceleration and a considerable portion of the flow reaches a slightly supersonic velocity. At the place of disintegration of the wake, a plane-front wave forms and changes the accelerated portion of the main flow back to subsonic velocity. The wave formation is apparently unstable for the wave then moves forward, a new one forms, and the cycle repeats.

Separation Point Phenomena

The failure of a critical Reynolds Number to develop in the drag coefficient function was most unexpected, for the Reynolds Numbers reached at the highest velocities were far greater than the critical Reynolds Numbers observed elsewhere and some additional corroborating evidence was sought. It was known that the reduction in drag at the critical resulted from a rearward transition of the separation point which greatly reduced the form drag. The location and characteristics of the separation point were carefully studied from the spark photographs in the hope that this phenomenon might give an explanation.

The point of separation at supersonic velocity is clearly marked by a shock wave, as mentioned previously. On examining the $^9/_{16}$-in. sphere photographs, it was thought at first that separation might have taken place a short distance after the shock wave. However, subsequent examination of the $1^1/_2$-in. sphere photographs, illustrated in Fig. 7, clearly shows that the separation point and shock wave are coincident. The edge of the wake, which marks the direction of flow, projects directly back to the base of the shock wave. A series of representative photographs were selected and the shock-wave angle, the inclination of the edge of the wake, and the location of the separation point were measured as shown in the sketch at the top of Fig. 6. The front of the sphere was distorted at supersonic velocities so the center was located as a point equidistant from the top, bottom, and rear. At subsonic velocities the separation point was considered to be the tangency point of a tangent to the sphere running along the edge of the wake. In view of this definition of the separation points, it should be noted that at subsonic velocity the value of S is equal to $\beta + 90°$; at supersonic velocity, however, the value of S is approximately equal to $\beta + 85°$, because of the action of the shock wave at the separation point. The measurements are plotted as a function of Mach Number in Fig. 6. The results for both the $^9/_{16}$- and the $1^1/_2$-in. sphere are given on this graph. It should be noted that the character of the photographs did not permit accurate measurement of these quantities and the values shown on the graph are subject to considerable scatter.

For the $^9/_{16}$-in. spheres the behavior of the separation point is about as follows: At the highest velocities, the separation point is well to the rear of the equatorial plane and the wake converges strongly. (The equatorial plane is defined as the plane perpendicular to the direction of motion through the center of the sphere.)

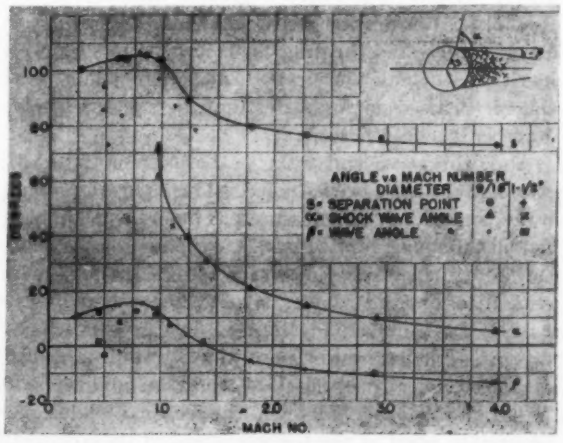

FIG. 6.

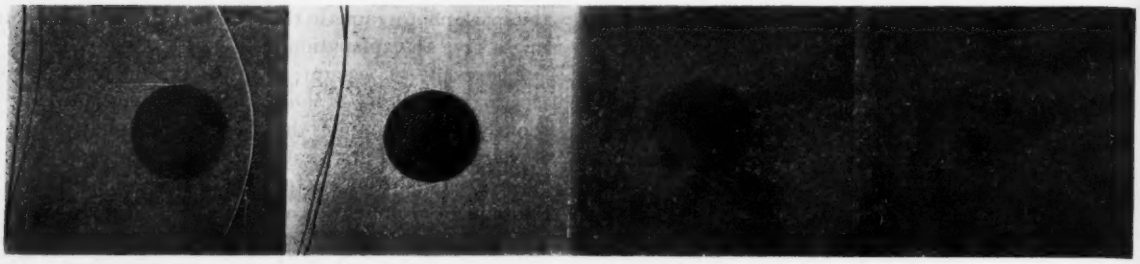

FIG. 7. *Left to right:* round 788, station 2, Mach Number 1.415, velocity 1,600 ft. per sec.; round 791, station 2, Mach Number 0.804, velocity 910 ft. per sec.; round 793, station 2, Mach Number 0.52, velocity 588 ft. per sec.; round 794, station 1, Mach Number 0.445, velocity 515 ft. per sec.

With decreasing velocity, the wake becomes divergent at $M = 1.4$. This is a slightly higher Mach Number than $M = 1.25$ given for the separation point crossing the equatorial plane, and the difference is due to the action of the shock wave as explained previously. The separation point moves still further forward and the wake becomes more divergent down to a Mach Number of about 0.8. At lower Mach Numbers the location of the separation point and the divergence of the wake remain about the same.

The separation point, as well as the drag coefficient function, shows no evidence of a critical Reynolds Number. Nowhere is there a rapid rearward transition of the separation point. Of course, it might be argued that the rearward shift starting at $M = 0.8$ indicates transition through a critical. However, the failure of the drag to respond makes it much more likely that the shift results from a gradual change in the overall flow pattern.

The $1^1/_2$-in. spheres were fired in the hope that the Reynolds Numbers reached in the subsonic region would be great enough to pass a critical before entering the compressible region. Unfortunately, the firings were limited in extent. Although the firings were not carried out at low enough subsonic velocities to verify the presence of a critical, the Reynolds Number for the lowest velocity round fired is greater than the critical Reynolds Number for free flight observed by other experimenters and the drag coefficient for this round is less than one-half the drag coefficient for the $^9/_{16}$-in. sphere. This result indicates that a critical Reynolds Number has been passed.

Also, the wave and wake patterns from the spark photographs have been studied. The separation point, wake, and wave were measured as before and are plotted on the same graph (Fig. 6). At $M = 1.4$, the highest fired, the separation point is a little further to the rear than for the smaller sphere, but otherwise the patterns are similar (Figs. 4 and 7). As the velocity decreases, the separation point moves rapidly forward. Near the velocity of sound a slight instability in its position was observed. On the vertical plates, the separation point at the top was ahead of the equatorial plane and on the bottom was behind. At first this was thought to be an effect due to the proximity of the horizontal plate. On examining the images recorded on the horizontal plates just the reverse effect was noted, so the cause of the asymmetry is not known. As the velocity decreases to $M = 0.8$, the symmetrical pattern returns and the separation point moves well forward of the equatorial plane to the same angle observed for the smaller spheres (Fig. 7).

For velocities down to a Mach Number of 0.8 the separation point phenomena for the large and small sphere are essentially similar, but at $M = 0.8$ the similarity ends. For the $^9/_{16}$-in. spheres the separation point stays well forward of the equatorial plane for all velocities lower than $M = 0.8$, but for the $1^1/_2$-in. spheres the separation point starts moving sharply to the rear as the velocity drops lower than $M = 0.8$ (Fig. 6). At $M = 0.65$, it has moved back near the equatorial plane and the wake is only slightly divergent. At $M = 0.52$, it has moved well back of the equatorial plane and the wake is convergent (Fig. 7). It is also significant that at $M = 0.8$ there are several well-formed cat's whiskers near the separation point; at $M = 0.65$ there is only a single, faint, tiny cat's whisker at the separation point; and at $M = 0.52$ there are no waves of any description any place on the sphere. At lower Mach Numbers, 0.46 and 0.44, the separation point has moved forward again and the wake is divergent (Fig. 7). On one round at $M = 0.442$, an asymmetry was noticed between top and bottom, but, in view of the fact that the separation point is subject to sharp fluctuations near the critical Reynolds Number, the asymmetry observed on this round is not considered unusual or inconsistent with the remaining rounds.

The behavior of the drag coefficient and the rearward dip in the separation point, together with the corresponding convergence of the wake at $M = 0.52$, are the only evidence from the sphere firings so far that show the presence of the critical Reynolds Number in free flight. The combination of evidence is quite convincing, but it must be verified by a more extensive firing at subsonic velocities before it can be regarded as conclusive.

The results from the $^9/_{16}$-in. sphere firings show that a critical Reynolds Number will not occur for this size

sphere in free flight or, at least, a critical similar to that observed elsewhere on large spheres at subsonic velocities. The wake patterns from the $1^1/_2$-in. sphere firings indicate that a critical Reynolds Number occurs at subsonic velocities. On passing through this Reynolds Number, the wake becomes convergent and the separation point moves to the rear as velocity increases. However, once the transsonic region is entered, the wake again becomes divergent and the separation point moves forward with further increase in velocity. This type of flow in the transsonic region resembles the flow at subcritical Reynolds Numbers. The study of the performance of spheres of different sizes over the complete range of velocities is only in its initial stages, and the experimental data so far are so brief that one hesitates to draw any general conclusions. Yet all the data obtained from the sphere firings to date point to the following statements: At subsonic velocities spheres fired through free air perform in the manner predicted by other experiments. On the other hand, at transsonic and supersonic velocities, the effects of compressibility control the flow, and such phenomena as separation are, in turn, controlled by conditions in the main flow rather than in the boundary layer.

A possible explanation of the flow changes on passing from subsonic velocities to supersonic may be given as follows: From the standpoint of a stationary sphere in a stream of air, the streamlines in the flow close to the sphere first converge and then diverge on following the contour around. At subsonic velocities the divergence in the streamline is associated with a decreasing velocity and an increasing pressure in the direction of flow. These conditions favor boundary-layer separation. On the other hand, at supersonic velocity, the divergence is associated with just the opposite condition of flow—an increasing velocity and a decreasing pressure in the flow direction. Such conditions tend to enable the flow to follow the contour around to a point where its direction is abruptly changed by a shock wave. This may be stated in slightly different terms by saying that, while at subsonic velocities the Reynolds Number is the controlling parameter, at supersonic velocities the Mach Number controls and the Reynolds Number is only secondary. All the experimental data obtained from firings to date agree with this general observation. A note of caution must be added that the data to date are far from complete.

Comparison with Other Experiments

Firings

Comparison with other firings is difficult since no strictly parallel measurements have been made. To the authors' knowledge, no other complete sphere shoot has been carried out in recent times using modern ballistic apparatus. The bluntest standard projectile is the Gavre type. It has a square base, a total length of 3.28 cal., and a 2-cal. radius tangent ogival head.

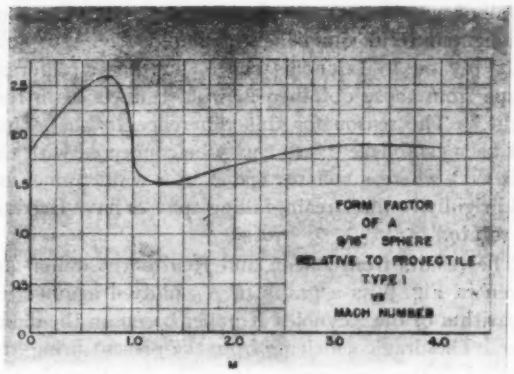

FIG. 8.

The ratio of K_D for the $^9/_{16}$-in. sphere divided by K_{D1} for the Gavre projectile (also designated as Type I) plotted against Mach Number is shown in Fig. 8. As can be seen, the drag coefficient of the sphere is considerably greater and the functions are not similar in shape.

Spheres at Subsonic Velocities

The drag of spheres at subsonic velocities has been investigated extensively by many methods. A splendid summary of the results is given in reference 1. A brief description of the experiments most nearly comparable to the present firings is quoted from Goldstein[1] as follows:

"Measurements of the drag of a sphere moving thru relatively calm air in the atmosphere have been made by Klein[2] with special apparatus designed for use on an aeroplane. . . . . Included . . . . are also . . . . dropping tests by Bacon and Reid[3] . . . . and Lunnon[4] . . . . . The results of Bacon and Reid were obtained from the rates of fall of wax, rubber, and wooden spheres known weight dropped from an aeroplane and falling thru calm air, and those of Lunnon from the rates of

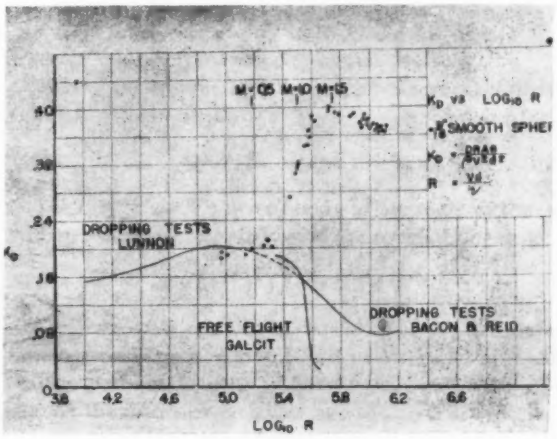

FIG. 9.

of fall of metal spheres in air and water. The curve of Bacon and Reid can be extrapolated . . . . to join smoothly on to Lunnon's curve, but has a different shape from those obtained in wind tunnels or in free flight.* The reason for this difference in shape has not been established, but it may be connected with the fact that whereas spheres tested in a wind tunnel are held rigidly in the stream, falling spheres have freedom to rotate."

The results from Bacon and Reid and Lunnon are given in Fig. 9 as a graph of K_D plotted against the logarithm of the Reynolds Number based on the diameter. The drag coefficients from the present firings are plotted on the same graph. It can be seen that the two are in good agreement at subsonic velocities.

* By free flight, Goldstein refers to the type of experiment made by Klein. (See reference 2.)

The characteristic wake pattern for a $1^1/_2$-in. sphere at subsonic velocities is shown in Fig. 7. The angle of separation point at subsonic velocities ($M = 0.3$) for a $^9/_{16}$-in. sphere is 101° (Fig. 6). The separation point observed on a 6-in. sphere mounted in an open jet tunnel at a velocity of 50 ft. per sec. is 97°.[5] The two are in remarkably good agreement considering the great difference in scale.

References

[1] Goldstein, S., *Modern Developments in Fluid Dynamics*, 1st Ed., Vol. II, p. 491; Oxford University Press, London, 1938.

[2] Millikan, C. B., and Klein, A. L., *The Effect of Turbulence*, Aircraft Engineering, Vol. 5, No. 54, p. 169, August, 1933.

[3] Bacon, D. L., and Reid, E. G., *The Resistance of Spheres in Wind Tunnels and in Air*, N.A.C.A. Report No. 185, 1923.

[4] Lunnon, G. R., *On Fluid Resistance to Moving Spheres*, Proc. Roy. Soc. A, 118 (1928), 680–694; 1B1D. 110 (1926), 304.

[5] Fage, A., *Experiments on a Sphere at Critical Reynolds Numbers*, A.R.C. Reports and Memoranda, No. 1766, 1937.

Letters to the Editor

Dear Sir:

The interesting paper "Shock Waves in Aerodynamics" by Prof. Howard W. Emmons (JOURNAL OF THE AERONAUTICAL SCIENCES, Vol. 12, No. 2, p. 188, April, 1945) contains an error of presentation which causes some points to be obscure.

Since a steady movement is assumed to exist in reference to a pipe (see "Shock Waves," second paragraph), the shock wave, per force, must be considered as stationary; otherwise Eqs. (1), (2), (3) and their consequence, Eq. (7), would not be valid. Thus, a stationary shock wave (if any such wave exists) being presupposed, it is logical to find this shock wave at the end of the reasoning. It results that the sentence "there must be . . . . some disturbance that remains between sections 1 and 2" does not explain the phenomenon, the more so as there is no reason against the existence of a nonstationary shock wave. In this last occurrence, all the equations remain valid, provided all the velocities are measured in reference to the shock wave. With this approach, the extraneous and restrictive system of reference constituted by the pipe is eliminated, Eqs. (1) to (7) remaining valid. Thus, velocities u_1 and u_2 are not absolute velocities or velocities in reference to the pipe, as seems to result from the text, but are differences between the velocity of the shock wave and the velocities of the fluid on both sides of the shock wave.

LEON BESKIN
Design Specialist
Consolidated Vultee Aircraft Corporation

Dear Sir:

In the comments of Mr. Beskin on my paper "Shock Waves in Aerodynamics" there is presented what is presumed to be an error in my discussion of fundamental equations of the shock wave. I perhaps did not make it clear in the paper that the "pipe" with respect to which velocities were measured need not be stationary. Consequently, nonsteady shock waves are governed by the same relations. I undoubtedly should, therefore, have added a sentence or two to make this clear.

HOWARD W. EMMONS
Harvard University

A Direct Method of Estimating the Performance of a Helicopter in Powered Flight

WALTER CASTLES, JR.*
Georgia School of Technology

SUMMARY

This paper presents a direct method of calculating the performance characteristics of a helicopter in powered flight. The method is based on the simple momentum theory but incorporates the primary effects of the vertical drag force and an empirical correction to the induced power.

Nomograms are included for the rapid solution of the useful equations.†

NOTATION

Angles in Radians

- α' = angle between the relative wind and longitudinal axis of the fuselage
- θ = angle of incidence measured in a plane perpendicular to the blade axis, with the blade at zero coning angle and between the zero lift chord line and a plane perpendicular to the axis of rotation
- ψ = azimuth angle between the blade axis and the vector, V_h

Areas

- A = rotor disc area
- f = parasite drag area measured in the direction of V_h

Forces

- D = parasite drag
- D_v = vertical component of parasite drag
- T = rotor thrust
- W = gross weight

Lengths

- c = chord of blade (at $0.7R$ if blade is tapered)
- r = radius of blade element, $c\,dr$
- R = radius of rotor

Miscellaneous

- b. hp. = engine brake horsepower
- ρ = air density
- ω = angular velocity of rotor in radians per second

Nondimensional Coefficients

- C_{D0} = profile drag coefficient of blade airfoil at $C_L = \bar{C}_L$
- $\bar{C}_L$ = mean blade lift coefficient in hovering flight
- k = $\dfrac{\text{parasite drag area measured in the direction of } V_v}{\text{parasite drag area measured in the direction of } V_h}$
- K = $\dfrac{\text{horsepower to lifting rotor}}{\text{engine brake horsepower}}$

Nondimensional Parameters

- B = number of blades in rotor
- F = $f/4A$
- σ = solidity = $Bc/\pi R$
- λ_i = V_i/V_0
- λ_v = V_v/V_0
- λ_h = V_h/V_0
- λ_t = V_t/V_0
- λ_{hc} = λ_h for maximum rate of climb and minimum power required in level flight
- λ_{hm} = λ_h for top speed in level flight
- λ_{hR} = λ_h for maximum range
- λ_{Vv} = λ_v for maximum rate of vertical climb
- λ_p = power parameter = $550\,K$ b.hp.$/2\rho A V^3 = 550K$ b.hp.$\div WV_0$
- Y = $\lambda_p - (\sigma C_{D0}/16)\,\lambda_i^3 - (3\sigma\, C_{D0}/16)\,\lambda_i\lambda_h^2 - F\lambda_h^3$
- Z = $\lambda_i + \lambda_v$

Velocities

- u = induced velocity of rotor
- V = velocity along the flight path
- V_h = horizontal component of the velocity along the flight path
- V_i = vertical component of the induced velocity
- V_0 = induced velocity of an actuator disc with a disc loading = W/A in hovering flight in a perfect fluid. $V_0 = (W/2\rho A)^{1/2}$
- V_t = tangential velocity of blade tips = ωR
- V_v = vertical component of the velocity along the flight path.

THEORY

THE ACCEPTED FORM for the general momentum equation of an actuator disc is,[1]

$$T = 2\rho\, A u V' \tag{1}$$

where V' = resultant velocity at the disc.

Taking the summation of forces in the vertical direction Eq. (1) can be written

$$W + D_v = 2\rho A V_i V' \tag{2}$$

The drag of an elongated body at an angle to the air stream can be written, to a good approximation, as

$$D = (\rho/2)\,(V')^2\,(f\cos\alpha' + kf\sin\alpha') \tag{3}$$

Assuming that the longitudinal axis of the helicopter fuselage remains horizontal and making the approximation that the velocity at the fuselage is the same as that at the rotor,

$$D_v = (\rho/2)\,kf(V_v + V_i)^2 \tag{4}$$

Received February 15, 1945. A revision of the paper presented at the Rotating Wing Aircraft Session, Twelfth Annual Meeting, I.A.S., New York, January 25–27, 1944.

* Research Assistant Professor, Guggenheim Aeronautical Laboratory, State Engineering Experiment Station.

† Nomograms by Walter Herbert Burrows, Research Associate, State Engineering Experiment Station.

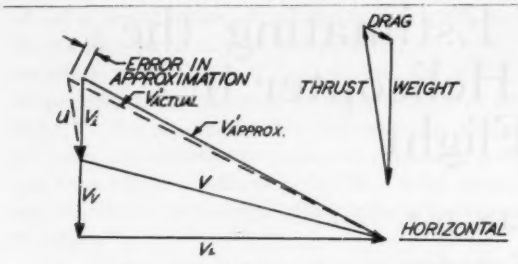

FIG. 1. Velocity and force diagrams.

Let $F = f/4A$. Then it is a good approximation that (see Fig. 1),

$$V' = [(V_v + V_i)^2 + V_h^2]^{1/2}$$

and Eq. (2) can be rewritten as

$$W + 2\rho AkF\,(V_v + V_i)^2 = 2\rho A\,V_i\,[(V_v + V_i)^2 + V_h^2]^{1/2} \quad (5)$$

By defining $V_0 = (W/2\rho A)^{1/2}$ (see Notation) and letting $Z = \lambda_v + \lambda_i$, Eq. (5) can be written in non-dimensional form as

$$\lambda_i = (1 + kFZ^2)/(Z^2 + \lambda_h^2)^{1/2} \quad (6)$$

or

$$\lambda_v = Z - [(1 + kFZ^2)/(Z^2 + \lambda_h^2)^{1/2}] \quad (7)$$

The general performance equation for a helicopter is:

$$WV_v = P_a - P_i - P_Q - P_{C_{D_0}} - P_D \quad (8)$$

where

P_a = power available to lifting rotor
P_i = induced power required
P_Q = power required for torque of profile drag
$P_{C_{D_0}}$ = power required for profile drag due to forward speed
P_D = power required for drag of parasite area

Let $P_a = 550K$ b.hp., where K = (horsepower to lifting rotor)/(engine brake horsepower). If a counter torque rotor is used, its power requirements can be estimated by the method given in reference 3, or the value of K can be found by successive approximations in the same manner as the power required for the lifting rotor.

By definition $P_i = WV_i$.

Evaluation of P_Q for Constant Chord Blades

Assuming a constant profile drag coefficient along the blades and making the approximation that the resultant velocity at a blade element, $c\,dr$, is equal to the vector sum of the tangential and horizontal velocities, the rotor torque, Q_r, due to the profile drag is:

$$Q_r = \frac{1}{2\pi}\int_0^{2\pi}\int_0^R \frac{\rho}{2} C_{D_0} Bcr\,(\omega r + V_h \sin\psi)^2\,d\psi\,dr$$

The expression for Q_r integrates to

$$Q_r = (\rho/8)\,C_{D_0}\,Bc\omega^2R^4 + (\rho/8)C_{D_0}\,BcR^2V_h^2$$

However, $BcR = \sigma A$, $\omega R = V_t$, and $P_Q = \omega Q_r$. Therefore,

$$P_Q = (\rho/8)\,C_{D_0}\,\sigma A(V_t^3 + V_tV_h^2)$$

Evaluation of $P_{C_{D_0}}$ for Constant Chord Blades

For the same assumptions and approximations used to determine P_Q

$$P_{C_{D_0}} = \frac{1}{2\pi}\int_0^{2\pi}\int_0^R \frac{\rho}{2} C_{D_0}\,BcV_h \times (\omega r + V_h \sin\psi)^2 \sin\psi\,d\psi\,dr$$

Integrating and making the substitutions for $BcR = \sigma A$ and $\omega R = V_t$ gives

$$P_{C_{D_0}} = (\rho/4)C_{D_0}\,\sigma A\,V_tV_h^2$$

Evaluation of P_D

$$P_D = (\rho/2)(V')^3\,(f\cos\alpha' + kf\sin\alpha')$$

As $f = 4AF$ and $V' = [(V_v + V_i)^2 + V_h^2]^{1/2}$

$$P_D = 2\rho A\,[(V_v + V_i)^2 + V_h^2]\,(FV'\cos\alpha' + kF\sin\alpha')$$

but $V'\cos\alpha' = V_h$ and $V'\sin\alpha' = V_v + V_i$

or

$$P_D = 2\rho AkF(V_v + V_i)^3 + 2\rho AF(V_v + V_i)^2V_h + 2\rho AFV_h^3 + 2\rho AkF\,(V_v + V_i)V_h^2$$

Rewriting Eq. (7) using the evaluated terms,

$$WV_v = 550K \text{ b.hp.} - WV_i - (\rho/8)C_{D_0}\,\sigma A(V_t^3 + V_tV_h^2) - (\rho/4)C_{D_0}\,\sigma A\,V_tV_h^2 - 2\rho AF\,[k(V_v + V_i)^3 + (V_v + V_i)^2V_h + k(V_v + V_i)V_h^2 + V_h^3] \quad (9)$$

Then let $\lambda_p = 550K/2\rho A\,V_0^3$. Since $W = 2\rho A\,V_0^2$, Eq. (8) can be written in nondimensional form as

$$\lambda_v = \lambda_p - \lambda_i - \left(\frac{\sigma C_{D_0}}{16}\right)\lambda_i^3 - \left(\frac{3\sigma C_{D_0}}{16}\right)\lambda_i\lambda_h^2 - kF(\lambda_v + \lambda_i)^3 - F(\lambda_v + \lambda_i)^2\lambda_h - kF(\lambda_v + \lambda_i)\lambda_h^2 - F\lambda_h^3 \quad (10)$$

Let $Y = \lambda_p - \left(\frac{\sigma C_{D_0}}{16}\right)\lambda_i^3 - \frac{3\sigma C_{D_0}}{16}\lambda_i\lambda_h^2 - F\lambda_h^3$

Then, as $Z = \lambda_v + \lambda_i$,

$$kFZ^3 + F\lambda_hZ^2 + (1 + kF\lambda_h^2)Z - Y = 0 \quad (11)$$

The equilibrium value of Z can be obtained from Eq. (11) for any given set of conditions and thus the value of λ_v from Eq. (7) and the rate of climb.

An Approximate Method for Finding the Values of λ_i and C_{D_0} for Use in the Other Equations

Assuming a constant angular velocity for the rotor, the value of λ_i will be constant at any given altitude

and the value for hovering flight can be used for all flight conditions at the same altitude.

In hovering flight the down-wash distribution along the blade from the hub to the tip is approximately triangular. Assume that the down-wash distribution is triangular, and make the close approximation that the resultant velocity at a blade element is equal in magnitude to the tangential velocity. Then, for an untwisted blade the angle of attack is constant along the blade, since both the induced and tangential velocities are proportional to the radius. It follows that

$$W = \int_0^R (\rho/2) B c \omega^2 r^2 \bar{C}_L \, dr$$

But $Bc/\pi R = \sigma$ and $\omega R = V_t$. Therefore,

$$W = (\rho/6)\, \sigma A\, V_t^2\, \bar{C}_L \qquad (12)$$

However, $W = 2\rho A\, V_0^2$ and $\lambda_t = V_t/V_0$ or

$$\lambda_t = (12/\sigma\, \bar{C}_L)^{1/2} \qquad (13)$$

Optimum values of $\bar{C}_L$ for hovering flight will be around 0.7 for most rotors and airfoils. Take C_{D_0} from the infinite aspect ratio polar of the blade airfoil at $C_L = \bar{C}_L$.

The foregoing analysis yields quite optimistic results. Because of the assumption of a uniform down-wash and the neglect of radial and tangential components implicit in the use of Eq. (1), the induced power will be underestimated for all flight conditions. In addition, for some flight conditions, portions of the blades will be operating at extreme angles of attack and the profile power will be considerably underestimated.

Although it does not necessarily result in the correct division of power required between profile and induced power, the incorporation of an experimentally determined constant in the induced power equation results in improved accuracy for performance estimation by this method. Therefore, values of λ_i (see Fig. 2) were calculated from the hovering flight wind-tunnel data of reference 2.

Figs. 3 and 4 show the experimental values of λ_i calculated from the previously unpublished wind-tunnel data in Table 1 on vertical ascent and horizontal flight, respectively, compared with the theoretical values of λ_i.

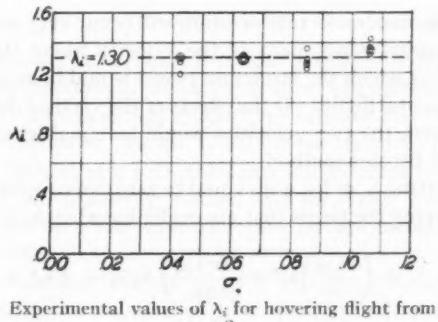

FIG. 2. Experimental values of λ_i for hovering flight from reference 2.

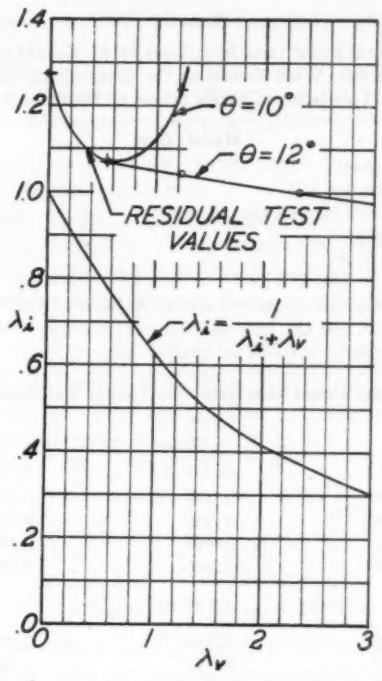

FIG. 3. Experimental values of λ_i vs. λ_V from Table 1 and theoretical values of λ_i vs. λ_V.

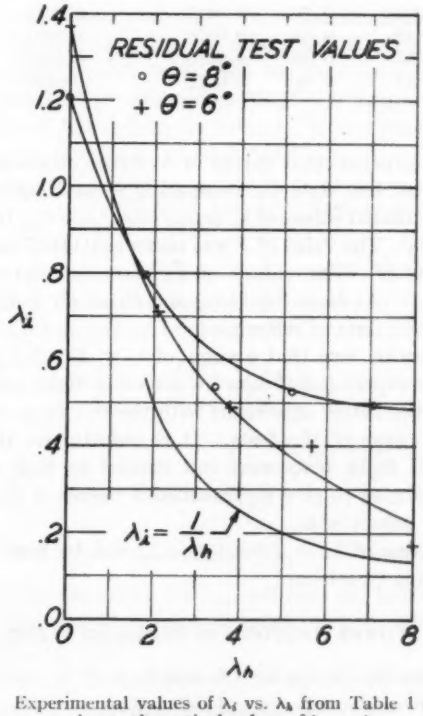

FIG. 4. Experimental values of λ_i vs. λ_h from Table 1 and approximate theoretical values of λ_i vs. λ_h.

TABLE 1

Experimental Rotor Data from Tests by M. Knight in the Open Jet of the 9-ft. Wind Tunnel at the Guggenheim Aeronautical Laboratory, Georgia School of Technology

Model Data

Dia. = 5 ft.
No. of blades = 3
Chord = 2 in. (constant, no twist)
$\sigma = 0.0636$
R.p.m. = 900
Airfoil = NACA 0015
A flapping hinge perpendicular to the blade axis and the axis of rotation and 1 in. from the center of the rotor
Approx. R.N. at $0.75R$ = 340,000

Vertical Ascent Test Data—No Tunnel Wall Correction

V_v/V_i	$\bar{C}_L = \frac{\text{Thrust}}{(\rho/6)\sigma A V_i^2}$	$\bar{C}_D = \frac{\text{Torque}}{(\rho/8)\sigma A V_i^2 R}$
	$\theta = 10°$	
0.00	0.646	0.0844
0.03	0.569	0.0852
0.06	0.450	0.0821
0.09	0.285	0.0673
	$\theta = 12°$	
0.00	0.530	0.0649
0.03	0.441	0.0633
0.06	0.297	0.0564

Horizontal Flight-Test Data—No Tunnel Wall Correction—Model Adjusted for Each Condition So That Coning Axis Was Perpendicular to Airstream

V_h/V_i	$\bar{C}_L$	$\bar{C}_D$	$C_{DH} = \frac{\text{Hor. Drag}}{(\rho/2)\sigma A V_i V_h}$
0.00	0.349	0.0436	....
0.09	0.474	0.0413	0.0013
0.18	0.535	0.0376	0.0011
0.27	0.516	0.0381	0.0010
0.36	0.491	0.0372	0.0010

The experimental values of λ_i were calculated from the rotor test data by computing λ_p and subtracting the calculated values of λ_v, $(\sigma C_{D_0}/16)\lambda_i^3$, $(3\sigma C_{D_0}/16)\lambda_i\lambda_h^2$, and $F\lambda_h^3$. The value of F was taken as 0.00027 for these rotor tests. The values of $\bar{C}_L$ were calculated from Eq. (12); λ_i, from Eq. (13); and C_{D_0} at $C_L = \bar{C}_L$, from the airfoil data of reference 2.

It can be seen that a value of $\lambda_i = 1.3\ (\lambda_i)_{\text{theoretical}}$ fits the experimental data for hovering flight quite well and gives better agreement with the test data over the whole range of the tests. It is unfortunate that the vertical flight tests were not carried to high enough blade angles to give representative values of $\bar{C}_L$ at the higher values of λ_v.

A value of $\lambda_i = 1.3(\lambda_i)_{\text{theoretical}}$ will be used in the following equations.

Power Required in Hovering Flight

From Eq. (6) for $Z = \lambda_i$ and $\lambda_h = 0$

$$\lambda_i = [1/(1 - kF)]^{1/3}$$

From Eq. (10)

$$\lambda_p = \lambda_i + (\sigma C_{D_0}/16)\,\lambda_i^3 + kF\lambda_i^3$$

Inserting the experimental correction factor, 1.3,

$$\lambda_p = 1.3[1/(1 - kF)]^{1/3} + \frac{\sigma C_{D_0}}{16}\lambda_i^3 + 2.20kF\,[1/(1 - kF)]^{3/3} \quad (14)$$

and $\text{b.hp.}_{\text{reg.}} = \lambda_p\, WV_0/550K$.

Maximum Rate of Vertical Climb

Neglecting, for the moment, the vertical drag forces

$$\lambda V_{v_{max.}} = \lambda_{p_{max.}} - (\sigma C_{D_0}/16)\lambda_i^3 - \lambda_i \quad (15)$$

from Eq. (10) and $\lambda_i = 1/(\lambda_v + \lambda_i)$ from Eq. 6.

Inserting the experimental correction factor 1.3,

$$\lambda V_{v_{max.}} = \lambda_{p_{max.}} - \frac{1.3}{\lambda_v + \lambda_i} - \left(\frac{\sigma C_{D_0}}{16}\right)\lambda_i^3$$

However, from Eq. (15),

$$\lambda_v + \lambda_i = \lambda_{p_{max.}} - (\sigma C_{D_0}/16)\lambda_i^3$$

or

$$\lambda V_{v_{max.}} = \lambda_{p_{max.}} - \left(\frac{\sigma C_{D_0}}{16}\right)\lambda_i^3 - \frac{1.3}{\lambda_p - (\sigma C_{D_0}/16)\lambda_i^3}$$

to a first approximation.

The primary effect of the vertical drag force is the additional power required to overcome it. Taking this into account to the extent of using the first approximation of the value of the vertical velocity at the fuselage but neglecting the secondary effect of the increased thrust required,

$$\lambda V_{v_{max.}} = \left(\lambda_{p_{max.}} - \frac{\sigma C_{D_0}}{16}\lambda_i^3\right) - \left[\frac{1.3}{\lambda_{p_{max.}} - (\sigma C_{D_0}/16)\lambda_i^3}\right] - kF[\lambda_{p_{max.}} - (\sigma C_{D_0}/16)\lambda_i^3] \quad (16)$$

The maximum vertical rate of climb in ft. per min. is then $60\,\lambda V_{v_{max.}} V_0$.

Horizontal Velocity for Maximum Rate of Climb and Maximum Endurance

The maximum rate of climb will occur very near that horizontal component of the velocity along the flight path at which the minimum power would be required in horizontal flight. If the effects of the vertical drag were ignored, the two velocities would be equal when calculated by this method.

Setting λ_v in Eq. (10) equal to zero, solving for λ_p, and dropping the terms that are negligible when $\lambda_h > 2$ gives

$$\lambda_p = \lambda_i + \left(\frac{\sigma C_{D_0}}{16}\right)\lambda_i^3 + \left(\frac{3\sigma C_{D_0}}{16}\right)\lambda_i\lambda_h^2 + F\lambda_h^3 + kF\lambda_i\lambda_h^2 \quad (17)$$

For $\lambda_h > 2$, which will be true for the present condition and all subsequent horizontal flight conditions dealt with, it is a good approximation that $\lambda_i = 1/\lambda_h$.

Incorporating the experimental correction factor gives $\lambda_i = 1.3/\lambda_h$ or for level flight

$$\lambda_p = \frac{1.3}{\lambda_h} + \left(\frac{\sigma C_{D_0}}{16}\right)\lambda_i^3 + \left(\frac{3\sigma C_{D_0}}{16}\right)\lambda_i\lambda_h^2 + F\lambda_h^3 + 1.3kF\lambda_h \quad (18)$$

Let λ_{h_c} be the value of λ_h for minimum power required in level flight. Then minimizing the power required gives:

$$\frac{\partial\lambda_p}{\partial\lambda_h} = \frac{-1.3}{\lambda_{h_c}^2} + \frac{3}{8}\sigma C_{D_0}\lambda_i\lambda_{h_c} + 3F\lambda_{h_c}^2 + 1.3kF = 0$$

or

$$24F\lambda_{h_c}^4 + 3\sigma C_{D_0}\lambda_i\lambda_{h_c}^3 + 10.4kF\lambda_{h_c}^2 - 10.4 = 0 \quad (19)$$

Substituting the value of λ_{h_c} given by the solution of Eq. (19) in Eq. (18) will give the value of λ_p and, thus, the engine brake horsepower, b.hp. $= \lambda_p WV_0/550K$ for minimum power required in level flight, the fuel consumption, and the endurance.

The horizontal component of the velocity along the flight path for maximum rate of climb and the velocity in level flight for minimum power required in level flight in miles per hour is equal to $\lambda_{h_c}V_0/1.47$.

Maximum Rate of Climb

By a similar derivation and based on the same approximations as used to obtain Eq. (16)

$$\lambda_{v_{max.}} = Y - \frac{1.3(1 + kFY^2)}{(Y^2 + \lambda_{h_c}^2)^{1/2}} - kFY^2 - FY^2\lambda_{h_c} - kFY\lambda_{h_c}^2 \quad (20)$$

where

$$Y = \lambda_{p_{max.}} - \left(\frac{\sigma C_{D_0}}{16}\right)\lambda_i^3 - \left(\frac{3\sigma C_{D_0}}{16}\right)\lambda_i\lambda_{h_c}^2 - F\lambda_{h_c}^3 \quad (21)$$

The maximum rate of climb along an inclined flight path in ft. per min. is then equal to $60\lambda_{v_{max.}}V_0$.

Absolute Ceiling

The theoretical approach to the problem of calculating the absolute ceiling of a helicopter will necessarily depend to a large extent on the type of rotor drive employed. However, for an "ideal" drive where λ_i (i.e., $\bar{C}_L$) can be held at a constant value independent of the altitude, the following method can be used, and it should also be a fair approximation for the usual mechanical drive.

At the absolute ceiling $\lambda_{v_{max.}} = 0$ and $\lambda_p = \lambda_p$ for minimum power required in level flight, which can be calculated from Eq. (18) using $\lambda_h = \lambda_{h_c}$.

However, $\lambda_p = 550K$ b.hp./WV_0 and $V_0 = (W/2\rho A)^{1/2}$ or

$$\frac{(\lambda_p)_{\text{ceiling}}}{(\lambda_p)_{\text{sea level}}} = \frac{\text{b.hp.}_{\text{ceiling}}}{\text{b.hp.}_{\text{sea level}}}\left(\frac{\rho}{\rho_0}\right)^{1/2}$$

where ρ_0 = sea level air density and $(\lambda_p)_{\text{sea level}}$ = maximum value at sea level.

The ratio, $(\text{b.hp.}_{\text{ceiling}}/\text{b.hp.}_{\text{sea level}})(\rho/\rho_0)^{1/2}$ can be plotted as a general curve for unsupercharged motors at constant r.p.m. (see Fig. 12) or can be calculated from the engine altitude curves for any particular supercharged motor.

Having found the ratio of $(\lambda_p)_{\text{ceiling}}/(\lambda_p)_{\text{sea level}}$ and thus its equivalent $(\text{b.hp.}_{\text{ceiling}}/\text{b.hp.}_{\text{sea level}}) \times (\rho/\rho_0)^{1/2}$, the absolute ceiling can be read from the aforementioned curve.

Top Speed in Level Flight

From Eq. (18), setting $\lambda_h = \lambda_{h_m}$

$$16F\lambda_{h_m}^4 + 3\sigma C_{D_0}\lambda_i\lambda_{h_m}^3 + 20.8kF\lambda_{h_m}^2 + (\sigma C_{D_0}\lambda_i^3 - 16\lambda_p)\lambda_{h_m} + 20.8 = 0 \quad (22)$$

which can be solved for λ_{h_m} and thus the top speed in level flight in miles per hour which is equal to $\lambda_{h_m}V_0 \div 1.47$.

Horizontal Velocity for Maximum Range

The maximum range will occur at that horizontal velocity and thus at that value of λ_h at which the greatest distance is made for the fuel consumed. Assuming still air conditions and flight at constant weight and specific fuel consumption, the distance flown in a given time is proportional to λ_h and the fuel consumed is proportional to λ_p. Maximum range will thus occur at that value of λ_h at which the ratio, λ_p/λ_h, is a minimum.

From Eq. (18) for horizontal flight

$$\lambda_p/\lambda_h = \frac{1.3}{\lambda_h^2} + \left(\frac{\sigma C_{D_0}}{16}\right)\left(\frac{\lambda_i^3}{\lambda_h}\right) + \left(\frac{3\sigma C_{D_0}}{16}\right)\lambda_i\lambda_h + F\lambda_h^2 + 1.3kF$$

Minimizing the above ratio with respect to λ_h and letting λ_h for maximum range equal λ_{h_R} gives:

$$\frac{\partial(\lambda_p/\lambda_h)}{\partial\lambda_h} = -\frac{2.6}{\lambda_{h_R}^2} - \left(\frac{\sigma C_{D_0}}{16}\right)\left(\frac{\lambda_i^3}{\lambda_{h_R}^2}\right) + \left(\frac{3\sigma C_{D_0}}{16}\right)\lambda_i + 2F\lambda_{h_R} = 0$$

or

$$32F\lambda_{h_R}^4 + 3\sigma C_{D_0}\lambda_i\lambda_{h_R}^3 - \sigma C_{D_0}\lambda_i^3\lambda_{h_R} - 41.6 = 0 \quad (23)$$

Eq. 23 can be solved for λ_{h_R} and thus the horizontal velocity for maximum range in miles per hour which is equal to $\lambda_{h_R}V_0/1.47$.

The value of λ_p corresponding to λ_{h_R} can be obtained from Eq. (18) and thus the horsepower required, fuel consumption, and range.

Instructions for Use of Nomograms

(Note: An estimated mean value of $k = 7$ has been used for these charts.)

Given values of the solidity, σ; the disc area, A; the gross weight, W; the parasite drag area measured along the longitudinal axis, f; the rated horse power, b.hp.; the rotor drive efficiency, K; and the altitude; then:

A. If the tip speed, V_t, is known:

(1) Obtain V_0 from Fig. 5.
(2) Calculate $\lambda_t = V_t/V_0$.
(3) Obtain $\sigma\bar{C}_L$ from Fig. 6 and calculate $\bar{C}_L$.
(4) Take C_{D_0} from blade airfoil infinite aspect ratio polar at $C_L = \bar{C}_L$ and calculate σC_{D_0}.

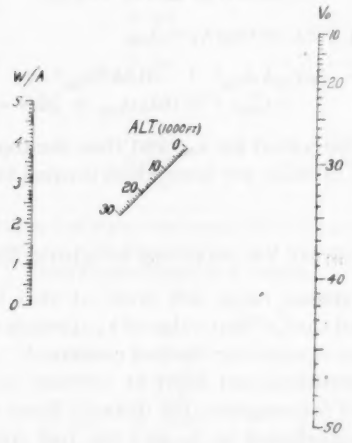

Fig. 5. Nomogram for obtaining the value of V_0.

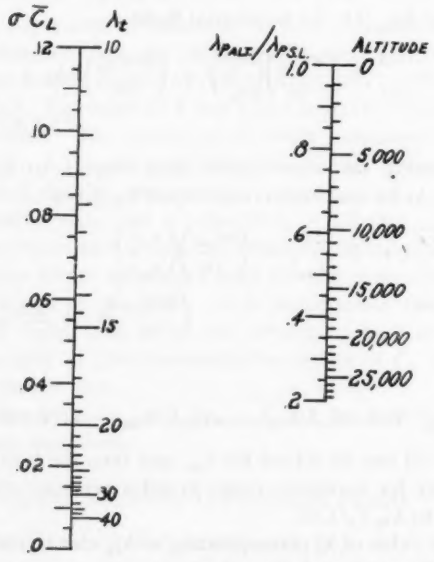

Fig. 6. Nomograms for obtaining the value of λ_t and the absolute ceiling.

B. If the desired mean lift coefficient in hovering flight, $\bar{C}_L$, is known:

(1) Calculate $\sigma\bar{C}_L$ and obtain λ_t from Fig. 6.
(2) Step four under **A**.
(3) Obtain V_0 from Fig. 5. Then $V_t = \lambda_t V_0$.

C. Calculate $\lambda_p = 550K$ b.hp./WV_0 and $F = f/4A$

D. Obtain the values of $A' = 3\sigma C_{D_0}\lambda_t$, $B' = \sigma C_{D_0}\lambda_t^3$, and $C' = \sigma C_{D_0}\lambda_t^3 - 16\lambda_p$ from Fig. 7.

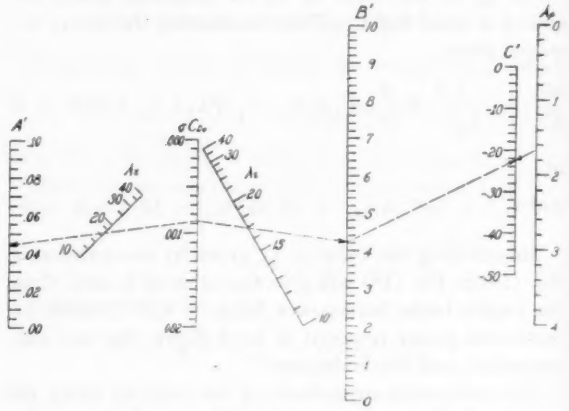

Fig. 7. Nomogram for obtaining the values of $A' = 3\sigma C_{D_0}\lambda_t$, $B' = \sigma C_{D_0}\lambda_t^3$, and $C' = \sigma C_{D_0}\lambda_t^3 - 16\lambda_p$.

E. Horsepower Required in Hovering Flight

(1) Obtain the value of the power parameter, λ_p, from Fig. 8. Then the horsepower required in hovering flight is equal to $\lambda_p WV_0/550K$.

F. Rate of Vertical Climb

(1) Obtain the value of λ_{V_v} from Fig. 9. Then the rate of vertical climb in ft. per min. is equal to $60\lambda_{V_v}V_0$.

G. Minimum Power Required in Level Flight

(1) Obtain λ_{h_c} from Fig. 10. Then the horizontal speed for maximum endurance and the hori-

Fig. 8. Nomogram for obtaining the value of the power parameter, λ_p, in hovering flight.

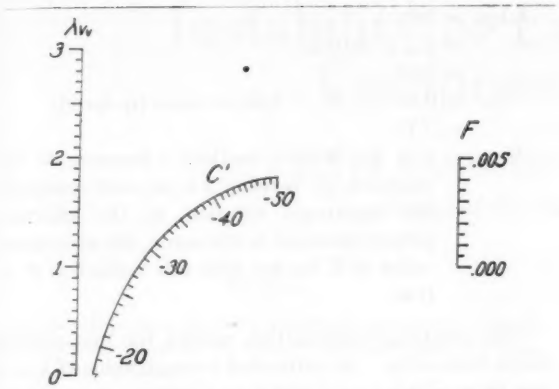

FIG. 9. Nomogram for obtaining the value of the vertical velocity parameter, λ_{V_v}, for vertical climb.

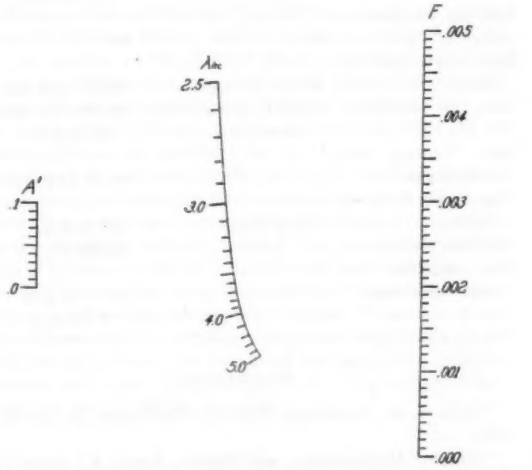

FIG. 10. Nomogram for obtaining the value of the horizontal velocity parameter, λ_{h_c}, for minimum power required in level flight.

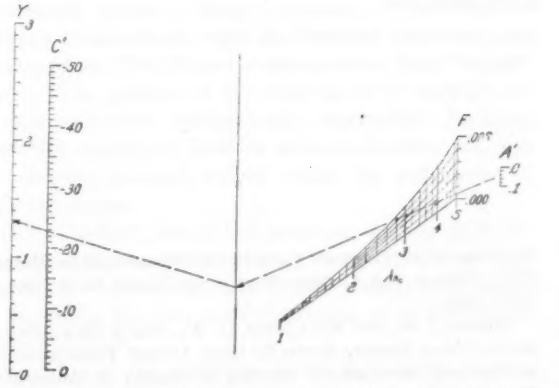

FIG. 11. Nomogram giving the value of Y used to obtain the maximum rate of climb.

zontal component of the velocity along the flight path for maximum rate of climb is $\lambda_{h_c} V_0/1.47$ m.p.h. The value of the power parameter, λ_p, for minimum power required or maximum endurance can be calculated from Eq. (18), using $\lambda_h = \lambda_{h_c}$. Thus the horsepower required, which is equal to $\lambda_p W V_0/550K$, and the fuel consumption and endurance can be calculated.

H. Absolute Ceiling

(1) Calculate the ratio of the value of λ_p for minimum power required obtained in step **G** to the maximum value of λ_p at sea level, which will usually have been calculated in step **C**. Then using this ratio, which is equal to $\lambda_{p_{\text{altitude}}}/\lambda_{p_{\text{sea level}}}$, read the absolute ceiling from Fig. 6.

I. Maximum Rate of Climb

(1) Obtain the value of Y from Fig. 11.

(2) Obtain the value of λ_v from Fig. 12. Then the maximum rate of climb in ft. per min. is $60\lambda_v V_0$.

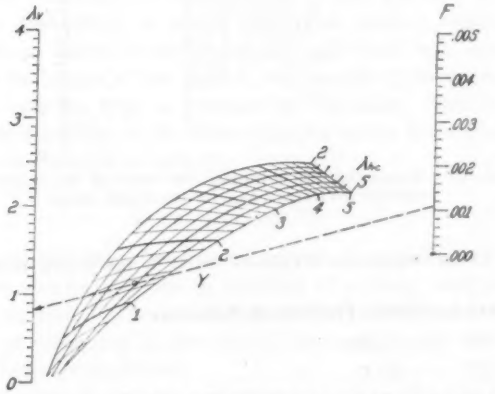

FIG. 12. Nomogram for obtaining the value of the vertical velocity parameter, λ_v, for maximum rate of climb.

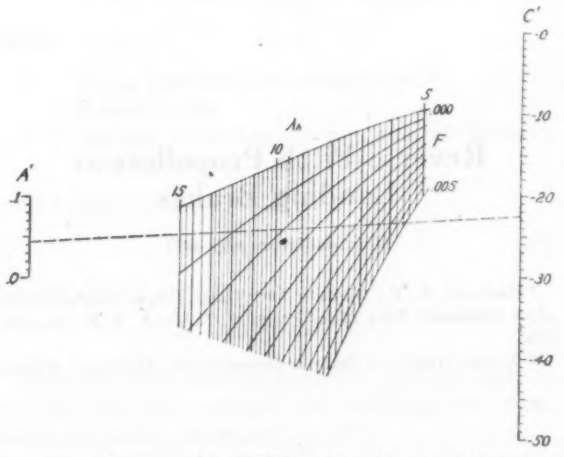

FIG. 13. Nomogram for obtaining the value of the horizontal velocity parameter, λ_h, for top speed in level flight.

J. Top Speed in Level Flight

(1) Obtain the value of λ_h from Fig. 13. Then the top speed in level flight in m.p.h. is $\lambda_h V_0/1.47$.

K. Maximum Range

(1) Obtain the value of λ_{h_R} from Fig. 14. Then the horizontal velocity in m.p.h. for maximum range is $\lambda_{h_R} V_0/1.47$.

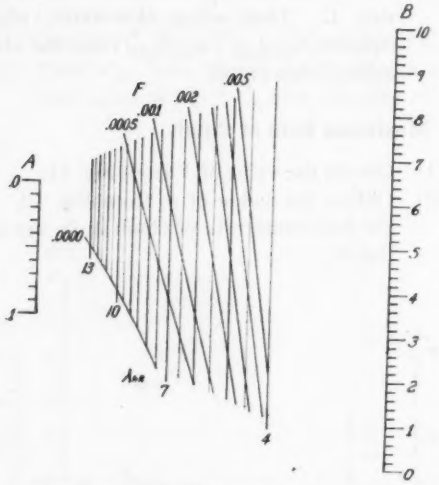

FIG. 14. Nomogram for obtaining the value of the horizontal velocity parameter, λ_{h_R}, for maximum range.

COMPARISON OF RESULTS WITH WALD'S METHOD[3]

Data for Wald's Problem in Reference 3

W = 1,500
D = 33.6
b.hp. = 100
δ = C_{D_0} = 0.0125
σ = 0.07
C_T/σ = 0.20 (i.e., $\bar{C}_L$ = 0.60 for same tip speed)
f = 3.75
K = 0.81 for Wald's method. Because of the inclusion by Wald of a 5 per cent reduction for slipstream rotation in the effective power delivered to the rotor, the equivalent value of K for use with this method is K = 0.86

The additional information needed for this method is the value of k. An estimated average value of $k = 7$ has been used.

Item	Wald's Results	Results by This Method
B.hp.$_{req.}$ for hovering	84	95
Max. vert. rate of climb	530 ft. per min.	526 ft. per min.
Max. rate of climb	1,050 ft. per min. at 48 m.p.h.	940 ft. per min. at 51 m.p.h.
Min. b.hp.$_{req.}$ in level flight	.....	43 at 51 m.p.h.
Top speed in level flight	125 m.p.h.	123 m.p.h.
Absolute ceiling	.....	15,800 ft.
Hor. velocity for maximum range	.....	82 m.p.h. (50 b.hp.$_{req.}$)

REFERENCES

[1] Glauert, H., *Horizontal Flight of a Helicopter*, R. and M. No. 1157.

[2] Knight, Montgomery, and Hefner, Ralph A., *Static Thrust Analysis of the Lifting Airscrew*, T.N. 626.

[3] Wald, Quentin, *A Method of Rapid Estimation of Helicopter Performance*, Journal of the Aeronautical Sciences, Vol. 10, No. 4, p. 131, April, 1943.

Reverse-Pitch Propellers as Landing Brakes

(*Continued from page 447*)

[4] Hartman, E. P., *Negative Thrust and Torque Characteristics of an Adjustable Pitch Metal Propeller*, N.A.C.A. T. R. No. 464, 1933.

[5] Welling, Omer, *A Study to Determine the Maximum Weights Permitted by the Tranpsort Category Requirements for the Douglas DC-3 Airplane*, C.A.A. Flight Engineering Report No. 9, November 1, 1943.

[6] Sheets, J. H., and MacKinney, G. W., *Reverse Thrust Propellers for Use as Landing Brakes for Large Aircraft*, Paper presented at National Aeronautical Meeting of Society of Automotive Engineers, Los Angeles, Calif., October 5–7, 1944.

[7] Wetmore, J. W., *The Rolling Friction of Several Airplane Wheels and Tires and the Effect of Rolling Friction on Take-Off*, N.A.C.A. T.R. No. 583, 1937

Instability of Extrusions Under Compressive Loads

WALTER RAMBERG* AND SAMUEL LEVY*

National Bureau of Standards

ABSTRACT

Critical compressive stresses were computed and were compared with measured values for 26 different aluminum-alloy and magnesium-alloy extrusions.

Critical stresses for local instability were computed, considering the flanges as plates of uniform thickness rigidly clamped along one edge. Critical stresses for primary instability were computed from Kappus' theory of torsional instability, taking account of the stiffening effect of fillets and the effect on the torsion bending constant of bending stresses varying across the thickness of the wall. An estimate of the effect of plastic yielding was made by reducing the critical stresses in the ratio of reduced modulus, for a column of rectangular section, to Young's modulus.

The measured and computed critical stresses for 120 of the 125 specimens differed less than 5,000 lbs. per sq.in.

Comparison of strength-weight ratios for buckling and for failure showed that in general the Z-sections were most efficient.

A procedure is outlined for calculating buckling stresses of unsupported extrusions of one material from measured buckling stresses of similar extrusions of a different material. The procedure was checked by comparing calculated buckling stresses with measured buckling stresses for extruded T-sections, L-sections, and Z-sections of several aluminum and magnesium alloys. The differences between the measured and calculated buckling stresses did not exceed 10,000 lbs. per sq.in. The average difference was less than 5,000 lbs. per sq.in.

PURPOSE

THIS PAPER DESCRIBES a portion of a research program on the compressive strength of open section extrusions which is being conducted at the National Bureau of Standards, with the financial assistance and cooperation of the Bureau of Aeronautics, Navy Department. The purpose of the program is to compare experimentally and theoretically determined buckling loads for extrusions used in aircraft construction and to compare strength-weight ratios for extrusions of different shapes.

Only the first part of the program, dealing with the strength of extrusions without support along their length, has been completed. Tests remain to be made to determine the compressive strength of extrusions attached to sheet.

A review of the literature on the instability of open section extrusions showed that the theory had been worked out in its essentials but that numerical solutions were confined to sections without the fillets and bulbs that are characteristic of extrusions. The theory will be outlined in some detail in order to make clear the computation of buckling loads for extrusions that are stiffened by fillets and bulbs and the wall thickness of which is not necessarily small compared to the width of flanges.

Received January 25, 1945. To have been presented at the I.A.S. Thirteenth Annual Meeting, which was canceled to cooperate with a Government appeal (January, 1945) to refrain from holding conventions and meetings.

* Physicists.

ELASTIC BUCKLING LOADS

An open section extrusion may buckle in the elastic range by local instability in which a portion of the section buckles like a plate while the remainder of the section continues to carry load, or it may fail by a primary instability in which the whole section rotates about an axis of twist the location of which will vary with the shape of the section, the length of the extrusion, and the type of restraint at the ends. This includes buckling of the Euler type for which the axis of twist is removed to infinity.

LOCAL INSTABILITY

Local instability for the extrusions described in this report was usually due to buckling of a flange with or without bulb. The critical stress for local instability may be estimated as the critical stress for a plate with suitable edge conditions.

The critical compressive stress for a plate of width b, thickness t, and length L is from reference 1, p. 605:

$$\sigma_{cr} = (k\pi^2/12)[E/(1 - \nu^2)](t/b)^2 \qquad (1)$$

where

E = Young's modulus, for compression
ν = Poisson's ratio
k = constant depending on condition of restraint and on ratio L/b

With Poisson's ratio

$$\nu = 0.3 \qquad (2)$$

Eq. (1) gives

$$\sigma_{cr} = 0.904Ek(t/b)^2 \qquad (3)$$

For a plate with one edge, parallel to the load, built-in and the other free, and with the remaining two edges simply supported (reference 1, p. 607)

$$k = 1.33, \; L/b > 3 \qquad (3a)$$

For a plate with both edges, parallel to the load, built-in and the remaining two edges simply supported (reference 1, p. 607)

$$k = 7.0, L/b > 2 \qquad (3b)$$

The first value of k was substituted in Eq. (3) to estimate the critical stress for local instability of a free flange without bulb, and the second value was substituted for local instability of a web. The width b was measured from the intersections of the median lines of the rectangular parts of the section. The resulting values of critical stress were generally higher than the values corresponding to the actual condition of edge restraint which was somewhere between the assumed conditions of rigid clamping and the condition of simple support.

No general value of k can be given for the local buckling of a flange with bulb. Rough estimates of critical load were computed in this report by taking $k = 1.33$, as for a flange without bulb, and taking the value of t in Eq. (3) as equal to the average thickness of the flange including the bulb.

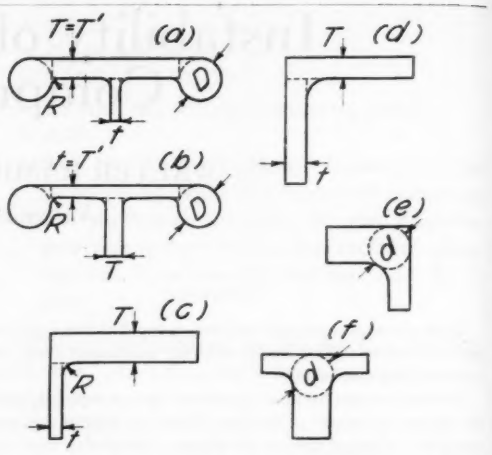

FIG. 1. Division of cross section into components for computing J_t according to reference 5: (a) bulb tee with flange thicker than leg, (b) bulb tee with leg thicker than flange, (c) angle with unequal legs, (d) angle with equal legs, (e) largest inscribed circle at angle junction, (f) largest inscribed circle at tee junction. Elementary sections shown dotted in (a) to (d) and inscribed circle shown dotted in (e) and (f).

PRIMARY INSTABILITY

The primary instability of thin-walled open section columns subjected to end compression has been discussed by Wagner,[2] Kappus,[3] and Lundquist and Fligg.[4] They show that the critical stress for primary instability is given by solving the differential equation

$$E\bar{C}\left(\frac{d^4\varphi}{dz^4}\right) + (\sigma_{cr}\bar{J}_p - GJ_T)\frac{d^2\varphi}{dz^2} = 0 \qquad (4)$$

where

z = axial coordinate
φ = angular rotation of section with axial coordinate z
$G = E/[2(1+\nu)]$
J_T = Saint-Venant torsion constant
$\bar{C}$ = torsion bending constant relative to axis of twist
$\bar{J}_p$ = polar moment of inertia of section about axis of twist

The Saint-Venant torsion constant J_T for a thin-walled specimen in which the section can be considered built up of n portions of constant wall thickness t_i and developed width b_i is given by (reference 1, p. 78):

$$J_T = {}^1/_3\sum_{i=1}^{n} b_i t_i^3 \qquad (5)$$

Eq. (5) is in error by less than 3 per cent so long as b_i/t_i is greater than 20. When this condition is not fulfilled, the torsion constant J_T may be computed by the following procedure.[5]

(1) Divide the section into component elementary sections (see Figs. 1a–1d) such as rectangles for legs, webs, and flanges and circles for bulbs. At the T-joint between a flange and a web, consider the flange to be continuous and the web to start from the side of the flange (reference 5, p. 29). At the L-joint between two legs, consider the thicker leg to be continuous to the edge of the section and the thinner leg to start from the edge of the thicker leg (reference 5, p. 30). At the joint between a leg or flange and a bulb, consider the web or flange to start from the bulb (this case is not given in reference 5, but the treatment suggested is similar to that given for the previous two cases).

(2) Compute the contribution to J_T of the elementary sections from the formulas $({}^1/_3)bt^3$ for the rectangular sections and $\pi D^4/32$ for the circular sections of diameter D (reference 5, p. 15). For tapered sections where the thickness varies gradually, compute the contributions to J_T from the formula $({}^1/_3)\int_0^b t^3\,dx$.

(3) Compute the correction to the torsion constant at the free ends of the elementary rectangular sections from the formula (reference 5, p. 16)

$$\Delta J_T = -0.105t^4 \qquad (5a)$$

This correction brings the value of J_T within 2 per cent of the exact value for $b > 1.5t$. Compute the correction to the torsion constant at the junctions between component elementary rectangular sections from the formulas (reference 5, Fig. 11)

$$\Delta J_T = d^4[0.071 + (0.077R/T)](t/T) \qquad (5b)$$

for L-sections, and

$$\Delta J_T = d^4[0.148 + (0.102R/T')](t/T) \qquad (5c)$$

for T-sections, where (see Figs. 1e and 1f)

R = radius of fillet
d = diameter of largest inscribed circle at junction

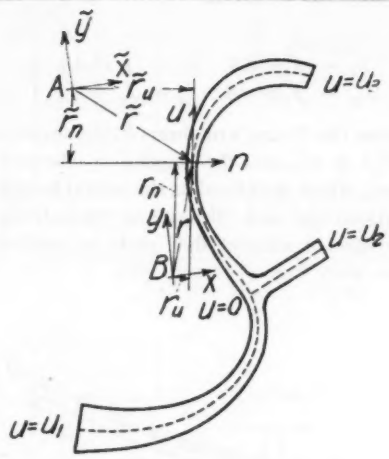

FIG. 2. Thin-walled open section showing meaning of symbols. *A*, center of twist; *B*, center of gravity.

T' = thickness of flange for T-sections
T = thickness of wide component rectangle
t = thickness of narrow component rectangle

Compute the correction to the torsion constant at the junction between a component elementary rectangle of thickness t and a component elementary circle from

$$\Delta J_T = 0.1t^4 \tag{5d}$$

This case is not given in reference 5, but the correction is similar in form to that given in Eqs. (5b) and (5c) and should be a good approximation when the diameter of the elementary circle is greater than $2t$.

The torsion-bending constant $\tilde{C}$ in Eq. (4) may be resolved into two components according to Wagner[2]

$$\tilde{C} = \tilde{C}_u + \tilde{C}_n$$

where

$\tilde{C}_u$ = torsion-bending constant for bending about axis normal to wall of section
$\tilde{C}_n$ = torsion-bending constant for bending about axis tangent to median line of section (shown dotted in Fig. 2)

The torsion-bending constants may be computed from

$$\left.\begin{aligned} \tilde{C}_u &= \int_A \tilde{w}_u^2\, dA \\ \tilde{C}_n &= \int_A \tilde{w}_n^2\, dA \end{aligned}\right\} \tag{7}$$

where

$\tilde{w}_u$ = axial displacement at point u for a twist of 1 rad. per unit length about longitudinal axis through center of twist (see Eq. (8) below)
u = coordinate along median line of section (the positive direction of u is arbitrary)
$\tilde{w}_n$ = axial displacement relative to median line of a point at a distance n from median line for a twist of 1 rad. per unit length about longitudinal axis through center of twist (see Eq. (8) below)
n = coordinate perpendicular to median line of section, zero at the median line, and positive toward the right as observed when looking in the positive u direction (see Fig. 2)

The total axial displacement at any given point (u, n) for a twist of 1 rad. per unit length about longitudinal axis through center of twist is

$$\left.\begin{aligned} \tilde{w} &= \tilde{w}_u + \tilde{w}_n \\ \tilde{w}_u &= \tilde{w}_0 + \int_0^u \tilde{r}_u\, du \\ \tilde{w}_n &= \int_0^n \tilde{r}_n\, dn = \tilde{r}_n n \end{aligned}\right\} \tag{8}$$

where

$\tilde{w}_0$ = arbitrarily chosen axial displacement for arbitrarily chosen reference point $u = 0$ (Fig. 2). The arbitrary value of $\tilde{w}_0$ is usually taken as zero for convenience
$\tilde{r}_u$ = distance from center of twist to tangent through point (u, n) (Fig. 2). A line drawn from the center of twist, A, in the positive n direction indicates the positive $\tilde{r}_u$ direction
$\tilde{r}_n$ = distance from center of twist to normal through point (u, n) (Fig. 2). A line drawn from the center of twist, A, in the negative u direction indicates the positive $\tilde{r}_n$ direction

The solution of Eq. (4) for the critical stress σ_{cr} depends on the end conditions for the twist φ and on the location of the center of twist. Let us consider the case in which the ends are free to warp but are not allowed to rotate about the axis of twist. If the ends are free to warp, the axial stresses at the ends caused by twisting must be equal to zero. These axial stresses are given by (reference 3, Eq. 17′):

$$\sigma = -E(d^2\varphi/dz^2)\tilde{w} \tag{9}$$

The axial stresses $\tilde{\sigma}$ will be zero for all points of the end sections if

$$d^2\varphi/dz^2 = 0,\ z = 0,\ l \tag{9a}$$

These end conditions together with the condition of zero rotation at the ends

$$\varphi = 0,\ z = 0,\ l \tag{9b}$$

are satisfied by

$$\varphi = a \sin(\pi z/l) \tag{10}$$

Substituting in Eq. (4) and solving for the critical stress gives

$$\sigma_{cr} = [GJ_T + \pi^2(E\tilde{C}/l^2)]/\tilde{J}_p \tag{11}$$

If the ends are rigidly clamped, the end conditions are:

$$\varphi = 0,\ d\varphi/dz = 0 \quad z = 0 \quad L$$

These are satisfied by

$$\varphi = a[1 - \cos(2\pi z/L)] \tag{12}$$

Substituting in Eq. (4) and solving for the critical stress gives

$$\sigma_{cr} = [GJ_T + 4\pi^2(E\bar{C}/L^2)]/J_p \tag{13}$$

It is seen that the critical stress for a specimen with fixed ends is equal to that for a specimen with ends free to warp having one-half the length.

Eqs. (11) and (13) give the critical stress for a known axis of twist. If the axis of twist is not known, the critical stress may be determined from the condition that the specimen will rotate about that axis which gives the minimum critical stress.

Kappus[3] has developed a convenient procedure for determining the minimum critical stress on the assumption that the specimen is thin-walled enough to neglect bending about the median line $n = 0$, Fig. 2. With this assumption

$$\bar{C}_n << \bar{C}_u$$

The following procedure is identical with that developed by Kappus, except for retaining the terms that take account of the bending about the median line.

Determine the center of gravity of the section and pass a right-handed rectangular coordinate system x, y through the center of gravity (Fig. 2). Let

$$\left.\begin{aligned} w_u &= \int_0^u r_u\,du \\ w_n &= r_n n \end{aligned}\right\} \tag{14}$$

r_u, $r_n = \bar{r}_u$, $\bar{r}_n$ (Fig. 2) if the center of gravity and the center of twist coincide.

Compute the warping moments:

$$\left.\begin{aligned} R_{xu} &= \int_0^{u_1} y w_u t\,du + \int_0^{u_2} y w_u t\,du + \ldots \\ R_{yu} &= \int_0^{u_1} x w_u t\,du + \int_0^{u_2} x w_u t\,du + \ldots \end{aligned}\right\} \tag{15}$$

$$\left.\begin{aligned} R_{xn} &= (1/12)\int_0^{u_1} t^3 r_n \cos\beta\,du + (1/12)\int_0^{u_2} t^3 r_n \cos\beta\,du + \ldots \\ R_{yn} &= (1/12)\int_0^{u_1} t^3 r_n \cos\alpha\,du + (1/12)\int_0^{u_2} t^3 r_n \cos\alpha\,du + \ldots \end{aligned}\right\} \tag{16}$$

where

α = angle between n and x
β = angle between n and y

and where the integration is carried out over the entire section.

Compute:

A = cross-sectional area of section.

Compute the torsion-bending constants relative to the center of gravity.

$$C_u = \int_0^{u_1} w_u^2 t\,du + \int^{u_2} w_u^2 t\,du + \ldots - (1/A)\left(\int_0^{u_1} w_u t\,du + \int_0^{u_2} w_u t\,du + \ldots\right)^2 \tag{17}$$

$$C_n = \int_0^{u_1}\int_{-t/2}^{t/2} w_n^2\,dn\,du + \int_0^{u_2}\int_{-t/2}^{t/2} w_n^2\,dn\,du + \ldots = (1/12)\left(\int_0^{u_1} r_n^2 t^3\,du + \int_0^{u_2} r_n^2 t^3\,du + \ldots\right) \tag{18}$$

and the moments of inertia relative to the center of gravity

$$\left.\begin{aligned} J_x &= \int_A y^2\,dA;\quad J_y = \int x^2\,dA \\ J_{xy} &= \int_A xy\,dA;\quad J_p = J_x + J_y \end{aligned}\right\} \tag{19}$$

Determine the Young's modulus E, the shear modulus $G = E/[2(1 + \nu)]$, and the length l = effective length of specimen, which is defined as the actual length for the end conditions (9a) and (9b) and as one-half the actual length for fixed or ideally "flat" ends, as pointed out in connection with Eqs. (11) and (13).

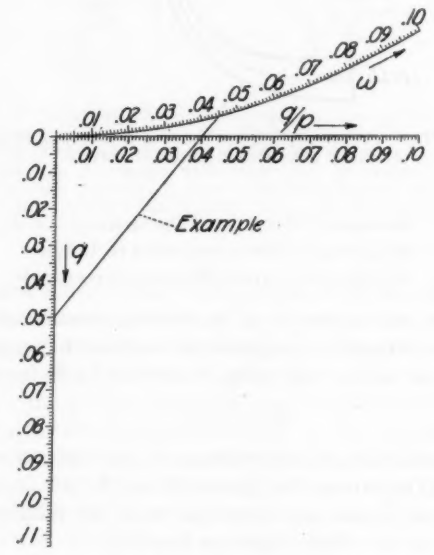

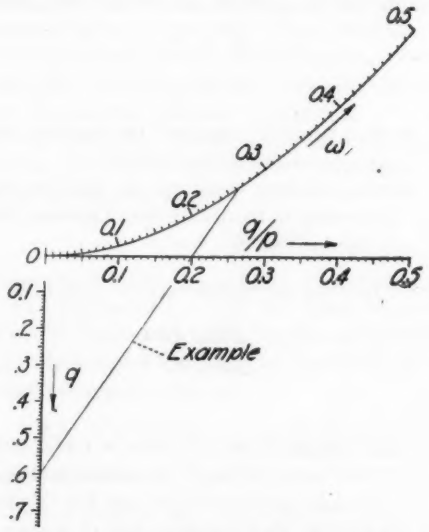

FIG. 3a (*top*). Solution of Eq. (23) when $0 < q < 0.11$ Example: given, $p = 1.25$, $q = 0.05$; then, $q/p = 0.04$ and $\omega = 0.045$.

FIG. 3b (*bottom*). Solution of Eq. (23) when $0.10 < q < 0.70$. Example: given, $p = 3$, $q = 0.6$; then, $q/p = 0.2$ and $\omega = 0.26$.

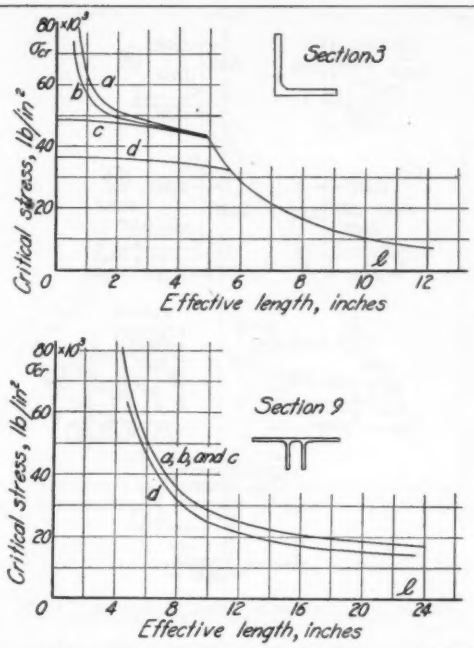

FIG. 4a (*top*). Effect on computed critical stress of neglecting C_n, R_n, and fillet for equal angle, section 3. Curve a, J_t from reference 5, $C_n \neq 0$, $R_n \neq 0$; curve *b*, J_t from reference 5, $C_n \neq 0$, $R_n = 0$; curve c, J_t from reference 5, $C_n = 0$, $R_n = 0$; curve d, J_t from Eq. (5), $C_n = 0$, $R_n = 0$.

FIG. 4b (*bottom*). Effect on computed critical stress of neglecting C_n, R_n, and fillet for pi-section 9. Curve a, J_t from reference 5, $C_n \neq 0$, $R_n \neq 0$; curve b, J_T from reference 5, $C_n \neq 0$, $R_n \neq 0$; curve c, J_t from reference 5, $C_n = 0$, $R_n = 0$; curve d, J_t from Eq. (5), $C_n = 0$, $R_n = 0$.

Compute the ratios

$$\left.\begin{aligned} \sigma_x &= \frac{\pi^2}{l^2}\frac{EJ_x}{A};\quad \sigma_y = \frac{\pi^2}{l^2}\frac{EJ_y}{A} \\ \sigma_s &= \frac{GJ_T + \pi^2 E(C_u + C_n)/l^2}{J_p} \\ \rho_x &= \frac{\pi^2}{l^2}\frac{ER_x}{\sqrt{AJ_p}};\quad \rho_y = \frac{\pi^2}{l^2}\frac{ER_y}{\sqrt{AJ_p}} \\ \rho_{xy} &= \frac{\pi^2}{l^2}\frac{EJ_{xy}}{A} \end{aligned}\right\} \tag{20}$$

From these ratios compute

$$\left.\begin{aligned} \sigma_m &= (\sigma_s + \sigma_x + \sigma_y)/3 \\ p &= \frac{\sigma_s\sigma_x + \sigma_s\sigma_y + \sigma_x\sigma_y - \rho_{xy}^2 - \rho_x^2 - \rho_y^2}{\sigma_m^2} \\ q &= \frac{\sigma_x\sigma_y\sigma_s + 2\rho_{xy}\rho_x\rho_y - \rho_{xy}^2\sigma_s - \rho_y^2\sigma_x - \rho_x^2\sigma_y}{\sigma_m^3} \end{aligned}\right\} \tag{21}$$

The critical stresses are then given by

$$\sigma_{cr} = \omega\sigma_m \tag{22}$$

where ω is a root of the cubic equation

$$\omega^3 - 3\omega^2 + p\omega - q = 0 \tag{23}$$

Figs. 3a and 3b give a nomogram for solving Eq. (23) for the lowest of the three values of ω with given values of p and q; Fig. 3a is used for $0 < q < 0.11$, while Fig. 3b is used for $0.10 < q < 0.70$.

In general there will be three solutions for ω and, hence, three values of critical stress. It is evident from Eq. (11) that each one of these solutions must correspond to a different axis of twist. In most cases the axis of twist for one solution is close to the center of shear of the section, while it is far out on the major and minor axes of inertia for the other two solutions. In the first case the buckling approaches twisting about the center of shear of the section, while in the other two it approaches Euler column failure about the major and minor axes of inertia, respectively.

SIMPLIFICATIONS

The general procedure outlined above can be simplified in many specific cases.

One timesaving simplification is that adopted by Kappus, who neglected the terms R_n of the warping moment and C_n of the torsion bending constant. These terms take account of bending about the median line of the section. The error introduced by this simplification was computed for the 0.5 by 0.5 by 0.045 in. L-section 3, Fig. 5a, and the 1.00 by 2.75 by 0.068 in. π-section 9, Fig. 5b. An L-section and a π-section were chosen for this purpose because twisting of these sections involves extreme cases of a maximum effect of R_n and C_n for the L-section and a relatively small effect of R_n and C_n for the π-section.

Curves a, Figs. 4a and 4b, show the critical stresses as a function of length, with C_n and R_n taken into account; curves b show the critical stresses with C_n taken into account but taking $R_n = 0$; and curves c show the critical stresses with both $C_n = 0$ and $R_n = 0$. C_n and R_n have a negligible effect for the π-section (Fig. 4b), but their effect is appreciable for the shorter lengths of the L-section (Fig. 4a). It was decided to take account of C_n and R_n for L- and T-sections, which behave similarly to L-section 3, but to neglect C_n and R_n for for π-, Z-, U-, and hat-sections, which behave similarly to π-section 9.

The second simplification frequently made is to compute J_T from Eq. (5) only, thereby neglecting the effect of fillets, bulbs, free ends, and junctions that are given in connection with Eqs. (5a) to (5d). The effect of this simplification was determined for the L- and π-sections also. Curves d in Figs. 4a and 4b show the critical stresses obtained by computing J_T from Eq. (5). Comparison of these curves with curves c, for which J_T was computed with Eqs. (5a) to (5d), shows that the more precise computation of J_T results in a substantial increase in critical stress for both the L- and π-sections. It was decided therefore to compute J_T with Eqs. (5a) to (5d) in all cases.

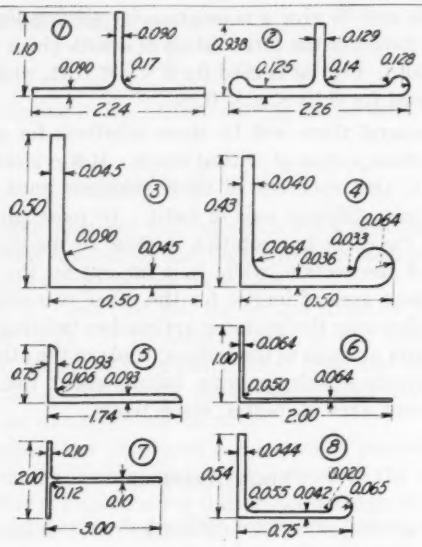

FIG. 5a. Dimensions in inches of sections 1 to 8.

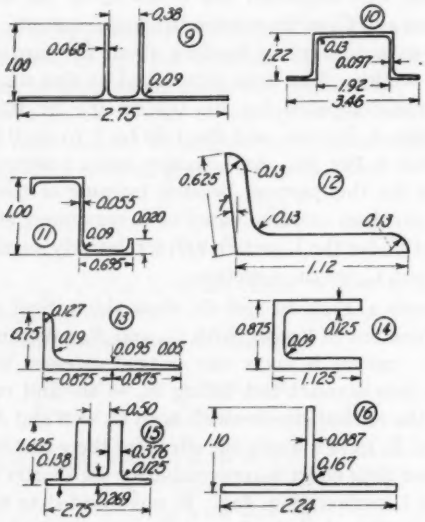

FIG. 5b. Dimensions in inches of sections 9 to 16.

A third simplification in the computation of the critical stresses is possible if the section has an axis of symmetry, as is the case for the equal-angle, T-, π-, hat-, and U-sections. Let us take the x-axis as this axis of symmetry. A displacement of the section parallel to the x-axis will then be free from twist, so that one of the critical stresses will correspond to pure Euler failure by bending about the y-axis

$$\sigma_{cr} = \sigma_y = (\pi^2/l^2)(EJ_y/A) \tag{24}$$

Kappus[3] has shown that the remaining two solutions of the cubic Eq. (23) may be determined directly from

$$\sigma_{cr} = \frac{\sigma_s + \sigma_x}{2} \pm \sqrt{\left(\frac{\sigma_s - \sigma_x}{2}\right)^2 + \rho_x^2} \tag{25}$$

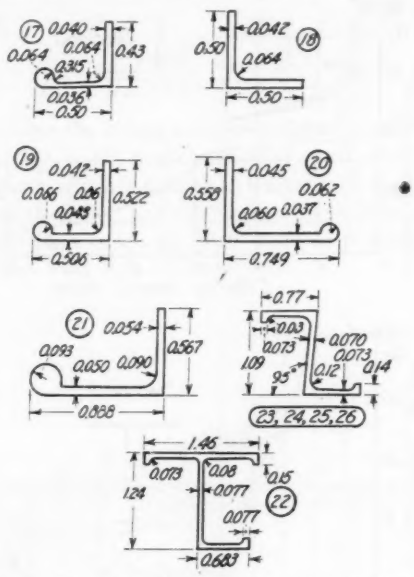

FIG. 5c. Dimensions in inches of sections 17 to 26.

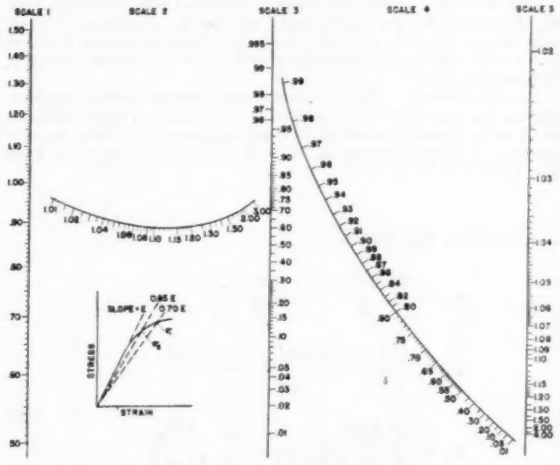

FIG. 6a. Nomogram to determine E_r/E and to take account of changes in properties of the material when σ_{cr} is near σ_1.

Taking the minus sign in front of the radical, corresponding to the lower critical stress, Eq. (25) may be rewritten as follows for convenience in computation:

$$\sigma_{cr} = \frac{\sigma_x\sigma_s - \rho_x^2}{\dfrac{\sigma_s + \sigma_x}{2} + \sqrt{\left(\dfrac{\sigma_s - \sigma_x}{2}\right)^2 + \rho_x^2}} \tag{25a}$$

A further simplification occurs if both x and y axes are axes of symmetry, as in a symmetrical I-section. In that case there is no coupling between torsion and column action. The three solutions are

$$\sigma_{cr} = \sigma_x, \sigma_y, \sigma_z \tag{26}$$

The first two are the Euler buckling stresses, while the

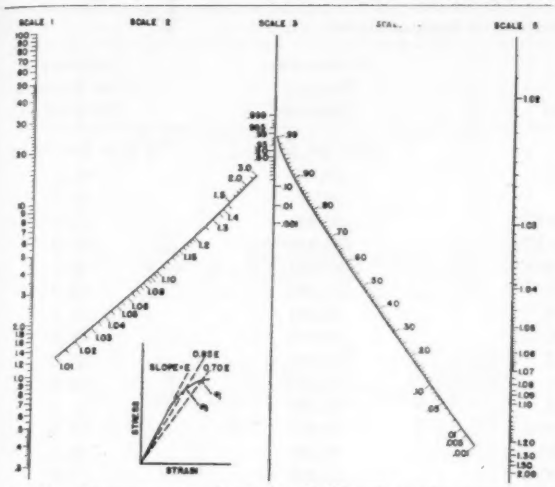

FIG. 6b. Nomogram to determine E_r/E and to take account of changes in properties of the material when σ_{cr} is not near σ_1.

third solution corresponds to twisting about the center of gravity.

The computation of the section constants R_{xu}, R_{yu}, and C_u can frequently be simplified by computing them first relative to a convenient set of axes $\bar{x}$, $\bar{y}$, related to the centroidal axes x, y by:

$$\bar{x} = \bar{x}_s + x; \quad \bar{y} = \bar{y}_s + y \tag{27}$$

where $\bar{x}_s$ and $\bar{y}_s$ are constants. The relations between the constants relative to the new axes

$$\left.\begin{aligned} \bar{R}_{\bar{x}u} &= \int_A \bar{y}\bar{w}_u\,dA; \quad \bar{R}_{\bar{y}u} = \int_A \bar{x}\bar{w}_u\,dA \\ \bar{C}_u &= \int_A \bar{w}_u^2\,dA - (1/A)\left(\int_A \bar{w}_u\,dA\right)^2 \end{aligned}\right\} \tag{28}$$

and R_{xu}, R_{yu}, and C_u are then, according to Kappus,[3]

$$\left.\begin{aligned} R_{xu} &= \bar{R}_{\bar{x}u} - \bar{x}_s J_x + \bar{y}_s\left(J_{xy} - \int_A \bar{w}_u\,dA\right) \\ R_{yu} &= \bar{R}_{\bar{y}u} + \bar{y}_s J_y - \bar{x}_s\left(J_{xy} + \int_A \bar{w}_u\,dA\right) \\ C_u &= \bar{C}_u + \bar{x}_s^2 J_x - 2\bar{x}_s\bar{y}_s J_{xy} + \bar{y}_s^2 J_y - \\ &\qquad 2\bar{x}_s\bar{R}_{\bar{x}u} + 2\bar{y}_s\bar{R}_{yu} \end{aligned}\right\} \tag{29}$$

PLASTIC BUCKLING

In the discussion so far it has been assumed that the stress-strain relation of the material is adequately represented by a straight line, the slope of which is Young's modulus. For higher stresses at which the tangent modulus differs appreciably from the initial modulus, the buckling stresses will be less than those given by Eqs. (1) and (13). The effect may be regarded as a decrease in the effective values of Young's modulus E and shear modulus G.

The amount of the decrease can be computed from the stress-strain curve and from the shape of the section for the case of pure column failure by replacing Young's modulus E by the reduced modulus E_r.[6]

There is no corresponding theory for the reduction in E and G in the presence of combined twisting and bending or of the type of local buckling considered in this paper. The amount of the reduction will probably depend in a complicated manner on the type of instability. The only simple statement that can be made safely with regard to it is that the reduction must be less than that for column action, since a smaller proportion of the material is highly stressed in this type of instability.

In view of the above it was decided to compute the critical stress in the plastic range by replacing E and G in Eqs. (1) and (13) by E_r and $E_r/[2(1+\nu)]$, respectively. For E_r the value for the rectangular section was chosen because it is readily calculated and because it is not an extreme value.[7] The reduced modulus for a column of rectangular section is

$$E_r = 4EE'/(\sqrt{E} + \sqrt{E'})^2 \tag{30}$$

where E = Young's modulus and E' = tangent modulus at stress σ_{cr} for which reduced modulus is desired.

With the above assumption the estimated value of critical stress at failure is given by

$$\sigma_{cr} = (E_r/E)(\sigma_{cr})_{el} \tag{31}$$

where $(\sigma_{cr})_{el}$ denotes the elastic buckling stress as computed from Eqs. (1) and (13) and where E_r is the reduced modulus corresponding to the stress σ_{cr}.

Eq. (31) was solved conveniently by a nomogram based on an expression with three parameters to describe the stress-strain curve. It is shown in reference 8 that a wide variety of stress-strain curves can be described by the simple expression

$$\epsilon = (\sigma/E) + K(\sigma/E)^n \tag{32}$$

where ϵ = strain, σ = stress, E = Young's modulus, and K, n = constants describing a given stress-strain curve.

It is also shown that in many cases K and n may be determined from the secant yield strengths σ_1 and σ_2 equal to the stresses at the intersections of the stress-strain curve and lines through the origin with slopes of $0.7E$ and $0.85E$, respectively. The quantities n, K, σ_1, and σ_2 are connected by the relations

$$n = 1 + [0.3853/\log_{10}(\sigma_1/\sigma_2)] \tag{33}$$

$$K = (3/7)(\sigma_1/E)^{1-n} \tag{34}$$

Taking the derivative of Eq. (32) and setting $1/E' = d\epsilon/d\sigma$,

$$\frac{1}{E'} = \frac{d\epsilon}{d\sigma} = \frac{1}{E} + \frac{nK}{E}\left(\frac{\sigma}{E}\right)^{n-1} \tag{35}$$

If we substitute Eq. (34) into Eq. (35) and multiply through by E,

$$1 + (3/7)n(\sigma/\sigma_1)^{n-1} = E/E' \tag{36}$$

Eq. (30) can be rewritten in the form

$$E/E' = [(2/\sqrt{E_r/E}) - 1]^2 \tag{37}$$

The value of E/E' in Eq. (36) can be equated to the value in Eq. (37). Doing this and rearranging terms,

TABLE 1. Material and Die Number of Sections Tested

Section	Material	Die No.	Compressive Young's Modulus, Kips per Sq.In.	Compressive Yield Strength (0.002 Offset), Kips per Sq.In.
1	24S-T Al alloy	Alcoa 12072-K	10,700	41.5
2	24S-T Al alloy	Alcoa 13477	10,700	42.5
3	24S-T Al alloy	Alcoa K-8848-KL	10,800	41.7
4	24S-T Al alloy	Alcoa K-8674-KL	10,600	41.2
5	24S-T Al alloy	Alcoa K-10498-K	10,600	43.1
6	24S-T Al alloy	Alcoa 13634-L	10,900	42.4
7	24S-T Al alloy	Alcoa 11485-K	10,800	40.4
8	24S-T Al alloy	Alcoa K-10282-KL	10,600	44.9
9	24S-T Al alloy	Alcoa 11461-K	10,900	45.0
10	24S-T Al alloy	Alcoa 12800-L	10,700	42.6
11	24S-T Al alloy	Alcoa 13686-K	10,800	41.4
12	24S-T Al alloy	Alcoa K-10438-K	10,800	45.6
13	24S-T Al alloy	Alcoa K-10480-KL	10,500	43.5
14	24S-T Al alloy	Alcoa K-12690-L	10,600	41.2
15	24S-T Al alloy	Alcoa 12098-K	10,900	50.5
16	X74S-T Al alloy	Alcoa 12072	10,100	67.2
17	X74S-T Al alloy	Alcoa K-8674	10,000	64.9
18	X74S-T Al alloy	Alcoa K-8848	10,300	59.8
19	Mg alloy Dow metal O	Dow Chem. DC-387	6,650	36.5
20	Mg alloy Dow metal O	Dow Chem. DC-388	6,650	36.5
21	Mg alloy Dow metal O	Dow Chem. DC-126	6,650	36.5
22	Mg alloy Dow metal O	Dow Chem. DC-401	6,650	36.5
23	Mg alloy Dow metal O	Dow Chem. DC-97	6,650	36.5
24	Mg alloy Dow metal G	Dow Chem. DC-97	6,540	33.2
25	Mg alloy Dow metal P	Dow Chem. DC-97	6,760	38.2
26	Mg alloy Dow metal R	Dow Chem. DC-97	6,880	33.2

$$n\left(\frac{\sigma}{\sigma_1}\right)^{n-1} = \frac{7}{3}\left[\left(\frac{2}{\sqrt{E_r/E}} - 1\right)^2 - 1\right] \qquad (38)$$

Taking the logarithm of both sides of this equation, setting $\sigma = \sigma_{cr}$, and substituting for n the value in Eq. (33),

$$\log_{10}\left(1 + \frac{0.3853}{\log_{10}(\sigma_1/\sigma_2)}\right) + \frac{0.3853}{\log_{10}(\sigma_1/\sigma_2)} \log_{10}\frac{\sigma_{cr}}{\sigma_1} = \log_{10}\left\{\frac{7}{3}\left[\left(\frac{2}{\sqrt{E_r/E}} - 1\right)^2 - 1\right]\right\} \qquad (39)$$

Substituting into Eq. (39) the value of σ_{cr} given by Eq. (31),

$$\log_{10}\left(1 + \frac{0.3853}{\log_{10}(\sigma_1/\sigma_2)}\right) + \frac{0.3853}{\log_{10}(\sigma_1/\sigma_2)} \log_{10}\frac{(\sigma_{cr})_{el}}{\sigma_1} = \frac{0.3853}{\log_{10}(\sigma_1/\sigma_2)} \log_{10}\frac{E}{E_r} + \log_{10}\left\{\frac{7}{3}\left[\left(\frac{2}{\sqrt{E_r/E}} - 1\right)^2 - 1\right]\right\} \qquad (40)$$

Eq. (40) can be conveniently solved for E_r/E from the known values of $(\sigma_{cr})_{el}$, σ_1, and σ_2 by use of the nomogram in Fig. 6a or 6b as follows. Draw a line from the value $(\sigma_{cr})_{el}/\sigma_1$ on scale 1 through the value σ_1/σ_2 on scale 2. From the intersection of this line with scale 3 draw a line through the value σ_1/σ_2 on scale 5. The intersection of the last line with scale 4 is the value of E_r/E that satisfies Eq. (40). The value of E_r/E determined in this way, together with the value of $(\sigma_{cr})_{el}$ computed from Eqs. (3a) or (13), was substituted into Eq. (31) to give the critical stress for plastic instability σ_{cr}.

COMPARISON OF MEASURED AND COMPUTED BUCKLING LOADS

Tests were made on 125 specimens including 26 different aluminum-alloy and magnesium-alloy extrusions. The lengths of the specimens were chosen to cover the range of about one to six times the greatest cross-sectional dimension. The material and die number of the extrusions are given in Table 1. The cross-sectional dimensions are given in Fig. 5. Stress-strain curves obtained from single-thickness compressive tests of the material in each extrusion are given in Fig. 7. The compressive Young's moduli and yield strengths (0.002 offset) determined from the stress-strain curves are given in Table 1.

Table 2 gives the values of k and of $(b/t)_{max.}$ for substitution in Eq. (3a) and the section constants A, J_x, J_y, J_p, J_{xy}, J_T, R_{xu}, R_{xn}, R_x, R_{yu}, R_{yn}, R_y, C_u, C_n, and C for substitution in Eqs. (20) to (26). The values of J_T were computed with Eqs. (5a) to (5d) (see discussion of Figs. 4a and 4b). The constants C_n and R_n were not included for sections other than L- and T-sections (see

TABLE 2. Constants for Computing Critical Stresses

Section No.	1	2	3	4	5	6	7	8	9	10	11	12
Reference Axes												
k	1.33	1.33	1.33	1.33	1.33	1.33	1.33	1.33	1.33	1.33	1.33	1.33
$(b/t)_{max.}$	12.5	7.7	11.1	10.1	18.1	30.8	29.5	14.3	20.2	7.5	10.0	8.6
A, in.^{2}	0.3049	0.4445	0.04471	0.04417	0.2216	0.1884	0.4962	0.06287	0.3207	0.5680	0.1483	0.2073
J_x, in.^{4}	0.02692	0.02287	0.0004371	0.0006099	0.007914	0.01463	0.4737	0.001414	0.02828	0.1312	0.02382	0.005122
J_y, in.^{4}	0.08445	0.16739	0.0016375	0.0014622	0.068847	0.08113	0.06695	0.004658	0.12463	0.5714	0.01869	0.026558
J_p, in.^{4}	0.11137	0.19026	0.0020746	0.0020721	0.076761	0.09575	0.5407	0.006072	0.15291	0.7026	0.04251	0.031680
J_{xy}, in.^{4}	0	0	0	−0.0004817	−0.012896	−0.01971	0	−0.001389	0	0	−0.01631	−0.006835
J_T, in.^{4}	0.001299	0.003269	0.0000384	0.00004456	0.0006818	0.0002606	0.001919	0.00006091	0.0006423	0.002104	0.000215	0.001241
R_{xu}, in.^{5}	0	0	0	−0.0001554	−0.005919	−0.012754	0	−0.0005248	0	0	0	−0.002274
R_{xn}, in.^{5}	0	0	0	0.0000030	0.000028	0.000014	0	0.0000068	0	0	....	0.000034
R_x, in.^{5}	0	0	0	−0.0001524	−0.005891	−0.012740	0	−0.0005180	0	0	0	−0.002240
R_{yu}, in.^{5}	0.014133	0.021348	0.00026894	0.00022131	0.014343	0.025868	0.05876	0.0008569	0.027959	0.5464	0	0.004602
R_{yn}, in.^{5}	−0.000020	−0.000039	−0.00000062	−0.00000025	−0.000011	−0.000007	−0.00015	−0.0000006	−0.000014	....	....	−0.000022
R_y, in.^{5}	0.014113	0.021309	0.00026832	0.00022106	0.014331	0.025861	0.05861	0.0008563	0.027944	0.5464	0	0.004580
C_u, in.^{6}	0.002365	0.002723	0.00004417	0.00004856	0.004888	0.0125027	0.05157	0.0002302	0.008241	0.5817	0.004592	0.001150
C_n, in.^{6}	0.000069	0.000573	0.00000025	0.00000079	0.000038	0.0000073	0.00032	0.0000027	0.000053	....	....	0.000031
C, in.^{6}	0.002434	0.003296	0.00004442	0.00004935	0.004926	0.0125100	0.05189	0.0002329	0.008294	0.5817	0.004592	0.001181

TABLE 2. Constants for Computing Critical Stresses (*Continued*)

Section No.	13	14	15	16	17	18	19	20	21	22	23, 24, 25, 26
Reference Axes											
k	1.33	1.33	1.33	1.33	1.33	1.33	1.33	1.33	1.33	1.33	1.33
$(b/t)_{max.}$	18.2	8.5	6.1	12.5	10.1	11.4	11.9	15.0	11.8	8.4	8.8
A, in.^{2}	0.2479	0.3629	1.5766	0.2950	0.04417	0.04112	0.05159	0.06024	0.09378	0.2730	0.1960
J_x, in.^{4}	0.009768	0.04538	0.4102	0.026123	0.0006099	0.000404	0.001131	0.001560	0.002031	0.06496	0.03738
J_y, in.^{4}	0.066346	0.04276	0.4714	0.081631	0.0014621	0.001542	0.001686	0.004491	0.010074	0.03415	0.02018
J_p, in.^{4}	0.076114	0.08814	0.8816	0.107754	0.0020721	0.001946	0.002817	0.006051	0.012105	0.09911	0.05756
J_{xy}, in.^{4}	−0.014525	0	0	0	−0.0004817	0	−0.000746	−0.001449	−0.002108	−0.01423	−0.01985
J_T, in.^{4}	0.001271	0.002017	0.05848	0.001166	0.00004456	0.00002752	0.0000555	0.00005248	0.0001862	0.0006914	0.0004383
R_{xu}, in.^{5}	−0.006332	0	0	0	−0.0001554	0	−0.0002773	−0.0005657	−0.0009489	−0.01467	0
R_{xn}, in.^{5}	0.000013	0	0	0	0.0000030	0	0.0000035	0.0000047	0.0000227	....	....
R_x, in.^{5}	−0.006319	0	0	0	−0.0001524	0	−0.0002738	−0.0005610	−0.0009262	−0.01467	0
R_{yu}, in.^{5}	0.014786	0.03645	0.4496	0.013682	0.00022131	0.00025668	0.0003192	0.0008954	0.0018116	−0.00433	0
R_{yn}, in.^{5}	−0.000025	....	....	−0.000021	−0.00000025	−0.00000051	−0.0000004	−0.0000006	−0.0000012	....	....
R_y, in.^{5}	0.014761	0.03645	0.4496	0.013661	0.00022106	0.00025617	0.0003188	0.0008948	0.0018104	−0.00433	0
C_u, in.^{6}	0.004749	0.03592	0.5452	0.002293	0.00004856	0.00004273	0.0000835	0.0002487	0.0005301	0.01159	0.006499
C_n, in.^{6}	0.000034	....	....	0.000064	0.00000079	0.00000020	0.0000010	0.0000021	0.0000101	....	....
C, in.^{6}	0.004783	0.03592	0.5452	0.002357	0.00004935	0.00004293	0.0000845	0.0002508	0.0005402	0.01159	0.006499

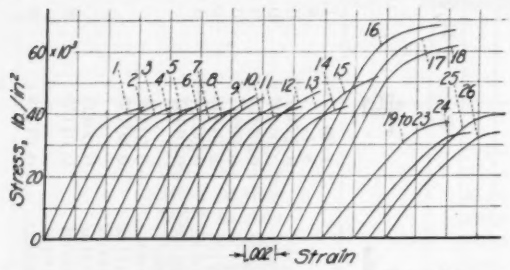

FIG. 7. Compressive stress-strain curves of material from sections 1 to 26.

discussion of Figs. 4a and 4b). Poisson's ratio was taken as $\nu = 0.3$.

The elastic buckling stresses for primary instability according to Eqs. (22) to (26) are shown as solid curves in Figs. 8a to 8e as a function of effective length (one-half of length between flat ends). The plastic buckling stresses for primary instability were estimated from the elastic buckling stresses, the compressive stress-strain curve of the material, Fig. 7, and the procedure outlined in the previous section. They are shown as dotted curves in Figs. 8a to 8e.

The elastic buckling stresses for local instability were either too high to be shown or they were so nearly equal to the plastic buckling stresses that they could not be differentiated from the latter. The buckling stresses for local instability are shown as horizontal broken lines in Figs. 8a to 8e.

The experimental values of buckling stress were determined from "flat-end" tests as follows. The ends of the specimen were ground flat and perpendicular to the axis, and the specimen was loaded in axial compression between ground steel blocks (*A*, Fig. 9). A plaster of paris cap (*B*, Fig. 9) was used between the top block and the head of the testing machine to obtain uniform loading. The distribution of strain across the section was measured with Tuckerman strain gages (*C*, Fig. 9), except for the extremely short specimens. Specimens showing a divergence of strain greater than 10 per cent at low loads were removed from the testing machine and were reground and retested. Twist was measured at the center of the specimen in some of the tests by measuring, with a Tuckerman autocollimator, the relative rotation of a prism (*D*, Fig. 9) attached to the specimen and a near-by prism connected to the bottom platen of the testing machine (*E*, Fig. 9). The buckling stress was determined as the stress for which there was a pronounced divergence of the curves for local strain or from Southwell plots of the twist at the center. When no strain gages were attached to the specimen, the buckling stress was visually observed. The experimental values of buckling stress are shown as individual points in Figs. 8a to 8e.

The measured buckling stress is plotted against the calculated buckling stress in Fig. 10. The 45° line in

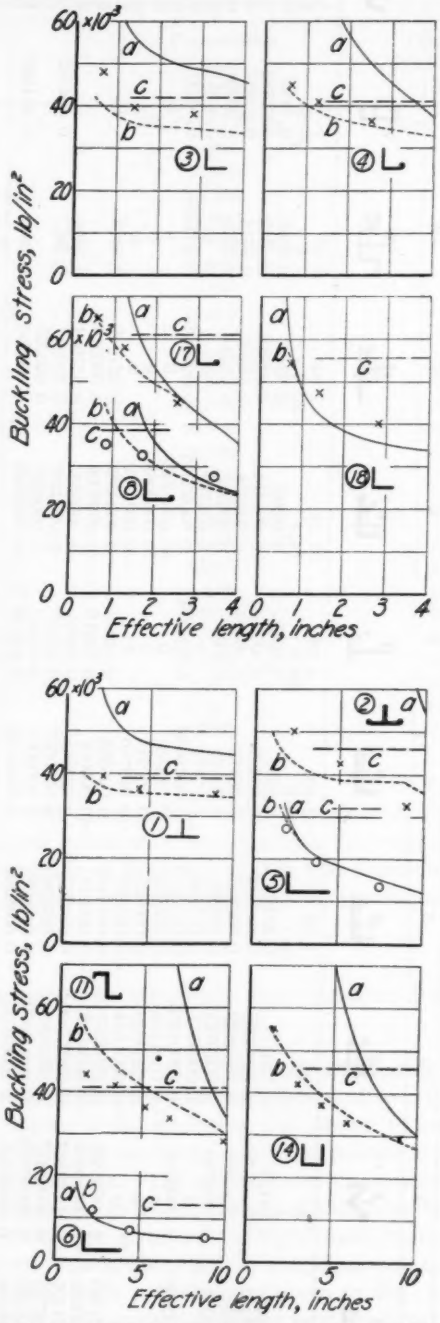

FIG. 8a (*top*). Computed and measured buckling stresses for sections 3, 4, 8, 17, and 18. Curve a, elastic primary instability; curve b, plastic primary instability; curve c, local instability.

FIG. 8b (*bottom*). Computed and measured buckling stresses for sections 1, 2, 5, 6, 11, and 14. Curve a, elastic primary instability; curve b, plastic primary instability; curve c, local instability. (For extrusion 6, curve a masks curve b.)

Fig. 10 corresponds to perfect agreement between measured and calculated stress, while the pair of dotted lines shows the band within which the measured and calcu-

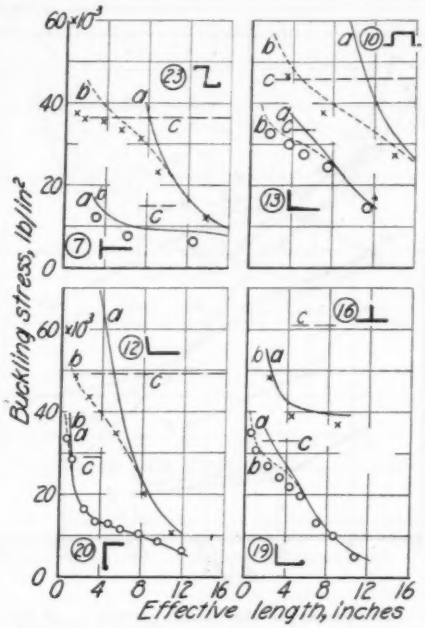

FIG. 8c. Computed and measured buckling stresses for sections 7, 10, 12, 13, 16, 19, 20, and 23. Curve a, elastic primary instability; curve b, plastic primary instability; curve c, local instability. (For extrusions 7 and 16, curve a masks curve b.)

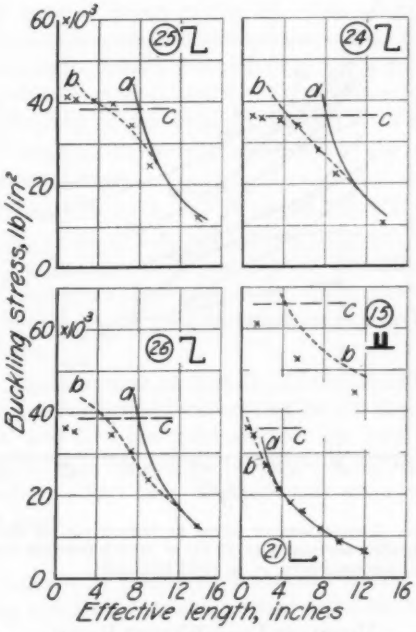

FIG. 8d. Computed and measured buckling stresses for sections 15, 21, 24, 25, and 26. Curve a, elastic primary instability; curve b, plastic primary instability; curve c, local instability. (For section 15, curve a is too high to be shown.)

lated stresses differed by less than 5,000 lbs. per sq.in. For 120 of the 125 specimens tested, the calculated and measured stresses differed less than 5,000 lbs. per sq.in. For the remaining five specimens the difference was

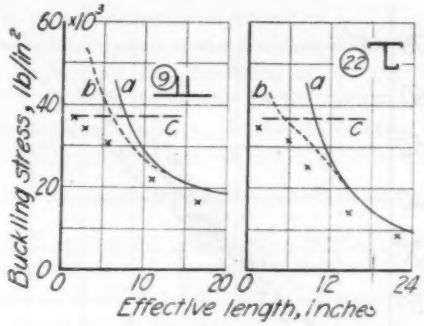

FIG. 8e. Computed and measured buckling stresses for sections 9 and 22. Curve a, elastic primary instability; curve b, plastic primary instability; curve c, local instability.

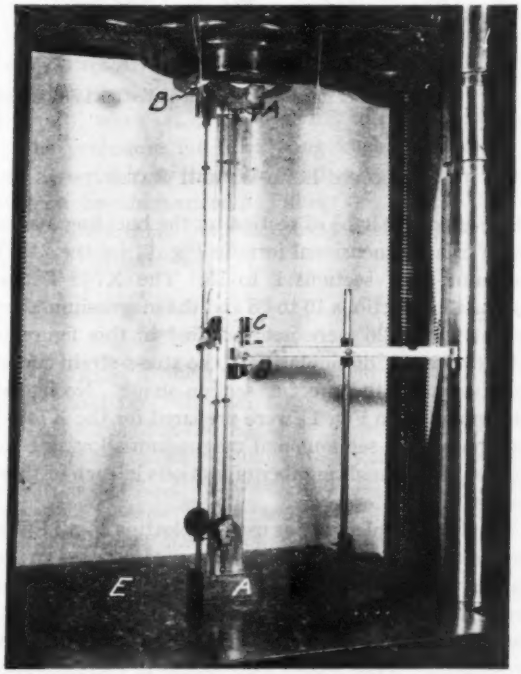

FIG. 9. Method of making compressive tests showing loading blocks *A*, plaster of paris cap *B*, strain gages *C*, prisms *D* used to measure twist, and testing machine *E*.

6,000 to 9,000 lbs. per sq.in. These differences were attributed to the uncertainty of about 2,000 lbs. per sq.in. in the experimentally determined buckling stress, the differences in cross-sectional dimensions among nominally similar extrusions, the initial curvature of some of the specimens, the use at stresses in the plastic range of a stress-strain curve described by three parameters[8] in place of the actual stress-strain curve, the use of approximate Eq. (3a) to compute local buckling stresses, the use of the reduced modulus defined by Eq. (30) to compute critical stresses in the plastic range, and the assumption that in the tests the effective length was equal to one-half the actual length.

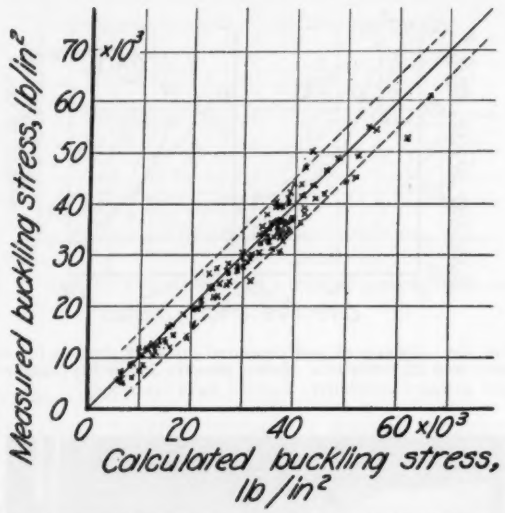

FIG. 10. Comparison of measured and calculated buckling stress.

BUCKLING LOAD-WEIGHT RATIO

The effect of shape of section on the buckling load is shown in nondimensional form in Fig. 11 for the 24S-T aluminum-alloy sections 1 to 15. The X74S-T aluminum-alloy sections 16 to 18 and the magnesium-alloy sections 19 to 26 were not included in this figure in order to prevent dissimilarity in the stress-strain curves from obscuring the effect of section shape. No figures corresponding to Fig. 11 were prepared for the X74S-T aluminum-alloy sections and magnesium-alloy sections because of the small number of sections in each of these groups.

The dimensionless ratios used in plotting Fig. 11 were chosen to give the best comparison of stresses in the plastic range and to plot sections of different shape but having the same length and weight at the same abscissa. The stress ratio used is σ_{cr}/σ_1 where σ_{cr} is the buckling stress and σ_1 is the secant yield strength corresponding to the intercept of the stress-strain curve and the line through the origin with a slope $0.7E$. The length ratio used is $l/\sqrt{A}$ where l is an effective length taken as one-half the actual length and A is the cross-sectional area. This ratio, just as the slenderness ratio, has the same value for all geometrically similar specimens. It was chosen in preference to the slenderness ratio because it has the advantage of having the same value for all specimens having the same length and weight.

The range of buckling-stress ratio shown in Fig. 11 is extremely large; the largest of the ratios are of the order of four times the smallest ratios. The thick-walled sections are generally near the top and the thin-walled sections near the bottom. The Z-section keeps most steadily near the top throughout the range of length ratios.

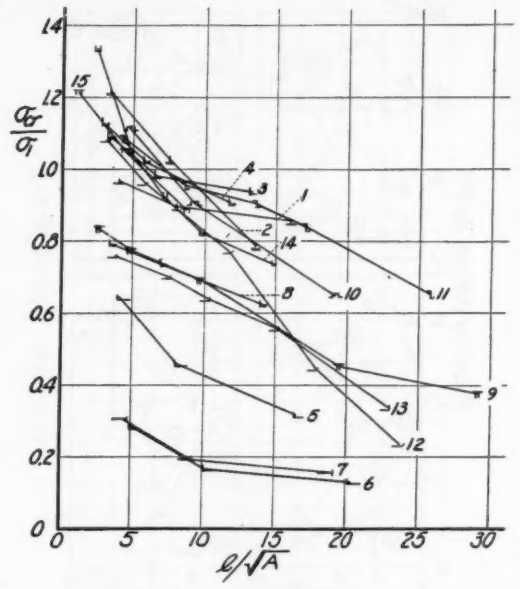

FIG. 11. Comparison of the buckling stress σ_{cr} of the 24S-T aluminum alloy sections 1 to 15 ($2l$ = length between flat ends, A = cross-sectional area, σ_1 = yield strength).

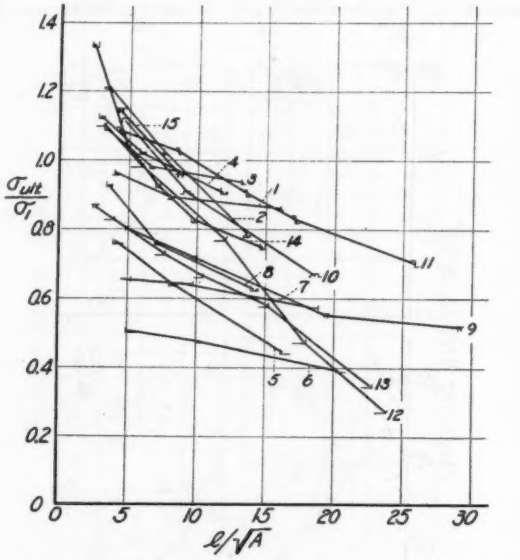

FIG. 12. Comparison of stress at failure $\sigma_{ult.}$ of the 24S-T aluminum alloy sections 1 to 15 ($2l$ = length between flat ends, A = cross-sectional area, σ_1 = yield strength).

ULTIMATE LOAD-WEIGHT RATIO

The effect of shape of section on strength-weight ratio for the 24S-T aluminum-alloy sections 1 to 15 is shown in Fig. 12, which is analogous to Fig. 11.

The range of strength-weight ratios in Fig. 12 for a specimen of given length and given weight is less than the range of buckling load-weight ratios, but it is still of the order of 2:1.

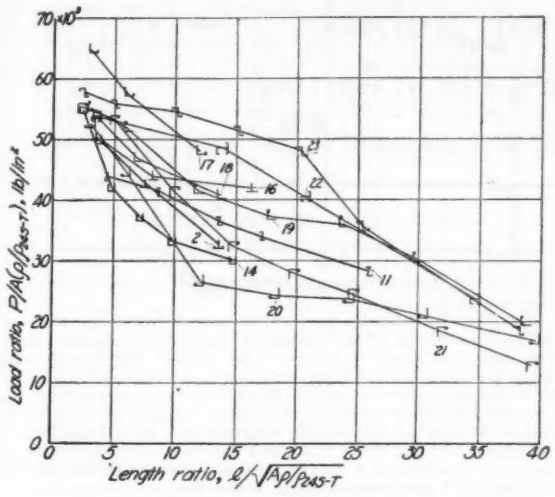

FIG. 13. Strength-weight ratio for extruded sections of two aluminum alloys and one magnesium alloy (ρ = density, $2l$ = length between flat ends, A = cross-sectional area).

Over the range of lengths investigated, the strength-weight ratio of the Z-extrusion was generally greater than that for the other extrusions.

The effect of both shape and material on strength-weight ratio is shown in Fig. 13. The coordinates in this figure are such that similar specimens of material with the same density are plotted at the same abscissa with ordinates proportional to the strength-weight ratio. The efficiency of the different sections on a strength-weight basis is, therefore, proportional to the ordinates at a given abscissa.

Only sections 2, 11, and 14 of the 24S-T aluminum-alloy extrusions are included, since these are shown in Fig. 12 to have generally the highest strengths for the 24S-T aluminum-alloy specimens. Only section 23 of the group 23, 24, 25, 26 is included, since it is typical of the others.

Fig. 13 shows that section 17 (X74S-T aluminum alloy) was most efficient for short lengths and that sections 19, 22, and 23 were most efficient for long lengths. Over the range of lengths investigated section 23 (O magnesium alloy) was most efficient on a strength-weight basis.

CALCULATION OF CURVE OF BUCKLING STRESS VERSUS LENGTH FOR ONE MATERIAL FROM THAT OF ANOTHER

The agreement between measured and computed buckling loads of unsupported extruded sections suggested a procedure for calculating the buckling stresses of extrusions of one material from measured buckling stresses of similar extrusions of a different material. With such a procedure it is possible to derive curves of buckling load versus length for material with minimum properties satisfying a given specification or to estimate the increase in buckling stress in going to a new material with increased compressive properties.

The determination of the buckling stress in the new material requires the determination of the value of $(\sigma_{cr})_{el}/E$ for the particular section shape from the known buckling stress, σ_{cr}, in the old material and the stress-strain curve of the old material. From Eq. (31)

$$(\sigma_{cr})_{el}/E = \sigma_{cr}/E_r = (\sigma_{cr}/E)(E/E_r) \qquad (41)$$

σ_{cr} and E are known for the old material. The corresponding value of E/E_r may be determined from σ_1, σ_2, and σ_{cr} by solving Eq. (39). A convenient way of doing this is to use the nomogram in Figs. 6a or 6b as follows. Draw a line through the value σ_{cr}/σ_1 on scale 1 and the value σ_1/σ_2 on scale 2. The intersection with scale 3 is the value of E_r/E which satisfies Eq. (39). The value of $(\sigma_{cr})_{el}/E$ is then given by Eq. (41).

Knowing $(\sigma_{cr})_{el}/E$ and E for the new material, $(\sigma_{cr})_{el}$ is readily computed and σ_{cr} is determined in the same way as was done previously (see discussion of Eq. (40)) when $(\sigma_{cr})_{el}$ was determined from the theory.

The procedure for calculating buckling stresses for one material from those for another, using Figs. 6a and 6b, may be summarized as follows.

(1) Determine from the stress-strain curves of the new and old material,

$$\begin{array}{lll} E_{\text{old}} & (\sigma_1)_{\text{old}} & (\sigma_2)_{\text{old}} \\ E_{\text{new}} & (\sigma_1)_{\text{new}} & (\sigma_2)_{\text{new}} \end{array}$$

(2) Draw a line through the value $(\sigma_{cr}/\sigma_1)_{\text{old}}$ on scale 1 and the value $(\sigma_1/\sigma_2)_{\text{old}}$ on scale 2. The line intersects scale 3 at $(E_r/E)_{\text{old}}$.

(3) Draw a line through the value $[(\sigma_{cr}/E)_{\text{old}} \times (E/E_r)_{\text{old}}(E/\sigma_1)_{\text{new}}]$ on scale 1 and the value $(\sigma_1/\sigma_2)_{\text{new}}$ on scale 2. From the intersection of this line with scale 3 draw another line through the value $(\sigma_1/\sigma_2)_{\text{new}}$ on scale 5. The last line intersects scale 4 at $(E_r/E)_{\text{new}}$.

(4) The desired value of the failing stress in the new material is

$$(\sigma_{cr})_{\text{new}} = \left(\frac{\sigma_{cr}}{E}\right)_{\text{old}} \left(\frac{E}{E_r}\right)_{\text{old}} \left(\frac{E_r}{E}\right)_{\text{new}} E_{\text{new}}$$

Example

An extruded section of 24S-T aluminum alloy buckles at a stress $(\sigma_{cr})_{\text{old}}$ = 41,000 lbs. per sq.in. What will be the buckling stress $(\sigma_{cr})_{\text{new}}$ of a similar section of X74S-T aluminum alloy if the stress-strain curves show, for the 24S-T aluminum alloy,

E_{old} = 10,800,000 lbs. per sq.in.
$(\sigma_1)_{\text{old}}$ = 45,000 lbs. per sq.in.
$(\sigma_2)_{\text{old}}$ = 40,000 lbs. per sq.in.

and for the X74S-T aluminum alloy

E_{new} = 10,300,000 lbs. per sq.in.
$(\sigma_1)_{\text{new}}$ = 63,000 lbs. per sq.in.
$(\sigma_2)_{\text{new}}$ = 59,000 lbs. per sq.in.

Proceeding as above:

Step 1, all in lbs. per sq.in.:

$E_{old} = 10.8 \times 10^6$, $E_{new} = 10.3 \times 10^6$,
$(\sigma_1)_{old} = 45 \times 10^3$, $(\sigma_1)_{new} = 63 \times 10^3$,
$(\sigma_2)_{old} = 40 \times 10^3$, $(\sigma_2)_{new} = 59 \times 10^3$

Step 2:

$(\sigma_{cr}/\sigma_1)_{old} = 0.911$, $(\sigma_1/\sigma_2)_{old} = 1.125$,
$(E_r/E)_{old} = 0.559$

Step 3:

$$\left(\frac{\sigma_{cr}}{E}\right)_{old}\left(\frac{E}{E_r}\right)_{old}\left(\frac{E}{\sigma_1}\right)_{new} = 1.110,$$

$(\sigma_1/\sigma_2)_{new} = 1.068$, $(E_r/E)_{new} = 0.763$

Step 4:

$(\sigma_{cr})_{old} = 41{,}000$ lbs. per sq.in.
$(E_r/E)_{new} = 0.763$
$(E_r/E)_{old} = 0.559$
$E_{new} = 10{,}300{,}000$ lbs. per sq.in.
$E_{old} = 10{,}800{,}000$ lbs. per sq.in.

$$(\sigma_{cr})_{new} = \left(\frac{\sigma_{cr}}{E}\right)_{old}\left(\frac{E}{E_r}\right)_{old}\left(\frac{E_r}{E}\right)_{new} E_{new} =$$

53,400 lbs. per sq.in.

The X74S-T aluminum alloy extruded section may be expected to buckle at 53,400 lbs. per sq.in.

Figs. 14a to 14c show a check of this procedure by comparing calculated buckling stresses (circles, triangles, and squares) and measured buckling stresses (crosses) for aluminum-alloy T-sections (Fig. 14a), magnesium-alloy Z-sections (Fig. 14b), and aluminum-alloy L-sections (Fig. 14c). The difference between the measured and calculated buckling stresses of these sections did not exceed 10,000 lbs. per sq.in. The average difference was less than 5,000 lbs. per sq.in.

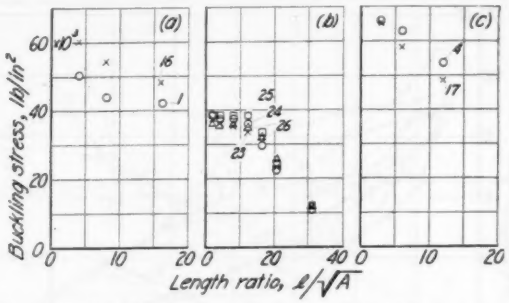

FIG. 14. (a) Comparison of measured buckling stress of X74S-T aluminum alloy T-section 16 and stress computed from the measured buckling stress on the similar 24S-T aluminum alloy T-section 1. (b) Comparison of measured buckling stress of magnesium alloy O Z-section 23 and stress computed from the measured buckling stress on the similar magnesium alloy G, P, and R sections 24, 25, and 26, respectively. (c) Comparison of measured buckling stress of X74S-T aluminum-alloy L-section 17 and stress computed from the measured buckling stress on the similar 24S-T aluminum-alloy L-section 4.

REFERENCES

[1] Timoshenko, S., *Strength of Materials;* Van Nostrand, New York, 1930.

[2] Wagner, Herbert, *Verdrehung und Knickung von offenen Profilen*, pp. 329–343; Festschrift, T. H. Danzig, 1929.

[3] Kappus, Robert, *Drillknicken zentrisch gedrueckter Staebe mit offenem Profil im elastischen Bereich*, Luftfahrtforschung, Vol. 14, No. 9, pp. 444–457, October, 1937.

[4] Lundquist, E. E., and Fligg, C. M., *A Theory for Primary Failure of Straight Centrally Loaded Columns*, N.A.C.A. Rep. 582, 1937.

[5] Trayer, George W., and March, H. W., *The Torsion of Members Having Sections Common in Aircraft Construction*, N.A.C.A. Rep. 334, 1930.

[6] Nadai, A., *Plasticity*, pp. 178–180; McGraw-Hill Book Company, Inc., New York, 1931.

[7] Osgood, William R., *Column Curves and Stress-Strain Diagrams*, J. of Research of the National Bureau of Standards, Vol. 9, pp. 571–582, October, 1932.

[8] Ramberg, Walter, and Osgood, William R., *Description of Stress-Strain Curves by Three Parameters*, N.A.C.A. T.N. 902, July, 1943.

Index to Volume 12

Journal of the Aeronautical Sciences

Numbers 1–4, January–October, 1945

No. 1, January, 1945, pages 1–126
No. 2, April, 1945, pages 127–252
No. 3, July, 1945, pages 253–378
No. 4, October, 1945, pages 379–504

Material that has appeared in the above volume has been indexed under a general subject heading and by author and has been further cross-indexed under various subheadings.

Aerodynamics—

Aerodynamic Performance of Small Spheres from Subsonic to High Supersonic Velocities, A. C. Charters and R. N. Thomas 468
Airfoil Theory for Flows of Variable Velocity, Rufus Isaacs 113
Analytic Investigation of Problems Concerning the Flow of Cooling Air in Light Airplane Engine Installations, John R. Weske 63
The Attenuation Method for Compressible Flow Systems, Leonard Michael Greene 329
Calculated Gust Loads for Tailless Airplanes, Raymond F. Anderson 118
Coefficient Method for Solving the Flutter Frequency Equation, M. V. Barton 164
Compressible Flows in Aeronautics (Eighth Wright Brothers Lecture), John Stack 127
Effect of Temperature Lapse Rate on Recovery from Compressibility Dives, C. E. Pappas and M. G. Harrison .. 379
The Effective Use of Aerodynamic Balance on Control Surfaces, L. E. Root 149
Elementary Considerations of Longitudinal Stability, Marion Thomas Hockman 370
Equivalent Circuits of Compressible and Incompressible Fluid Flow Fields, Gabriel Kron 221
A General Stability Index for Flow Near Plane Boundaries, Hunter Rouse 429
The Glauert-Prandtl Approximation for Subsonic Flows of a Compressible Fluid, Hsue-Shen Tsien and Lester Lees 173
The Influence of Structural Deformation on Airplane Characteristics, Alexander H. Flax 94
Investigation of the Wing-Wake Frequency with Application of the Strouhal Number, M. Zbigniew Krzywoblocki ... 51
Letters to the Editor
Bailey, Neil P. 220
Beskin, Leon 476
Emmons, Howard W. 476
Laitone, Edmund V. 220
Lu, Hoshen 432
Numerical and Network-Analyzer Tests of an Equivalent Circuit for Compressible Fluid Flow, G. K. Carter and G. Kron 232
A Review of the Aerodynamics of Flight Load Factors in Relation to the Safety Regulations, Hugh B. Freeman .. 320
Shock Waves in Aerodynamics, Howard W. Emmons 188
The Simplification of Flutter Calculations by Use of an Extended Form of the Routh-Hurwitz Discriminant, S. Sherman, J. DiPaola, and H. F. Frissel 385
The Thermodynamics of the Laminar Boundary Layer of a Heated Body in a High-Speed Gas Flow Field, Arthur N. Tifford 241
Vibrations of Composite Structures, H. Serbin 108
Wing Flaps in Light Aircraft Design, Maurice A. Garbell 14
Aircraft, high-speed, performance methods for 345
Airfoil theory for flows of variable velocity 113
Airplane structures, the applicability of Saint-Venant's principle to 455
Airplanes, tailless, calculated gust loads for 118
Altimeter systems, lag determination of 85
Aluminum-alloy compressive test results for material properties using reduced moduli, correction of 305
Aluminum-alloy sheets, curved, in compression for monocoque constructions 357
ANDERSON, RAYMOND F. Calculated Gust Loads for Tailless Airplanes 118
ANSEL, G., F. A. RAPPLEYEA, AND R. E. PERRY. Influence of Prestressing and Cyclic Stressing on Stress-Strain Characteristics of Magnesium Alloys 448

BAILEY, NEIL P. Letter to the Editor (Aerodynamics) ... 220
BARBA, JOSEPH F. Letter to the Editor (Stress Analysis and Structures) 123
BARTON, M. V. Coefficient Method for Solving the Flutter Frequency Equation 164
Beams, four-element box, shear lag and torsion bending of 461
Beams, hollow, with longitudinal webs subjected to torsional loads, a simplified analysis of 103
Beams, the stress-area method of designing 298
Beams of variable section, stress analysis of nondevelopable semimonocoque structures considered as 203
Bearing strength in airplane design 67
BENCKERT, WILLIS J. Letter to the Editor (Stress Analysis and Structures) 431
Bending, plastic—approximate solution 408
Bending beyond the proportional limit, a note on 21
Bending, plastic—further considerations 253
Bending with buckled stringers, note on analysis for 403
BESKIN, LEON. Letter to the Editor (Aerodynamics) 476
——— Letters to the Editor (Stress Analysis and Structures) 122, 355, 407, 432
——— Stress Analysis of Nondevelopable Semimonocoque Structures Considered as Beams of Variable Section 203
BEST, GILBERT C. The Stress-Area Method of Designing Beams 298
BONNEY, E. ARTHUR, AND HAROLD B. CROCKETT. Reverse-Pitch Propellers as Airplane Landing Brakes 441

Boundary layer, laminar, of a heated body in a high-speed gas flow field, the thermodynamics of the..... 241
Brakes, airplane landing, reverse-pitch propellers as..... 441
Buckling, elastic, on the dynamics of..... 433
Buckling of sandwich-type panels..... 285
Buckling of stiffener and elastic sheet combinations under pure bending..... 393
BURGHARDT, JOSEPH E., AND JOHN D. PIERSON. A Specific Chart for Flying Boat Take-Off Performance..... 169
BUZZETTI, C. J., AND W. L. HOWLAND. Measurement of Maneuvering Loads in Flight..... 195

CARTER, G. K., AND G. KRON. Numerical and Network-Analyzer Tests of an Equivalent Circuit for Compressible Fluid Flow..... 232
CASTLES, WALTER, JR. A Direct Method of Estimating the Performance of a Helicopter in Powered Flight..... 477
CHARTERS, A. C., AND R. N. THOMAS. Aerodynamic Performance of Small Spheres from Subsonic to High Supersonic Velocities..... 468
Columns, magnesium-alloy, strength of..... 339
Compressible flow systems, the attenuation method for... 329
Compressible fluid, the Glauert-Prandtl approximation for subsonic flows of a..... 173
Compressible fluid flow, numerical and network-analyzer tests of an equivalent circuit for..... 232
Compressible and incompressible fluid flow fields, equivalent circuits of..... 221
Compressibility dives, effect of temperature lapse rate on recovery from..... 379
CONTINI, ROBERTO. A Graphic Solution for Strains and Stresses from Strain Rosette Data..... 47
Control surfaces, the effective use of aerodynamic balance on..... 149
CROCKETT, HAROLD B., AND E. ARTHUR BONNEY. Reverse-Pitch Propellers as Airplane Landing Brakes..... 441

Design—
Bearing Strength in Airplane Design, Albert Epstein.... 67
Determination of the Axis of Rotation of a Skewed Axis Landing Gear, J. J. Jerger..... 217
Graphical Analysis of Performance of Hydraulic Shock Absorbers in Aircraft Landing Gears, Alexander J. Yorgiadis 421
Measurement of Maneuvering Loads in Flight, C. J. Buzzetti and W. L. Howland..... 195
Motogliders—A Natural Link Between Gliders and Light Planes, Wieslaw Z. Stepniewski..... 39
A Specific Chart for Flying Boat Take-Off Performance, John D. Pierson and Joseph E. Burghardt..... 169
Wing Flaps in Light Aircraft Design, Maurice A. Garbell 14
DIPAOLA, J., S. SHERMAN, AND H. F. FRISSEL. The Simplification of Flutter Calculations by Use of an Extended Form of the Routh-Hurwitz Discriminant..... 385

EASTMAN, E. J., J. C. MCDONALD, AND A. A. MOORE. The Relation of Stress to Strain in Magnesium Base Alloys.. 273
EMMONS, HOWARD W. Letter to the Editor (Aerodynamics) 476
———— Shock Waves in Aerodynamics..... 188
Engines—
Analytic Investigation of Problems Concerning the Flow of Cooling Air in Light Airplane Engine Installations, John R. Weske..... 63
Design and Application of High-Pressure Coefficient Axial-Flow Fans, J. G. Sawyer..... 281
A Vibration Theory Combining the Dynamic Stiffness and Mobility Methods, Hugh B. Stewart..... 349
EPSTEIN, ALBERT. Bearing Strength in Airplane Design.. 67
Extrusions under compressive loads, instability of..... 485

Fans, high-pressure coefficient axial-flow, design and application of..... 281
Flaps, wing, in light aircraft design..... 14
FLAX, ALEXANDER H. The Influence of Structural Deformation on Airplane Characteristics..... 94
Flow near plane boundaries, a general stability index for.. 429
Flows, compressible, in aeronautics (Eighth Wright Brothers Lecture)..... 127
Flutter calculations by use of an extended form of the Routh-Hurwitz discriminant, the simplification of..... 385
Flutter frequency equation, coefficient method for solving the..... 164
Flying boat take-off performance, a specific chart for..... 169
FREEMAN, HUGH B. A Review of the Aerodynamics of Flight Load Factors in Relation to the Safety Regulations 320
FRISSEL, H. F., S. SHERMAN, AND J. DIPAOLA. The Simplification of Flutter Calculations by Use of an Extended Form of the Routh-Hurwitz Discriminant..... 385

GARBELL, MAURICE A. Wing Flaps in Light Aircraft Design..... 14
Gliders and light planes, a natural link between—Motogliders..... 39
GORAN, LENARD A., AND JACOB KAROL. Letter to the Editor (Stress Analysis and Structures)..... 251
GREENE, LEONARD MICHAEL. The Attenuation Method for Compressible Flow Systems..... 329

HARRISON, M. G., AND C. E. PAPPAS. Effect of Temperature Lapse Rate on Recovery from Compressibility Dives 379
HAYES, WALLACE D. Performance Methods for High-Speed Aircraft..... 345
HEAD, RICHARD M. Effect of Pressure Variations on Speed Runs..... 311
———— Lag Determination of Altimeter Systems. 85
Helicopter in powered flight, a direct method of estimating the performance of a..... 477
HOCKMAN, MARION THOMAS. Elementary Considerations of Longitudinal Stability..... 370
HOFF, N. J. The Applicability of Saint-Venant's Principle to Airplane Structures..... 455
———— AND S. E. MAUTNER. The Buckling of Sandwich-Type Panels..... 285
HOWLAND, W. L., AND C. J. BUZZETTI. Measurement of Maneuvering Loads in Flight..... 195

Instruments—
Lag Determination of Altimeter Systems, Richard M. Head 85
Operational Methods in Servomechanism Design, William E. Restemeyer..... 313
ISAACS, RUFUS. Airfoil Theory for Flows of Variable Velocity..... 113

JERGER, J. J. Determination of the Axis of Rotation of a Skewed Axis Landing Gear..... 217

KAROL, JACOB. Correction of Aluminum-Alloy Compressive Test Results for Material Properties Using Reduced Moduli..... 305
———— AND LENARD A. GORAN. Letter to the Editor (Stress Analysis and Structures)..... 251
KIEHLE, M. H., AND A. VANTINE. A Consideration of Calculated Versus Flight Test Take-Off Performance..... 263
KOSKO, ERYK. Letter to the Editor (Stress Analysis and Structures)..... 407

KOSKO, ERYK. A Simplified Analysis of Hollow Beams with Longitudinal Webs Subjected to Torsional Loads.. 103
KRON, GABRIEL. Equivalent Circuits of Compressible and Incompressible Fluid Flow Fields..... 221
———— AND G. K. CARTER. Numerical and Network-Analyzer Tests of an Equivalent Circuit for Compressible Fluid Flow..... 232
KRZYWOBLOCKI, M. ZBIGNIEW. Investigation of the Wing-Wake Frequency with Application of the Strouhal Number..... 51

LAITONE, EDMUND V. Letter to the Editor (Aerodynamics) 220
Landing gear, skewed axis, determination of the axis of rotation of a..... 217
Landing gears, aircraft, graphical analysis of performance of hydraulic shock absorbers in..... 421
LEES, LESTER, AND HSUE-SHEN TSIEN. The Glauert-Prandtl Approximation for Subsonic Flows of a Compressible Fluid..... 173
LEVY, SAMUEL, AND WALTER RAMBERG. Instability of Extrusions Under Compressive Loads..... 485
Light airplane engine installations, analytic investigation of problems concerning the flow of cooling air in..... 63
Load factors, flight, in relation to the safety regulations, a review of the aerodynamics of..... 320
Loads, maneuvering, in flight, measurement of..... 195
Longitudinal stability, elementary considerations of..... 370
LU, HOSHEN. Letter to the Editor (Aerodynamics)..... 432

MACK, CHARLES E., JR. Three-Dimensional Analysis of Engine Mount Rings by a Strain Energy Method..... 1
MACLEAN, EDWARD A. Note on Analysis for Bending with Buckled Stringers..... 403
Magnesium alloys, influence of prestressing and cyclic stressing on stress-strain characteristics of..... 448
Magnesium base alloys, the relation of stress to strain in.. 273
MARTELL, G. M., AND R. T. SCHWARTZ. Mechanical Properties of Magnesium-Alloy Tubing..... 31
Materials—
Correction of Aluminum-Alloy Compressive Test Results for Material Properties Using Reduced Moduli, Jacob Karol..... 305
Curved Aluminum-Alloy Sheets in Compression for Monocoque Constructions, Georges Welter..... 357
Influence of Prestressing and Cyclic Stressing on Stress-Strain Characteristics of Magnesium Alloys, F. A. Rappleyea, R. E. Perry, and G. Ansel..... 448
Mechanical Properties of Magnesium-Alloy Tubing, R. T. Schwartz, and G. M. Martell..... 31
The Relation of Stress to Strain in Magnesium Base Alloys, E. J. Eastman, J. C. McDonald, and A. A. Moore.... 273
Strength of Magnesium-Alloy Columns, F. A. Rappleyea. 339
MAUTNER, S. E., AND N. J. HOFF. The Buckling of Sandwich-Type Panels..... 285
MCDONALD, J. C., E. J. EASTMAN, AND A. A. MOORE. The Relation of Stress to Strain in Magnesium Base Alloys.. 273
MEIER, J. H. On the Dynamics of Elastic Buckling..... 433
MOORE, A. A., E. J. EASTMAN, AND J. C. MCDONALD. The Relation of Stress to Strain in Magnesium Base Alloys.. 273

NEWTON, R. E. Shear Lag and Torsion Bending of Four-Element Box Beams..... 461
NILES, ALFRED S. Letter to the Editor (Stress Analysis and Structures)..... 240

OSGOOD, WM. R. Plastic Bending—Approximate Solution 408
———— Plastic Bending—Further Considerations 253

Panels, sandwich-type, the buckling of..... 285
PAPPAS, C. E., AND M. G. HARRISON. Effect of Temperature Lapse Rate on Recovery from Compressibility Dives 379
Performance—
A Consideration of Calculated Versus Flight Test Take-off Performance, M. H. Kiehle and A. Vantine..... 263
A Direct Method of Estimating the Performance of a Helicopter in Powered Flight, Walter Castles, Jr..... 477
Effect of Pressure Variations on Speed Runs, Richard M. Head..... 311
Performance Methods for High-Speed Aircraft, Wallace D. Hayes..... 345
A Specific Chart for Flying Boat Take-Off Performance, John D. Pierson and Joseph E. Burghardt..... 169
PERRY, R. E., F. A. RAPPLEYEA, AND G. ANSEL. Influence of Prestressing and Cyclic Stressing on Stress-Strain Characteristics of Magnesium Alloys..... 448
PIERSON, JOHN D., AND JOSEPH E. BURGHARDT. A Specific Chart for Flying Boat Take-Off Performance..... 169
Plates with intermediate rigid supports, buckling of..... 375
POLIVKA, J. J. Letter to the Editor (Stress Analysis and Structures)..... 107
Pressure variations on speed runs, effect of..... 311
Propellers—
Reverse-Pitch Propellers as Airplane Landing Brakes, Harold B. Crockett and E. Arthur Bonney..... 441

RAMBERG, WALTER, AND SAMUEL LEVY. Instability of Extrusions Under Compressive Loads..... 485
RAPPLEYEA, F. A. Strength of Magnesium-Alloy Columns. 339
————, R. E. PERRY, AND G. ANSEL. Influence of Prestressing and Cyclic Stressing on Stress-Strain Characteristics of Magnesium Alloys..... 448
REISSNER, ERIC. Buckling of Plates with Intermediate Rigid Supports..... 375
RESTEMEYER, WILLIAM E. Operational Methods in Servomechanism Design..... 313
Ring loaded normal to its plane, stresses in a..... 235
Rings, engine mount, three-dimensional analysis of, by a strain energy method..... 1
ROOT, L. E. The Effective Use of Aerodynamic Balance on Control Surfaces..... 149
Rotating Wing Aircraft—
A Direct Method of Estimating the Performance of a Helicopter in Powered Flight, Walter Castles, Jr..... 477
ROUSE, HUNTER. A General Stability Index for Flow Near Plane Boundaries..... 429

SAIBEL, EDWARD. Letter to the Editor (Stress Analysis and Structures)..... 251
SAWYER, J. G. Design and Application of High-Pressure Coefficient Axial-Flow Fans..... 281
SCHWARTZ, R. T., AND G. M. MARTELL. Mechanical Properties of Magnesium-Alloy Tubing..... 31
SERBIN, H. Vibrations of Composite Structures..... 108
Servomechanism design, operational methods in..... 313
SHERMAN, S., J. DIPAOLA, AND H. F. FRISSEL. The Simplification of Flutter Calculations by Use of an Extended Form of the Routh-Hurwitz Discriminant..... 385
Shock waves in aerodynamics..... 188
STACK, JOHN. Compressible Flows in Aeronautics (Eighth Wright Brothers Lecture)..... 127
STEPNIEWSKI, WIESLAW Z. Motogliders—A Natural Link Between Gliders and Light Planes..... 39
STEWART, HUGH B. A Vibration Theory Combining the Dynamic Stiffness and Mobility Methods..... 349

Strain rosette data, a graphic solution for strains and stresses from 47
Stress Analysis and Structures—
The Applicability of Saint-Venant's Principle to Airplane Structures, N. J. Hoff 455
Buckling of Plates with Intermediate Rigid Supports, Eric Reissner 375
The Buckling of Sandwich-Type Panels, N. J. Hoff and S. E. Mautner 285
Buckling of Stiffener and Elastic Sheet Combinations Under Pure Bending, E. E. Weibel 393
A Graphic Solution for Strains and Stresses from Strain Rosette Data, Roberto Contini 47
Instability of Extrusions Under Compressive Loads, Walter Ramberg and Samuel Levy 485
Letters to the Editor
Barba, Joseph F. 123
Benckert, Willis J. 431
Beskin, Leon 122, 355, 407, 432
Goran, Lenard A., and Jacob Karol 251
Karol, Jacob, and Lenard A. Goran 251
Kosko, Eryk 407
Niles, Alfred S. 240
Polivka, J. J. 107
Saibel, Edward 251
Wang, Chi-Teh 432
Note on Analysis for Bending with Buckled Stringers, Edward A. MacLean 403
A Note on Bending Beyond the Proportional Limit, M. Yachter 21
On the Dynamics of Elastic Buckling, J. H. Meier 433
Plastic Bending—Approximate Solution, Wm. R. Osgood. 408
Plastic Bending—Further Considerations, Wm. R. Osgood. 253
Shear Lag and Torsion Bending of Four-Element Box Beams, R. E. Newton 461
A Simplified Analysis of Hollow Beams with Longitudinal Webs Subjected to Torsional Loads, Eryk Kosko 103
Stress Analysis of Nondevelopable Semimonocoque Structures Considered as Beams of Variable Section, Leon Beskin 203
The Stress-Area Method of Designing Beams, Gilbert C. Best 298
Stresses in a Ring Loaded Normal to Its Plane, E. R. Walters 235
Three-Dimensional Analysis of Engine Mount Rings by a Strain Energy Method, Charles E. Mack, Jr. 1
Structural deformation on airplane characteristics, the influence of 94

THOMAS, R. N., AND A. C. CHARTERS. Aerodynamic Performance of Small Spheres from Subsonic to High Supersonic Velocities 468
TIFFORD, ARTHUR N. The Thermodynamics of the Laminar Boundary Layer of a Heated Body in a High-Speed Gas Flow Field 241
TSIEN, HSUE-SHEN, AND LESTER LEES. The Glauert-Prandtl Approximation for Subsonic Flows of a Compressible Fluid 173
Tubing, magnesium-alloy, mechanical properties of 31

VANTINE, A., AND M. H. KIEHLE. A Consideration of Calculated Versus Flight Test Take-Off Performance 263
Vibrations of composite structures 108
Vibration theory combining the dynamic stiffness and mobility methods 349

WALTERS, E. R. Stresses in a Ring Loaded Normal to Its Plane 235
WANG, CHI-TEH. Letter to the Editor (Stress Analysis and Structures) 432
WEIBEL, E. E. Buckling of Stiffener and Elastic Sheet Combinations Under Pure Bending 393
WELTER, GEORGES. Curved Aluminum-Alloy Sheets in Compression for Monocoque Constructions 357
WESKE, JOHN R. Analytic Investigation of Problems Concerning the Flow of Cooling Air in Light Airplane Engine Installations 63
Wing-wake frequency with application of the Strouhal Number, investigation of the 51

YACHTER, M. A Note on Bending Beyond the Proportional Limit 21
YORGIADIS, ALEXANDER J. Graphical Analysis of Performance of Hydraulic Shock Absorbers in Aircraft Landing Gears 42

Services of the Aeronautical Archives of the Institute of the Aeronautical Sciences

The services of the Aeronautical Archives are available to all members of the Institute, to Corporate Members, to advertisers in the Aeronautical Engineering Review and, under usual library limitations, to the public. Four specialized services are available.

The Paul Kollsman Library

This lending library service makes available, *without charge*, the latest and more important aeronautical books.

As far as the facilities permit, any person in the United States over 18 years of age who can furnish references which certify to his or her responsibility may become a member of the library.

Members may request the loan of any aeronautical or technical book they wish to borrow. Through an exchange agreement with the Engineering Societies Library, any book on general engineering may be borrowed from its great collection of over 160,000 volumes.

A photostating service is available at usual library rates.

Applications for membership in the library and further information will be sent on request.

The Burden Reference Library

This reference library contains over 12,000 aeronautical books, magazines, pamphlets, and reports gathered from world-wide sources and is one of the most complete aeronautical libraries in the world. Material from this library is not available for loan but may be used for reference purposes at the Aeronautical Archives.

The Pacific Aeronautical Library
6715 Hollywood Boulevard
Hollywood, California

Established in cooperation with the aircraft companies the library serves. The leading aircraft companies in or near Los Angeles participate in its support and operation.

This service library for aeronautical research is available to the public for reading privileges. Source material includes aerodynamic and structural research reports, as well as books on drafting, production methods, history, and allied sciences. It furnishes books, periodicals, and pamphlet material to the participating aircraft companies to supplement their engineering libraries.

The Aeronautical Archives Technical Information Service

This service has experienced personnel under the supervision of trained aeronautical engineers to compile any information desired. The services range from listing specialized reference books to the preparation of exhaustive bibliographies, digesting of reports, and general surveys of any aeronautical subject. Some of the available services are:

Bibliographies on any aeronautical subject.
Reports on any aeronautical subject.
Digests of aeronautical books, papers, periodicals, and references.
Translations.
Engineering investigations of special aeronautical subjects.
Biographies of individuals engaged in aeronautics.
Photostats of any aeronautical or general engineering material.
Microfilms made on special order.
Photographs made from the Institute's photographic collection.
Drawings and tracings made.

In addition to the services mentioned any commission which comes within the scope of the Service will be accepted. Special arrangements may be made for work requiring several weeks or months.

Translators are available for accurate transcriptions of all foreign language data. Translations are carefully edited by trained engineers.

Reproductions of any material in the Aeronautical Archives of the Institute may be ordered at standard photostat rates.

INSTITUTE OF THE AERONAUTICAL SCIENCES
1505 RCA BUILDING WEST
30 ROCKEFELLER PLAZA, NEW YORK 20, N. Y.

SUGGESTIONS FOR CONTRIBUTORS TO THE PUBLICATIONS *of the* INSTITUTE *of the* AERONAUTICAL SCIENCES

The Institute of the Aeronautical Sciences invites both members and nonmembers from any country to submit papers for publication in the JOURNAL OF THE AERONAUTICAL SCIENCES and the AERONAUTICAL ENGINEERING REVIEW. The Institute, following the practice of other societies, does not pay for contributions.

The following directions for the preparation of papers, if followed by authors, will save correspondence, avoid the return of papers for changes, minimize the work of preparation for the printer, and save the expense due to the charges made for "author's corrections."

MANUSCRIPTS: Papers must be written in English, in original typewriting on one side only of white paper sheets, consecutively numbered and be double or triple spaced with wide margins. Manuscripts should be prepared with great care so that they will be typographically accurate. Paragraphing should be given special attention. Papers should be written in the third person, reference to the writer being made as "the author." Avoid the use of the words "I," "we," and "you." Blueprint copies of papers are unacceptable as it is impossible to mark directions to the printer on them. Correcting, changing, or adding to papers after they are in type is costly. It is, therefore, imperative that papers submitted be in final form. Typographical errors may be corrected on proofs, but if authors wish to add material, they may do so at their own expense. In mailing, drawings may be rolled, but manuscripts should be sent flat. Send by first class mail (register if you wish for your own protection) to the Editorial Office, Institute of the Aeronautical Sciences, 1505 RCA Bldg. West, 30 Rockefeller Plaza, New York 20, N.Y. All manuscripts will be examined by the Editorial Committee and by the Editor. Authors will be advised as promptly as possible whether the paper is acceptable for publication.

TITLES: The title of the paper should be brief. The name and initials of the author should be written as he prefers. The use of the full name of an author is advocated because of the frequent duplication of initials and surnames which sometimes makes it difficult to establish the identity of the author. This is particularly important for large annual indexing and abstracting services. All titles and degrees or honors are omitted. The name of the organization with which the author is associated should be placed after his name on a separate line. The date on which the paper is received will be inserted by the Editor.

SUMMARIES OR ABSTRACTS: An abstract to be printed at the beginning should accompany each article. It should be adequate as an *index* and as a *summary*. It should contain a statement of major conclusions reached, since summaries in many cases constitute the only source of information used in compiling scientific reference indexes. Abstracts printed in other journals, especially foreign, in most cases, consist of summaries from printed papers. The summary should explain as adequately as possible the major conclusions to a nonspecialist in the subject. The summary should contain from 100 to 300 words, depending on the length of the paper.

SUBHEADINGS: Subheadings should be inserted by the author at frequent intervals. The work of editorial preparation will be simplified by the author providing many subheadings. Owing to the breaking of columns and the insertion of illustrations, some of the subheadings may have to be omitted.

SHORTENING OF PAPERS: Some papers, at the end, fill in only a portion of a page. This leaves much wasted blank space as succeeding articles are started at the top of a page. Authors should indicate by notation on the left-hand side of the page what matter may be omitted when "runovers" occur. This request is important as the Journal cannot afford in the future, as it has in its earlier issues, to have blank half pages or more at the end of papers.

MATTER USUALLY DELETED: Acknowledgments of assistance in preparation of paper, except by collaborators. Photographs or illustrations of little technical interest and not showing advances in general practice. Too detailed tabular matter (general results of such tables may be included in the text). Lengthy descriptions of materials or processes or of preliminary experiments or theories that preceded final results; salient features only are of interest.

REFERENCES AND FOOTNOTES: References should appear as footnotes only, numbered consecutively, grouped together at the end of the manuscript. The arrangement should be as follows: (for books)—[1] Durand, W. F., *Aerodynamic Theory*, 1st Ed., Vol. 1, p. 23; Julius Springer, Berlin, 1934. (For magazines)—

[1]Englund, C. R., Crawford, A. B., and Mumford, W. W., *Some Results of a Study of Ultra-Short-Wave Transmission Phenomenon*, Proc. I. R. E., Vol. 20, No. 12, pp. 481 and 482, March, 1933. Please give author, title, edition, volume, page, publisher and date of publication as indicated. Omission of one required fact causes much extra editorial work and possible inaccuracies. All references should be grouped at the end of the article.

ILLUSTRATIONS: Illustrations should accompany manuscripts and each should always be referred to in the text, preferably by number. Drawings or graphs should not be larger than 12 × 16 inches, and must be made with jet black India Ink on white paper or tracing cloth, the latter being preferred. *Do not use typewriter for lettering.* The smallest lettering on 8 × 10 inch figures should be no less than 1/4 inch high. Cross-section paper (white with black lines) may be used, but should not have more than 4 lines per inch. If finer ruled paper is used, the major division lines should be drawn in with black ink, omitting the finer divisions. In the case of finely ruled paper, only blue-lined paper can be accepted. *Tracing paper and blueprints* are not acceptable. Lettering and all markings must be large enough to be readable after reduction. Mail rolled or flat, never fold. Drawings that cannot be reproduced (including pencil drawings) will be returned to the author for redrawing, thus delaying publication of the paper. Photographs should be distinct and show clear black and white contrasts. They must be on glossy white paper. Avoid round and oval photographs.

CAPTIONS AND LEGENDS: Legends or captions must accompany each drawing or photograph submitted. If written on the drawing or photograph, they should be placed below and well outside the part to be reproduced. It is better to place them on separate sheets of paper pasted to the back of the drawings or photographs. Each table should have a caption such as Table 1, Table 2, Table 3, etc. Captions should be complete in themselves so as to make the data intelligible to the reader without reference to the text. A duplicate list of captions for figures should be included as the last page of the manuscript. Use "Fig. 1" (not Figure 1), Figs. 3 and 4, etc., in both the text and the numbering of illustrations. In the text, "Eq. (1)," or "Eqs. (1) and (2)" are preferable to "Equation (1)." In captions and legends, except for "Fig." and "Eq." and table headings, write all words in full; do not abbreviate. Avoid placing explanatory written matter in the drawings; it should be in the text.

MATHEMATICAL WORK: Only the simplest formulas should be typewritten; all others should be carefully written in pen and ink, the writing to be large enough so that ample room is provided to mark mathematical matter for the printer. A considerable space for marking should be allowed above and below all equations. All complicated equations should be repeated on separate sheets with plenty of space left for marking. The solidus should be used for simple fractions appearing within the text. Make all expressions clear to the typesetter. Greek letters used in formulas should be clearly designated by name on the margin of the manuscript. All symbols should be clearly written and carefully checked. The difference between capital and lower-case letters should be clearly distinguished and care taken to avoid confusion between zero (0) and the letter (o), between the numeral (one) and the letter (ell) and the prime (′), between alpha and a, kappa and k, u and mu, v and nu, n and eta. All subscripts and exponents should be clearly marked and dots and bars over letters or mathematical expressions should be avoided. Avoid complicated exponents and subscripts. When it is necessary to repeat a complicated expression, it should be represented by some convenient symbol.

NOMENCLATURE AND ABBREVIATIONS: The National Advisory Committee for Aeronautics Nomenclature should be used in preference to any others. Standard abbreviations should be used, and it should be noted that most abbreviations are lower case, such as m.p.h., b.m.e.p., i.hp., b.hp., hp., . . . etc.

EDITORIAL AND PROFESSIONAL ACTIVITIES COMMITTEE

HUGH L. DRYDEN, *Chairman*

Aerodynamics
William Bollay
Kenneth S. M. Davidson
Walter S. Diehl
Hugh L. Dryden
R. Paul Harrington
P. E. Hemke
Eastman N. Jacobs
Th. von Kármán
Alexander Klemin
W. B. Klemperer
Otto C. Koppen
A. M. Kuethe
John G. Lee
John R. Markham
Clark B. Millikan
Shatswell Ober
W. Bailey Oswald
Manfred Rauscher
Elliott G. Reid
H. J. E. Reid
Hans Reissner
Benjamin F. Ruffner
G. B. Schubauer
Abe Silverstein
R. H. Smith
Th. Theodorsen
M. J. Thompson
Starr Truscott
Richard von Mises
Michael Watter
K. D. Wood

Air Transport
Ralph S. Damon
Charles Froesch
Melvin N. Gough
J. A. Herlihy
William Littlewood
A. A. Priester
Paul E. Richter
N. F. Scudder
T. P. Wright

Aircraft Design
Karl Arnstein
Rex B. Beisel
B. C. Boulton
C. P. Burgess
C. H. Chatfield
J. W. Crowley, Jr.
R. C. Gazley
Leroy R. Grumman
Hall L. Hibbard
A. L. Klein
Otto C. Koppen
I. M. Laddon
John G. Lee
C. J. McCarthy
William H. Miller
R. H. Prewitt
Igor I. Sikorsky
E. A. Stalker
Th. Troller
Starr Truscott
R. H. Upson
Fred E. Weick
Robert J. Woods

Aircraft Production
John L. Atwood
W. E. Beall
Carl de Ganahl
W. K. Ebel
Fredric Flader
Hall L. Hibbard
Guy A. Luburg
C. J. McCarthy
A. E. Raymond
W. T. Schwendler
Harry A. Sutton
John Tjaarda
Robert J. Woods

Radio
C. S. Draper
Lloyd Espenschied
C. G. Fick
Lewis M. Hull
Haraden Pratt
F. X. Rettenmeyer

Physiologic Problems
H. G. Armstrong
Louis H. Bauer
David B. Dill
Eugene Du Bois
W. Randolph Lovelace, II
Ross A. McFarland
A. D. Tuttle

Power Plants and Propellers
M. A. Biot
George W. Brady
Frank W. Caldwell
Ivan H. Driggs
Louis H. Enos
David Gregg
L. S. Hobbs
Albert R. Jacobs
E. E. Johnson
H. M. McCoy
W. C. Nelson
Arthur Nutt
Shatswell Ober
Elliott G. Reid
Hans Reissner
David R. Shoults
C. Fayette Taylor
E. S. Taylor
Th. Theodorsen
A. V. Willgoos
D. H. Wood

Structures and Materials
M. A. Biot
W. B. Bleakney
C. P. Burgess
E. W. Conlon
George W. DeBell
J. P. Den Hartog
L. H. Donnell
L. G. Dunn
Richard C. Gazley
W. C. Geer
E. C. Hartmann
N. J. Hoff
Zay Jeffries
W. B. Klemperer
E. E. Lundquist
C. J. McCarthy
C. F. Nagel, Jr.
J. S. Newell
Alfred S. Niles
Thomas D. Perry
W. Ramberg
E. Reissner
F. R. Shanley
H. W. Sibert
S. Timoshenko
H. S. Tsien
L. B. Tuckerman
George Tweney
Th. von Kármán
J. A. Wise
J. E. Younger

Meteorology
C. F. Brooks
Karl O. Lange
D. M. Little
E. J. Minser
Sverre Pettersen
F. W. Reichelderfer
A. F. Spilhaus
P. V. H. Weems
H. C. Willett

Education
R. Paul Harrington
C. S. Jones
Alexander Klemin
Clark B. Millikan
W. C. Nelson
George B. Pegram
Richard H. Smith
Ben D. Wood

Fuels and Oils
D. P. Barnard
A. L. Beall
Luis de Florez
J. H. Doolittle
Graham Edgar
R. T. Goodwin
S. D. Heron
A. M. Rothrock

Instruments
P. R. Bassett
W. G. Brombacher
Charles H. Colvin
C. S. Draper
Lucien L. Friez
Walter McKay
W. A. Reichel
C. F. Savage
A. F. Spilhaus
S. J. Zand

I.A.S. REPRESENTATIVES TO OTHER ORGANIZATIONS

Aircraft Industries Association of America, Inc.—CHARLES MARCUS

American Association for the Advancement of Science—J. C. HUNSAKER

American Society of Mechanical Engineers—JOHN E. YOUNGER

American Standards Association—P. R. BASSETT

Engineering Society of Detroit—DONALD C. HUNT, GEORGE TWENEY

Greater New York Safety Council—WILLIAM LITTLEWOOD

Daniel Guggenheim Medal Board of Award—CHARLES H. COLVIN, RALPH S. DAMON, LESTER D. GARDNER

Institute of Radio Engineers—L. M. HULL

Manufacturers Aircraft Association—J. T. HARTSON

National Aeronautic Association—WILLIAM R. ENYART

National Research Council Engineering Division—FRANK W. CALDWELL

National Safety Council—JEROME LEDERER

New York Museum of Science and Industry—LESTER D. GARDNER

Society of Automotive Engineers—EDWARD P. WARNER

INSTITUTE *of the* AERONAUTICAL SCIENCES
1932–1945

Since its incorporation in October, 1932, as a scientific membership society to advance the art and science of aeronautics, the Institute of the Aeronautical Sciences, in over thirteen years of service to aviation, has become the representative technical society for the aviation industry and profession. It is the only organization in the United States which brings together all of the sciences and branches of engineering and technology which are applied to aeronautics.

Activities

In this year, coincident with the great increase in aeronautical production and research in the nation's war effort, the Institute has expanded its membership and activities in keeping with the greater demands made upon its services. Beginning with aeronautical students, the Institute has increased the number and activities of Student Branches. Members of the Institute in aeronautical centers are organized in local Sections which hold their own meetings. More of these Sections have been formed this year and additional services provided for members. The Annual Meeting and other national meetings provide forums where specialists in all the aeronautical sciences may present and receive reports on progress made in their particular fields and learn of developments in other fields that have a bearing on their own work. Several annual awards and honors are conferred by the Institute to recognize and encourage outstanding achievement in the aeronautical sciences.

Publications

Papers presented at meetings or submitted to the Editorial Board are published in the JOURNAL OF THE AERONAUTICAL SCIENCES or the AERONAUTICAL ENGINEERING REVIEW. The JOURNAL prints in each issue several full length scientific papers on new research and developments in various fields applied to aviation. The REVIEW keeps members and subscribers up to date on aeronautical news and literature through reviews of new books and periodical articles, government publications and trade literature and publishes papers on applied engineering and aircraft production.

The AERONAUTICAL ENGINEERING CATALOG, published yearly, is a guide to sources and specifications of materials, parts, and accessories used in the design and production of aircraft, aircraft engines, and parts.

Research Facilities

Through the Aeronautical Archives of the Institute, members have for their use the most complete aeronautical library and reference research facilities maintained by any technical society. At Institute headquarters in New York, The W. A. M. Burden Reference Library of books, reports and periodicals, the Aeronautical Index of subject files, biographic files and bibliography, and the historical and art collections in the Archives are available for study. The Pacific Aeronautical Library at 6715 Hollywood Boulevard, Los Angeles, maintains a reference collection and reading room for members and loans books to company libraries in the area. Through The Paul Kollsman Library, aeronautical books are lent by mail without charge to members anywhere in the continental United States. In addition to a complete collection of standard aeronautical reference works, the Kollsman Library has available for loan new aviation books as they are reviewed in the AERONAUTICAL ENGINEERING REVIEW.

Membership

In addition to membership in professional societies representing their particular fields, specialists applying their knowledge and experience to aeronautics find membership in the Institute of great value in the contacts made with others engaged in aeronautical work and in the broad coverage of all aeronautical problems furnished through its meetings and publications. All applications for membership are carefully reviewed by the Admissions Committee, which recommends the grade of membership for which the applicant is found eligible. There are advanced grades of membership—Associate Fellow, Fellow, Honorary Fellow—to which members may be elected as their experience warrants. Thus, a member receives due recognition—more valuable because it is given by his colleagues—for his contributions to the progress of aeronautics. New applicants may be elected initially by the Admissions Committee to the grade of MEMBER if they are engineering graduates with at least three years of experience or have had over five years' experience in research, engineering, or other special work applied to aviation; to the grade of Industrial Member if they have acquired a recognized standing in an administrative capacity in the aviation industry; to the grade of Technical Member if they are recent engineering school graduates or are engaged in technical aeronautical work. For those interested or engaged in aeronautics or fields related to aeronautics who wish to participate in the activities of the Institute, the grade of Affiliate is provided. Student Members are admitted by application through Student Branches organized at their schools. Aeronautical companies, as well as individuals, are affiliated with, and participate in, the support of the Institute through Corporate Membership.

Dues

An entrance fee of $5.00 is required of all new members who apply for admission to a grade of membership to be specified by the Admissions Committee (Corporate Members, Student Members, and those who apply specifically for the grade of Affiliate being excepted).

Annual membership dues include a subscription to the AERONAUTICAL ENGINEERING REVIEW. For the various grades of membership they are as follows: Fellows—$16.50; Associate Fellows—$12.50; MEMBERS—$10.50; Industrial Members—$10.50; Technical Members—$6.50; Affiliates—$6.50.

The regular subscription price for the JOURNAL OF THE AERONAUTICAL SCIENCES and the AERONAUTICAL ENGINEERING REVIEW is $7.00 and $3.00 per year, respectively. Members may subscribe to the JOURNAL at one-half the regular subscription rate.

Those who are engaged in aeronautical work or who have an interest in any technical phase of aviation will find the services of the Institute to be a necessary aid in keeping abreast of developments in these times of such rapid progress. An application form and further information about membership can be obtained from an Institute member or by writing to the Secretary.

INSTITUTE OF THE AERONAUTICAL SCIENCES
1505 RCA BUILDING WEST
30 ROCKEFELLER PLAZA
NEW YORK 20, N. Y.